UNIVERSITÄT
BAYREUTH

Lehrstuhl für Kristallographie

Dynamic charge densities of amino acids and proteins

Von der Universität Bayreuth
zur Erlangung des akademischen Grades eines
Doktors der Naturwissenschaften (Dr. rer. nat)
genehmigte Abhandlung

vorgelegt von
Prathapa Siriyara Jagannatha
aus Mallesara, Indien

1. Gutachter: Prof. Dr. Sander van Smaalen
2. Gutachter: PD. Dr. Birger Dittrich

Tag der Einreichung: 25. 03. 2013
Tag der Kolloquiums: 19. 07. 2013

Dedicated To...

My beloved Family & Teachers

Contents

Chapter 1

Introduction

In conventional notion, a crystal is defined as a solid material formed by a periodic arrangement of atoms. The atoms in crystals are always vibrating about their mean positions even at very low-temperatures. Knowing the exact structure is essential to understand the chemical bonding, physical and chemical properties and also mechanisms of chemical reactions. The atomic structure of a crystal can be determined by the X-ray diffraction method. In this method a beam of X-rays strikes a crystal, displaying a diffraction pattern that, in turn, can be transformed into a 3D model of the crystal structure. Since X-ray scattering by electrons is much stronger than that of the nuclei, intensities of scattered X-rays are almost exclusively determined by the distribution of the electrons. Hence the electron density distribution of crystals can be studied by the method of X-ray diffraction.

Routine crystal structure solution from the X-ray diffraction data provides simple descriptions of crystal structures with positional parameters representing positions of the atoms in the unit cell and anisotropic displacement parameters (ADPs) representing their thermal motion. This method is known as Independent Atom Model (IAM) and is based on spherical-atom approximation. To get the detailed information about the chemical bonding, it is necessary to study the aspherical electron density distribution.

The detailed aspherical electron density analysis of crystalline materials using low-temperature and high-resolution X-ray diffraction data can provide insight into the nature of chemical interactions. And it allows the evaluation of one-electron properties in crystalline materials (Hirshfeld, 1991; Spackman, 1992; Coppens, 1997; 1998; Martin and Pinkerton, 1998; Koritsanszky and Coppens, 2001). Electron-density analysis has become truly accessible by the advances made in experimental techniques with the availability of intense X-ray sources and modern area detectors for rapid data collection. On the other hand, by the help of ever increasing computational power, it is now possible to calculate with reasonable accuracy electron densities of molecules theoretically, using quantum-chemical methods (Coppens, 2005). These developments offer a possibility to directly compare the theoretical density with the experimental one, and hence help to access the reliability of both theory and the experiment.

However, the major obstacle in comparing theoretical electron density with experimental electron density lies in the type of the electron density obtained by these methods. The electron density obtained from experiment is time-averaged over the thermal motion of a crystal and is denoted as dynamic electron density. Whereas theoretical estimates of electron densities are based on *ab-initio* calculations within the Born-Oppenheimer approximation and are static. Therefore, for comparisons one has to either thermally smear the theoretical electron density or deconvolute the experimental electron density from the thermal motion (Stevens et al., 1977). The former case is difficult, since the exact knowledge about vibrational motion of the atoms is usually not available. Therefore the later case of deconvoluting the thermal motion from the electron density has become the method of choice. This method of determining static electron density from the experimental data has become more prevalent, especially after the advent of the quantum theory of atoms in molecules (QTAIM) (Bader, 1990), which is defined for static electron densities. With the aid of QTAIM, information on chemical interactions and properties can be retrieved from the electron densities.

The deconvolution of static density from the thermal motion can only be achieved through a structure model (Hirshfeld, 1976; Coppens, 1997). For this purpose Hansen and Coppens (1978) proposed the multipole (MP) model. It describes the aspherical electron density. It accounts for the reorganization of valence electrons due to chemical bonding by MP parameters and it accounts for thermal smearing by ADPs. Details about the MP model for electron-density analysis are given in Chapter 2.

On the other hand, atomic thermal vibrations plays an important role in chemical interactions and reactivity. For example, in temperature-dependent phase transitions or in temperature-dependent chemical reactions. Therefore it is important to take into account the effects of temperature and thermal vibrations on the electron densities. One way to understand the effect of temperature on electron densities is by considering dynamic electron densities in association with the corresponding static electron density (for example MP model density) which might be helpful in revealing the effects of temperature on chemical interactions and properties.

Although, the dynamic electron density calculation is an old concept and is stated as early as 1968 (Stewart, 1968a), the quantitative analysis of the total dynamic electron density and its topological properties remained a neglected field. The dynamic density analysis have been restricted to the study of dynamic deformation densities (Ruysink and Vos, 1974; Stevens et al., 1977; Nijveldt and Vos, 1988; Coppens, 1997; Jelsch et al., 1998; Coppens and Volkov, 2004). This is mainly due to the presence of series-termination effects in the calculated maps (Stevens et al., 1977; Jelsch et al., 1998) which is the result of the limited set of structure factors available from the experiment.

The objective of the present thesis is to develop a method for the calculation of total dynamic electron density from the corresponding structural model by avoiding series termination effects. A topological analysis of dynamic model densities in association with the corresponding static electron densities is presented for selected compounds, in order to find out the effect of temperature on electron densities. For these purposes, we have employed high-quality data sets of several amino acids, a tripeptide and a protein from the literature. It will be shown that dynamic electron densities can be successfully reconstructed from the structure model of any size (even for proteins). By using the multi-temperature data set of D, L-serine, the effect of temperature on electron densities and its chemical bond properties are illustrated.

The dynamic electron densities from different static model densities such as, IAM, IAM obtained by high-order refinement (referred to as IAM-HO), MP model and invariom model (INV) are constructed and results are presented. By using these dynamic model densities as prior or reference densities in maximum entropy calculations (MEM), electron-density analysis have been performed. As opposite to the MP model, MEM provides a model-independent, dynamic electron density, and it does not suffer from correlated parameters by its very principle. It will be shown that the MEM provides a good estimation of electron density distribution together with good characterization of chemical bonding and its properties. Also it will be shown that, the electron densities obtained by MEM are independent from the MP refinement and will become especially important for the intended application to large systems (for example proteins) where the free refinement of MP model is not possible.

Different methods of obtaining static and dynamic electron densities are described in Chapter 2. A brief introduction followed by principle of determination of electron density by both MP method and MEM are given. Recent developments towards enhancing the quality of the electron density map obtained by MEM are discussed. A short description about the topological analysis of electron density maps according to the Bader's Quantum Theory of Atoms in molecules (QTAIM) is given.

Chapter 3 concentrates on the computer program EDMA (Electron Density Map analysis) for topological analysis of discrete electron densities according to QTAIM. The program EDMA has been written in 2002–2003 (Palatinus, 2003). Recently, several developments have been made to improve the functionality of the program. This chapter provides the current functionality of EDMA together with recent developments and algorithms used in the program. A series of test calculations were performed for the validation of EDMA and they demonstrate the accuracy of the methods.

In the Chapter 4, we describe the procedure of construction of dynamic electron densities corresponding to a structure model and demonstrate the results of dynamic electron densities calculated both from IAM and MP model using the data of α-glycine and multi-temperature data set of D, L-serine. In order to find an empirical description of the differences and similarities between the static and dynamic electron densities, topological analysis according to QTAIM have been performed. The effect of temperature on dynamic electron density have been presented by comparing the results of multi-temperature data set of D, L-serine. The optimal grid size has been established in order to avoid any series termination effects. A topological analysis of the dynamic electron densities provides a quantitative measure for the effects of zero-point vibrations and of temperature on electron densities.

Chapter 5 reports on the effect of choice of prior on the MEM densities. For this purpose, we have employed four different dynamic model densities as prior in MEM calculation. The dynamic model densities are obtained from structure models of IAM, IAM-HO, INV and MP models of α-glycine, D, L-serine, L-alanine and Ala-Tyr-Ala. Topological analysis of both dynamic model densities and MEM densities are compared to find out the variation of properties. The influence of the different dynamic model densities in regard to MEM densities is discussed.

The electron-density analysis of the protein Crambin is described in Chapter 6. Both the static and dynamic electron densities have been calculated and the electron density maps are analyzed. The topological properties obtained were compared in order to find out the influence of thermal vibration on the electron densities and to get information about the structural stability.

Appendices provide supplementary information of the compounds studied in this thesis including comprehensive sets of electron density maps, difference density maps, deformation density maps and all the topological properties obtained by static and dynamic densities.

Chapter 2

Methods for electron density studies

There are several established methods for describing the electron density in a crystal. One method is the conventional Independent Atom Model (IAM). It is based on the assumption that the atomic electron density is well described by the spherically averaged density of the isolated atom. According to IAM, any molecular crystal is formed by the collection of such independent spherical atoms. It provides a simple description of the crystal structure, with positional and displacement parameters (due to thermal motion) of the atoms in the unit cell, using X-ray diffraction data. However, it does not account for charge transfer and any bonding effects on the electron density.

To overcome this deficiency Coppens et al. (1979) have proposed the idea of using the kappa formalism (kappa, κ) or radial refinement. It gives a simple modification to the IAM by separating the core (ρ_c) and the valence (ρ_v) electron density of an atom in the model and allowing ρ_v to expand. Therefore, the scattering contribution of the valence electrons is separated from that of inner shells to consider the adjustment of population and radial dependence of the valence shell.

According to the kappa formalism, atomic density is expressed as,

$$\rho(\mathbf{r}) = \rho_c(r) + P_v \kappa^3 \rho_v(\kappa r) \tag{2.1}$$

where, P_v is the valence shell population parameter and κ represents the radial parameter which allows the contraction and expansion of the valence shell. The parameter κ scales the radial coordinate r. If $\kappa > 1$ then the same density is obtained at a smaller r value and consequently, the valence shell is contracted. On other hand for $\kappa < 1$, the valence shell expands. This model allows calculating the magnitude and direction of dipole moments and atomic charges. The obtained results from the kappa formalism are found to be in good agreement with the experimentally and theoretically measured values (Coppens et al., 1979). However, this model fails to describe the non-spherical distribution of the atomic electron density between the atoms, since the formalism still treats ρ_v as spherical in the model.

2.1 Multipole method

In order to understand the bonding effects on the electron density, aspherical modelling of electron density have been established. Multipole (MP) model is one such model to describe the aspherical electron density and thereby providing insight into the nature of chemical bonding and intermolecular interactions involved in crystalline materials (Coppens, 1997).

In the multipole approach, electron densities of atoms involve not only just the spherical contraction/expansion of the valence shell, but also include an aspherical description depending on the neighbouring atoms. It uses an aspherical model for the description of the electron density based on a nucleus-centered finite multipole expansion. This approach was first developed by Stewart (1968b; 1969; 1973; 1976) and later modified by Hansen and Coppens (1978).

According to the Hansen and Coppens (1978) multipole model, individual atomic densities are divided into three components: the core, a spherical valence density, and the valence deformation density. The atomic density, $\rho(\mathbf{r})$, becomes (Coppens, 1997)

$$\rho(\mathbf{r}) = P_c \rho_c(r) + P_v \kappa^3 \rho_v(\kappa r) + \sum_{l=0}^{l_{max}} \kappa'^3 R_l(\kappa' r) \sum_{m=0}^{l} P_{lm\pm}\, d_{lm\pm}(\theta, \phi)\,, \tag{2.2}$$

where, P_c, P_v and P_{lm} are the refinable population parameters. P_v gives an estimate of the net atomic charge q $= N_v - P_v$, where N_v is the number of valence electrons in a free neutral atom. $\rho_c(r)$ and $\rho_v(\kappa r)$ are the spherical core and valence electron densities. The last term corresponds to the deformation density, which consists of density-normalized real spherical harmonics $d_{lm\pm}$ and the radial functions R_l. κ and κ' are screening parameters, which account for radial expansion or contraction of the valence shell. Usually $l_{max} \leq 4$ is employed.

The radial function R_l in Eq. (2.2) is defined as a Slater type function,

$$R_l(r) = \frac{\zeta_l^{n_l+3}}{(n_l+2)!}\, r^{n_l}\, exp\,(-\zeta_l r) \tag{2.3}$$

where, n_l are positive integers with $n_l \geq l$ and the ζ_l are single-Slater orbital exponents (Coppens, 1997).

A number of software packages have been developed for structure refinements of the parameters of the Hansen and Coppens (1978) multipole formalism against X-ray diffraction data (Stewart and Spackman, 1983; Stash and Tsirelson, 2002b; Bianchi and Forni, 2005; Volkov, Abramov, Coppens and Gatti, 2000; Jelsch et al., 2005; Volkov et al., 2006). However, the most widely used packages are XD2006 (Volkov et al., 2006) and MoPro (Jelsch et al., 2005). In this thesis I present results of multipole electron density analysis using XD2006 for small molecules and MoPro for proteins.

The aspherical multipole modelling approach gives a much more accurate description of the measured electron density than IAM. It accounts for the distribution of the electrons in bonds and in lone pairs. It also allows to quantitatively measure any charge transfer between atoms. And with the aid of quantum theory of atoms in molecules (QTAIM) (Bader, 1990) one can evaluate the nature of chemical interactions, topological properties, electrostatic properties including the energy, the electrostatic potential, atomic and molecular dipole moments.

The multipole refinement of molecular crystals involves a large number of parameters. In addition to the three positional coordinates and the six ADPs that are to be refined in the IAM, in the multipole model up to 31 parameters for the monopole P_v, the multipole populations P_{lm} and the radial expansion/contraction parameters κ and κ' are to be refined for each individual atom. As a result, the data to parameter ratio in MP refinement are often small, especially in case of large molecules. In addition to space group symmetry, symmetry constraints and chemical constraints can be used to reduce the number of refinable parameters. However in case of proteins and when high resolution data is not available even these extra constraints are not sufficient to perform *ab-initio* multipole refinement. Therefore to achieve an aspherical description of electron density, multipole parameters from a database can be used as an alternative. In the last decades, a number of multipolar databases have been developed both from theory and experiment. They include the UBDB (University at Buffalo Databank) (Volkov et al., 2004) and Invariom databases (Dittrich et al., 2006), which are theory based, and the ELMAM

(Experimental Library of Multipolar Atoms Model) (Pichon-Pesme et al., 1995) and ELMAM2 (Domagała et al., 2012) databases, which are experiment based. These databases have been extensively tested and established (Jelsch et al., 1998; 2000; 2005; Dittrich et al., 2005; 2007; 2008; 2006;a; 2009;a; Volkov et al., 2007; Zarychta et al., 2007; Bak et al., 2009). In the Chapter 5, we have employed the invariom database for the calculation of multipolar electron density of amino acids. In Chapter 6 the multipolar electron density of a protein is presented on the basis of the ELMAM2 database.

2.2 Maximum Entropy Method

2.2.1 A brief introduction

Apart from model-based methods, the maximum entropy method (MEM) can be used to obtain electron densities in crystalline materials from X-ray diffraction data. Unlike the multipole method, which gives the static density deconvoluted from the thermal parameters through a structure model, the MEM produces a time-averaged electron density, denoted as the dynamic electron density. It is model-independent and yields an electron-density distribution even from a limited number of diffraction data.

The MEM has been first proposed by Jaynes (1957; 1979; 1986) in the field of statistical mechanics for data analysis and in order to extract the maximum information from available data without introducing any artifacts. Later Gull and Daniell (1978) have used this MEM approach for image-reconstruction from noisy data in the field of radio astronomy. Gull and Daniell (1978) also proposed its application to all types of image-processing methods, including X-ray crystallography, spectroscopy and electron microscopy. The first usage of the MEM in the field of X-ray crystallography has been reported by Collins (1982). He reconstructed the electron density from the X-ray diffraction data using MEM. Later, several groups have employed the MEM to obtain electron density distributions, and they contributed towards the improvement of the performance of the MEM (Sakata and Sato, 1990; de Vries et al., 1994; Roversi et al., 1998; Palatinus and van Smaalen, 2002; Tanaka et al., 2002; Papoular et al., 2002; Ohno et al., 2007; Takata, 2008; van Smaalen et al., 2003; Hofmann et al., 2007a;b; Netzel et al., 2008; van Smaalen and Netzel, 2009). Essential features of an accurate MEM are briefly described in Section 2.2.3.

The MEM electron density analysis now has become a promising approach to qualitatively reveal the chemical bonding features in the crystalline materials (van Smaalen and Netzel, 2009). The MEM electron density map provides a precise description of the aspherical distribution of electron density. Several MEM studies have reported electron densities that are comparable to those obtained by MP refinements (Hofmann et al., 2007a;b; Netzel et al., 2008; van Smaalen and Netzel, 2009). However, the accuracy of MEM electron densities can be improved by employing prior information which is ever closer to the true density (van Smaalen and Netzel, 2009). In this direction, we have obtained and compared the electron densities of amino acids and a tripeptide by the MEM, employing different prior densities, which is described in the Chapter 5.

Other than electron-density analysis, the MEM also has applications in describing atomic disorder (Dinnebier et al., 1999; Wang et al., 2001), anharmonic thermal motion (Kumazawa et al., 1995; Bagautdinov et al., 1998), deconvolution of powder diffraction data (Gilmore, 1996), the extraction of phases from intensities of Bragg reflections (Bricongne, 1988) and others. In combination with the Rietveld method, the MEM has been successful in obtaining a structural model from powder diffraction data (Takata et al., 1995). It also has application in deriving electron density in (3+d)-dimensional space (van Smaalen et al., 2003; van Smaalen, 2007) and in determining the shapes of modulation functions of modulated crystals from the derived electron densities (Palatinus and van Smaalen, 2004; van Smaalen and Li, 2009).

2.2.2 Principle of the MEM

In order to reconstruct the electron density by the MEM, the unit cell of a crystal structure is divided into a grid of N_p=$(N_1 \times N_2 \times N_3)$ pixels. The grid is defined in such a way that grid points lie on the symmetry elements and in between them, so that each grid point is transformed onto itself or onto another grid point by all symmetry operators (van Smaalen et al., 2003). The electron density $\rho_k = \rho(\mathbf{x}_k)$ is discretized on this grid, where $\mathbf{x}_k$ is the position of the pixel k $(k = 1, ..., N_p)$.

The informational entropy S of the discretized electron density is defined as,

$$S = -\sum_{k=1}^{N_p} \left[\rho_k \log\left(\frac{\rho_k}{\rho_k^{prior}}\right) - \rho_k + \rho_k^{prior} \right] \tag{2.4}$$

where $\rho_k^{prior} = \rho^{prior}(\mathbf{x}_k)$ is the reference electron density or PRIOR density, which should incorporate all the information available about the electron density prior to using the experimental data in the MEM. In case of absence of prior information, a uniform prior (number of electrons distributed uniformly over the the unit cell) should be used. However this is not suitable for accurate electron-density studies (Palatinus and van Smaalen, 2002).

According to the principle of Maximum Entropy, the most probable electron density distribution maximizes the entropy of the discrete electron density (Eq. 2.4) subjected to normalization constraint as well as subjected to the constraint of fitting the diffraction data (Jaynes, 1957; Shannon, 1948). In case of absence of diffraction data, the MEM will produce the prior density as solution, that is $\rho_k = \rho_k^{prior}$.

The normalization constraint of electron density is given by C_N=0, with

$$C_N = \frac{V}{N_p} \sum_{k=1}^{N_p} \rho_k - N_e, \tag{2.5}$$

where V is the volume of the unit cell and N_e is the number of electrons in the unit cell.

Another constraint considered here is the F-constraint on the diffraction data (Sakata and Sato, 1990; Palatinus and van Smaalen, 2002; Hofmann et al., 2007a). The maximum of S is searched for variation of $\{\rho_k\}$ subject to the F-constraint, C_{F^2}=0 with

$$C_{F^2} = -\chi^2_{aim} + \frac{1}{N_F} \sum_{i=1}^{N_F} w_i \left(\frac{|F_{obs}(\mathbf{H}_i) - F_{MEM}(\mathbf{H}_i)|}{\sigma(\mathbf{H}_i)} \right)^2 \tag{2.6}$$

where $F_{obs}(\mathbf{H}_i)$ is the phased observed structure factor of the Bragg reflection with scattering vector $\mathbf{H}_i$. $\sigma(\mathbf{H}_i)$ is the standard uncertainty of $|F_{obs}(\mathbf{H}_i)|$ and w_i is the static weight. $F_{MEM}(\mathbf{H}_i)$ is obtained by discrete Fourier transform of the electron density $\{\rho_k\}$. The summation in Eq. (2.6) extends over all measured reflections N_F. The value of χ^2_{aim} defines the point of convergence through C_{F^2}=0. Reflection phases are the calculated phases of the structure model or they can come from the method of charge flipping (Palatinus, 2004; Samy et al., 2010).

To obtain the most probable density, the problem of maximum entropy has to be solved. The method of undetermined Lagrange multipliers is employed for that purpose. The maximum of Lagrangian

$$Q = S - \lambda C_{F^2} \tag{2.7}$$

has to be determined for variation of λ and $\{\rho_k\}$. Q reaches maximum when C_{F^2}=0 and $\{\rho_k\}$ need to fulfill a set of N_p nonlinear equations for which an analytical solution does not exist (Skilling and Bryan, 1984; Sakata and Sato, 1990):

$$\rho_j = \rho_j^{prior} exp\left[-\lambda \frac{\partial C_{F^2}}{\partial \rho_j}\right] \tag{2.8}$$

Therefore Eq. (2.8) has to be solved by an iterative procedure.

The Cambridge algorithm (Skilling and Bryan, 1984; Skilling, 1989; Gull, 1989) and Sakata-Sato algorithm (Sakata and Sato, 1990) are the two most popular algorithms existing for the iterative solution of Eq. (2.8) and Eq. (2.6). The Cambridge algorithm is based on simultaneous optimization of the Lagrange parameter λ and of the electron density by following

$$\rho_j^{(n+1)} = \rho_j^{prior} exp\left[-\lambda \left(\frac{\partial C_{F^2}}{\partial \rho_j}\right)^{(n)}\right] \tag{2.9}$$

The iteration starts with a small λ value with $\left\{\rho_j^{(0)}\right\} = \left\{\rho_j^{prior}\right\}$. The value of λ is marginally increased in the next iteration step and the optimized $\left\{\rho_j^{n+1}\right\}$ is determined. This process goes on with a small increments in the value of λ until the convergence of iteration is reached. The iterations are considered to be converged, when C_{F^2} of Eq. (2.6) drops below zero (C_{F^2}=0).

The Sakata-Sato algorithm follows a similar strategy of iteration like the Cambridge algorithm. But additionally it updates the values of $\left\{\rho_j^{prior}\right\}$ in each cycle, according to

$$\rho_j^{(n+1)} = \rho_j^{(n)} exp\left[-\lambda \left(\frac{\partial C_{F^2}}{\partial \rho_j}\right)^{(n)}\right] \tag{2.10}$$

However the principle of MEM does not allow an updating of the PRIOR. Moreover, van Smaalen et al. (2003) has shown that the electron density obtained by employing the Cambridge algorithm leads to a density which is marginally better than the Sakata-Sato algorithm. Therefore we have performed all the MEM electron density analysis of amino acids studied in this thesis using the Cambridge algorithm incorporated in the computer program BayMEM (van Smaalen et al., 2003) via the MEMSys5 package.

2.2.3 Development

There have been several attempts to enhance the quality of the electron density maps obtained by MEM, since the electron densities obtained by MEM may suffer from noise and artifacts (Jauch and Palmer, 1993; Jauch, 1994; de Vries et al., 1994; Roversi et al., 1998; Palatinus and van Smaalen, 2002). Some of the main reasons for these noise and artifacts are

- inappropriate weighting scheme w_i
- use of uninformational PRIOR densities (e.g. uniform PRIOR)
- series termination effects
- inaccuracy of data and their quality
- wrong choice of the value of χ^2_{aim}

Jauch and Palmer (1993) were the first to show that the distribution of normalized residuals for the MEM electron density is non-Gaussian. But according to the criterion of MEM (Eq. 2.6), the residual distribution

$$\frac{\triangle F_{MEM}(H_i)}{\sigma(H_i)} = \frac{F_{obs}(H_i) - F_{MEM}(H_i)}{\sigma(H_i)} \tag{2.11}$$

should be a Gaussian distribution. This problem has been observed in the standard version of MEM which uses the value $w_i = 1$. This lead to large normalized residual values for very few low-order reflections and the remaining reflections however possessing very small residuals. To overcome this problem an *ad hoc* weighting scheme is applied by Hofmann et al. (2007a) in the F-constraints (Eq. 2.6) as suggested by de Vries et al. (1994):

$$w_i = \frac{1}{|\mathbf{H}_i|^n} \left(\frac{1}{N_F} \sum_{i=1}^{N_F} \frac{1}{|\mathbf{H}_i|^n} \right)^{-1} \tag{2.12}$$

where $|\mathbf{H}_i|$ is the length of the scattering vector of Bragg reflection i and n are small positive integers. This weighting scheme leads to reduced residuals of low-order reflections by giving larger weight to those reflections (with short scattering vectors) and in turn giving rise to a Gaussian distribution of normalized residuals. Several tests have confirmed this and suggested the optimum choice of $n = 4$ for obtaining best electron density map (de Vries et al., 1994; Hofmann et al., 2007a;

Netzel et al., 2008). We have performed the MEM calculation in the Chapter 5 by using weights according to Eq. (2.12) with $n = 4$.

Initially a flat prior density (total number of electrons in the unit cell, which are uniformly distributed over the volume of the unit cell) has been used for the electron density calculation using the MEM (Sakata and Sato, 1990). This approach has resulted in the existence of noise and artifacts (non-nuclear maxima) in the electron density map, whose magnitudes are larger than the effects of chemical bonding (Sakata and Sato, 1990; Iversen et al., 1995; Palatinus and van Smaalen, 2002). To overcome this problem de Vries, Briels and Feil (1996) first proposed the idea of using a non-uniform prior density and established the absence of non-nuclear maxima in Si-Si bonds in crystalline silicon, which was present before in the electron density map analyzed by Sakata and Sato (1990). Palatinus and van Smaalen (2002) also confirm a reduction in noise and artifacts in the MEM density by employing a non-unform prior, which is generated by using the coordinates and ADPs from the IAM. From this one can understand that the magnitude of noise and artifacts depends on the type of the prior density used (van Smaalen and Netzel, 2009), since the maximum value of the entropy is obtained for $\rho_k = \rho_k^{prior}$ (Eq. 2.4). Deviation of the ρ_k from ρ_k^{prior} always leads to a lowering of the entropy, but it is allowed to do so if it is required to fit the data (Eq. 2.7). Noise and artifacts increase with increase in magnitude of this difference. Therefore it has been recommended to use the IAM as prior for electron-density analysis using the MEM (Palatinus and van Smaalen, 2002; Hofmann et al., 2007a;b; Netzel et al., 2008; van Smaalen and Netzel, 2009). However van Smaalen and Netzel (2009) suggested the idea of using multipole model as an alternative choice for prior density in the MEM, since it is more informative than IAM and probably closer to the true densities. With this idea, in Chapter 5 we report MEM electron densities calculated with either a MP model, an invariom model (multipoles transferred from the database and not varied in the structure refinement) and an IAM model created by high-order refinement (IAM-HO) as prior, with the purpose to investigate the effect of different prior densities on the MEM.

Although the series termination effects in the MEM are by far not as big a problem as in conventional Fourier synthesis of electron densities, still it can be one of the reasons for artifacts (de Vries et al., 1994; Gilmore, 1996). This might arise due to limited number of reflections available from the data set (Jauch, 1994), which can be suppressed by employing the sufficiently informative prior i.e. non-uniform prior (Palatinus and van Smaalen, 2005). MEM generally de-emphasises the series termination but does not remove them (Gilmore, 1996).

The other main source of errors which produces artifacts in MEM is the inaccuracy of the data specially at higher scattering angles. This happens due to decreasing scattered intensities with increasing scattering angle and the corresponding structure factors may be measured as weak or unobserved. To overcome this problem, Palatinus and van Smaalen (2005) have suggested the method of prior-derived F-constraints (PDC) (Palatinus and van Smaalen, 2005) with

$$\begin{aligned} C_{F^2}^{PDC} = -\chi^2_{aim} + \tfrac{1}{N_{all}} \sum_{i=1}^{N_F} w_i \left(\tfrac{|F_{obs}(\mathbf{H}_i) - F_{MEM}(\mathbf{H}_i)|}{\sigma(\mathbf{H}_i)} \right)^2 \\ + \tfrac{1}{N_{all}} \sum_{j=1}^{N_{PDC}} w_j \left(\tfrac{|F_{prior}(\mathbf{H}_j) - F_{MEM}(\mathbf{H}_j)|}{\sigma(\mathbf{H}_j)} \right)^2 \end{aligned} \qquad (2.13)$$

where $N_{all} = N_F + N_{PDC}$. $F_{prior}(\mathbf{H}_j)$ are obtained by the discrete Fourier transform of ρ_k^{prior} for e.g. up to $\sin(\theta)/\lambda = 2.5$ Å^{-1} which are not available from the experiment. The standard uncertainties $\sigma(\mathbf{H}_j)$ are chosen to be equal to the smallest standard uncertainty amongst the experimental data. The iterations are performed with the summation of Eq. (2.13). The calculated structure factors by the method of PDC gives a good estimate for structure factors at high-angle reflections and PDC enhances the quality of electron density map obtained by MEM (Palatinus and van Smaalen, 2005; Hofmann et al., 2007a;b; Netzel et al., 2008; van Smaalen and Netzel, 2009). However to consider employing the method of PDC in MEM, the minimum resolution of the experimental data should be available up to $\sin(\theta)/\lambda = 0.9$ Å^{-1}.

The choice of optimal χ^2_{aim} is very important to get a good-quality MEM electron density map, otherwise MEM electron density map will have under-fitted data or noise (Netzel et al., 2008; van Smaalen and Netzel, 2009), since the value of χ^2_{aim} determines the point of convergence through the criterion C_{F^2}=0 (Eq. 2.6). If the PDC ($C_{F^2}^{PDC}$) is included, the MEM still checks the convergence through the C_{F^2}=0 on the experimental data only Eq. (2.6).

The standard version of MEM employs $\chi^2_{aim} = 1$ (Skilling and Bryan, 1984; Sakata and Sato, 1990; Tanaka et al., 2002). However it is recommended to determine the value of χ^2_{aim} for each individual MEM calculation (Hofmann et al., 2007b; Netzel et al., 2008; van Smaalen and Netzel, 2009). One way to evaluate the optimum χ^2_{aim} values is by comparing the difference Fourier map and dynamic deformation density map generated at different sections of the studied molecule for different χ^2_{aim} values. For the optimum value of χ^2_{aim}, the difference Fourier map

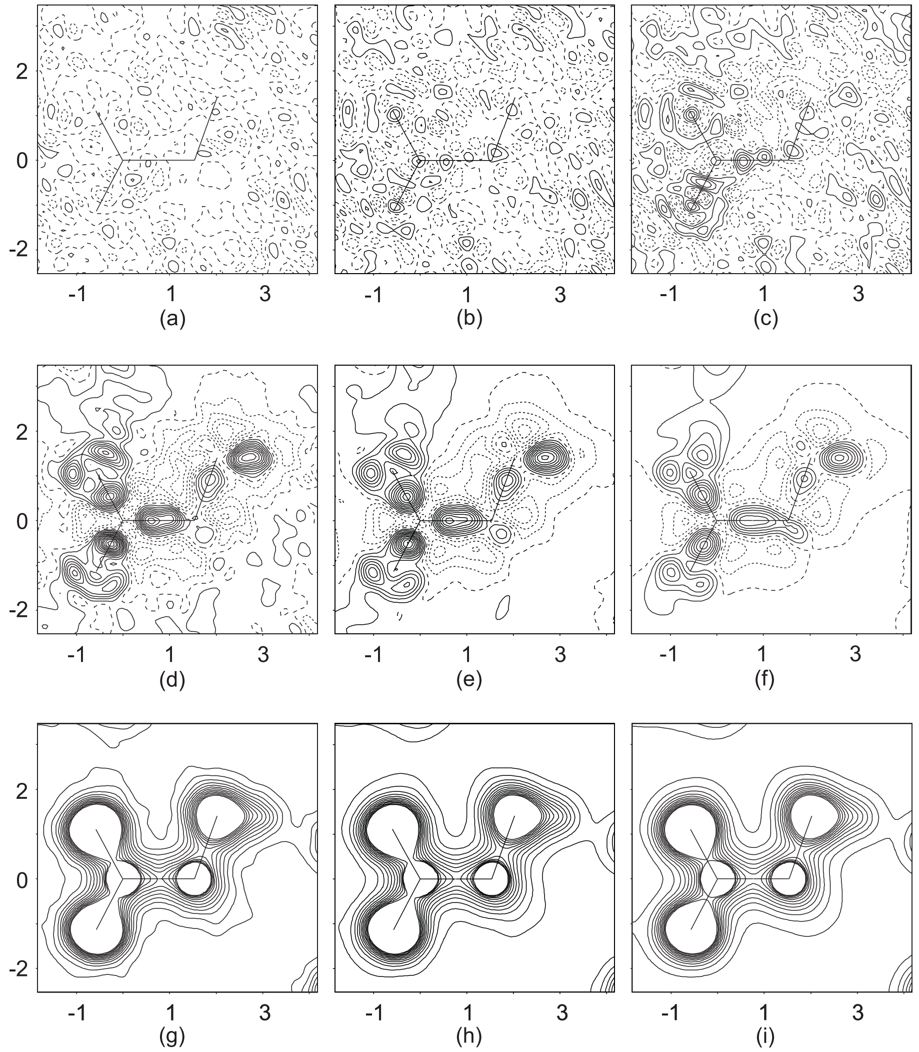

Figure 2.1: C1-C2-N plane of density maps of D, L-serine for the IAM model (compare to Chapter 5). (a, b, c) difference Fourier map with contours at 0.05 e/Å^3; (d, e, f) dynamic deformation density with contours at 0.05 e/Å^3 ; and (g, h, i) MEM density with contours at 0.2 e/Å^3 up to 2.5 e/Å^3. For (a, d, g) $\chi^2_{aim} = 0.2$; (b, e, h) $\chi^2_{aim} = 0.55$; and (c, f, i) $\chi^2_{aim} = 0.9$. Solid lines denote positive values, dotted values denote negative values and dashed lines are zero contour.

needs to be featureless [see for example Fig. 2.1(b)] and the dynamic deformation density map should exhibit smooth features [Fig. 2.1(e)] (Hofmann et al., 2007b; Netzel et al., 2008; van Smaalen and Netzel, 2009). Too large values of χ^2_{aim} lead to under-fitted data and it will possess larger residual densities in the difference Fourier map [Fig. 2.1(c)]. Too small values will lead to the over-fitting of the data. Noise will be added to the electron density [Fig. 2.1(g)], such that the difference Fourier map will be flat [Fig. 2.1(a)]. Therefore the optimum χ^2_{aim} value can easily be determined by examining these maps. The corresponding electron density obtained will be free of noise and artifacts.

By employing all the above extensions in the computer program BayMEM (van Smaalen et al., 2003), we have obtained the electron densities by MEM for three amino acids and a tripeptide and described in the Chapter 5.

2.3 Topological analysis according to the QTAIM

Any electron density can be subjected to Baders "Quantum Theory of Atoms in Molecules" (QTAIM) (Bader, 1990; 1998) approach, which allows the interpretation of detailed topological analysis of charge distribution for the understanding of chemical and physical properties. Ideally it provides a quantitative link between the total electron density and all important properties of molecule in the analysis. The theory of QTAIM provides a methodology for the understanding of bonding between any two atoms in a molecule and allows the evaluation of nature of intermolecular interactions. This includes the analysis of electron density at critical points, $\rho_{cp}(\mathbf{r})$, where the gradient of the electron density vanishes, $(\nabla\rho_{cp}(\mathbf{r}) = 0)$. The critical points correspond to local minima, local maxima and saddle points of electron density distribution.

Atomic basins are defined as a region in space which contains exactly one attractor (maximum in electron density), and all charges within this region belongs to that attractor. The surface of the basin is defined by the zero flux surface, defined as

$$\nabla\rho(\mathbf{r}) \cdot \mathbf{n}(\mathbf{r}) = 0\,, \tag{2.14}$$

where $\nabla\rho(\mathbf{r})$ is the gradient of electron density and $\mathbf{n}(\mathbf{r})$ is normal to the surface. The integration over the volume of the atomic basin will give the atomic charge.

The line of the highest electron density between two atoms is referred to as the interaction line (R_{ij}), and defined as "bond path" between any two atoms. The bond path is based on distribution of electron density features and it may be quite different from the straight line which joins two atoms. The second derivative of the electron density given by the Hessian matrix is known as the Laplacian $\nabla^2\rho(\mathbf{r}) = (\lambda_1 + \lambda_2 + \lambda_3)$, where λ_i define the eigenvalues of Hessian matrix. The rank and signature of the Hessian matrix classify critical points into nuclear critical points (NCP), bond critical points (BCP), ring critical points (RCP) and cage critical points (CCP) with (3, -3), (3, -1), (3, +1) and (3, +3) labels, respectively. The Laplacian value is a measure of the local curvature of $\rho(\mathbf{r})$. If the electron density is locally concentrated then $\nabla^2\rho(\mathbf{r}) < 0$ and $\nabla^2\rho(\mathbf{r}) > 0$ for locally depleted electron density at a given point in space. In the case of shared interactions, the value of $\rho(\mathbf{r}_{bcp})$ is high and $\nabla^2\rho(\mathbf{r}_{bcp}) < 0$, which are typical for covalent bonds. Whereas in closed shell nature of interactions, the value of $\rho(\mathbf{r}_{bcp})$ is small and $\nabla^2\rho(\mathbf{r}_{bcp}) > 0$, which represents the non-covalent characteristic such as hydrogen bonds, ionic bonds, van der Waals bonds and dipolar interactions. Thus, the bond paths and values at BCPs of the electron density and the Laplacian together represent the topology of the electron density distribution of the bonds in a given molecule.

The static electron density maps obtained by the multipole model have been analyzed according to the QTAIM (Bader, 1990) using the module XDPROP of the computer program XD2006 (Volkov et al., 2006) for small molecules and VMoPro of the computer program MoPro for proteins (Jelsch et al., 2005), whereas the dynamic electron density maps obtained from the computer program PRIOR and from BayMEM were analyzed by the computer program EDMA. The complete description of program EDMA and the procedure of topological analysis are given in detail in Chapter 3.

Chapter 3

EDMA: a computer program for topological analysis of discrete electron densities[1]

3.1 Abstract

EDMA is a computer program for topological analysis of discrete electron densities according to Bader's theory of atoms in molecules. It locates critical points of the electron density and calculates their principal curvatures. Furthermore, it partitions the electron density into atomic basins and integrates the volume and charge of these atomic basins. EDMA can also assign the type of the chemical element to atomic basins based on their integrated charges. The latter feature can be used for interpretation of *ab initio* electron densities obtained in the process of structure solution. A particular feature of EDMA is that it can handle superspace electron densities of aperiodic crystals in arbitrary dimensions. EDMA first generates real-space sections at a selected set of phases of the modulation wave, and subsequently analyzes each section as an ordinary three-dimensional electron density. Applications of EDMA to model electron densities have shown that the relative accuracy of the positions of the critical points, the electron densities at the critical points and the Laplacian is of the order of 10^{-4} or better.

---

[1] This Chapter has been published as EDMA: a computer program for topological analysis of discrete electron densities. L. Palatinus, S. J. Prathapa, S. Van Smaalen. *Journal of Applied Crystallography*, **45**, 575-580, (2012)

3.2 Introduction

Studies of accurate electron density distributions have become an important part of theoretical and experimental chemistry and crystallography. With the increased accuracy of theoretical calculations and with the availability of modern experimental facilities it has become possible to obtain electron densities with sufficient accuracy to allow a meaningful quantitative analysis of local and global topological properties.

Bader's atoms-in-molecules (AIM) formalism (Bader, 1990) has offered a well defined theoretical basis for the topological analysis of electron densities. This formalism is nowadays probably the most frequently used framework for this purpose.

There are three predominant types of electron density that can be analyzed for topological properties. The first type are theoretically computed electron densities of molecules or crystals. They are typically available as analytical functions based on some basis set of functions. The second type are experimental electron densities obtained from multipole refinements, which are described in terms of a product of radial and multipole functions (exponential and spherical harmonic functions), usually with parameters refined against experimental data. The third type are discrete electron densities described by values on a regular grid. Such electron densities typically result from maximum entropy calculations, but they can obviously be generated from both previous types of electron densities (van Smaalen et al., 2003; Katan et al., 2003).

A rich collection of software tools for topological analysis of electron densities is nowadays available. A large number of these tools are linked to the multipole-refinement programs: VALTOPO (Bianchi and Forni, 2005), VALRAY (Stewart et al., 1998), WinXPRO (Stash and Tsirelson, 2002a; 2005), TOPXD part of the XD package (Volkov, Gatti, Abramov and Coppens, 2000) and Jana2006 (Petříček et al., 2006). These programs take as input the multipole functions describing the electron density. Another large group of programs serves for an analysis of theoretically computed electron densities described by the wave functions: AIMPAC (Bader, 2012), AIMAll (Keith, 2011) and Aim2000 (Biegler-König et al., 2001; Biegler-König and Schönbohm, 2002), ELECTROS (Ghermani et al., 1992), Morphy (Popelier, 1996), NEWPROP (Souhassou and Blessing, 1999), and TopMoD (Noury et al., 1999). All the programs mentioned so far have in common that they work with electron densities that are represented analytically. The last group of programs take as input a discrete electron density sampled on a regular grid over the unit cell. These programs either provide only integral properties of the electron density, like the integrated atomic charges (Bader; Henkelman et al. (2006)), or use an interpolation scheme to access the off-grid values of the electron density and its derivatives (InteGriTy; Katan et al. (2003)).

Here we present the computer program EDMA, which belongs to the third category. It takes as input a discrete electron density, and it calculates atomic volumes, integrated charges, and positions and properties of the critical points according to Bader's AIM formalism. The first version of EDMA was written in 2002–2003 (Palatinus, 2003), and it has been improved and expanded since then. It has been used for the analysis of electron densities in several studies. The present article provides an overview of the current functionality of EDMA, it gives comments on some of the algorithms used in the program, and it presents results of applications to simple electron densities, which demonstrate that the algorithms provide reliable topological properties of electron densities defined on a grid.

3.3 Program description and functions

EDMA is an acronym of 'electron density map analysis'. Originally it was part of the BayMEM suite (van Smaalen et al., 2003). It has been written with the purpose of analysing electron densities obtained as 'prior' or those obtained by the maximum entropy method (van Smaalen et al., 2003). More recently, EDMA has been made into a standalone program, and its functionality has been expanded with an option of asserting the chemical element for each atomic basin in the electron density.

EDMA requires two input files: an electron density file and an instruction file with keywords that control the running of the program. No interaction with the program is necessary during run time. This makes it easy to use EDMA as a part of a script or as an element of an automatic workflow.

The input electron density is a discrete density distribution sampled on a regular grid. However, the location and characterization of the critical points of the electron density require knowledge of the electron density values between the grid points, and thus an interpolation procedure has to be used. Out of many possible choices we decided to use cubic splines, as described in Numerical Recipes (Press et al., 1996). The advantage of using cubic splines is that the procedure is robust, reliable, easily generalizable to arbitrary dimensions and fast.

EDMA can also analyze the electron densities of incommensurately modulated structures and composite crystal structures described in (3+d)-dimensional superspace. The number d of modulation vectors is not limited ($d = 0, 1, 2, \dots$). The analysis of a superspace electron density is performed in two steps. First real-space sections are produced from the superspace electron density for a series of modulation phases ('t-sections'), and then each three-dimensional electron density — which is not periodic — is analyzed by the standard procedures.

In summary, EDMA can perform five basic tasks:

- Locate maxima in the electron density
- Locate and characterize the critical points of the electron density
- Determine the boundaries of the atomic basins
- Determine the volume and integrated charge of each basin
- Assign a chemical element to each atomic basin

The positions of the maxima and other critical points can be searched either in the whole electron density or in user-defined regions. The latter option is especially useful for modulated structures, where the full analysis of the superspace electron density can be prohibitively time consuming. In such cases restricting the search to predefined regions of interest may reduce the computing time to a manageable amount. Each of the tasks will be described in detail in the following sections.

3.3.1 Local maxima and other critical points

Locating maxima in the electron density is a fundamental task of the electron density analysis. In spite of occasional discussions about the possible existence of non-nuclear maxima in the electron density, it is generally accepted that every maximum in the electron density corresponds to the position of an atom (Iversen et al., 1995; de Vries, Briels and Feil, 1996).

Local maxima are one type of critical point. In general, a critical point of the electron density is defined as a point in the unit cell where the electron density has vanishing gradient,

$$\nabla\rho(\mathbf{r}) = (0,\, 0,\, 0)\,. \tag{3.1}$$

Each critical point can be characterized by its position in the unit cell and the values of the three principal curvatures (second derivatives) of the electron density at this point, with corresponding eigenvectors. Depending on the sign of the three principal curvatures, four types of critical points can be distinguished: maxima, bond critical points (BCPs), ring critical points (RCPs) and minima. In the case of BCPs and RCPs, particular attention is given to the Laplacian, $\nabla^2\rho(\mathbf{r})$, which is the sum of the three principal curvatures.

In order to quickly locate the approximate positions of critical points, EDMA uses a procedure inspired by the method used in NEWPROP (Souhassou and Blessing, 1999) and Jana2006 (Petříček et al., 2006). First an approximate gradient map is calculated at every grid point. Then the minima in the gradient map with sufficiently low estimates of the gradient are marked as candidates for critical points, and their exact positions are determined by refining the position of the minimum of the gradient. If the minimum of the gradient is zero within the numerical accuracy, the candidate for a critical point is considered to be a real critical point.

The electron density at the critical point is evaluated using cubic spline interpolation. When we calculated the first and second derivatives of the fitted spline functions analytically, they appeared to provide unreliable estimates of the derivatives. Instead, we now obtain the derivatives of the electron density at the grid points by numerical difference formulae (Li, 2005), and the Hessian matrix at the critical point is then calculated by cubic spline interpolation of the numerical derivatives. The Hessian matrix is transformed from crystal to Cartesian coordinates, and the principal curvatures are obtained by diagonalization of the latter matrix.

3.3.2 Atomic volumes and atomic charges

The AIM theory provides a consistent definition of an atom for nearly all situations encountered in practice, although some discussions about the uniqueness of this definition and possible pathological cases have appeared in the literature (Cassam-Chenaï and Jayatilaka, 2001; Mohallem, 2002; Kryachko, 2002; Delle Site, 2002; Bader, 2002; Cassam-Chenaï and Jayatilaka, 2002). The space is split into disjunct regions, each of which contains exactly one local maximum of the electron density (Bader, 1990). Such a region is called an atomic basin, and it defines the space occupied by the atom located at the position of the maximum of the electron density. Atomic basins have finite volumes for crystal structures. The number of electrons of an atom—among other properties—is obtained by integration of the electron density over its basin.

The AIM definition of atoms is based on the existence of interatomic surfaces.

These surfaces are an assembly of points $\mathbf{r}$ with the property

$$\nabla\rho(\mathbf{r}) \cdot \mathbf{n}(\mathbf{r}) = 0\,, \tag{3.2}$$

where $\mathbf{n}(\mathbf{r})$ is the normal to the interatomic surface at point $\mathbf{r}$. The atomic volume of an atom is the volume that contains the corresponding local maximum of the electron density, and that is delimited by the nearest interatomic surfaces.

Many approaches have been used to determine the boundaries of the atomic basins in electron densities. EDMA initially used an algorithm that follows the gradient path from a grid point to one of its neighbors (Palatinus, 2003). This algorithm has been developed independently by Henkelman et al. (2006). However, it was shown by Sanville et al. (2007) that this simple algorithm suffers from a bias: the atomic surfaces tend to align with special directions and planes in the grid. This bias does not disappear with finer grid spacings. Sanville et al. (2007) and Tang et al. (2009) proposed different solutions to this problem. We opted for the solution of Tang et al. (2009), because it is conceptually simpler, computationally faster and does not require interpolation between the grid points. However, the algorithm as published by Tang et al. (2009) contains one imperfection. The x-component of the gradient vector at a selected grid point is computed from the differences between the electron density values at the neighboring grid points along x, and similarly for the other two coordinates [see equation (4) of (Tang et al., 2009)]. This definition may be appropriate for continuous electron densities, where grid points can be chosen at arbitrarily small spacing, but for realistic discrete electron densities this approximation is bound to fail in many cases, notably close to bond paths that run diagonally to the coordinate axes [Fig. 3.1]. In fact, one can consider this approximation as a fit of a trilinear function to the six nearest neighbors of the selected grid point, approximating the true gradient by the gradient of that trilinear function. An obvious remedy to the problem is thus to fit the trilinear function to the electron density values at all 26 neighbors using a least-squares procedure with weights equal to the square of the reciprocal distance to the central grid point. This approach is used in EDMA. Figure 3.1 illustrates the difference for a simple two-dimensional example.

The algorithm assigns each grid point to a single atomic basin. Thus, grid points that are cut by the atomic surfaces are not split between the atomic basins, and the total integrated volume and charge are biased by this effect. Moreover, the algorithm does not always respect the symmetry of the structure, and consequently some symmetry-equivalent grid points can be assigned to atomic basins of inequivalent atoms. It would be possible to impose symmetry on the shapes of the atomic basins at the cost of increased computation time. However, from a practical point of view it is advantageous to preserve these differences, because they provide a measure of the accuracy of the integration procedure. Applications to simple electron densities (Section 3.5) have shown that at sufficient grid resolution both mentioned sources of errors are minor and can be neglected.

The integrated number of electrons in an atomic basin can be used to compute atomic charges by subtraction from the atomic number. EDMA also determines the center of charge for each atomic basin, which can be used, for example, to compute the dipole moment of the atom, whereby the positive charge of the nucleus is assigned to the position of the maximum in the electron density or to the position of the atom in the structural model (if available). EDMA can easily be extended to include the calculation of other integrated properties, like higher-order moments of the electron density.

3.3.3 Assignment of element types to atomic basins in the electron density

A topological analysis of the electron density is one of the last steps of structure analysis. At this stage the type of element and the positions of all atoms are known. At the beginning of the procedure of structural analysis electron density maps need to be analysed for another purpose: determination of the crystal structure from an electron density obtained by one of the methods of phase determination. This task is quite different from an accurate topological analysis, but several aspects are common, notably the need to find local maxima in the electron density and to determine the number of electrons in their basins. This capability was therefore included in EDMA.

An electron density resulting from a method of structure solution can be on an arbitrary scale. It typically contains several prominent peaks representing the atoms, and noise in low-density regions. It is therefore necessary to locate the maxima and decide which peaks represent atoms and which are noise. Furthermore, the atomic basins around each maximum and their integrated number of electrons should be estimated, from which the elemental symbol of each atom can be determined. The integrated charges of atomic basins appear to provide more reliable estimates of the chemical elements than the simple consideration of peak heights. EDMA offers three modes of assignment of element types to atoms, which differ in their use of the

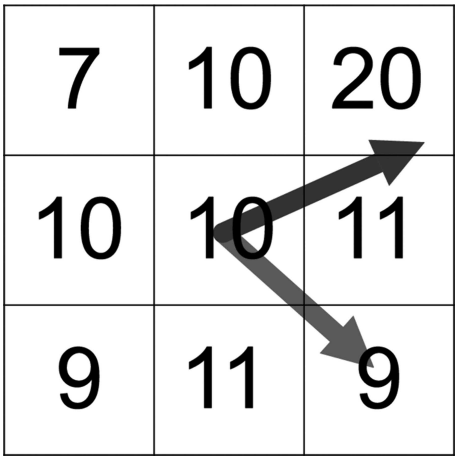

Figure 3.1: A schematic example of the calculation of the gradient of a discrete electron density. A 3 × 3 pixel section of a hypothetical two-dimensional grid are shown. The numbers in each box represent the electron density value at that grid point. The gray arrow shows the gradient estimated by taking into account only the four nearest neighbors of the central point [cf. equation (4) of Tang et al. (2009)]. The black arrow shows the gradient estimated by fitting a least-squares plane to the eight neighbors of the central point.

Table 3.1: Parameters of the two models used for generating density maps at various resolutions (see Eq. 3.3).

	Model 1	Model 2
Lattice parameters		
a (Å)	3.30	3.30
b (Å)	3.50	3.50
c (Å)	3.70	3.70
β (°)	95	95
Atom A at $(0, 0, 0)$		
N_e	37.5	37.5
σ (Å)	0.191978	0.191978
Atom B at (x, x, x)		
x	0.248233	0.248233
N_e	37.5	56.5
σ (Å)	0.191978	0.188986

information about the chemical composition. If the exact chemical composition is provided, EDMA can interpret the peaks so that the resulting composition exactly matches the required composition. This mode is the most robust and it is able to interpret even quite noisy electron densities. If only the chemical elements contained in the compound are available together with the total number of atoms in the unit cell, EDMA can interpret the electron density so that the heaviest atom is assigned to the basin with the largest number of electrons. Then all the electron counts of the basins are rescaled so that the largest peak has exactly the number of electrons corresponding to the atomic number of the heaviest atom, and other peaks are assigned the chemical type according to the atomic number of the atom nearest to their rescaled charge. The third mode is applied if there is an uncertainty in both the elemental types and the numbers of the atoms, and only a list of possible atomic types is available. EDMA then tries to assign atomic types by a least-squares procedure so that the discrepancy between scaled integrated charges and the atomic numbers is minimal, while some of the candidate atoms need not be present in the final list of assigned atoms. Clearly, the last option is most prone to errors caused by noise in the electron density, but it allows a first tentative interpretation of an electron density obtained with only a very vague idea about the chemical composition. Such situations are actually fairly common in chemical crystallography, when many crystallization attempts are characterized, and some of them yield results quite different from the expected composition or molecule.

3.4 Input and output

EDMA takes two input files. The instruction file is a simple ASCII file, containing keywords and parameter values in free format. The electron density file can have either the binary format m81 of the crystallographic computing system Jana2006 (Petříček et al., 2006) or the X-PLOR format of the software package X-PLOR for structural biology (Brünger, 1992). Additional formats can easily be added.

The principal output of EDMA is a single file with extension .coo, which contains all the information extracted from the electron density, *i.e.* the list and properties of local maxima with their basins and, if requested, the list and properties of the critical points. Furthermore, if the assignment of the atomic types to the basins is requested, the structure is also written to a file in either the CIF format, the INS format for the software package SHELX (Sheldrick, 2008b), or the m40 format for

Jana2006.

EDMA can also produce maps of the unit cell in one of the supported formats. Two types of electron density maps are available:

- Map of atomic basins: this map contains for each grid point the sequence number of the basin to which it belongs to. This map thus allows visualization of the partitioning of the unit cell into atomic basins.
- t-maps or projection maps: in modulated structures the electron density map has more than three dimensions and is not easily visualized. EDMA offers two possibilities to facilitate visualization. The projection map is a three-dimensional electron density obtained by projecting the $(3+d)$-dimensional electron density along the d additional dimensions. It corresponds to the average electron density. The t-sections are three-dimensional electron densities obtained as real-space sections of the $(3+d)$-dimensional superspace electron density, and they represent the real three-dimensional electron density at different phases of the modulation.

3.5 Validation of EDMA

The algorithms in EDMA have been validated by a series of calculations on model electron densities for which we have been able to compute the topological properties analytically. Unfortunately, electron densities corresponding to realistic structure models are not accessible to simple analytical computation. On the other hand, computer programs are available which compute topological properties analytically from wave functions or multipole parameters, but here we were unable to calculate exactly the corresponding gridded electron densities. Therefore, we have constructed a simple structure-like model, for which we can accurately compute both the gridded densities and, analytically, the topological properties. The model consist of two Gaussian peaks placed in monoclinic unit cells:

$$\rho_G(\mathbf{r}) = \frac{N_e}{(2\pi)^{3/2}\sigma^3}\exp\left(-\frac{r^2}{2\sigma^2}\right) \tag{3.3}$$

where N_e is the number of electrons of the "atom" and σ is the width of the peak. Both "atoms" are equal in model 1, while in the second model the "atoms" have different width and different numbers of electrons (Table 3.1). Atom A has been placed on the origin; atom B has been put between grid points.

Table 3.2: Properties of model 1 at the BCP obtained by EDMA and obtained analytically (last row). The BCP is located at (x, x, x).

Grid				Laplacian		
Points	Resolution (Å)	Location x_{BCP}	Electron density (e/Å^3)	Value (e/Å^5)	Absolute error (e/Å^5)	Relative error (e/Å^5)
64^3	0.055	0.124106	0.4769	148.8759	0.0188	0.126
72^3	0.049	0.124109	0.4769	148.8688	0.0117	0.079
84^3	0.042	0.124139	0.4773	148.9519	0.0948	0.637
96^3	0.036	0.124113	0.4769	148.8627	0.0056	0.038
108^3	0.032	0.124126	0.4771	148.9089	0.0518	0.348
128^3	0.027	0.124115	0.4769	148.8618	0.0047	0.032
132^3	0.027	0.124121	0.4770	148.8892	0.0321	0.216
144^3	0.024	0.124115	0.4769	148.8616	0.0045	0.030
192^3	0.018	0.124116	0.4769	148.8615	0.0044	0.030
216^3	0.016	0.124116	0.4769	148.8614	0.0043	0.029
Analytical		0.124117	0.4769	148.8571	–	–

Table 3.3: Properties of model 2 at the BCP obtained by EDMA and obtained analytically (last row). The BCP is located at (x, x, x).

Grid				Laplacian		
points	Resolution (Å)	Location x_{BCP}	Electron density (e/Å^3)	Value (e/Å^5)	Absolute error (e/Å^5)	Relative error (10^{-3})
64^3	0.055	0.122933	0.5326	172.2412	0.0326	0.190
72^3	0.049	0.122939	0.5326	172.2343	0.0257	0.149
84^3	0.042	0.122975	0.5329	172.3021	0.0935	0.543
96^3	0.036	0.122947	0.5326	172.2297	0.0211	0.123
108^3	0.032	0.122963	0.5327	172.2506	0.0420	0.244
128^3	0.027	0.122951	0.5326	172.2288	0.0202	0.117
132^3	0.027	0.122959	0.5326	172.2285	0.0199	0.116
144^3	0.024	0.122963	0.5326	172.2284	0.0198	0.115
192^3	0.018	0.122954	0.5326	172.2259	0.0173	0.101
216^3	0.016	0.122954	0.5326	172.2251	0.0165	0.096
Analytical		0.122956	0.5325	172.2086	–	–

Electron density maps have been generated with the computer program PRIOR for both models and several grid sizes (Tables 3.2 and 3.3). The most important result of the calculations is that all topological quantities at the BCP are determined to a very good accuracy regardless of the grid spacing. The error in the x-coordinate of the BCP is always below 8×10^{-5} Å; the error in the density at the BCP is never larger than $0.0004\,\mathrm{e/A^3}$; and the relative accuracy of the Laplacian is always better than 10^{-3}. Finer grid spacings give more accurate values. However, the accuracy does not increase monotonically with increasing grid size. The best results are obtained for grid spacings where the BCP is located near a grid point, while grids where the BCP is between the grid points (84^3, 108^3, 132^3) result in somewhat larger discrepancies. In any case the errors introduced by interpolation are much smaller than errors from other sources, like experimental errors and methodological artifacts. The integrated charges of the atoms in Model 1 do not differ from the expected value of 37.5 electrons by more than 10^{-4} electrons, regardless of the resolution. In Model 2 the integrated charges of atoms 1 and 2 are 37.49971 and 56.50029 electrons, respectively, for the finest grid of 216^3 points. The results for coarser grids do not deviate by more than 10^{-4} electrons, and in most cases only by 10^{-5} electrons. These results show that the integration procedure works well, and that neglecting the partitioning of the grid points at the borders between atomic basins introduces negligible errors.

Models 1 and 2 comprise two atoms lying on the diagonal of the unit cell. We have performed another series of calculations for models where the orientation of the interatomic vector as well as the distance between the atoms A and B vary in a wide range (other parameters are those of model 2). Computations for a grid size of 128^3 points show large variations of the densities and Laplacians at the BCPs for the different models (Table 3.4), but error values are consistent with those of model 2 (Table 3.3), regardless of the positions of the atoms and the distance between them.

It can be concluded that EDMA is able to calculate the properties of critical points and atomic basins with very good accuracy. The original version of EDMA (Palatinus, 2003) has been used to determine the atomic positions (atomic modulation functions) of aperiodic $[\mathrm{LaS}]_{1.14}[\mathrm{NbS}_2]$ and $\mathrm{Rb_2ZnCl_4}$ (van Smaalen et al., 2003; Li et al., 2011). Properties at BCPs and ionic charges (number of atoms in atomic basins) have been determined for several amino acids and tripeptides (Netzel et al., 2008; Netzel and van Smaalen, 2009). A major difference between the original and current versions of EDMA is the algorithm for determination of the atomic basins (Section 3.3.2). The original algorithm (Palatinus, 2003; Henkelman et al., 2006)

Table 3.4: Properties at the BCPs of models with different distances between the atoms. The grid resolution is 128^3 points.

	Electron density at BCP		Laplacian			
Distance (Å)	EDMA (e/Å^3)	Analytical (e/Å^3)	EDMA (e/Å^5)	Analytical (e/Å^5)	Absolute error (e/Å^5)	Relative error (10^{-3})
0.9905	28.6163	28.6139	2960.8328	2960.9189	-0.0861	-0.029
1.1171	11.4283	11.4270	1762.2181	1762.1835	0.0346	0.020
1.1325	10.1361	10.1351	1630.1352	1630.1174	0.0178	0.011
1.1767	7.1353	7.1337	1285.7641	1285.6844	0.0797	0.062
1.3949	1.0344	1.0339	296.6280	296.5378	0.0902	0.304
1.4335	0.7099	0.7097	218.3109	218.2778	0.0331	0.152
1.4623	0.5326	0.5325	172.2370	172.2153	0.0217	0.126
1.4639	0.5242	0.5241	169.9820	169.9503	0.0317	0.187
1.4725	0.4803	0.4803	158.0710	158.0726	-0.0016	-0.010
1.4932	0.3888	0.3886	132.4896	132.4274	0.0622	0.470
1.4993	0.3651	0.3649	125.6588	125.6279	0.0309	0.246
1.5367	0.2471	0.2469	90.3665	90.3293	0.0372	0.412
1.5880	0.1421	0.1421	56.3160	56.3006	0.0154	0.274

and the new procedure (Section 3.3.2; (Tang et al., 2009)) are both available in EDMA. A comparison of the two methods for analysis of the electron density corresponding to the independent atom model of α-glycine (Netzel et al., 2008) shows a substantial difference in the volumes and integrated charges of the atomic basins (Table 3.5), illustrating the need for advanced methods of determination of zero-flux boundaries. EDMA is also used frequently to locate atoms and assign element types in electron densities solved *ab initio* by charge flipping. To highlight just one of the numerous references, EDMA was used in the analysis of structures in the Al-Cu-Ta system, some of them ranking among the largest known inorganic structures (Weber et al., 2009).

Table 3.5: Number of electrons and Volumes of the atomic basins for the electron density of the independent atom model of α-glycine, obtained with EDMA at a grid of 0.04 Å resolution.
Compare with Netzel et al. (2008). Method 'on grid' corresponds to the algorithm described by Palatinus (2003) and Henkelman et al. (2006). Method 'near grid' corresponds to the algorithm by Tang et al. (2009), improved according to this work (Section 3.3.2)

	Method 'on grid'		Method 'near grid'	
Atom	Electrons	Volume (Å^3)	Electrons	Volume (Å^3)
C(1)	5.017	6.08	5.082	6.82
C(2)	6.197	11.17	6.094	9.99
N	8.419	15.58	8.107	12.82
O(1)	8.711	13.61	8.563	12.53
O(2)	8.466	12.27	8.563	12.86
H(1)	0.423	1.43	0.624	3.24
H(2)	0.758	3.82	0.637	3.38
H(3)	0.981	6.96	0.843	5.82
H(4)	0.423	1.85	0.649	3.33
H(5)	0.598	3.00	0.829	5.00
Total	39.993	75.77	39.991	75.79

3.6 Software and hardware requirements and availability

EDMA has been written in Fortran 90/95. It does not use any external libraries or other resources. It has successfully been compiled with the free compiler g95 (`http://www.g95.org/`), and it has been tested on several platforms (Mac OS X, Linux and Windows). Special hardware is not required to run EDMA.

EDMA was originally developed as part of the software package BayMEM (van Smaalen et al., 2003). The more recent versions of EDMA are standalone programs, interfacing with BayMEM, Superflip (a program for structure solution by charge flipping; (Palatinus and Chapuis, 2007)), WinGX (Farrugia, 1999), Crystals (Betteridge et al., 2003) and Jana2006 (Petříček et al., 2006). Other interfaces, *e.g.* for density files of different formats, can easily be incorporated. EDMA can be downloaded from the web page `http://superflip.fzu.cz`.

3.7 Conclusions

EDMA is a software tool for topological analysis of discrete electron densities. Although it duplicates to certain extent the capabilities of other programs [notably InteGriTy by Katan et al. (2003) and Bader by Henkelman et al. (2006)], it is unique in that it offers at the same time the partitioning of the electron density into atomic basins, analysis of the critical points of the electron density and interpretation of the density in terms of atomic types. Furthermore, EDMA is the only software of its kind that can interpret $(3+d)$-dimensional superspace electron densities. In a series of test calculations we have proven that EDMA provides accurate estimates of the positions, density values and Laplacians of the critical points in the electron densities. EDMA is particularly useful in connection with the maximum-entropy software BayMEM and the charge-flipping program Superflip, because it shares with them the format and many keywords of the instruction file. However, it can be used for analyzing any discrete electron density obtained from other sources.

Chapter 4

Experimental dynamic electron densities of multipole models at different temperatures[1]

4.1 Abstract

It is shown that the dynamic electron density corresponding to a structure model can be computed by inverse Fourier transform of accurately calculated structure factors, employing the method of fast Fourier transform. Maps free of series-termination effects are obtained for resolutions better than 0.04 Å in direct space, corresponding to resolutions larger than 6 $Å^{-1}$ in reciprocal space. Multipole (MP) models of α-glycine and D, L-serine at different temperatures have been determined by refinement against X-ray diffraction data obtained from the scientific literature. The successful construction of dynamic electron densities is demonstrated by their topological properties, which indicate local maxima and bond-critical points (BCPs) at positions expected on the basis of the corresponding static electron densities, while non-atomic maxima have not been found. Density values near atomic maxima are much smaller in dynamic than in static electron densities. Static and low-temperature (∼20 K) dynamic electron density maps are found to be surprisingly similar in the low-density regions. Especially at BCPs, values of the ∼20 K dynamic density maps are only slightly smaller than values of corresponding static

---

[1] This Chapter has been published as Experimental dynamic electron densities of multipole models at different temperatures. S. Mondal, S. J. Prathapa, S. Van Smaalen. *Acta Crystallographica A*, **68**, 568-581 (2012).

density maps. The major effect of these zero-point vibrations is a modification of the second derivatives of the density, which is most pronounced for values at the BCPs of polar C–O bonds. Nevertheless, dynamic MP electron densities provide an estimate of reasonable accuracy for the topological properties at BCPs of the corresponding static electron densities. The difference between static and dynamic electron densities increases with increasing temperature. These differences might provide information on temperature-dependent molecular or solid state properties like chemical stability and reactivity. In regions of still lower densities, like in hydrogen bonds, static and dynamic electron densities have similar appearances within the complete range of temperatures that have been considered (20-298K), providing similar values of both the density and its Laplacian at BCPs in static and dynamic electron densities at all temperatures.

4.2 Introduction

Electron-density studies of molecular materials have been rationalized by the advent of the *quantum theory of atoms in molecules* (QTAIM) (Bader, 1990; Matta and Boyd, 2007). One fundamental aspect of the QTAIM is that it is only defined for static electron densities. As a consequence, the analysis of deconvoluted static densities has become prevalent in the field of experimental electron-density studies (Coppens and Volkov, 2004). Based on the static electron densities obtained from an experimental multipole (MP) model, information on chemical interactions and chemical properties can be retrieved with the aid of the QTAIM.

On the other hand, chemical interactions depend on temperature, as is illustrated by the ubiquitous occurrence of temperature-dependent phase transitions between different crystalline states of a single compound. One way to take into account the effects of temperature is the consideration of time-averaged electron densities, denoted as dynamic electron densities. In fact, the intensities of Bragg reflections measured in X-ray diffraction experiments directly reflect the dynamic electron density. It is only through a structure model that the static density and thermal vibrations can be deconvoluted (Hirshfeld, 1976; Coppens, 1997). The analysis of dynamic electron densities in association with the corresponding static electron density may thus be helpful in revealing the effects of temperature on chemical interactions and properties.

Dynamic electron densities corresponding to a structure model are defined as the convolution of the static electron density with the probability distribution functions of the atomic positions—where the latter follow from the thermal parameters. A direct numerical evaluation of this convolution product is too resource intensive, while a tractable analytical expression does not exist in case the static density is described by the MP model (Roversi et al., 1998). Instead, dynamic electron densities can be computed by inverse Fourier transform of the structure factors of the structure model (Coppens, 1997). However, electron densities obtained by inverse Fourier transform of the structure factors suffer from series- termination effects, unless all reflections are included in the Fourier summation up to a resolution much higher than any resolution that can be achieved experimentally (de Vries, Briels, Fell, Velde and Baerends, 1996; de Vries, Briels and Feil, 1996). In a different approach, Roversi et al. (1998) have demonstrated that structure factors of high-order reflections can be added to the structure factors of low-order reflections, thereby compensating for the series-termination effects in a so-called anti-aliasing procedure.

Despite their potential, these methods have not been applied to MP models. One reason is that the computation of the structure factors for so many reflections has become feasible only in recent years with the increase of available computational power. Earlier work has concentrated on dynamic electron densities or dynamic deformation densities as obtained by inverse Fourier transform of a limited set of structure factors (Ruysink and Vos, 1974; Stevens et al., 1977; Nijveldt and Vos, 1988; Coppens, 1997; Jelsch et al., 1998; Coppens and Volkov, 2004). A qualitative analysis of these maps has shown that the dynamic density near nuclei is lower than the corresponding static density, and that the accumulation of charge in covalent bonds in static densities is retained in the dynamic densities. However, a quantitative analysis of the topological properties of these dynamic electron densities has not been achieved, mainly due to the presence of series-termination effects in the calculated maps (Stevens et al., 1977; Jelsch et al., 1998). Since experimental dynamic density maps with series-termination effects were not suitable for comparison with the theoretical maps, Stevens *et al.* (1977) have proposed to include comparable amount of series-termination effects in the theory. However, any further development in this direction has not been found in the literature. A quantitative description of the effect of temperature on the density is of interest especially in the bonding region and at bond-critical points (BCPs), because these regions define the chemical interactions.

Here we present a method of computing dynamic electron densities corresponding to structure models, including independent atom models (IAM) and MP models.

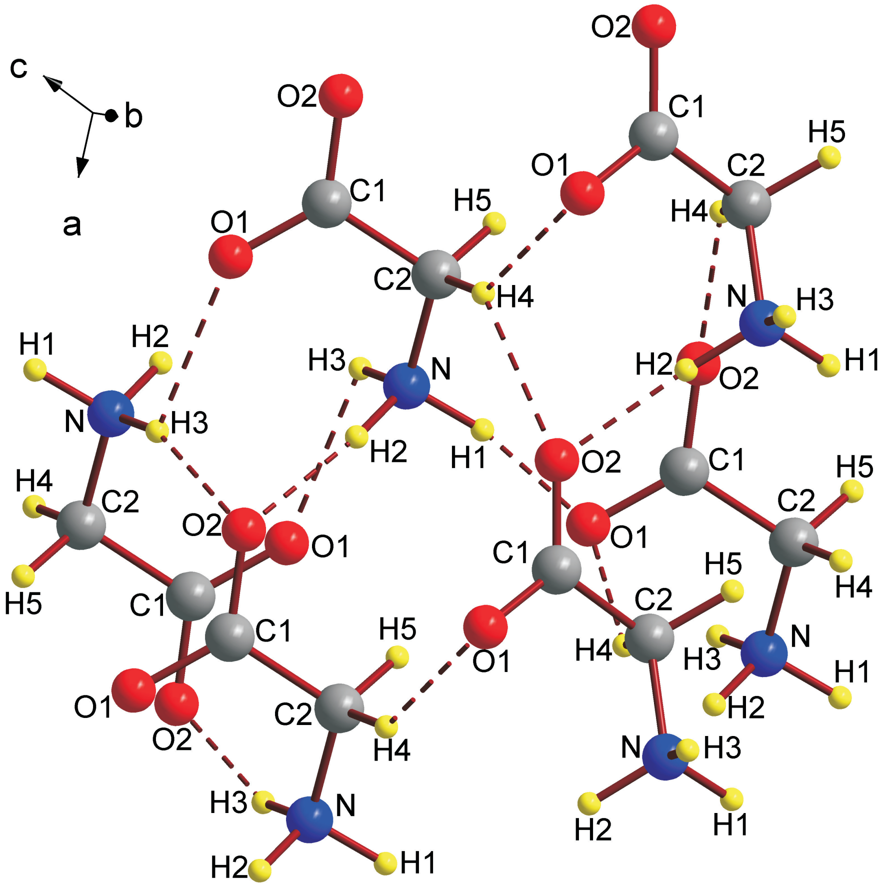

Figure 4.1: A perspective view of the crystal structure of α-glycine along with the atom-numbering scheme. Hydrogen bonds are shown as dashed lines.

The method comprises an inverse Fourier transform by the method of fast Fourier transform (FFT) of accurately computed structure factors up to very high resolution. It is applied to two amino acids, α-glycine and D, L-serine [Figs. 4.1 and 4.2], for which low-temperature, high-resolution X-ray diffraction data are available from the literature (Destro et al., 2000; Dittrich et al., 2005).

Diffraction data at ~20 K for both compounds have allowed us to establish quantitatively the effects of zero-point vibrations on the electron densities, with the result that topological properties at BCPs are surprisingly similar between static and dynamic densities. The main difference is a reduction of the magnitudes of Laplacians.

In this respect it should be noticed that, unlike the QTAIM for static densities, a

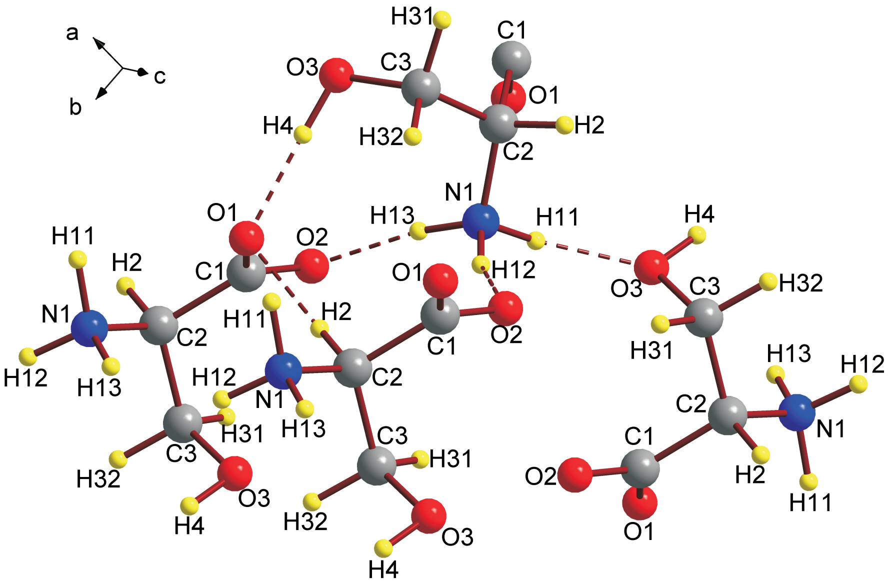

Figure 4.2: A perspective view of D,L-serine including hydrogen bonds along with the atom-numbering scheme.

theoretical foundation does not exist for the interpretation of topological properties of dynamic electron densities. Instead, theoretical approaches accounting for the effects of temperature on properties retain the Born-Oppenheimer approximation for calculating the electronic structure, but combine this with different geometrical arrangements of the atoms, as obtained, for example, in the 'frozen phonon' approach or from molecular dynamics in the Car-Parrinello method (Car and Parrinello, 1985). The Car-Parrinello method has been applied to investigate influence of temperature on molecular structure and properties (Cavazzoni et al., 2002; Cyranski et al., 2008; Gaigeot, 2008).

From these methods one could compute a time-averaged theoretical electron density, but such an approach would depend on an exact knowledge of the vibrational motion of the atoms, which is usually not available.

In the absence of a theoretical foundation for interpreting dynamic charge densities, we have performed a comparative topological analysis of static and dynamic electron densities of α-glycine and D,L-serine. The results provide an empirical description of the differences and similarities of these two entities. The effect of temperature on the dynamic charge density is studied by analyzing diffraction data of D,L-serine measured at temperatures of 20, 100 and 298 K, respectively (Dittrich et al., 2005).

4.3 The dynamic electron density

4.3.1 Method

The time-averaged electron density of a crystal with N_{atom} atoms in the unit cell is defined as,

$$\langle\rho(\mathbf{r})\rangle = \sum_{\mathbf{L}}^{volume} \sum_{\mu=1}^{N_{atom}} \int \rho_\mu(\mathbf{r} - \mathbf{L} - \mathbf{r}_\mu^0 - \mathbf{u}_\mu) P(\mathbf{u}_\mu)\, \mathrm{d}\mathbf{u}_\mu, \tag{4.1}$$

where $\rho_\mu(\mathbf{r} - \mathbf{L} - \mathbf{r}_\mu^0 - \mathbf{u}_\mu)$ is the static electron density of atom μ located at $(\mathbf{r}_\mu^0 + \mathbf{u}_\mu)$ in unit cell $\mathbf{L}$; $P(\mathbf{u}_\mu)$ is the probability of finding atom μ at position $\mathbf{r}_\mu^0 + \mathbf{u}_\mu$; and $\mathbf{r}_\mu^0$ is the equilibrium position of atom μ. The Fourier transform of equation Eq. (4.1) defines the structure factors of the model. Within the harmonic approximation of lattice vibrations, the structure factor has the form,

$$F(\mathbf{H}) = \sum_{\mu=1}^{N_{atom}} f_\mu(\mathbf{H}) \exp\left(-2\pi^2\, \mathbf{H}^T \mathbf{U}_\mu \mathbf{H}\right)\ \exp\left(2\pi i\, \mathbf{H} \cdot \mathbf{r}_\mu^0\right), \tag{4.2}$$

where $f_\mu(\mathbf{H})$ is the aspherical atomic scattering factor of atom μ, including contributions of any multipole functions; $\mathbf{U}_\mu$ is the tensor of the atomic displacement parameters (ADPs); and $\mathbf{H}$ is a reciprocal-lattice vector with indices $(h\ k\ l)$ defined by

$$\mathbf{H} = h\,\mathbf{a}^* + k\,\mathbf{b}^* + l\,\mathbf{c}^*. \tag{4.3}$$

$\mathbf{H}^T$ is the transpose of the vector $\mathbf{H}$. The electron density can be obtained by inverse Fourier transform of the structure factors according to

$$\rho(\mathbf{r}) = \frac{1}{V_{cell}} \sum_{j=1}^{N_{refl}} F(\mathbf{H}_j)\ \exp(-2\pi i\, \mathbf{H}_j \cdot \mathbf{r}), \tag{4.4}$$

where V_{cell} is the volume of the unit cell and the summation runs over all reflections up to a desired resolution.

The electron density is obtained from the structure factors according to Eq. 4.4 by FFT. For this purpose, the electron density is defined on a grid of $N_{pix} = N_1 \times N_2 \times N_3$ pixels. In reciprocal space this allows the storage of structure factors with indices up to $h_{max} \simeq N_1/2$, $k_{max} \simeq N_2/2$ and $l_{max} \simeq N_3/2$. The mesh of sampling the density is given by the grid size of a/N_1 along **a**, and similarly along **b** and **c**. Hence, the relationship between maximum resolution of the reflections and grid size is

$$\left[\frac{\sin(\theta)}{\lambda}\right]_{max} \simeq \frac{0.25}{\text{grid size}}. \tag{4.5}$$

For example, for a grid size of 0.04 Å, the resolution of the reflections that can be taken into account in the Fourier summation is $[\sin(\theta)/\lambda]_{max} \simeq 6.25$ Å^{-1}.

Experimentally, structure factors are typically available up to resolutions of 1.3 Å^{-1} or worse. However, the structure factors of a structure model can be computed up to any resolution. This task has been implemented for the MP model in the latest version of the computer program PRIOR (see Appendix 4.8), which also provides a code for computing the inverse Fourier transform (Eq. 4.4) (van Smaalen et al., 2003). The same code can be used to compute the dynamic electron density of the IAM, if MP parameters are set to zero.

4.3.2 Computational details

Dynamic electron densities of α-glycine at 23 K and of D, L-serine at 20, 100 and 298 K have been computed by inverse FFT of the model structure factors, employing the modified version of the computer program PRIOR (Appendix 4.8). Different grid sizes have been employed for the dynamic electron density of α-glycine, while for D, L-serine the calculations have been restricted to the optimal grid size of 0.04 Å (Table 4.1 and Section 4.5). In each case, all structure factors have been included in the FFT, which can be stored on the chosen grid. Dynamic electron densities have been calculated both for the MP model and the corresponding IAM model.

In the present context, dynamic deformation densities are defined as the difference between the dynamic density of an MP model and the dynamic density of the corresponding IAM:

$$\Delta\rho_{MP}^{dyn-def}(\mathbf{r}) = \rho_{MP}^{dynamic}(\mathbf{r}) - \rho_{IAM}^{dynamic}(\mathbf{r}) \tag{4.6}$$

Dynamic deformation densities have been computed by a simple computer program, which subtracts the two relevant densities on a pixel-by-pixel basis.

Static electron densities and static deformation densities have been visualized by contour maps emphasizing the regions of low density. They have been generated by the module XDGRAPH of the program XD2006 (Volkov et al., 2006). Contour

Table 4.1: Crystallographic data for α-glycine at 23 K and for D, L-serine at temperatures of 20, 100 and 298 K.

	α-glycine[1]	D, L-serine[2]	D, L-serine[2]	D, L-serine[2]
Chemical formula	$C_2O_2NH_5$	$C_3O_3NH_7$	$C_3O_3NH_7$	$C_3O_3NH_7$
Temperature (K)	23	20	100	298
Crystal System	Monoclinic	Monoclinic	Monoclinic	Monoclinic
Space group	$P2_1/n$	$P2_1/a$	$P2_1/a$	$P2_1/a$
Z	4	4	4	4
a (Å)	5.0866	10.7764	10.7621	10.7355
b (Å)	11.7731	9.1947	9.1771	9.1456
c (Å)	5.4595	4.7788	4.7883	4.8304
β (°)	111.99	106.87	106.76	106.46
V (Å^3)	303.16	453.13	452.82	454.83
F(000)	160	224	224	224
Wavelength (Å)	0.7107	0.7107	0.7107	0.7107
$[\sin\theta/\lambda]_{max}$ (Å^{-1})	1.15	1.18	1.19	0.98
Observed criteria	$F > 3\sigma_F$	$F > 4\sigma_F$	$F > 4\sigma_F$	$F > 4\sigma_F$
Unique reflections (obs/all)	3603/3822	4288/5136	4101/5146	2707/3551
Multipole refinement[3]				
$R_F(obs/all)$	0.0124/0.0145	0.0176/0.0253	0.0206/0.0326	0.0211/0.0335
$wR_{F^2}(obs)$	0.0293	0.0398	0.0434	0.0489
GoF	1.18	1.17	1.13	1.28
$\triangle\rho_{min}/\triangle\rho_{max}$ (eÅ^{-3})	-0.132/0.154	-0.224/0.210	-0.210/0.207	-0.194/0.228
Dynamic density[3]				
Approximate pixel size (Å)	0.04	0.04	0.04	0.04
No. of pixels	128 × 288 × 144	256 × 216 × 128	256 × 216 × 128	256 × 216 × 128

[1] X-ray diffraction data from Destro *et al.* (2000)

[2] X-ray diffraction data from Dittrich *et al.* (2005)

[3] Present work

maps of dynamic densities and dynamic deformation densities have been generated with the computer program JANA2006 (Petříček et al., 2006).

Topological properties of static densities have been calculated with XDPROP (Volkov et al., 2006). Topological properties of dynamic charge densities have been calculated with the latest version of the computer program EDMA (Palatinus et al., 2012).

4.4 Choice of the aspherical model

There are different multipolar formalisms established in the literature. For α-glycine, Destro et al. (2000) have used the formalism of Stewart (1976) as implemented in the computer program VALRAY (Stewart and Spackman, 1983). For D,L-serine, Dittrich et al. (2005) have used an invariom model (Dittrich et al., 2004) within the Hansen and Coppens formalism (Coppens, 1997). In order to have a consistent approach, we have decided to employ a single formalism and single procedure for obtaining the aspherical structure models of both compounds. For this, we have chosen the multipolar formalism of Hansen and Coppens (Coppens, 1997) as implemented in the computer program XD2006 (Volkov et al., 2006). During the process of developing an MP model with XD2006, we have failed to exactly reproduce the model of Destro et al. (2000) [see supplementary material **A.1** for details]. The differences between the present model and that of Destro et al. (2000) can be attributed to the use of different multipolar formalisms, different software and different atomic scattering factors. We do not concentrate further on reproducing previous results since our results are very similar to those for other amino acids, including those from Destro et al. (2000), and the observed differences fall within the range of experimental values reported for amino acids (Mebs et al., 2006). We have chosen the procedure that is the state of the art for performing multipole refinements using the software XD2006.

4.4.1 Multipole refinement of α-glycine

A strategic refinement according to the IAM has been performed by the computer program SHELXL97 (Sheldrick, 2008a) under the WinGX (Farrugia, 1999) software package. High-order data ($d \leq 0.50$ Å) have been used for refining the coordinates and ADPs of the non-H atoms, and they were kept fixed afterwards. Low-order data ($d \geq 1.0$ Å) have been used for refining coordinates of H atoms. U(iso) of H atoms have been taken as $1.2 \times U_{eq}$ of their parent atoms. The resulting structure model was then introduced into the program XD2006 (Volkov et al., 2006) by the XDINI module. Atomic scattering factors have been taken from Su and Coppens (1998). In accordance with the environments of the atoms in α-glycine, local three-fold symmetry (3) has been applied to the MP parameters of the N atom, and local mirror symmetry (m) has been applied to the MP parameters of all other non-H atoms (C1, C2, O1 and O2), which form the planar skeleton of the amino acid (Fig. 4.1). For non-H atoms, only those multipoles ($l_{max} = 4$) have been refined which are allowed by the local symmetry. Different κ and κ' parameters have been assigned to different atoms, depending on their chemical environment. For H atoms, fixed values of $\kappa = 1.10$ and $\kappa' = 1.18$ have been used. Only bond-directed multipoles truncated at quadrupole level have been used for H atoms. All H atoms were initially set to neutron distances, subsequently refined against low-order data [$\sin(\theta)/\lambda \leq 0.5$ Å^{-1}] and then fixed to neutron distances again. The function minimized during least square refinements is $\sum[w|F_o| - k|F_c|]^2$ with a weight of $1/\sigma^2[F_{obs}]$ (Table 4.1).

4.4.2 Multipole refinement of *D*, *L*-serine

Dittrich et al. (2005) have used the invariom model – containing MP parameters determined by quantum chemical calculations (Dittrich et al., 2004) - for all three data sets of D, L-serine. To be more experimentally oriented, we have decided to perform a complete multipole refinement for the 20 K data. However, for the structure refinements against data sets measured at 100 and 298 K, we have fixed the values of the MP parameters to those determined at 20 K. In this respect it should be noticed that the 298 K data are unsuitable for an *ab initio* MP refinement. The use of fixed MP parameters will contribute to our understanding, whether or not the present procedure for computing dynamic electron-density distributions is extendable to so-called normal data sets, where *ab initio* MP refinement is not possible.

The feasibility of obtaining electron densities from such datasets has recently been studied by Dittrich et al. (2009) by initially using an invariom model to obtain ADPs followed by the refinement of the MP parameters.

The MP refinement at 20 K has been performed following the same strategy as we have used for α-glycine (Table 4.1 and Fig. 4.2).

Table 4.2: Properties of dynamic electron densities of α-glycine at 23 K for various grid sizes.

Grid size (Å)	No. of pixels	$[\sin(\theta)/\lambda]_{max}$ (Å^{-1})	d_{min} (Å)	ρ_{min} (e/Å^3)	ρ_{max} (e/Å^3)
0.01	$512 \times 1152 \times 576$	25.000	0.02	0.0065	153.6673
0.02	$256 \times 576 \times 288$	12.500	0.04	0.0065	153.4111
0.04	$128 \times 288 \times 144$	6.250	0.08	0.0065	152.0316
0.05	$96 \times 216 \times 108$	5.000	0.10	0.0065	146.4684
0.07	$72 \times 162 \times 72$	3.571	0.14	0.0030	148.7689
0.08	$64 \times 144 \times 72$	3.125	0.16	-0.0284	138.2838
0.1	$48 \times 108 \times 54$	2.500	0.20	-0.3577	127.1692

4.5 Establishing the grid size

Electron densities obtained by means of the FFT may suffer from series-termination effects (Section 4.2). The grid size in direct space is directly related to the number of structure factors that can be incorporated into the Fourier summation (Eq. 4.5). Therefore, the dependence of series-termination effects on the grid size has been determined by calculations of the dynamic electron densities of α-glycine for seven different grid sizes (Table 4.2).

Ripples in the neighborhood of a BCP are visible in the dynamic electron densities computed with grid sizes larger than 0.05 Å [Fig. 4.3]. For a grid size of 0.07 Å, these ripples prevent a meaningful definition of the BCP and its properties. For a grid size of 0.08 Å the amplitude of the ripples is so large that negative density values are found at some points, a feature that is obviously unphysical.

Ripples in the electron densities have not been found for grid sizes of 0.05 Å and below. The dynamic electron densities are essentially the same when calculated with grid sizes of 0.04 Å and 0.02 Å. The contours of equal density appear smooth in these maps at any density level. For a grid size of 0.05 Å, the map does not suffer from ripples, but shapes of the contours are slightly different from the maps at better resolutions, and the contours of low density are not perfectly smooth [Fig. 4.3]. These observations suggest that a grid size of 0.04 Å or better is sufficient and necessary for computation of a dynamic charge density free of series-termination effects.

Series-termination effects are also apparent from the minimum values of the

Table 4.3: Electron densities (e/Å^3; first line) and Laplacians (e/Å^5; second line) at the BCPs of covalent bonds of the dynamic multipole densities of α-glycine at four grid sizes.

	Grid size (Å)			
Bond	0.01	0.02	0.04	0.05
C1-O1	2.701	2.701	2.701	2.701
	-19.45	-19.44	-19.44	-19.46
C1-O2	2.648	2.648	2.648	2.649
	-23.63	-23.63	-23.61	-22.95
C1-C2	1.698	1.698	1.698	1.698
	-13.28	-13.28	-13.28	-13.66
C2-N	1.657	1.657	1.657	1.657
	-10.22	-10.22	-10.21	-10.21

electron densities obtained at various resolutions, converging to a small positive value for grid sizes better than 0.05 Å (Table 4.2), again suggesting that the maps at resolutions of 0.04 Å or better are essentially the same. A true convergence is not achieved for the dependence on grid size of the maximum density (Table 4.2). This is explained by the spiky nature of the maximum, while smaller grid sizes mean that the density at maximum is averaged over the smaller volume of a single voxel, thus leading to a larger value. Values of topological properties at the BCPs of the dynamic electron densities are identical for grid sizes of 0.01, 0.02 and 0.04 Å, while they are slightly different from these values for a grid size of 0.05 Å (Table 4.3).

All these results indicate the absence of series-termination effects in dynamic charge densities computed with grid sizes of 0.04 Å and below. Therefore, we have chosen a grid size of 0.04 Å as optimum grid size for the computation of dynamic electron densities by inverse FFT of the structure factors. The corresponding resolution of the structure factors is $[\sin(\theta)/\lambda]_{max} \simeq$ 6.25 Å^{-1} (Eq. 4.5). This resolution is similar to the resolution of 5.5 Å^{-1} proposed by de Vries, Briels and Feil (1996), and to the resolution of 6 Å^{-1} proposed by Roversi et al. (1998). The grid size of 0.04 Å also falls within the range (0.025–0.05 Å) suitable for precise calculation of topological properties of electron densities as suggested earlier in the literature (Katan et al., 2003; Rabiller et al., 2004; Palatinus et al., 2012).

The present results clearly demonstrate the need of include weak reflections in the Fourier summations, with resolutions far beyond those that can be reached in a

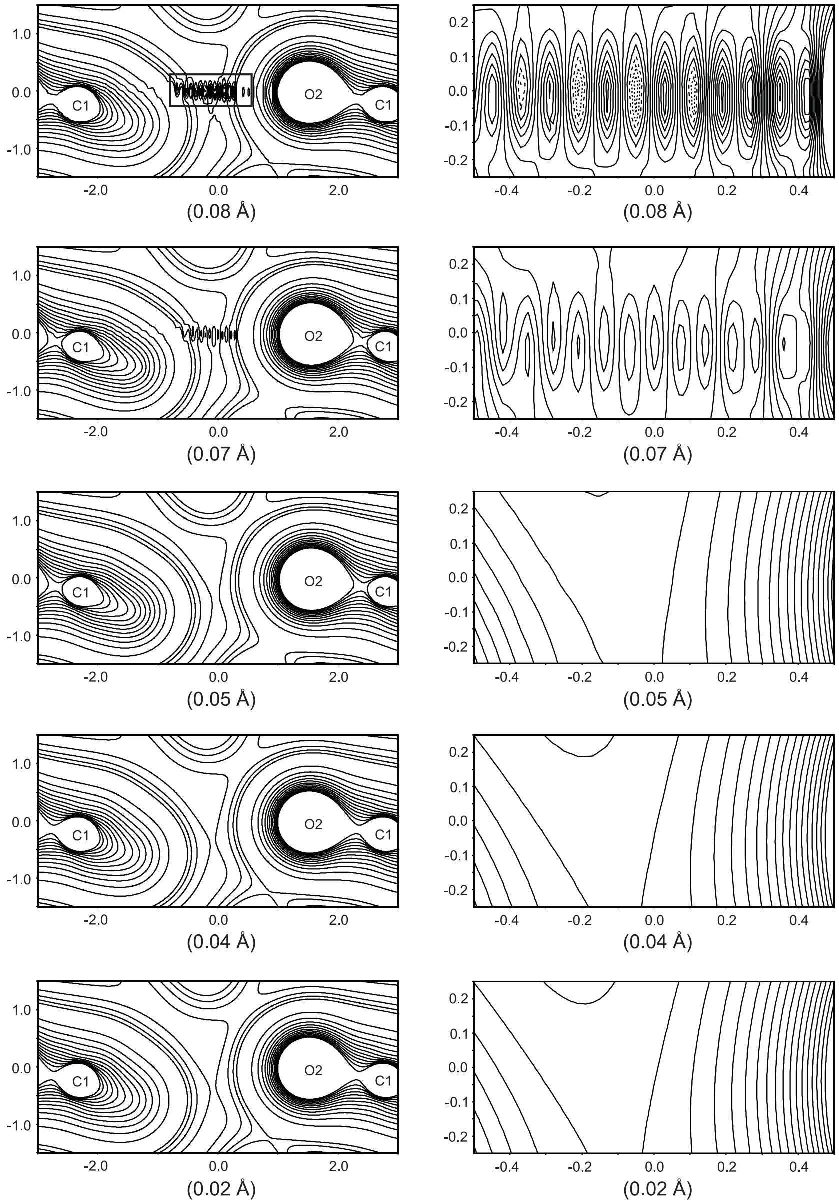

(0.08 Å) (0.08 Å)

(0.07 Å) (0.07 Å)

(0.05 Å) (0.05 Å)

(0.04 Å) (0.04 Å)

(0.02 Å) (0.02 Å)

Figure 4.3: Effect of the grid size on the dynamic electron density of α-glycine. Left column: cross section of the dynamic electron density in the plane in which the maximum series- termination effect occurs. Contour lines are at an interval of 0.02 $e\,\text{Å}^{-3}$ from 0 to 0.1 $e\,\text{Å}^{-3}$ and of an interval of 0.2 $e\,\text{Å}^{-3}$ from 0.1 to 2.5 $e\,\text{Å}^{-3}$. Right column: expanded view of the region marked by the rectangle in the top left map, which contains series-termination ripples. Contour lines are at an interval of 0.01 $e\,\text{Å}^{-3}$ from 0.0 to 0.2 $e\,\text{Å}^{-3}$.

diffraction experiment. The computation of static electron densities by inverse FFT of the structure factors (ADPs are equal to zero) failed to converge to maps free of series-termination effects, down to grid sizes of 0.01 Å. This can be understood from the form of the atomic form factors, which have a simple exponential dependence on the distance to the nucleus for large distances (Coppens, 1997). The Debye–Waller factor represents a Gaussian distribution at large distances, which goes to zero much faster than the exponential dependence. Apparently, the exponential dependence is insufficiently fast to allow high-order structure factors to be neglected. In direct space, this failure demonstrates that any resolution of reflections will be insufficient for describing the spikes in the static electron density at the nuclei.

4.6 Dynamic versus static electron densities

4.6.1 Atomic maxima

Static electron densities possess local maxima of very large values at the positions of the nuclei. Thermal motion of any magnitude leads to smearing of this density, resulting in much lower values at corresponding local maxima of the dynamic charge density (Stewart, 1968a). The major difference between dynamic and static densities can thus be expected at positions close to the locations of the atoms.

Topological analyses of the dynamic electron densities of α-glycine and D,L-serine unveil local maxima at positions of all non-H atoms, which closely match the positions of local maxima in the corresponding static electron densities. Non-atomic maxima have not been found. Local maxima in the dynamic electron densities are not obtained for most H atoms. This feature has been explained previously by the very small values of the dynamic electron densities of H atoms, which, even at their maximum values, are smaller than the densities at distances of $\sim$ 1 Å from the positions of non-H atoms to which the H atoms are covalently bonded (Hofmann et al., 2007a).

Density values at local maxima of dynamic electron densities are much smaller than density values at corresponding maxima of static densities (Figs. 4.4, 4.5, and 4.6). This feature indicates that zero-point vibrations are sufficient for smearing of the high magnitude of the static electron densities near the nuclei. Thermal smearing beyond zero-point vibrations leads to a further large decrease of the density values at local maxima (Fig. 4.5).

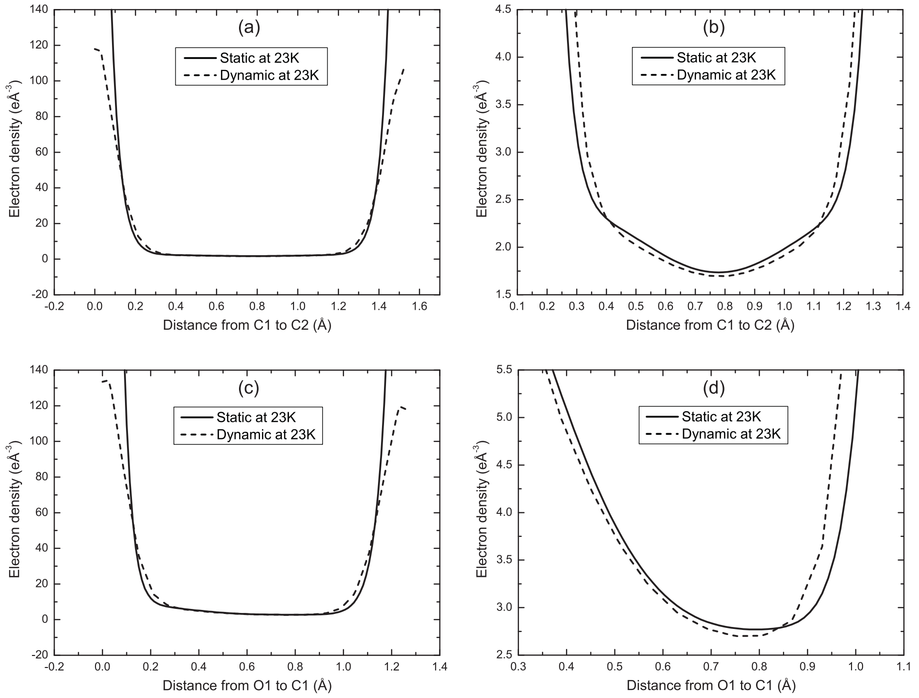

Figure 4.4: Distribution of static and dynamic MP electron densities of α-glycine *versus* distance from nuclei along bond paths. (a) Electron density distribution along the bond path C1–C2. Static densities close to nuclei are truncated at 140 $e\,\text{Å}^{-3}$. (b) Electron densities are scaled up to show details of electron density distribution near the BCP of C1–C2. (c) Electron-density distribution along the bond path O1–C1. Static densities close to nuclei are not shown. (d) Static and dynamic electron densities along O1-C1; densities are scaled up near the BCP of O1–C1.

4.6.2 Electron densities outside local maxima

The low-density regions of the static and dynamic electron densities can hardly be distinguished from each other on the basis of a global consideration of the electron-density distributions, as it is apparent from contour plots of the densities on the main skeletal planes (O1–O2–C1–C2–N) of α-glycine and D,L-serine [Figs. 4.7 and 4.8]. Especially for the electron densities at 20 K, the dynamic deformation densities and corresponding static deformation densities exhibit the same features, while for increasing temperature, the dynamic deformation density becomes progressively flatter [Figs. 4.7b,d and 4.8b,d,f,h].

These observations are corroborated by a quantitative analysis of the topological

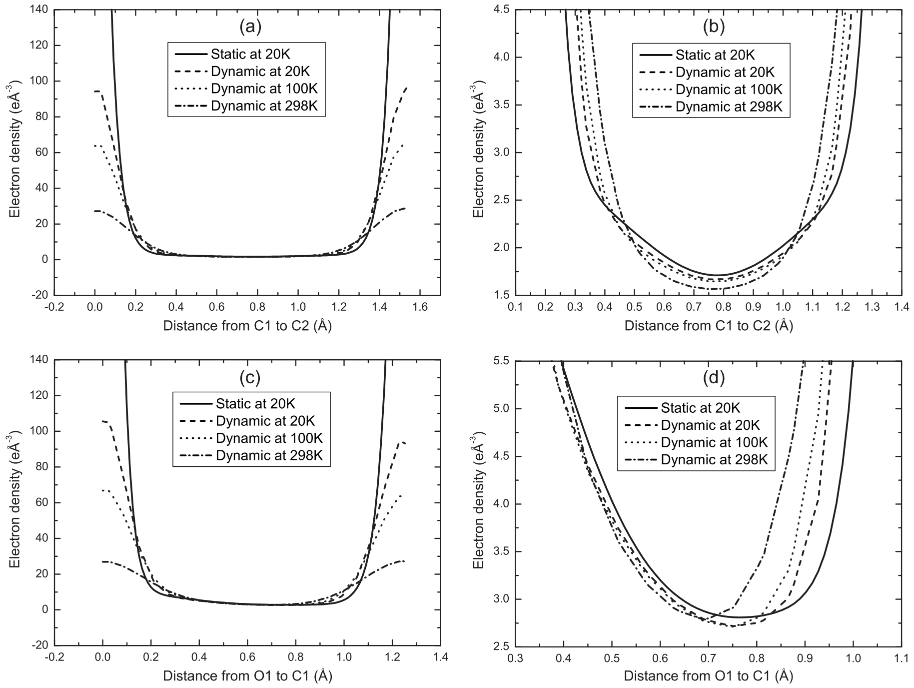

Figure 4.5: Distribution of static and dynamic MP densities of D,L-serine *versus* distance from nuclei along bond paths. (a) Electron-density distribution along the bond path C1–C2. Static densities close to nuclei are not shown. (b) Expanded view of (a), showing details of the variations of the electron densities near the BCP. (c) Electron-density distribution along the bond path O1–C1. Static densities close to nuclei are excluded. (d) Expanded view of (c), showing details of the variations of the electron densities near the BCP.

properties of dynamic electron densities. BCPs are found for all covalent bonds and all hydrogen bonds at positions expected on the basis of the BCPs in the static electron densities, which indicates a successful calculation of the dynamic electron densities (Coppens, 1997). Values of the dynamic densities at BCPs are only weakly dependent on temperature, and they are close to the corresponding values of the static densities (Tables 4.4, 4.5, 4.6, 4.7).

For covalent bonds, dynamic electron densities at BCPs are systematically smaller than corresponding static electron densities, with an average difference of 0.06 e/Å^3 at 20 K, increasing to 0.08 e/Å^3 at 100 K and 0.09 e/Å^3 at 298 K (Table 4.6). At the lower temperatures, these differences cannot be explained by the small differences in the positions of the BCPs in dynamic and static electron densities: the

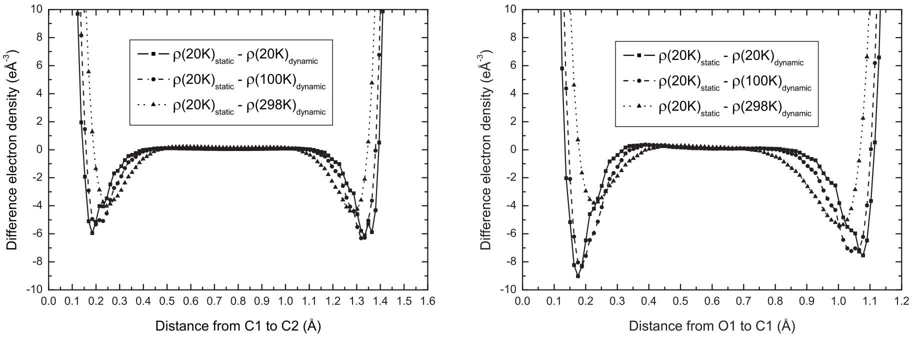

Figure 4.6: Differences between static MP density at 20 K and dynamic MP densities at different temperatures for D, L-serine plotted along bond paths. (a) Difference densities along the bond path C1–C2. (b) Difference densities along the bond path O1–C1.

maximum distance between positions of corresponding BCPs is 0.01 Å at 20 K and 0.02 Å at 100 K (supplementary material **A.2**). The distance between positions of corresponding BCPs at 298 K (maximum distance of 0.08 Å for a C–O bond) partly accounts for the difference in density values at BCPs between dynamic and static MP electron densities, although a general trend cannot be established. These differences in values of electron densities can be compared to the much larger differences between density values at corresponding BCPs of dynamic IAM and dynamic MP electron densities, which amount to 0.4–0.6 e/Å^3 (Tables 4.4 and 4.6). In general, differences between dynamic and static MP electron densities are more pronounced for polar-covalent C–O bonds, and to a lesser extent for C–N bonds, than for symmetric C–C bonds.

Hydrogen bonds possess much smaller electron densities at their BCPs than covalent bonds do. For the compounds studied, electron densities at BCPs of hydrogen bonds are between 0.06 and 0.31 e/Å^3 (Tables 4.5 and 4.7). For hydrogen bonds in corresponding BCPs, the value of the static MP electron density is slightly smaller than the value of the dynamic MP electron density, which is then much smaller than the value of the dynamic IAM electron density. Although absolute differences are small, relative differences between values of static and dynamic electron densities at corresponding BCPs of hydrogen bonds are equal to or larger than those of covalent bonds. Essential features of the static deformation densities of hydrogen bonds are preserved in the dynamic deformation densities [Fig. 4.9], while features become flatter on increasing temperature.

Dynamic effects on electron densities can be rationalized as follows. In principle,

Table 4.4: Electron densities (e/Å^3; first line) and Laplacians (e/Å^5; second line) at the BCPs of covalent bonds of the dynamic IAM density, the dynamic MP density and the static MP density of α-glycine.

	Dynamic		Static
Bond	IAM	MP	MP
C1-O1	2.043	2.701	2.770
	12.37	-19.44	-36.57
C1-O2	2.017	2.648	2.733
	6.81	-23.61	-35.07
C1-C2	1.184	1.698	1.735
	0.25	-13.28	-12.80
C2-N	1.401	1.657	1.691
	1.87	-10.21	-10.42

Table 4.5: Electron densities (e/Å^3; first line) and Laplacians (e/Å^5; second line) at the BCPs of hydrogen bonds of the dynamic IAM electron density, the dynamic MP electron density and the static MP electron density of α-glycine.

	Dynamic		Static
Bond	IAM	MP	MP
O1...H1-N	0.338	0.289	0.283
	2.57	2.51	2.68
O2...H2-N	0.294	0.249	0.240
	3.06	2.77	2.29
O2...H3-N	0.194	0.158	0.151
	1.95	1.61	1.51
O1...H3-N	-	0.072	0.065
	-	1.29	1.24
O1...H4-C2	0.095	0.070	0.063
	1.09	1.04	0.95
O2...H4-C2	0.103	0.077	0.070
	1.14	1.13	1.09

thermal smearing leads to much smaller values of dynamic electron densities at the atomic maxima than of static electron densities at corresponding atomic maxima (Section 4.6.1). In regions of lowest values of static electron densities, thermal smearing must lead to larger values in the dynamic electron densities, since the total number of electrons is constant, and only their distribution over the unit cell is modified by thermal smearing. At points with density values between highest and lowest values, a general trend cannot be established on going from static to dynamic electron densities. The different values of static and dynamic electron densities depend on the value of the density, the temperature, the distances to and the types of the atoms.

This is illustrated by comparing dynamic electron densities and corresponding static electron densities along bond paths between two atoms. Maximum differences are found at the local maxima (at the positions of the atoms). After an initial decrease of this difference on increasing distance to the atom, two points of intersection are found where static and dynamic electron densities are equal to each other, before reaching the BCP [Figs. 4.4, 4.5 and 4.6]. The locations of these points of intersection depend on temperature as well as on the type of atoms comprising the bond, with a largest shift of 0.12 Å for a C–O bond of D,L-serine.

4.6.3 Topological descriptors beyond electron densities

While static and dynamic electron densities possess comparable values at their BCPs, this is not true for the second derivatives of the electron densities.[2] At BCPs, the Hessian matrix of second derivatives has two negative eigenvalues corresponding to directions perpendicular to the bond path, and one positive eigenvalue corresponding to the direction along the bond path. For C–C and C–N bonds at 20 K (zero-point vibrations), the magnitudes of the three curvatures are smaller for dynamic than for static densities (Tables 4.8 and 4.9), indicating that near the BCPs of these bond types dynamic electron densities are less steep than static electron densities, in agreement with a naive understanding of thermal smearing. The largest effect of zero-point vibrations is for C–O bonds, for which the magnitudes of the two negative eigenvalues decrease, but for which the positive eigenvalues increase, indicating that the curvature at BCPs along the bond paths of C–O bonds is larger in dynamic electron densities than in static electron densities. This effect is magnified at higher temperatures, whereas there is only a moderate temperature dependence

---

[2] The first derivatives or gradients of the electron density are zero at BCPs.

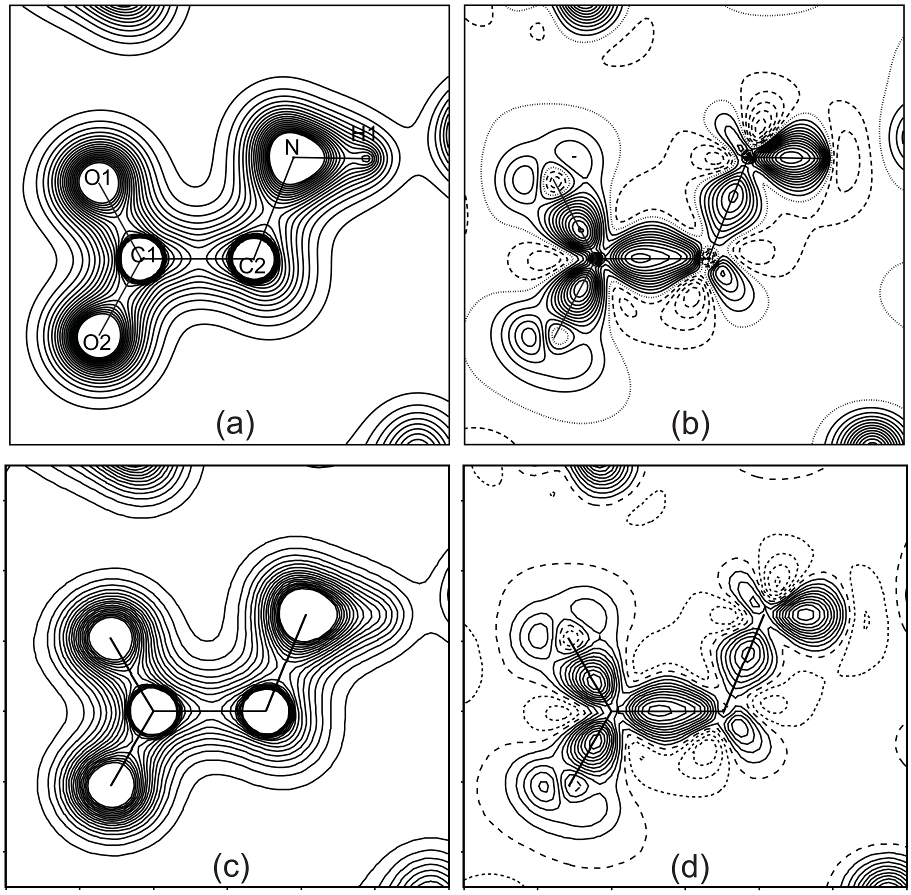

Figure 4.7: C1-C2-N plane of (a, c) the electron density, and (b, d) the deformation density of α-glycine. (a, b) present the static density, and (c, d) give the dynamic density for T = 23 K. Contours are at 0.2 up to 3.6 $e\,\text{Å}^{-3}$ for densities and at an interval 0.05 $e\,\text{Å}^{-3}$ for deformation densities. Positive density values are indicated by solid lines; negative values by dashed lines; and the zero contour by either dotted or long-dashed lines.

of the other curvatures at BCPs of dynamic electron densities (Table 4.9).

We did not find a simple explanation for these different behaviors, except for the observation that values of the second derivatives will depend on a detailed balance of bond asymmetry, distance of the BCPs to the atoms and anisotropic thermal smearing. The similar values at BCPs of static and dynamic electron densities might have been the reason for interpreting high-density values at mid-points of bonds as indications for covalent bonding (Kato et al., 2005; Nishibori et al., 2007). The present results show that such a simple relation does not hold for dynamic electron densities.

The most interesting single quantity is the Laplacian, which is the sum of the eigenvalues of the Hessian matrix. The opposite trends in the positive and negative curvatures at BCPs of C–O bonds are responsible for the observed large differences between dynamic and static electron densities concerning the values of the Laplacian at BCPs of these bonds (Table 4.9), while Laplacians at BCPs of the other bonds have comparable values in static and dynamic electron densities at 20 K and at 100 K (Tables 4.4 and 4.6; Fig. 4.10). Substantial differences are furthermore found for the Laplacian at the BCPs of the C–N bonds in the dynamic electron density at 298 K. These differences must be considered in view of the spread of values of Laplacians at BCPs of single-bond types in static electron densities, which have been reported to be as large as 4.7 $e/\text{Å}^5$ for the C–O bond in the series of amino acids (Mebs et al., 2006). The presently observed difference between 20 K dynamic and static electron densities of $\sim 12\ e/\text{Å}^5$ thus will partly reflect the effect of zero-point vibrations on the Laplacians, but it might also indicate a non-perfect modeling of electron densities by the chosen MP model or a non-accurate deconvolution of static density and thermal motion by the MP refinement. Difficulties in accurately describing C–O bonds have been noticed earlier in electron-density studies (Roversi et al., 1996; Benabicha et al., 2000; Birkedal et al., 2004; Netzel and van Smaalen, 2009).

Allowing for an uncertainty of the magnitude observed by Mebs et al. (2006), a general trend is observed for covalent bonds, with $\rho_{IAM}^{dynamic}(\mathrm{BCP}) < \rho_{MP}^{dynamic}(\mathrm{BCP}) < \rho_{MP}^{static}(\mathrm{BCP})$ and $\nabla^2\rho_{IAM}^{dynamic}(\mathrm{BCP}) > \nabla^2\rho_{MP}^{dynamic}(\mathrm{BCP}) > \nabla^2\rho_{MP}^{static}(\mathrm{BCP})$.

The different temperature dependence of topological descriptors of different bonds might be related to their different chemical properties. This topic will be the subject of future research. In any case, the present results show that topological properties of dynamic electron densities at very low temperatures (20 K) provide at least a semi-quantitative estimate for the values expected for static densities.

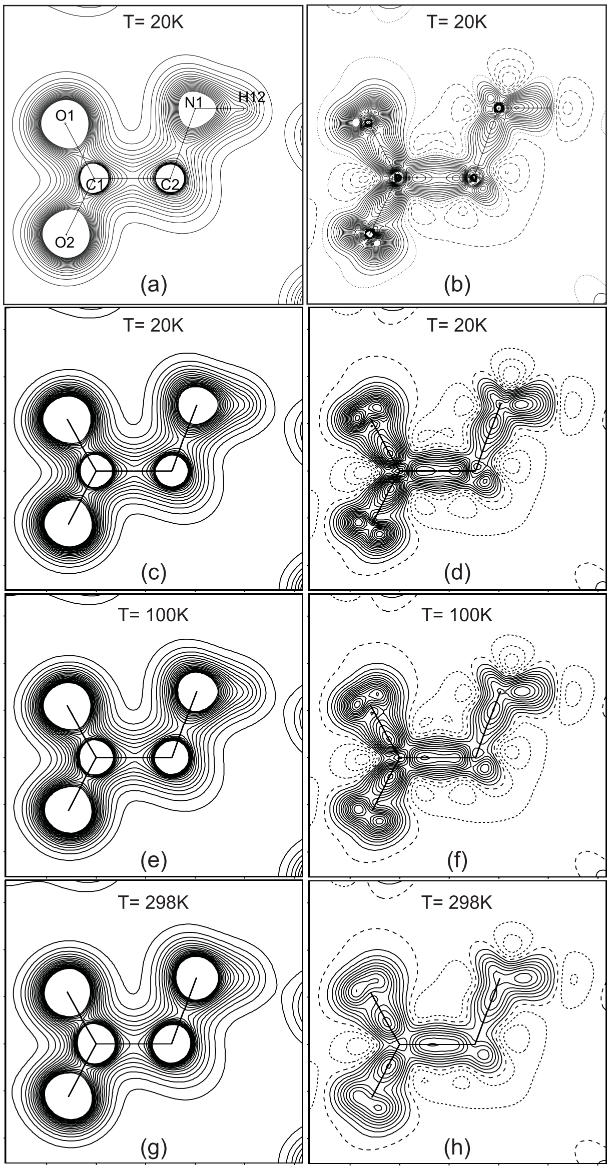

Figure 4.8: C1-C2-N plane of (a, c, e, g) the electron density, and (b, d, f, h) the deformation density of D, L-serine at different temperatures. (a, b) present the static density, and (c,...,h) give the dynamic density. Contours at 0.2 up to 3.6 $e\,\text{Å}^{-3}$ for densities and at an interval 0.05 $e\,\text{Å}^{-3}$ for deformation densities. Positive density values are indicated by solid lines; negative values by dashed lines; and the zero contour by either dotted or long-dashed lines.

Table 4.6: Electron densities (e/Å^3; first line) and Laplacians (e/Å^5; second line) at the BCPs of covalent bonds of the dynamic IAM electron density, the dynamic MP electron density and the static MP electron density of D, L-serine at three different temperatures.

	20 K			100 K			298 K		
	Dynamic		Static	Dynamic		Static	Dynamic		Static
Bond	IAM	MP	MP	IAM	MP	MP	IAM	MP	MP
C1–O1	2.062	2.723	2.810	2.106	2.716	2.814	2.319	2.793	2.831
	8.19	-23.40	-32.18	15.70	-12.04	-32.30	25.50	8.03	-32.82
C1–O2	2.025	2.693	2.791	2.050	2.661	2.795	2.191	2.648	2.814
	9.77	-24.15	-35.32	16.84	-13.22	-35.50	27.78	8.90	-36.28
C3–O3	1.566	1.807	1.869	1.582	1.795	1.874	1.731	1.874	1.888
	6.12	-9.02	-16.64	9.74	-2.16	-16.80	26.10	18.63	-17.30
C1–C2	1.174	1.669	1.710	1.174	1.649	1.713	1.166	1.568	1.716
	1.01	-11.23	-11.77	0.60	-11.25	-11.84	0.25	-10.09	-11.87
C2–C3	1.201	1.684	1.726	1.202	1.662	1.730	1.201	1.584	1.735
	-0.63	-13.60	-12.29	-1.00	-13.41	-12.36	-0.69	-11.10	-12.46
C2–N1	1.395	1.664	1.684	1.408	1.661	1.686	1.458	1.669	1.690
	0.28	-12.20	-10.06	0.085	-11.19	-10.09	4.64	-2.62	-10.17

Hydrogen bonds possess Laplacians and eigenvalues of the Hessian matrix of similar values in the static electron density and the dynamic electron densities at all three temperatures. A possible explanation is that electron densities around BCPs of hydrogen bonds are so small that they exhibit only small variations with position, with increasingly small effects of thermal smearing (Tables 4.5, 4.7).

Thermal smearing has been found to have only a small effect on the number of electrons in each atomic basin (Table 4.10). This is explained by the fact that small shifts of the boundaries of the atomic basins take place in low-density regions and thus hardly affect integral properties, like the number of electrons. Ionic charges can thus be extracted from dynamic densities with values nearly equal to the ionic charges based on static densities.

Table 4.7: Electron densities (e/Å^3; first line) and Laplacians (e/Å^5; second line) at the BCPs of hydrogen bonds of the dynamic IAM electron density, the dynamic MP electron density and the static MP electron density of D, L-serine at three different temperatures.

	20K			100K			298K		
	Dynamic		Static	Dynamic		Static	Dynamic		Static
Bond	IAM	MP	MP	IAM	MP	MP	IAM	MP	MP
O1...H4-O3	0.376	0.279	0.258	0.381	0.288	0.259	0.386	0.305	0.252
	2.87	3.91	4.29	2.74	3.79	4.31	2.03	3.00	4.20
O3...H11-N1	0.324	0.237	0.219	0.322	0.238	0.217	0.324	0.248	0.209
	3.16	4.10	3.89	3.10	4.02	3.83	2.77	3.71	3.71
O2...H12-N1	0.304	0.218	0.200	0.310	0.224	0.200	0.310	0.233	0.187
	2.99	3.71	3.47	2.97	3.74	3.51	2.62	3.40	3.29
O2...H13-N1	0.288	0.202	0.185	0.291	0.207	0.183	0.298	0.221	0.175
	3.09	3.84	3.42	3.04	3.81	3.40	2.78	3.58	3.27
O1...H2-C2	0.137	0.086	0.075	0.141	0.090	0.075	0.155	0.104	0.074
	1.87	1.97	1.53	1.90	2.03	1.53	1.94	2.19	1.52

Table 4.8: Principal curvatures (λ_1, λ_2 and λ_3) and Laplacians (e/Å^5) at BCPs of the static MP electron density (first line) and the dynamic MP electron density (second line) of α-glycine at 23 K.

Bond	λ_1	λ_2	λ_3	$\nabla^2\rho$
C1-O1	-25.78	-23.99	13.20	-36.57
	-23.13	-22.47	26.16	-19.44
C1-O2	-26.24	-22.02	13.18	-35.07
	-24.35	-20.45	21.18	-23.61
C1-C2	-13.28	-11.28	11.75	-12.80
	-12.85	-10.58	10.16	-13.28
C2-N	-12.26	-12.00	13.83	-10.42
	-11.44	-11.11	12.34	-10.21
O1...H1-N	-1.73	-1.69	6.09	2.68
	-1.72	-1.63	5.86	2.51
O2...H2-N	-1.39	-1.37	5.05	2.29
	-1.36	-1.30	5.43	2.77
O2...H3-N	-0.77	-0.70	2.98	1.51
	-0.80	-0.69	3.10	1.61
O1...H3-N	-0.25	-0.14	1.63	1.24
	-0.27	-0.16	1.72	1.29
O1...H4-C2	-0.23	-0.17	1.34	0.95
	-0.25	-0.20	1.48	1.04
O2...H4-C2	-0.28	-0.21	1.58	1.09
	-0.29	-0.23	1.66	1.13

Table 4.9: Principal curvatures (λ_1, λ_2 and λ_3) and Laplacians (e/Å^5) at BCPs of electron densities of $D, L-$serine at temperatures of 20, 100 and 298 K.
Values are given for the static MP density at 20 K (first line), the dynamic MP density at 20 K (second line), the dynamic MP density at 100 K (third line) and the dynamic MP density at 298 K (fourth line).

Bonds	λ_1	λ_2	λ_3	$\nabla^2\rho$
C1–O1	-26.84	-24.68	19.34	-32.18
	-26.98	-24.26	27.84	-23.40
	-26.40	-24.15	38.51	-12.04
	-25.28	-24.15	57.46	8.03
C1–O2	-28.00	-25.38	18.06	-35.32
	-27.72	-22.62	26.19	-24.15
	-26.97	-21.50	35.25	-13.22
	-25.25	-18.88	53.03	8.90
C3–O3	-16.12	-15.54	15.02	-16.64
	-13.82	-12.44	17.24	-9.02
	-13.28	-12.04	23.16	-2.16
	-13.62	-12.43	44.69	18.63
C1–C2	-13.32	-12.43	13.97	-11.77
	-12.94	-10.84	12.55	-11.23
	-12.49	-10.34	11.58	-11.25
	-10.90	-8.72	9.53	-10.09
C2–C3	-13.17	-12.61	13.49	-12.29
	-13.42	-11.17	10.99	-13.60
	-12.81	-10.64	10.04	-13.41
	-11.00	-9.03	8.92	-11.10
C2–N1	-13.85	-12.47	16.26	-10.06
	-15.01	-10.85	13.66	-12.20
	-14.61	-10.58	13.99	-11.19

Continued on next page...

Table 4.9: Continued

Bonds	λ_1	λ_2	λ_3	$\nabla^2\rho$
	-14.02	-10.37	21.76	-2.63
O1. . . H4–O3	-1.42	-1.40	7.11	4.29
	-1.75	-1.35	7.01	3.91
	-1.79	-1.38	6.97	3.79
	-1.77	-1.38	6.14	3.00
O3. . . H11–N1	-1.09	-1.08	6.05	3.89
	-1.24	-1.05	6.40	4.10
	-1.23	-1.04	6.30	4.02
	-1.25	-1.02	5.98	3.71
O2. . . H12–N1	-1.02	-0.97	5.46	3.47
	-1.13	-1.00	5.83	3.71
	-1.16	-1.01	5.91	3.74
	-1.17	-0.99	5.57	3.40
O2. . . H13–N1	-0.93	-0.90	5.25	3.42
	-1.05	-0.91	5.79	3.84
	-1.07	-0.92	5.80	3.81
	-1.10	-0.95	5.63	3.58
O1. . . H2–C2	-0.28	-0.27	2.07	1.53
	-0.33	-0.27	2.56	1.97
	-0.34	-0.29	2.66	2.03
	-0.41	-0.35	2.95	2.19

4.7 Conclusions

We have demonstrated that dynamic electron densities of MP and IAM models can be successfully constructed by inverse Fourier transform of the model structure factors, employing the method of FFT. For organic compounds, an electron density

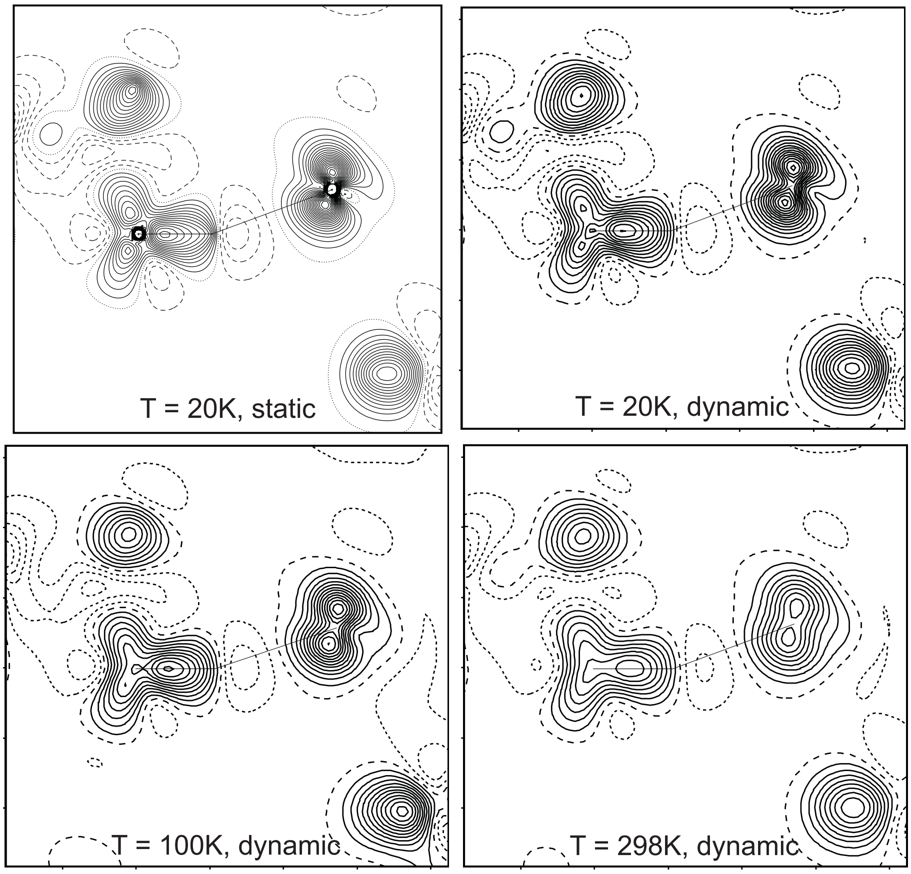

Figure 4.9: Static and dynamic deformation densities of D,L-serine in the plane defined by N1, H12 and O2, showing the N1–H12...O2 hydrogen bond. The contour interval is 0.05 $e\,\text{Å}^{-3}$. Positive density values are indicated by solid lines; negative values by dashed lines; and the zero contour by either dotted or long-dashed lines.

sampled on a grid of mesh 0.04 Å or smaller guarantees a dynamic electron density free of series- termination effects. This mesh corresponds to a resolution better than $[\sin(\theta)/\lambda]_{\max} \simeq 6$ Å^{-1} in reciprocal space (Section 4.5). Employing the same method of interpolation as in XD2006 for calculating the spherical parts of atomic scattering factors, we have demonstrated that the software PRIOR accurately computes the structure factors of a MP model. Exact calculation of atomic scattering factors leads to significantly different values of the structure factors, and thus is the preferred procedure (Appendix 4.8).

The absence of series-termination effects is demonstrated by a topological analysis of the dynamic electron densities, which exhibit features similar to static electron

Table 4.10: Charges from the basin integration for all atoms in D, L-serine.
H atoms in the brackets are included in the atomic basin of the corresponding parent atom.

Atom	Static MP model (20 K)	Dynamic MP model (20 K)	Dynamic MP model (100 K)	Dynamic MP model(298 K)
C3(+H31+H32)	7.7267	7.6988	7.6945	7.7139
C2(+H2)	6.5763	6.5798	6.5820	6.6185
O2	8.8825	8.9041	8.8908	8.8214
N1(+H11+H12+H13)	9.7152	9.7220	9.7223	9.6977
O3(+H4)	9.5142	9.5335	9.5350	9.4935
C1	4.6216	4.5747	4.5995	4.7668
O1	8.9705	8.9872	8.9759	8.8882
Total charge	-0.0070	0.0000	0.0000	0.0000
H2	0.9174	0.7901	0.7046	
H4	0.3836			
H11	0.5238			
H12	0.5267			
H13	0.5296			
H31	0.9596	0.8283		
H32	0.9590	0.7901		

densities, including the occurrence of atomic maxima and BCPs at expected positions, and the absence of non-atomic maxima. An exception is H atoms, which do not necessarily lead to a local maximum in the dynamic electron density, a feature that is due to the very small contribution to dynamic densities of the thermally smeared maxima of H atoms (Hofmann et al., 2007a). Integral properties over atomic basins, like ionic charges, are nearly equal between static and dynamic densities (Section 4.6.2).

Major differences between static and dynamic electron densities are already found for zero-point vibrations, as it has become apparent from the analysis of dynamic electron densities at a temperature of $\sim$ 20 K. Values at atomic maxima are much smaller in dynamic electron densities than in static electron densities, in agreement with the general understanding of thermal smearing. The different values of topological descriptors at BCPs of covalent bonds in dynamic and static electron densities cannot be predicted with simple arguments, but seem to be the result of

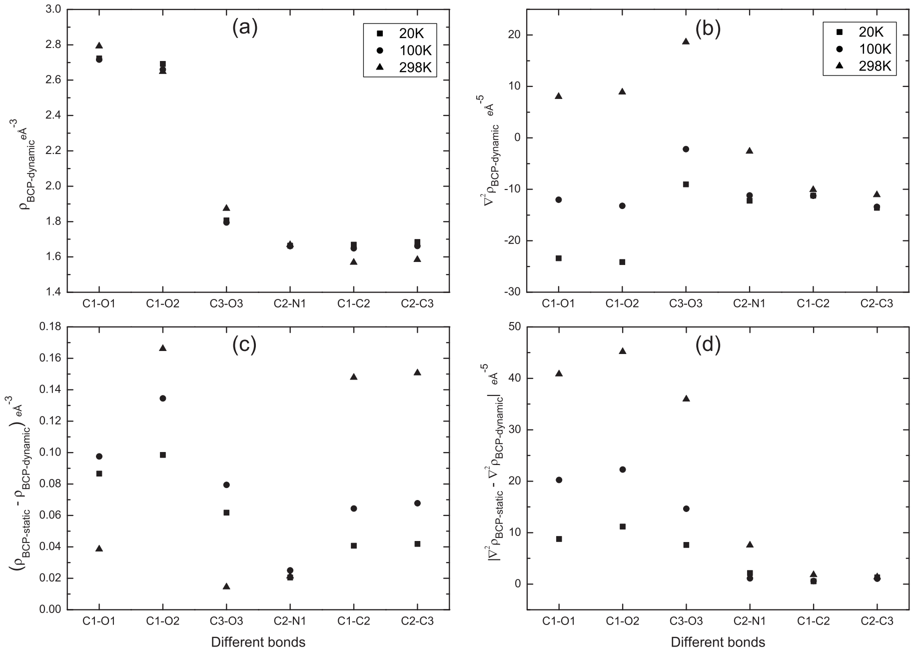

Figure 4.10: Topological properties for covalent bonds from dynamic densities of the MP model and the differences with corresponding static properties. (a) ρ_{BCP} from dynamic MP densities at different temperatures. (b) $\nabla^2\rho_{BCP}$ from dynamic MP densities at different temperatures. (c) Differences between ρ_{BCP} from static and dynamic densities of the MP model at different temperatures. (d) Absolute values of differences between $\nabla^2\rho_{BCP}$ from static densities and dynamic densities of the MP model at different temperatures.

a delicate balance between the magnitude of the electron density, distances to the atoms and anisotropic thermal smearing.

In general, dynamic electron densities have slightly smaller density values at BCPs than static electron densities have, but rather larger differences have been found for Laplacians of polar covalent bonds, with differences of increasing magnitude for increasing polarity and for dynamic densities of increasing temperature (Section 4.6.2). Nevertheless, at temperatures below 100 K, and especially at $\sim$ 20 K, topological properties at BCPs of dynamic electron densities provide at least a semi-quantitative estimate of the topological properties of static electron densities. This shows that chemical bonding can approximately be described by topological properties of low-temperature dynamic densities, although the QTAIM has not been developed for dynamic densities.

Topological properties of different bonds of the same type (the same chemical environment) have been found to be similar in static electron densities (Mebs et al., 2006). Here we have found that this property holds true for dynamic electron densities too.

Differences in values of Laplacians at BCPs in dynamic electron densities at different temperatures, along with the temperature dependencies of other descriptors not considered here, might be helpful to understand the chemical properties of compounds. This is the subject of future research. Particular useful would be a theory relating topological properties of dynamic electron densities to chemical properties at finite temperatures.

Hydrogen bonds have relatively small density values at their BCPs in both static and dynamic electron densities of either the MP model or the IAM. Accordingly, electron densities are only weakly varying in these regions. This observation explains why both the density values and the Laplacians at BCPs of a hydrogen bond are of similar magnitudes in static and dynamic electron densities at all three temperatures, while these quantities have again similar values between dynamic MP electron densities and dynamic IAM electron densities. These observations explain that one might employ static or dynamic IAM densities instead of the true MP densities for describing properties of hydrogen bonds (Spackman, 1999; Downs et al., 2002). However, it has been shown that the observed dependencies of the topological properties at BCPs on the length of the hydrogen bond follow different trends in cases of IAM and MP electron densities (Espinosa et al., 1999; Netzel and van Smaalen, 2009). Therefore, the true electron densities cannot be replaced by IAM electron densities.

4.8 Appendix A: The computer program PRIOR

The modified computer program PRIOR (van Smaalen et al., 2003) reads an instruction file followed by reading of the multipole parameters from a crystallographic information file (CIF) (Hall and McMahon, 2006). The CIF standard, which is followed by many refinement programs, specifies that values of parameters should be given up to one or two significant digits, followed by the one or two digits of the standard uncertainty (s.u.) enclosed in brackets. A quantity computed from these parameters can be more accurate than suggested by the s.u.'s, if high correlations exist between the parameters.[3] This is the situation for the MP model, which

---

[3] For an example in a different context see Röttger et al. (2012).

usually suffers from high correlations between, and large s.u.'s of, parameters, but which provides an accurate description of the electron density. Since the purpose of our procedure is to compute a dynamic electron density which exactly corresponds to the structure models presented by computer programs like XD and MOPRO (Volkov et al., 2006; Jelsch et al., 2005), we need values of the MP parameters with more digits than usually contained in the CIF files produced by these computer programs. This can be achieved by editing the CIF files. Alternatively, the output file of XD2006 contains values with six significant digits for all parameters. Therefore, an option has been included in PRIOR for reading the values of the MP parameters from the output file `XD_LSM.OUT` of XD2006.

The present implementation of the computation of structure factors of the MP model employs double-precision variables for all real and complex numbers. This turned out to be necessary in view of the huge dynamic range of values of structure factors when they are incorporated up to resolutions of ~ 6 Å^{-1}.

The computation of structure factors in PRIOR has been validated by comparing the computed values with the values of the real and imaginary parts of $F(\mathbf{H})$ as computed in XD2006. Since the structure factors for inverse Fourier transform should not contain contributions of anomalous scattering nor corrections for extinction or scale factor, a special version of XD2006 has been kindly provided by L.J. Farrugia (Farrugia, 2012), which produces an additional output file containing the real and imaginary parts of $F(\mathbf{H})$ with six significant digits. The XD2006 software computes the spherical parts of the atomic scattering factors by interpolation of a previously computed table of values {step size of 0.1 Å^{-1} in $[\sin(\theta)/\lambda]$)}. The procedure of interpolation has been kindly provided by P. Macchi (Macchi, 2012), and it has been implemented in PRIOR. For the list of experimental reflections (which are contained in the output of XD2006) a maximum relative difference of less than 10^{-5} has been found in the structure factors as calculated by XD2006 and PRIOR, respectively. In view of the available six significant digits for both MP parameters and structure factors from XD, this discrepancy is within the expected range, and it is concluded that the computation of structure factors of the MP model is performed correctly in PRIOR.

PRIOR also contains the option of exact computation of the atomic scattering factors for each reflection. For this case, a maximum relative difference between XD2006 and PRIOR has been found of 0.2% for a model composed of a single carbon atom, and of 14% for a weak reflection of α-glycine. These discrepancies reflect the error made by the interpolation procedure of computing atomic form factors. However, for most reflections the difference is smaller, because errors may cancel each other and because the deviation of interpolated values from true values of the atomic form factors will be small for scattering vectors with a length close to the points used for the procedure of interpolation. A comparison of the two different calculations as performed with PRIOR showed that the exact computation needs about four times more CPU time than the calculations with interpolated atomic form factors. In view of the increased computational power that is presently available as compared to 15 years ago, the exact computation of atomic form factors seems to be the advisable procedure.

We are grateful to R. Destro for providing the diffraction data of α-glycine, and to B. Dittrich for providing the diffraction data of D, L-serine. Financial support has been obtained from German Science Foundation (DFG).

Chapter 5

Electron densities by the maximum entropy method (MEM) for various types of prior densities: a case study on three amino acids and a tripeptide[1]

5.1 Abstract

Dynamic model densities according to Mondal *et al.* [Acta Cryst. A**68**, 568-581 (2012)] are presented for independent atom models (IAM), IAMs after high-order refinements (IAM-HO), invariom (INV) models and multipole (MP) models of α-glycine, D,L-serine, L-alanine and Ala-Tyr-Ala at $T \backsimeq 20$ K. Each dynamic model density is used as prior in the calculation of electron density according to the maximum entropy method (MEM). We show that at the bond-critical points (BCPs) of covalent C–C and C–N bonds the IAM-HO and INV priors produce reliable MEM density maps, including reliable values of the density and its Laplacian. The agreement between these MEM density maps and dynamic MP density maps is less good for polar C–O bonds, which is explained by the large spread of values of topolog-

---

[1] This Chapter has been published as Electron densities by the maximum entropy method (MEM) for various types of prior densities: a case study on three amino acids and a tripeptide. S. J. Prathapa, S. Mondal, S. Van Smaalen. *Acta Crystallographica B*, **69**, 203-213 (2013).

ical descriptors of C–O bonds in static MP densities. The density and Laplacian at BCPs of hydrogen bonds have similar values in MEM density maps obtained with all four kinds of prior densities. This feature is related to the smaller spatial variation of the densities in these regions, as expressed by small magnitudes of the Laplacians and the densities. It is concluded that the use of the IAM-HO prior instead of the IAM prior leads to improved MEM density maps. This observation shows interesting parallels to MP refinements, where the use of the IAM-HO as an initial model is the accepted procedure for solving MP parameters. A deconvolution of thermal motion and static density that is better than the deconvolution of the IAM appears to be necessary in order to arrive at the best MP models as well as at the best MEM densities.

5.2 Introduction

Knowledge of electron densities in molecular materials provides insight into the nature of interatomic and inter-molecular interactions. The Multipole (MP) formalism is the established method of aspherical electron density analysis. The maximum entropy method (MEM) (Jaynes, 1957; 1979; 1986) has emerged as a promising alternative in recent years, especially because it gives an unbiased estimate of the electron density (Ohno et al., 2007; Takata, 2008; van Smaalen and Netzel, 2009). However, electron densities produced by the MEM may suffer from noise and artifacts (Jauch and Palmer, 1993; Jauch, 1994; de Vries et al., 1994; Roversi et al., 1998; Palatinus and van Smaalen, 2002). Several extensions have been introduced into the MEM aimed at removing these problems, but which, at the same time, introduce a structure model into the calculation (van Smaalen and Netzel, 2009). Although successful to a large extent, unexplained discrepancies have remained between, especially, Laplacians at bond critical points (BCPs) from MP models and MEM densities (Hofmann et al., 2007b;a; Netzel et al., 2008). Here we present a systematic study of the dependence of MEM densities on the kind of structure model employed as prior in the calculation of the MEM.

The dependence of MEM densities on the prior was first discussed by de Vries, Briels and Feil (1996). They have proposed that noise and artifacts in MEM densities can be reduced by using prior densities as close as possible to the true densities. Until now, dynamic densities of independent atom models (IAMs) have been used as prior for electron-density studies using the MEM (de Vries, Briels and Feil, 1996; Papoular et al., 2002; Takata, 2008; Hofmann et al., 2007b;a; Netzel et al., 2008). We have recently established a procedure to obtain dynamic model densities of both the MP model and the IAM (Mondal et al., 2012). Here we use this procedure to generate dynamic electron densities for four kinds of structure models, which are then used as prior in the MEM.

The goal of the MEM is to provide an alternative to the MP refinement, especially in those cases where free refinement of all MP parameters is not possible. Suitable prior densities then are the densities corresponding to the IAM and an invariom (INV) model (Dittrich et al., 2005; 2013). The accepted procedure of determination of MP parameters involves an IAM obtained by refinement against high-order diffraction data (Jelsch et al., 2005; Domagała et al., 2012). The principal difference between the IAM obtained by refinement against all data and the IAM obtained by high-order refinement is that the latter (referred to as IAM-HO) contains a better estimate of the atomic displacement parameters (ADPs). Analogous to this method we propose here to employ the IAM-HO as prior in the MEM. Finally, we employ the result of a full MP refinement as prior.

Three amino acids, namely α-glycine (Destro et al., 2000), D,L-serine (Dittrich et al., 2005) and L-alanine (Destro et al., 1988), and the tripeptide L-alanyl-L-tyrosyl-L-alanine with ethanol solvate (Ala-Tyr-Ala$_{Etoh}$) (Checinska et al., 2006) have been analysed in this study. High-quality low-temperature (~20K) data sets of all these compounds were taken from the literature. For all four compounds MEM densities have been produced with the four types of prior densities. It is shown that densities at BCPs have a weak dependence on the prior, especially when comparing IAM-HO, INV and MP priors. A larger influence of the prior is observed for Laplacians at BCPs, with increasing differences for covalent bonds of increasing ionic character.

The article is organized as follows. Sections 5.3.1–5.3.4 describe the structure refinements involving the four types of models. Section 5.3.5 provides details on the computation of the dynamic model densities. The MEM and the definitions of dynamic deformation density and dynamic difference density are introduced in Section 5.3.6. The topological analysis of the various density maps is described in Section 5.3.7. The discussion first concentrates on global features of model densities and MEM electron density maps (Sections 5.4.1 and 5.4.2). Topological properties at bond critical points (BCPs) of covalent bonds and hydrogen bonds are analyzed in Sections 5.4.3 and 5.4.4. Conclusions are presented in Section 5.5.

Table 5.1: Crystallographic data for α-Glycine, D,L-Serine, L-Alanine and Ala-Tyr-Ala$_{Etoh}$

	α-Glycine[1]	D,L-Serine[2]	L-Alanine[3]	Ala-Tyr-Ala$_{Etoh}$[4]
Chemical formula	$C_2O_2NH_5$	$C_3O_3NH_7$	$C_3O_2NH_7$	$C_{15}O_5N_3H_{21}\cdot C_2H_5OH$
Crystal system, space group	Monoclinic, $P2_1/n$	Monoclinic, $P2_1/a$	Orthorhombic, $P2_12_12_1$	Monoclinic, $P2_1$
Z	4	4	4	2
a, b, c (Å)	5.0866, 11.7731, 5.4595	10.7764, 9.1947, 4.7788	5.9279, 12.2597, 5.7939	8.845, 9.057, 12.364
$\beta(°)$	111.99	106.87	90	94.56
V (Å^3)	303.16	453.13	421.10	987.30
F(000)	160	224	192	396
Temperature (K)	23	20	23	20
$[sin\theta/\lambda]_{max}$ (Å^{-1})	1.15	1.18	1.08	1.11
Observed criteria	$F > 3\sigma_F$	$F > 4\sigma_F$	$F > 3\sigma_F$	$F > 6\sigma_F$
No. of unique reflections (obs/all)	3603/3822	4288/5136	2420/2535	10899/11703
Multipole refinement[5]				
$R_F(obs/all)$	0.0124/0.0145	0.0176/0.0253	0.0184/0.0208	0.0223/0.0264
$wR_{F^2}(obs)$	0.0293	0.0398	0.0298	0.0350
GoF	1.18	1.17	1.10	1.63
$\Delta\rho$(min/max) (e/Å^3)	-0.13/0.15	-0.22/0.21	-0.18/0.15	-0.23/0.27
Invariom refinement[5]				
$R_F(obs/all)$	0.0142/0.0162	0.0195/0.0272	0.0216/0.0240	0.0250/0.0291
$wR_{F^2}(obs)$	0.0374	0.0451	0.0415	0.0422
GoF	1.47	1.32	1.50	1.92
$\Delta\rho$(min/max) (e/Å^3)	-0.21/0.22	-0.29/0.22	-0.26/0.16	-0.28/0.39
IAM refinement[5]				
$R_F(obs/all)$	0.0220/0.0247	0.0298/0.0348	0.0277/0.0309	0.0353/0.0392
$wR_F(obs/all)$	0.0495/0.0505	0.0375/0.0379	0.0354/0.0358	0.0405/0.0411

Continued on next page...

Table B.16: Continued

	α-Glycine[1]	D, L-Serine[2]	L-Alanine[3]	Ala-Tyr-Ala$_{Etoh}$[4]
GoF(obs/all)	1.91/1.86	1.65/1.54	1.72/1.67	2.21/2.16
$\Delta\rho$(min/max) (e/Å^3)	-0.27/0.38	-0.39/0.44	-0.21/0.37	-0.27/0.62
IAM-HO refinement[5]				
$R_F(obs/all)$	0.0229/0.0256	0.0351/0.0400	0.0277/0.0308	0.0358/0.397
$wR_F(obs/all)$	0.0510/0.0520	0.0425/0.0429	0.0365/0.0369	0.0416/0.0421
GoF(obs/all)	1.95/1.89	1.85/1.73	1.75/1.69	2.23/2.18
$\Delta\rho$(min/max) (e/Å^3)	-0.26/0.41	-0.39/0.64	-0.21/0.37	-0.28/0.63

[1] X-ray diffraction data from Destro *et al.*(2000)

[2] X-ray diffraction data from Dittrich *et al.*(2005)

[3] X-ray diffraction data from Destro *et al.*(1988)

[4] X-ray diffraction data from Checinska *et al.*(2006)

[5] Present work - results of multipole refinements have also been presented in Destro et al. (1988), Destro et al. (2000) and Checinska et al. (2006). Invariom refinements have been presented in Dittrich et al. (2005).

5.3 Computational details

5.3.1 Independent Atom Model (IAM)

The IAM refinement of D, L-serine was carried out using the program JANA2006 (Petříček et al., 2006). Reflections with $I > 2\sigma(I)$ were classified as observed. Atomic coordinates and ADPs were taken from Dittrich et al. (2005). The initial refinement varied the coordinates and anisotropic ADPs of non-hydrogen atoms. This was followed by a free refinement of hydrogen atoms, including isotropic ADPs. Hydrogen atoms were subsequently shifted to neutron distances (Allen and Bruno, 2010). Finally, a refinement of coordinates and ADPs of all atoms was performed with strong distance restraints according to neutron values on C–H, N–H and O–H bond lengths (Table 5.1). The IAMs of α-glycine (Netzel et al., 2008), L-alanine (Netzel and van Smaalen, 2009) and Ala-Tyr-Ala$_{Etoh}$ (Netzel and van Smaalen, 2009) were obtained by following the same strategy (Table 5.1).

5.3.2 Independent Atom Model–High Order refinement (IAM-HO)

High-order IAM (IAM-HO) refinement is a strategic refinement method, generally used to improve the deconvolution of atomic thermal motion from static electron densities (Jelsch et al., 2005; Domagała et al., 2012). IAM-HO refinements have been performed for all compounds using the program JANA2006. For α-glycine and D, L-serine, coordinates and ADPs of non-hydrogen atoms were refined against high-order data defined by $\sin(\theta)/\lambda \geq 0.9$ Å^{-1}, and were kept fixed afterwards. Coordinates and U_{iso} of hydrogen atoms were refined with bond restraints on neutron distances (Allen and Bruno, 2010) against low-order data defined by $\sin(\theta)/\lambda \leq 0.7$ Å^{-1}. A similar procedure for L-alanine and Ala-Tyr-Ala$_{Etoh}$ employed high-order data defined by $\sin(\theta)/\lambda \geq 0.8$ Å^{-1}, since these data sets were limited to 1.08Å^{-1} and 1.11 Å^{-1}, respectively (Table 5.1).

5.3.3 Invariom (INV) model

The invariom (INV) model is a multipole model where the MP parameters are obtained from quantum-chemical calculations on small model molecules (Dittrich et al., 2013). Exactly the same parameters are refined as in a refinement of the IAM. The fixed MP parameters are supposed to provide an improved description of the scattering of each atom in its bonded environment compared with the atomic form factors of spherical atoms. (Dittrich et al., 2009) The computer program MoleCoolQt was used for the application of invarioms from the database to the structure model (Dittrich et al., 2006; Hübschle and Dittrich, 2011). Invariom refinements of each of the four compounds were carried out with XD2006 (Volkov et al., 2006) according to the procedure given by Hübschle et al. (2007). Hydrogen atoms were kept at neutron distances (Allen and Bruno, 2010), and atomic scattering factors were taken from Su and Coppens (1998). Final refinement results are given in Table 5.1. The present invariom refinement of D, L-serine essentially reproduces that of Dittrich et al. (2005). Invariom refinements have not been considered in the literature for the other compounds.

5.3.4 Multipole refinement (MP)

Multipole refinements with XD2006 successfully reproduced the multipole model of Ala-Tyr-Ala$_{Etoh}$ as reported by Checinska et al. (2006). As discussed in Mondal et al. (2012), we could not exactly reproduce the MP model of α-glycine. For similar reasons, we also failed to exactly reproduce the published MP model of L-alanine. Instead, we have followed the procedure described in Mondal et al. (2012) for refinements of the MP models of all three amino acids (Table 5.1).

5.3.5 Dynamic model density

The computer program PRIOR has been used to compute dynamic model densities for all sixteen structure models, employing the method of fast Fourier transform (FFT) with a grid of N_p=($N_1 \times N_2 \times N_3$) points over the unit cell (van Smaalen et al., 2003; Mondal et al., 2012). Series termination effects were avoided by the choice of a small grid size of $\sim$ 0.04 Å (Table 5.2). The resulting density maps are denoted by $\rho^{\mathrm{IAM}}(\mathbf{x})$, $\rho^{\mathrm{IAM-HO}}(\mathbf{x})$, $\rho^{\mathrm{INV}}(\mathbf{x})$ and $\rho^{\mathrm{MP}}(\mathbf{x})$ for the IAM, IAM-HO, INV and MP models, respectively.

5.3.6 Maximum entropy method (MEM)

The MEM considers electron densities on the same grid over the unit cell as have been used for computation of the corresponding prior densities. The informational

Table 5.2: Details of MEM calculations. The initial R_F is the R_F value for the prior, the final R_F is the R_F value for the MEM-optimized electron density map (MEM electron density). $\Delta\rho$(min/max) refers to the minimum and maximum values in the difference Fourier map calculated for the MEM electron density.

	α-Glycine	D, L-Serine	L-Alanine	Ala-Tyr-Ala$_{Etoh}$
Grid size (Å)	0.04	0.04	0.04	0.04
No. of pixels	$128 \times 288 \times 144$	$256 \times 216 \times 128$	$144 \times 324 \times 144$	$216 \times 216 \times 324$
IAM PRIOR				
χ^2_{aim}	0.3131	0.55	0.70	1.35
Initial R$_F$	0.0253	0.0356	0.0327	0.0406
Final R$_F$	0.0105	0.0180	0.0193	0.0255
$\Delta\rho$(min/max) (e/Å^3)	-0.15/0.13	-0.18/0.20	-0.18/0.18	-0.29/0.26
IAM-HO PRIOR				
χ^2_{aim}	0.3131	0.55	0.70	1.40
Initial R$_F$	0.0259	0.0404	0.0325	0.0409
Final R$_F$	0.0108	0.0183	0.0193	0.0258
$\Delta\rho$(min/max) (e/Å^3)	-0.20/0.14	-0.19/0.19	-0.19/0.18	-0.30/0.24
INV PRIOR				
χ^2_{aim}	0.90	0.80	1.05	2.80
Initial R$_F$	0.0143	0.0196	0.0217	0.0252
Final R$_F$	0.0088	0.0129	0.0157	0.0196
$\Delta\rho$(min/max) (e/Å^3)	-0.12/0.11	-0.13/0.15	-0.16/0.16	-0.23/0.19
MP PRIOR				
χ^2_{aim}	0.85	0.90	0.90	2.50
Initial R$_F$	0.0125	0.0176	0.0184	0.0224
Final R$_F$	0.0086	0.0144	0.0142	0.0186
$\Delta\rho$(min/max) (e/Å^3)	-0.11/0.11	-0.13/0.17	-0.16/0.16	-0.20/0.20

entropy S is defined as,

$$S = -\sum_{k=1}^{N_p} \left[\rho_k \log \left(\frac{\rho_k}{\rho_k^{prior}} \right) - \rho_k + \rho_k^{prior} \right] \tag{5.1}$$

where $\rho_k = \rho(\mathbf{x}_k)$ is the value of the electron density at the grid point k with coordinates $\mathbf{x}_k$; $\rho_k^{prior} = \rho^{prior}(\mathbf{x}_k)$ is the corresponding value of the prior density. The maximum of S is searched for variation of $\{\rho_k\}$ subject to the F-constraint $C_{F^2} = 0$, with (Sakata and Sato, 1990; Hofmann et al., 2007a).

$$C_{F^2} = -\chi^2_{aim} + \frac{1}{N_F} \sum_{i=1}^{N_F} w_i \left(\frac{|F_{obs}(\mathbf{H}_i) - F_{MEM}(\mathbf{H}_i)|}{\sigma(\mathbf{H}_i)} \right)^2 \tag{5.2}$$

where $F_{obs}(\mathbf{H}_i)$ is the phased observed structure factor of Bragg reflection $\mathbf{H}_i$ with standard uncertainty $\sigma(\mathbf{H}_i)$ and static weight w_i. $F_{MEM}(\mathbf{H}_i)$ is obtained by discrete Fourier transform of the electron density $\{\rho_k\}$. The summation in Eq. (5.2) extends over all measured reflections N_F.

The MEM is an iterative procedure, where the value of χ^2_{aim} defines the point of convergence through $C_{F^2} = 0$. Phases of $F_{obs}(\mathbf{H}_i)$ are the phases of the calculated structure factors of the structure model. The model thus enters into the procedure in two ways: as values of the model density $\{\rho_k^{prior}\}$ in the expression of S [Eq. (5.1)], and as reflection phases in the constraint on the data [Eq. (5.2)].

MEM calculations have been performed with the computer program BayMEM (van Smaalen et al., 2003). Four MEM-electron densities—denoted by $\rho^{\mathrm{MEM}}_{\mathrm{IAM}}(\mathbf{x})$, $\rho^{\mathrm{MEM}}_{\mathrm{IAM-HO}}(\mathbf{x})$, $\rho^{\mathrm{MEM}}_{\mathrm{INV}}(\mathbf{x})$ and $\rho^{\mathrm{MEM}}_{\mathrm{MP}}(\mathbf{x})$—have been generated for each compound, with a prior given by the dynamic model density of the IAM, IAM-HO, INV and MP models, respectively. Following procedures given in Hofmann et al. (2007a), we have determined optimal values of χ^2_{aim} for each of the sixteen MEM calculations (Table 5.2). Previous values of χ^2_{aim} for the IAM priors of α-glycine, L-alanine and Ala-Tyr-Ala$_{Etoh}$ are basically confirmed (Netzel and van Smaalen, 2009). Almost the same values are presently found for the IAM-HO priors. Input data for BayMEM for the INV and MP priors have been generated on the basis of the final refinements with XD2006, instead of JANA2006 that has been used for IAM and IAM-HO priors. XD2006 and JANA2006 employ different weighting schemes, *i.e.* different sets of standard uncertainties of the reflections (the instability factor cannot be used in XD2006). This corresponds to smaller standard uncertainties in XD2006. Accordingly, following the procedure by Hofmann et al. (2007a), we find larger

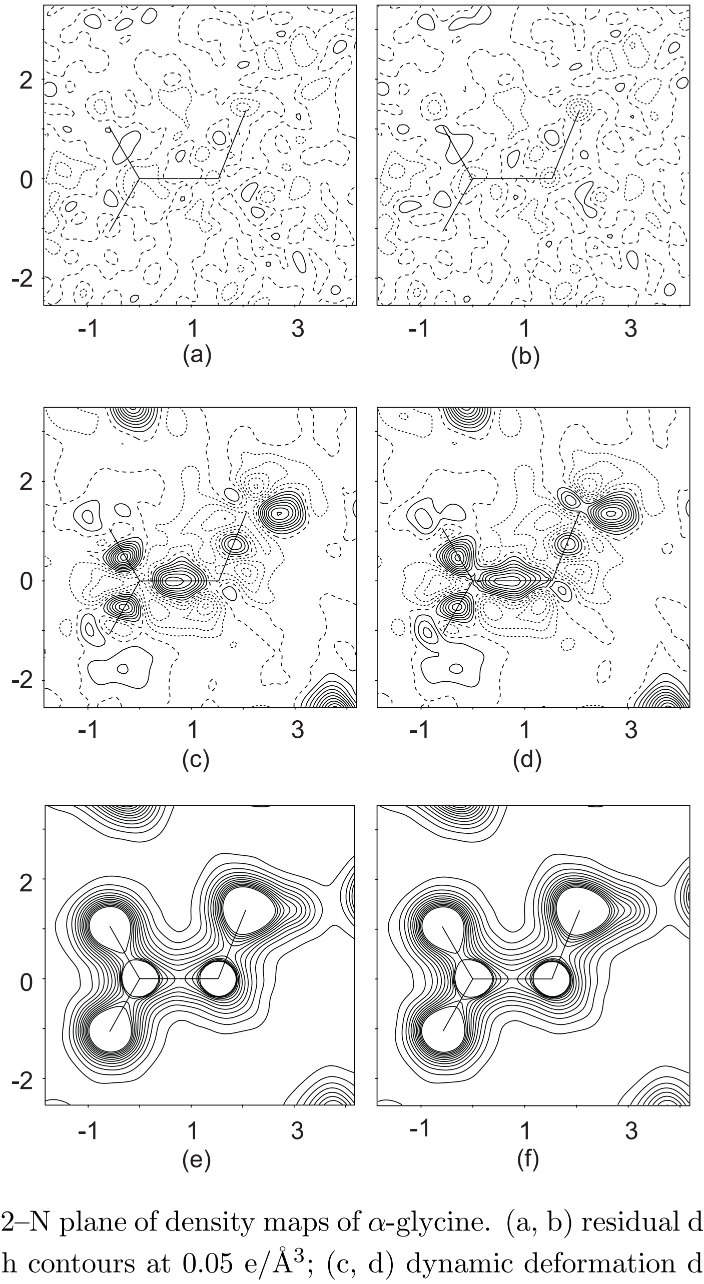

Figure 5.1: C1–C2–N plane of density maps of α-glycine. (a, b) residual density (difference Fourier map) with contours at 0.05 e/Å^3; (c, d) dynamic deformation density [Eq. (5.4)] with contours at 0.05 e/Å^3; and (e, f) MEM density with contours at 0.2 e/Å^3 up to 2.5 e/Å^3. For (a, c, e) the IAM prior, and for (b, d, f) the IAM-HO prior has been used. The numbers on the axes indicate the distance in Å with respect to an arbitrarily selected origin. Solid lines denote positive values, dotted lines denote negative values and dashed lines are the zero contour.

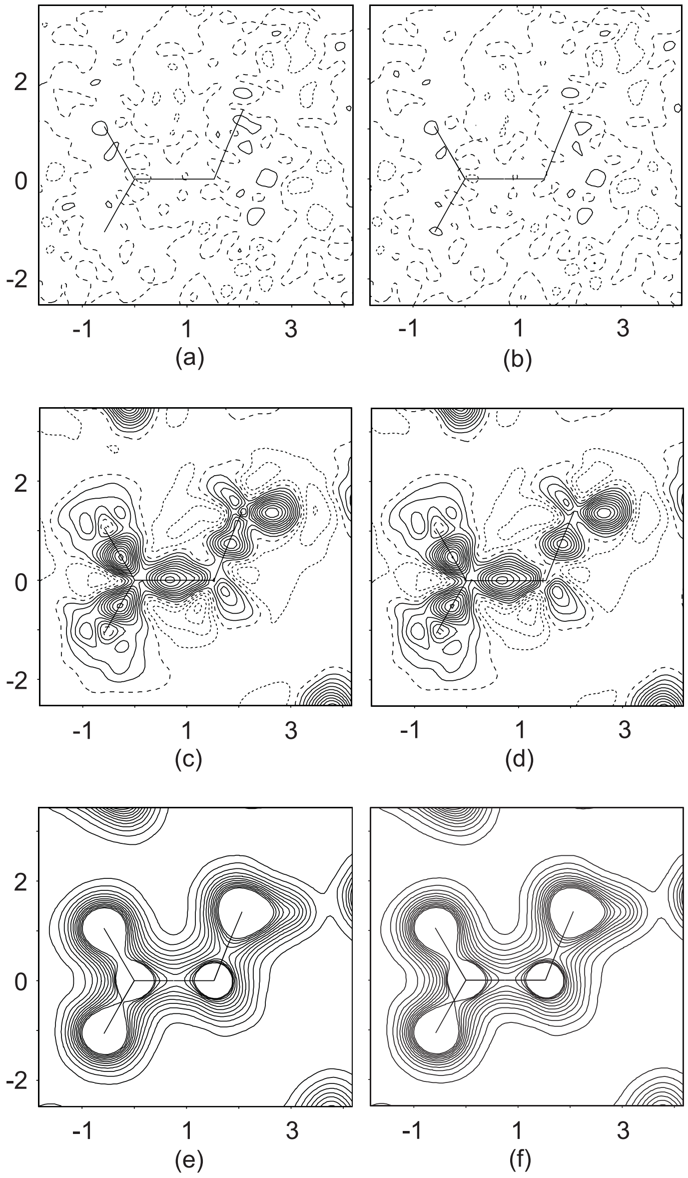

Figure 5.2: C1–C2–N plane of density maps of α-glycine. (a, b) residual density (difference Fourier map) with contours at 0.05 e/Å^3; (c, d) dynamic deformation density [Eq. (5.4)] with contours at 0.05 e/Å^3; and (e, f) MEM density with contours at 0.2 e/Å^3 up to 2.5 e/Å^3. For (a, c, e) the INV prior, and for (b, d, f) the MP prior has been used. The numbers on the axes indicate the distance in Å with respect to an arbitrarily selected origin. Solid lines denote positive values, dotted lines denote negative values and dashed lines are the zero contour.

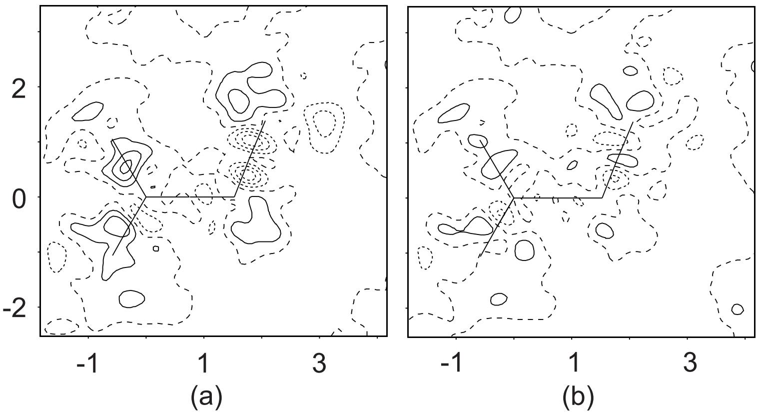

(a) (b)

Figure 5.3: C1–C2–N plane of difference density maps [Eq. (5.3)] of α-glycine for (a) INV prior and (b) MP prior. The numbers on the axes indicate the distance in Å with respect to an arbitrarily selected origin. Contours are at 0.05 e/Å^3; solid lines denote positive values, dotted lines denote negative values and dashed lines are the zero contour.

optimal values of χ^2_{aim} for INV and MP priors than in the case of the IAM priors (Table 5.2).

Bindzus and Iversen (2012) have recently employed the residual density analysis of Meindl and Henn (2008) as a criterion for finding the optimal value of χ^2_{aim}. We like to stress that the method of Hofmann et al. (2007a)—by its very principle—leads to smooth MEM electron density maps with zero or very few spurious maxima, thus facilitating a meaningful topological analysis of the resulting electron density maps.

MEM densities and dynamic model densities have been visualised by four types of maps. Contour maps of sections of the density itself show atomic maxima as well as BCPs [Figs. 5.1(e),(f) and 5.2(e),(f)].[2] Difference Fourier maps provide the residual density $\Delta\rho_{MEM}$ of remaining misfit between model and data [Figs. 5.1(a),(b) and 5.2(a),(b)]. The difference between the MEM density $\rho^{\mathrm{MEM}}_{\mathrm{PRIOR}}(\mathbf{x})$ and the prior density $\rho^{\mathrm{PRIOR}}(\mathbf{x})$ is defined as $\rho^{\mathrm{diff}}(\mathbf{x})$ with [Fig. 5.3]

$$\rho^{\mathrm{diff}}(\mathbf{x}) = \rho^{\mathrm{MEM}}_{\mathrm{PRIOR}}(\mathbf{x}) - \rho^{\mathrm{PRIOR}}(\mathbf{x}) \tag{5.3}$$

where PRIOR stands for any of the four types of structure model. Finally, in analogy with static deformation densities, the dynamic deformation density is [Figs.

---

[2] Sections of maps similar to Figs. 5.1–5.3 are given for the other three compounds in the supplementary material B.

Table 5.3: Topological properties of covalent bonds of α-Glycine: ρ_{BCP} (e/Å^3; first line) and $\nabla^2\rho_{BCP}$ (e/Å^5; second line) for eight different density maps.

	Dynamic Model density				MEM density			
Bond	IAM	IAM-HO	INV	MP	IAM	IAM-HO	INV	MP
C1–O1	2.042	2.044	2.636	2.701	2.482	2.526	2.749	2.735
	12.76	12.30	-17.18	-19.44	8.03	-10.66	-15.93	-15.25
C1–O2	2.016	2.020	2.598	2.648	2.341	2.376	2.611	2.601
	7.15	6.96	-21.83	-23.61	7.18	-3.68	-15.53	-14.48
C1–C2	1.184	1.183	1.696	1.698	1.552	1.566	1.681	1.694
	0.24	0.28	-14.28	-13.28	-12.29	-13.75	-14.00	-15.16
C2–N	1.400	1.401	1.749	1.657	1.500	1.518	1.656	1.649
	1.88	1.86	-11.65	-10.21	-7.62	-10.01	-6.89	-7.67

5.1(c),(d) and 5.2(c),(d)]

$$\rho^{\mathrm{def}}(\mathbf{x}) = \rho^{\mathrm{MEM}}_{\mathrm{PRIOR}}(\mathbf{x}) - \rho^{\mathrm{IAM}^*}(\mathbf{x})\,. \tag{5.4}$$

$\rho^{\mathrm{IAM}^*}(\mathbf{x})$ is the dynamic model density constructed from the IAM*, which is defined as an IAM obtained by removing any MP parameters from the model. So, for IAM and IAM-HO priors, IAM* is equal to the respective model and $\rho^{\mathrm{def}}(\mathbf{x}) = \rho^{\mathrm{diff}}(\mathbf{x})$, while for INV and MP priors, IAM* borrows atomic positions and ADPs from the respective models and it differs from the IAM.

5.3.7 Topological properties of density maps

A topological analysis of each MEM density and each dynamic model density has been performed with the computer program EDMA (Palatinus et al., 2012). Local maxima and BCPs have thus been found at nearly equal positions in the four dynamic model densities and the four MEM densities of each compound (Supplementary Material B). Values of the density and its Laplacian at BCPs are summarized for each map in Tables 5.3, 5.4, 5.5, 5.6, 5.7, 5.8, 5.9 and 5.10.

Local maxima can be identified with atomic positions, except for two spurious maxima in the MEM densities of Ala-Tyr-Ala$_{Etoh}$ (five for the dynamic IAM density of Ala-Tyr-Ala$_{Etoh}$ and one for the dynamic IAM density of D,L-serine). The spurious maxima are small, comprising ”atomic” basins containing less than 0.02 electrons. Their presence demonstrates the less than optimal quality of diffraction

Table 5.4: Topological properties of hydrogen bonds of α-Glycine: ρ_{BCP} (e/Å^3; first line) and $\nabla^2\rho_{BCP}$ (e/Å^5; second line) for eight different density maps.

	Dynamic Model density				MEM density			
Bond	IAM	IAM-HO	INV	MP	IAM	IAM-HO	INV	MP
O1···H1–N	0.341	0.341	0.256	0.289	0.301	0.298	0.242	0.255
	2.53	2.56	3.46	2.51	2.90	3.31	3.56	3.02
O2···H2–N	0.296	0.295	0.209	0.249	0.250	0.247	0.257	0.258
	3.01	3.00	3.61	2.77	3.92	3.81	1.82	1.22
O2···H3–N	0.203	0.204	0.127	0.158	0.197	0.196	0.155	0.163
	1.91	1.90	2.01	1.61	1.37	0.95	1.14	1.09
O1···H3–N	0.096	0.096	0.069	0.072	0.109	0.101	0.082	0.088
	1.18	1.17	1.24	1.29	-1.38	-0.82	0.03	0.17
O1···H4–C2	0.099	0.099	0.082	0.070	0.129	0.122	0.100	0.091
	1.13	1.13	1.11	1.04	-0.16	0.03	0.22	0.22
O2···H4–C2	0.099	0.099	0.086	0.077	0.125	0.120	0.094	0.085
	1.11	1.11	1.16	1.13	-1.25	-1.07	-0.13	0.18

data of Ala-Tyr-Ala$_{Etoh}$,[3] and they are not further considered in this article.

5.4 Discussion

5.4.1 Dynamic model densities

Mondal et al. (2012) have found that the dynamic MP densities at ~20 K of α-glycine and D,L-serine provide an estimate of reasonable accuracy for the static MP densities at BCPs, including values of the densities and the Laplacians. Here we confirm these results for L-alanine and Ala-Tyr-Ala$_{Etoh}$ (Supplementary material B). For all four compounds, dynamic and static INV densities are similar to the corresponding MP densities.

Here we have introduced the dynamic IAM-HO density as a possible prior (Section 5.3.2). Topological descriptors at BCPs are surprisingly similar for dynamic

---

[3] A comparison of values of R indices and residual densities $\Delta\rho$(min/max) across all refinements (Table 5.1) and of the same quantities for the MEM calculations (Table 5.2) shows that the quality of the diffraction data of Ala-Tyr-Ala$_{Etoh}$ is not as good as the quality of the diffraction data of the other three compounds.

Table 5.5: Topological properties of covalent bonds of D,L-Serine: ρ_{BCP} (e/Å^3; first line) and $\nabla^2\rho_{BCP}$ (e/Å^5; second line) for eight different density maps.

	Dynamic Model density				MEM density			
Bond	IAM	IAM-HO	INV	MP	IAM	IAM-HO	INV	MP
C1–O1	2.067	2.062	2.632	2.723	2.474	2.617	2.617	2.664
	9.66	7.98	-19.44	-23.40	-0.53	-20.98	-16.76	-20.65
C1–O2	2.027	2.027	2.585	2.693	2.505	2.621	2.625	2.671
	11.27	9.87	-16.79	-24.15	0.57	-25.05	-19.38	-24.18
C3–O3	1.557	1.569	1.752	1.807	1.695	1.731	1.718	1.751
	6.23	6.10	-6.83	-9.02	-10.26	-8.18	-7.79	-8.57
C1–C2	1.175	1.173	1.674	1.669	1.563	1.585	1.613	1.621
	0.91	1.03	-12.67	-11.23	-14.32	-14.45	-14.25	-13.76
C2–C3	1.203	1.201	1.707	1.684	1.637	1.680	1.679	1.699
	-0.69	-0.59	-14.28	-13.60	-12.06	-15.27	-14.78	-15.41
C2–N	1.393	1.394	1.746	1.664	1.524	1.570	1.573	1.600
	0.28	0.31	-12.33	-12.20	-9.68	-11.76	-9.72	-11.28

IAM and IAM-HO densities of all four compounds (Tables 5.3, 5.4, 5.5, 5.6, 5.7, 5.8, 5.9, 5.10). Major differences exist near local maxima corresponding to the atomic positions. Both density values and magnitudes of Laplacians are larger for dynamic IAM-HO densities than for dynamic IAM densities (Supplementary Material B). These differences directly reflect the smaller values of ADPs in the IAM-HO than in the IAM. Topological properties near BCPs substantially differ between IAM and IAM-HO densities on the one hand, and MP and INV densities on the other hand.

5.4.2 MEM density maps

For each of the four compounds the MEM densities obtained with the four different prior densities are almost indistinguishable in the low-density region including bonding regions [Figs. 5.1(e),(f) and 5.2(e),(f)].[4] Differences between MEM densities of a single compound are much smaller than the differences between the four dynamic model densities, as shown by the spread of R values, encompassing a factor of two for each set of four dynamic model densities (initial R_F in Table 5.2) but differ-

---

[4] Similar maps for the other three compounds exhibit the same qualitative features as the maps for α-glycine—see Supplementary material B.

Table 5.6: Topological properties of hydrogen bonds of D,L-Serine: ρ_{BCP} (e/Å^3; first line) and $\nabla^2\rho_{BCP}$ (e/Å^5; second line) for eight different density maps.

	Dynamic Model density				MEM density			
Bond	IAM	IAM-HO	INV	MP	IAM	IAM-HO	INV	MP
O1···H4–O3	0.374	0.373	0.287	0.279	0.353	0.339	0.320	0.307
	2.32	2.30	3.94	3.91	0.08	1.92	1.42	2.67
O3···H11–N	0.332	0.331	0.235	0.237	0.275	0.264	0.251	0.240
	2.82	2.79	3.93	4.10	1.29	2.15	1.57	2.65
O2···H12–N	0.310	0.308	0.220	0.218	0.256	0.239	0.233	0.223
	2.80	2.75	3.61	3.71	1.17	1.97	2.69	3.22
O2···H13–N	0.290	0.289	0.210	0.202	0.231	0.228	0.201	0.199
	2.94	2.95	3.65	3.84	2.00	2.32	3.62	3.61
O1···H2–C2	0.136	0.136	0.119	0.086	0.153	0.143	0.144	0.121
	1.87	1.86	1.88	1.97	1.99	1.39	1.17	2.16

ing by at most 25% for the MEM densities (final R_F in Table 5.2). Accordingly, the MEM density differs the most from the prior density in case of the IAM and IAM-HO priors and it is close to the prior in the case of INV and MP priors. This feature is also apparent from the close agreement between topological properties of dynamic MP densities and MEM densities obtained with the MP prior (Tables 5.3–5.10). Furthermore, it is shown by the dynamic difference densities [Eq. (5.3)], which exhibit weak structure for INV and MP priors (Fig. 5.3), but are much larger for IAM and IAM-HO priors, in which case the dynamic difference density equals the dynamic deformation density [Figs. 5.1(c),(d)]. In this respect it is noticed that dynamic deformation densities differ not only with respect to the MEM density, but also in the spherical atom model (IAM, IAM-HO or IAM*) as employed in its definition according to Eq. (5.4) [Figs. 5.1(c),(d) and 5.2(c),(d)]. These results show that the MEM and the MP refinements lead to models of comparable quality.

Therefore, a tendency is observed for the MEM to converge to a density map that is independent of the choice of prior, in a first approximation. Nevertheless, the best fit to the diffraction data is provided by MEM densities with INV and MP priors, as indicated by slightly lower R values and less structured residual densities than in the case of IAM and IAM-HO priors. A quantitative estimate of the differences follows from the topological properties of the various density maps (Section 5.4.3).

5.4.3 Topological properties of covalent bonds

Electron densities at BCPs of covalent bonds are almost identical for IAM and IAM-HO dynamic model densities. They are similar for INV and MP dynamic model densities, with a largest difference of only 0.1–0.2 electrons/Å^3 for the most polar bonds (the C–O bonds) (Tables 5.3, 5.5, 5.7, 5.9). However, $\rho^{\mathrm{IAM}}(\mathrm{BCP})$ and $\rho^{\mathrm{IAM-HO}}(\mathrm{BCP})$ are substantially lower than $\rho^{\mathrm{INV}}(\mathrm{BCP})$ and $\rho^{\mathrm{MP}}(\mathrm{BCP})$, with an average difference of 0.57, 0.42 and 0.53 e/Å^3 for C–O, C–N and C–C bonds, respectively.

As discussed in Section 5.4.2, MEM density maps are more alike to each other than the corresponding dynamic model densities, indicating the tendency of the MEM to converge to a density independent of the prior. Accordingly, differences between $\rho^{\mathrm{MEM}}_{\mathrm{INV}}(\mathrm{BCP})$ and $\rho^{\mathrm{MEM}}_{\mathrm{MP}}(\mathrm{BCP})$ are smaller than differences between $\rho^{\mathrm{INV}}(\mathrm{BCP})$ and $\rho^{\mathrm{MP}}(\mathrm{BCP})$. Differences between $\rho^{\mathrm{MEM}}_{\mathrm{IAM}}(\mathrm{BCP})$ on the one hand and $\rho^{\mathrm{MEM}}_{\mathrm{INV}}(\mathrm{BCP})$ or $\rho^{\mathrm{MEM}}_{\mathrm{MP}}(\mathrm{BCP})$ on the other hand are much smaller than the differences between corresponding dynamic model densities. Nevertheless, sizeable discrepancies remain of average values of 0.22, 0.11 and 0.14 e/Å^3 for C–O, C–N and C–C bonds, respectively. They can be attributed to the use of different priors [Eq. (5.1)] rather than wrong reflections phases [Eq. (5.2)]. This feature is demonstrated by two additional MEM calculations for D,L-serine (Tables 5.11 and 5.12). In method 1 the IAM prior has been combined with reflection phases from the INV model, while in method 2 the INV prior has been combined with reflection phases from the IAM model. Method 1 leads to topological properties at BCPs similar to those of $\rho^{\mathrm{MEM}}_{\mathrm{IAM}}(\mathbf{x})$. Method 2 leads to topological properties at BCPs similar to those of $\rho^{\mathrm{MEM}}_{\mathrm{INV}}(\mathbf{x})$, although reflection phases of the IAM have been used in the constraint [Eq. (5.2)].

Despite nearly equal values of $\rho^{\mathrm{IAM}}(\mathrm{BCP})$ and $\rho^{\mathrm{IAM-HO}}(\mathrm{BCP})$, MEM-density maps obtained with these priors attain quite different values at BCPs (Tables 5.3, 5.5, 5.7, 5.9). Instead, $\rho^{\mathrm{MEM}}_{\mathrm{IAM-HO}}(\mathrm{BCP})$ is much closer to $\rho^{\mathrm{MEM}}_{\mathrm{INV}}(\mathrm{BCP})$. An explanation for this feature lies in the different values of $\rho^{\mathrm{IAM}}(\mathbf{x})$ and $\rho^{\mathrm{IAM-HO}}(\mathbf{x})$ near the local maxima, as it is governed by different ADPs of IAM and IAM-HO (Section 5.4.2). Used as prior, they apparently force a different convergence of the MEM, and thus indirectly lead to different density values at corresponding BCPs in MEM density maps obtained with these two priors.

The relations between the values at BCPs of the various density maps can be

Table 5.7: Topological properties of covalent bonds of L-Alanine: ρ_{BCP} (e/Å^3; first line) and $\nabla^2\rho_{BCP}$ (e/Å^5; second line) for eight different density maps.

	Dynamic model density				MEM density			
Bond	IAM	IAM-HO	INV	MP	IAM	IAM-HO	INV	MP
C1–O1	2.073	2.074	2.656	2.807	2.378	2.434	2.687	2.781
	13.91	13.04	-17.82	-27.51	15.77	4.45	-16.81	-25.78
C1–O2	1.999	1.997	2.577	2.649	2.297	2.356	2.628	2.660
	9.25	8.21	-20.13	-24.01	13.90	0.75	-20.71	-25.48
C1–C2	1.172	1.166	1.673	1.696	1.498	1.500	1.659	1.686
	0.88	0.98	-12.90	-12.51	-8.19	-8.24	-12.67	-13.31
C2–C3	1.200	1.200	1.642	1.611	1.516	1.519	1.679	1.658
	0.51	0.53	-11.16	-10.67	-12.28	-11.58	-16.68	-15.90
C2–N	1.380	1.387	1.736	1.614	1.585	1.592	1.688	1.630
	2.33	2.25	-10.06	-11.52	-8.90	-8.55	-10.90	-13.33

summarized as follows:

$$\begin{aligned}&\rho^{\mathrm{IAM}}(\mathrm{BCP}) \backsimeq \rho^{\mathrm{IAM-HO}}(\mathrm{BCP}) < \rho^{\mathrm{INV}}(\mathrm{BCP}) \leq \rho^{\mathrm{MP}}(\mathrm{BCP})\\ &\rho^{\mathrm{MEM}}_{\mathrm{IAM}}(\mathrm{BCP}) < \rho^{\mathrm{MEM}}_{\mathrm{IAM-HO}}(\mathrm{BCP}) \leq \rho^{\mathrm{MEM}}_{\mathrm{INV}}(\mathrm{BCP}) \backsimeq \rho^{\mathrm{MEM}}_{\mathrm{MP}}(\mathrm{BCP})\end{aligned} \tag{5.5}$$

The implication is that, as far as density values at BCPs are concerned, both the IAM-HO and INV priors appear to be of sufficient quality to produce reliable MEM densities.

For Laplacians, $\nabla^2\rho(\mathbf{x})$, a larger spread of values at BCPs is observed among the density maps (Tables 5.3, 5.5, 5.7, 5.9). These variations appear to depend on the amount of polar character of the bond. For covalent C–C bonds the agreement between $\nabla^2\rho(\mathrm{BCP})$ in various density maps is even better than for $\rho(\mathrm{BCP})$, now with

$$\begin{aligned}&\nabla^2\rho^{\mathrm{IAM}}(\mathrm{BCP}) \backsimeq \nabla^2\rho^{\mathrm{IAM-HO}}(\mathrm{BCP}) >> \nabla^2\rho^{\mathrm{INV}}(\mathrm{BCP}) \geq \nabla^2\rho^{\mathrm{MP}}(\mathrm{BCP})\\ &\nabla^2\rho^{\mathrm{MEM}}_{\mathrm{IAM}}(\mathrm{BCP}) \backsimeq \nabla^2\rho^{\mathrm{MEM}}_{\mathrm{IAM-HO}}(\mathrm{BCP}) \geq \nabla^2\rho^{\mathrm{MEM}}_{\mathrm{INV}}(\mathrm{BCP}) \backsimeq \nabla^2\rho^{\mathrm{MEM}}_{\mathrm{MP}}(\mathrm{BCP})\end{aligned} \tag{5.6}$$

where the replacement of "<" in Eq. (5.5) by ">" in Eq. (5.6) reflects the generally negative values of the Laplacians. Noteworthy is that the positive values of Laplacians at BCPs of C–C bonds in $\rho^{\mathrm{IAM}}(\mathbf{x})$ and $\rho^{\mathrm{IAM-HO}}(\mathbf{x})$ turn into negative values in

Table 5.8: Topological properties of hydrogen bonds of *L*-Alanine: ρ_{BCP} (e/Å^3; first line) and $\nabla^2\rho_{BCP}$ (e/Å^5; second line) for eight different density maps.

	Dynamic model density				MEM density			
Bond	IAM	IAM-HO	INV	MP	IAM	IAM-HO	INV	MP
O2···H3–N	0.328	0.327	0.231	0.258	0.336	0.336	0.296	0.297
	2.68	2.66	3.61	3.52	-1.63	-1.45	1.70	1.19
O2···H2–N	0.283	0.281	0.195	0.215	0.292	0.282	0.237	0.235
	2.54	2.52	3.19	3.22	0.22	1.16	2.35	2.55
O1···H1–N	0.286	0.282	0.188	0.206	0.253	0.250	0.212	0.216
	2.32	2.27	3.05	3.00	1.14	1.28	1.83	2.23

$\rho^{\rm MEM}_{\rm IAM}(\mathbf{x})$ and $\rho^{\rm MEM}_{\rm IAM-HO}(\mathbf{x})$ of magnitudes similar to the magnitudes in $\rho^{\rm MEM}_{\rm INV}(\mathbf{x})$ and $\rho^{\rm MEM}_{\rm MP}(\mathbf{x})$. These results show that the MEM gives a good description of covalent C–C bonds for all four priors, and that IAM-HO, INV and MP priors lead to density maps of comparable quality at those BCPs. Covalent C–N bonds possess a small polar component. With one exception for Ala-Tyr-Ala$_{Etoh}$, which can be attributed, in part, to the lower quality of the data, they obey the same relations as C–C bonds.

An accurate description of C–O bonds is difficult to obtain by multipole refinements, as has been noted by several authors (Roversi et al., 1996; Benabicha et al., 2000; Birkedal et al., 2004). The relatively large variations in the magnitudes of Laplacians at BCPs have been attributed to the large variations of magnitudes of second-order derivatives over short distances and possibly less than perfect radial functions, while at the same time moderate variations in the three eigenvalues λ_i of the Hessian matrix are magnified into large variations of the Laplacian. Specifically, for the carboxylic C–O bonds in the amino acids Mebs et al. (2006) have reported a spread of 20 e/Å^5 for values of Laplacians at BCPs of static MP densities. In view of this spread, we find relations between $\nabla^2\rho$(BCP) at C–O bonds of dynamic model densities that are similar to the relations obtained for C–C bonds [Eq. (5.6)],

$$\begin{aligned}&\nabla^2\rho^{\rm IAM}({\rm BCP}) \backsimeq \nabla^2\rho^{\rm IAM-HO}({\rm BCP}) >> \nabla^2\rho^{\rm INV}({\rm BCP}) \geq \nabla^2\rho^{\rm MP}({\rm BCP})\\ &\nabla^2\rho^{\rm MEM}_{\rm IAM}({\rm BCP}) > \nabla^2\rho^{\rm MEM}_{\rm IAM-HO}({\rm BCP}) > \nabla^2\rho^{\rm MEM}_{\rm INV}({\rm BCP}) \geq \nabla^2\rho^{\rm MEM}_{\rm MP}({\rm BCP})\end{aligned} \tag{5.7}$$

The discrepancies between values of $\nabla^2\rho$(BCP) in MEM density maps are larger for C–O bonds than for C–C bonds [Eq. (5.7)]. Especially, $\nabla^2\rho^{\rm MEM}_{\rm IAM}$(BCP) is positive for most bonds, and $\nabla^2\rho^{\rm MEM}_{\rm IAM-HO}$(BCP) attains positive values for several bonds

(Tables 5.3, 5.5, 5.7, 5.9). Based on the fact that the MP model describes chemical bonding better than the IAM does, one can conclude that the large positive values of $\nabla^2\rho^{\mathrm{MEM}}_{\mathrm{IAM}}(\mathrm{BCP})$ probably will not reflect the values of this quantity in "true" density maps. On the other hand, large values of $\rho(\mathrm{BCP})$ along with positive values of $\nabla^2\rho(\mathrm{BCP})$ could indicate the presence of charge-shift bonds (Shaik et al., 2005; Zhang et al., 2009). Further research will be required for the development of a better understanding of C–O bonds.

Table 5.9: Topological properties of covalent bonds of Ala-Tyr-Ala$_{Etoh}$: ρ_{BCP} (e/Å^3; first line) and $\nabla^2\rho_{BCP}$ (e/Å^5; second line) for eight different density maps.

	Dynamic model density				MEM density			
Bond	IAM	IAM-HO	INV	MP	IAM	IAM-HO	INV	MP
C2-O1	2.095	2.092	2.495	2.711	2.492	2.540	2.574	2.710
	18.36	17.29	-8.97	-14.97	26.04	15.26	-1.03	-11.66
C4-O2	2.061	2.058	2.462	2.807	2.529	2.595	2.633	2.860
	14.24	13.12	-12.46	-24.86	18.33	5.91	-12.33	-29.37
C6-O3	2.073	2.071	2.609	2.728	2.515	2.567	2.691	2.743
	20.87	20.01	-7.73	-11.58	18.66	9.41	-8.29	-12.69
C6-O4	1.950	1.953	2.473	2.594	2.412	2.446	2.518	2.563
	9.58	9.16	-16.32	-20.73	11.71	6.68	-11.82	-14.35
C24-O5	1.660	1.669	1.904	1.954	1.852	1.870	1.946	1.961
	3.41	3.55	-10.25	-11.12	1.77	0.58	-10.51	-10.17
C31-O6	1.496	1.505	1.656	1.607	1.711	1.737	1.648	1.594
	4.34	4.55	-5.30	-3.16	0.37	-1.21	-2.62	0.65
C1-N1	1.365	1.369	1.700	1.665	1.624	1.648	1.684	1.697
	2.85	2.83	-8.81	-8.40	-6.40	-7.15	-11.14	-12.66
C2-N2	1.736	1.738	2.203	2.319	2.128	2.166	2.204	2.277
	-1.67	-1.81	-19.98	-21.60	-1.82	-7.76	-17.29	-17.92
C3-N2	1.433	1.436	1.732	1.779	1.700	1.724	1.727	1.780
	1.14	1.11	-10.38	-12.35	-8.62	-10.10	-13.18	-14.57
C4-N3	1.754	1.753	2.222	2.416	2.227	2.262	2.288	2.408
	-1.38	-1.66	-20.09	-24.30	-8.96	-14.38	-20.57	-22.07
C5-N3	1.428	1.430	1.720	1.797	1.740	1.747	1.718	1.769
	1.76	1.74	-9.30	-12.99	-10.48	-10.89	-11.04	-12.61
C1-C2	1.175	1.172	1.744	1.692	1.552	1.562	1.756	1.749
	0.31	0.37	-12.23	-13.48	-12.38	-13.19	-20.61	-22.01
C1-C7	1.190	1.191	1.613	1.733	1.574	1.583	1.701	1.717

Continued on next page...

Table 5.9: Continued

Bond	IAM	IAM-HO	INV	MP	IAM	IAM-HO	INV	MP
	-0.08	-0.06	-11.39	-13.90	-9.36	-8.69	-14.22	-12.77
C3-C4	1.169	1.168	1.742	1.708	1.551	1.561	1.764	1.748
	0.88	0.91	-11.46	-12.48	-10.73	-11.22	-17.12	-18.16
C3-C20	1.140	1.137	1.628	1.603	1.452	1.450	1.634	1.573
	0.55	0.60	-11.08	-11.57	-2.97	-1.43	-10.76	-9.83
C5-C6	1.155	1.154	1.634	1.715	1.487	1.478	1.662	1.718
	-0.01	0.04	-13.51	-14.84	-11.39	-9.81	-15.41	-16.99
C5-C8	1.167	1.163	1.580	1.614	1.522	1.520	1.610	1.594
	0.78	0.85	-9.78	-9.99	-5.84	-5.34	-9.70	-8.89
C20-C21	1.216	1.215	1.700	1.636	1.495	1.483	1.656	1.614
	-0.05	-0.01	-11.31	-9.61	-5.17	-3.93	-8.83	-8.28
C21-C22	1.433	1.433	1.955	1.999	1.882	1.889	1.982	2.002
	-3.04	-3.02	-16.61	-17.94	-14.38	-13.04	-16.00	-16.24
C22-C23	1.451	1.448	1.984	2.011	1.871	1.861	2.021	2.017
	-3.20	-3.14	-16.57	-16.92	-14.02	-11.49	-17.10	-15.70
C23-C24	1.439	1.437	2.019	2.029	1.926	1.929	2.066	2.062
	-2.74	-2.69	-16.01	-16.00	-15.05	-14.49	-17.80	-16.99
C24-C25	1.440	1.439	1.997	2.021	1.944	1.944	2.034	2.055
	-3.24	-3.21	-17.07	-18.06	-18.62	-16.11	-20.11	-20.86
C25-C26	1.446	1.441	1.999	1.984	1.913	1.902	2.007	1.998
	-3.13	-3.03	-16.04	-15.02	-16.85	-13.73	-14.03	-13.65
C21-C26	1.434	1.435	1.957	1.995	1.945	1.964	1.989	2.025
	-2.55	-2.55	-15.97	-15.40	-16.51	-15.82	-16.72	-16.71
C31-C32	1.256	1.258	1.670	1.680	1.606	1.612	1.688	1.698
	0.76	0.80	-11.02	-10.37	-8.18	-8.28	-11.79	-11.13

5.4.4 Topological properties of hydrogen bonds

For hydrogen bonds, approximate relations between the density values at BCPs are

$$\begin{gathered}\rho^{\mathrm{IAM}}(\mathrm{BCP}) \backsimeq \rho^{\mathrm{IAM-HO}}(\mathrm{BCP}) > \rho^{\mathrm{INV}}(\mathrm{BCP}) \backsimeq \rho^{\mathrm{MP}}(\mathrm{BCP}) \\ \rho^{\mathrm{MEM}}_{\mathrm{IAM}}(\mathrm{BCP}) \backsimeq \rho^{\mathrm{MEM}}_{\mathrm{IAM-HO}}(\mathrm{BCP}) > \rho^{\mathrm{MEM}}_{\mathrm{INV}}(\mathrm{BCP}) \backsimeq \rho^{\mathrm{MEM}}_{\mathrm{MP}}(\mathrm{BCP})\end{gathered} \tag{5.8}$$

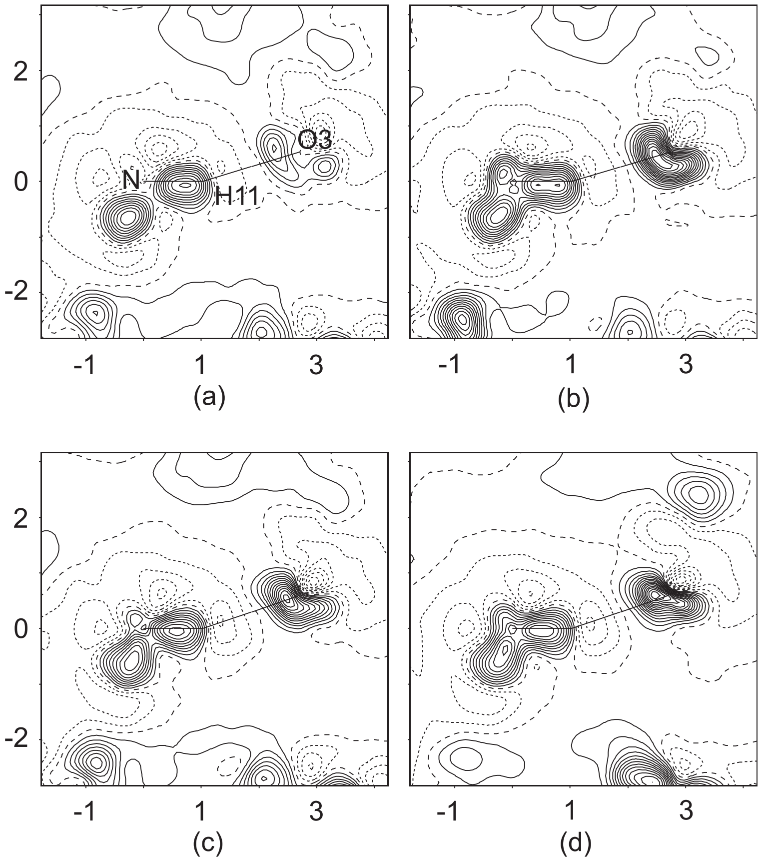

Figure 5.4: Sections of 6 × 6 Å^2 of dynamic deformation maps [Eq. (5.4)] of D, L-serine through the plane of the N1–H11$\cdots$O3 hydrogen bond for (a) IAM prior, (b) IAM-HO prior, (c) INV prior, and (d) MP prior. The numbers on the axes indicate the distance in Å with respect to an arbitrarily selected origin. Contours are at 0.05 e/Å^3; solid lines denote positive values, dotted lines denote negative values and dashed lines are the zero contour.

Table 5.10: Topological properties of hydrogen bonds of Ala-Tyr-Ala$_{Etoh}$: ρ_{BCP} (e/Å^3; first line) and $\nabla^2\rho_{BCP}$ (e/Å^5; second line) for eight different density maps.

	Dynamic model density				MEM density			
Bond	IAM	IAM-HO	INV	MP	IAM	IAM-HO	INV	MP
O6…H15-O5	0.408	0.408	0.308	0.310	0.435	0.420	0.329	0.338
	2.55	2.65	3.54	4.48	1.33	2.28	2.68	3.55
O3…H16-O6	0.362	0.362	0.284	0.285	0.310	0.302	0.289	0.291
	2.28	2.23	3.66	3.63	2.29	2.94	3.46	2.96
O4…H11A-N1	0.335	0.334	0.246	0.251	0.283	0.275	0.258	0.248
	2.64	2.66	3.33	3.28	1.97	2.31	3.27	3.17
O2…H11C-N1	0.352	0.351	0.250	0.268	0.338	0.339	0.243	0.267
	2.33	2.35	3.61	3.59	1.91	2.12	4.15	3.53
O5…H11B-N1	0.294	0.292	0.198	0.210	0.294	0.277	0.225	0.237
	2.47	2.50	2.98	3.43	0.44	1.17	1.58	2.03
O4…H13-N3	0.215	0.214	0.150	0.104	0.184	0.191	0.152	0.145
	2.13	2.14	2.19	2.50	1.77	1.56	1.31	1.90
O1…H1-C1	0.130	0.128	0.118	0.105	0.125	0.125	0.118	0.098
	1.51	1.50	1.70	1.63	0.62	0.45	0.80	1.36
O1…H12-N2	0.186	0.185	0.119	0.107	0.118	0.112	0.110	0.101
	1.87	1.87	1.84	2.09	2.16	1.78	1.70	1.84

Laplacians are positive for most hydrogen bonds and show the following relations

$$\begin{aligned}
&\nabla^2\rho^{\mathrm{IAM}}(\mathrm{BCP}) \backsimeq \nabla^2\rho^{\mathrm{IAM-HO}}(\mathrm{BCP}) < \nabla^2\rho^{\mathrm{INV}}(\mathrm{BCP}) \backsimeq \nabla^2\rho^{\mathrm{MP}}(\mathrm{BCP}) \\
&\nabla^2\rho^{\mathrm{MEM}}_{\mathrm{IAM}}(\mathrm{BCP}) \backsimeq \nabla^2\rho^{\mathrm{MEM}}_{\mathrm{IAM-HO}}(\mathrm{BCP}) \backsimeq \nabla^2\rho^{\mathrm{MEM}}_{\mathrm{INV}}(\mathrm{BCP}) \backsimeq \nabla^2\rho^{\mathrm{MEM}}_{\mathrm{MP}}(\mathrm{BCP})
\end{aligned} \tag{5.9}$$

These relations are in agreement with the previous analysis of $\rho^{\mathrm{IAM}}(\mathbf{x})$, $\rho^{\mathrm{MEM}}_{\mathrm{IAM}}(\mathbf{x})$ and static MP densities (Netzel and van Smaalen, 2009).

Dynamic deformation densities in hydrogen bonds exhibit similar features for the IAM-HO, INV and MP priors, as shown in Fig. 5.4 for the example of the N–H11$\cdots$O3 hydrogen bond of D,L-serine. The qualitatively similar appearances of the dynamic deformation densities with different priors and the numerical analysis at BCPs indicate that a reasonably accurate description of hydrogen bonding can be obtained with both IAM-HO and INV priors.

Table 5.11: Topological properties of covalent bonds of MEM densities of D, L-Serine as obtained by three methods. Method 1: Dynamic IAM model as prior and reflection phases from the INV model. Method 2: Dynamic INV model as prior and reflection phases from the IAM model. INV: prior and reflection phases from the INV model (from Table 5.5). ρ_{BCP} (e/Å^3: first line) and $\nabla^2\rho_{BCP}$ (e/Å^5; second line).

Bond	Method 1	Method 2	INV
C1–O1	2.498	2.589	2.617
	-1.36	-18.31	-16.76
C1–O2	2.480	2.614	2.625
	4.15	-26.36	-19.38
C3–O3	1.684	1.734	1.718
	-4.23	-11.11	-7.79
C1–C2	1.606	1.573	1.613
	-18.56	-10.96	-14.25
C2–C3	1.669	1.665	1.679
	-15.91	-13.71	-14.78
C2–N	1.531	1.571	1.573
	-9.05	-11.11	-9.72

5.5 Conclusions

Mondal et al. (2012) have demonstrated, for α-glycine and D, L-serine, that at BCPs the dynamic MP density maps at $T \backsimeq 20$ K provide a good approximation to the static MP density maps. Here we confirm this observation for L-alanine and the tripeptide Ala-Tyr-Ala$_{Etoh}$. Furthermore, we show that at both covalent bonds and hydrogen bonds the dynamic INV density maps are good approximations to the dynamic MP density maps.

Four types of dynamic density maps have been employed as prior in MEM calculations on the low-temperature X-ray diffraction data of three different amino acids and one tripeptide. Both the IAM-HO and INV priors lead to reliable MEM densities at covalent and hydrogen bonds. The agreement for C–C and C–N bonds is excellent between density values and between Laplacians at BCPs of MEM electron densities obtained with the IAM-HO, INV and MP priors [Eqs. (5.5) and (5.6)]. The agreement is less good for polar C–O bonds, which is commensurate with the large spread of values of topological descriptors of C–O bonds in static MP density

Table 5.12: Topological properties of hydrogen bonds of MEM densities of D,L-Serine as obtained by three methods. Method 1: Dynamic IAM model as prior and reflection phases from the INV model. Method 2: Dynamic INV model as prior and reflection phases from the IAM model. INV: prior and reflection phases from the INV model (from Table 5.6). ρ_{BCP} (e/Å^3; first line) and $\nabla^2\rho_{BCP}$ (e/Å^5; second line).

Bond	Method 1	Method 2	INV
O1$\cdots$H4–O3	0.352	0.316	0.320
	-0.36	2.97	1.42
O3$\cdots$H11–N	0.278	0.245	0.251
	0.52	3.21	1.57
O2$\cdots$H12–N	0.249	0.234	0.233
	1.86	3.39	2.69
O2$\cdots$H13–N	0.226	0.208	0.201
	2.61	3.87	3.62
O1$\cdots$H2–C2	0.152	0.143	0.144
	0.86	2.39	1.17

maps. Density values and Laplacians at BCPs of hydrogen bonds adopt similar values in MEM electron-density maps obtained with all four kinds of prior. This can be explained by the small values and small spatial variation of the densities in these regions, as expressed by small magnitudes for the Laplacians.

The MEM density map obtained with the IAM prior is clearly different from the other MEM density maps. Despite similar behavior in bonding regions of dynamic IAM and IAM-HO densities, used as prior the latter leads to more reliable MEM density maps than the former does. These observations show interesting parallels to MP refinements (Jelsch et al., 2005; Domagała et al., 2012). One accepted procedure of solving for MP parameters involves the generation of those parameters on the basis of the IAM-HO, while the IAM generally leads to less good MP models (Jelsch et al., 2005; Domagała et al., 2012). In other approaches it has been suggested that the use of an invariom model for providing initial values for the MP parameters in a MP refinement will lead to the most reliable MP model (Dittrich et al., 2005; 2008). We therefore conclude that a deconvolution of thermal motion and static density that is better than the deconvolution of the IAM appears to be necessary in order to arrive at reliable MP models as well as reliable MEM densities.

The MEM is intended to provide an estimate of the electron density distribution independently from a MP refinement. Both the IAM-HO and INV priors serve this purpose. This feature becomes especially important for the intended applications to large systems (*e.g.* protein crystals), where the free refinement of the MP model is not possible (Jelsch et al., 2000; Housset et al., 2000; Guillot et al., 2008; Schmidt et al., 2011).

Chapter 6

Dynamic electron density of the protein Crambin using a high resolution X-ray diffraction data[1]

6.1 Introduction

In recent years there is an increase in the number of protein structures solved at subatomic resolution (Jelsch et al., 2000; Housset et al., 2000; Podjarny et al., 2002; Ko et al., 2003; Kang et al., 2004; Bönisch et al., 2005; Hakanpää et al., 2006; Wang et al., 2007; Guillot et al., 2008; Schmidt et al., 2011). Protein structures at subatomic resolution ($d_{min} < 1$Å) allow detailed analysis of electron density distribution, which in turn may help to understand the enzymatic action and intermolecular interactions involved in proteins (Dauter et al., 1997; Housset et al., 2000; Schmidt and Lamzin, 2002). Generally, protein structures are described on the basis of the independent atom model (IAM). However to understand the effect of chemical bonding, consideration of the aspherical multipole (MP) model is necessary. While the MP method (see Chapter 2) is the established method for studying the electron density distribution of small molecules, only few protein structures were studied by this method (Jelsch et al., 2000; Housset et al., 2000; Guillot et al., 2008; Schmidt et al., 2011). However, due to the large number of atoms in proteins, such MP refinements suffer from correlated parameters. In an alternative approach, MP models can also

---

[1] Part of this Chapter has been published as Topological Properties of Chemical Bonds from Static and Dynamic Electron densities. S. J. Prathapa, J. Netzel, S. Van Smaalen. *Z. Anorg. Allg. Chem.* **in press**, (2013)

be obtained by using fixed MP parameters from a database and refining only the positional and thermal parameters like in an IAM refinement (Pichon-Pesme et al., 1995; Dittrich et al., 2006).

Information on chemical bonding of proteins can be rationalised by the QTAIM (Bader, 1990) applied on the static densities obtained from an MP model. The static density obtained from an MP model is deconvoluted from the thermal motion. However, the atomic thermal motion plays an important role in proteins (Parthasarathy and Murthy, 2000; Yuan et al., 2003). Generally, atomic thermal vibrations are taken into account by atomic displacement parameters (ADPs) and are included in the B-factors [$B = 8\pi^2 < U_{eq} >$] which gives insights into protein dynamics and defines the degree of flexibility of protein molecule. The degree of flexibility is often related to their function and chemical properties (Branden and Tooze, 1999). The consideration of dynamic electron density (time-averaged) can reveal the effect of thermal motion on electron densities, as we have successfully demonstrated in Chapter 4 and 5 by computing the dynamic electron densities of small molecules.

Here we consider the small protein Crambin (PDB ID:3NIR) (Schmidt et al., 2011) for dynamic electron density analysis. The protein Crambin was chosen, because of the availability of high-resolution diffraction data (d_{min} = 0.48 Å). The crystallographic details of Crambin are given in Table 6.1. Crambin is a small hydrophobic plant protein (VanEtten et al., 1965) formed by 46 amino acids. The biological function of Crambin is not discovered yet and still is an open scientific issue. The crystal structure of Crambin (Fig. 6.1) was first reported by Teeter and Hendrickson (1979), it consist of two α helices and two β strands which are cross-linked by three disulfide bridges giving stability to the structure. It has been proposed that the structure of Crambin is further stabilised by a salt-bridge interaction, formed by an ion pairing through hydrogen bonds between the guanidinium group of the arginine residue ARG10 and the carboxyl group of the C-terminal asparagine residue ASN46 (Yamano and Teeter, 1994; Bang et al., 2009) (Fig. 6.1). Here the analysis of static and dynamic densities is mainly focussed on the two residues of Crambin which are involved in the salt-bridge interaction. The dynamic electron density, both from the IAM-HO and ELMAM2 model densities have been constructed and compared together with the corresponding static model densities in order to find out the effect of thermal motion on electron densities. And thereby understanding the properties of chemical bonds in Crambin. The effect of B-factors on electron densities and corresponding topological properties are analyzed and compared with a small molecule D, L-serine presented in Chapter 4.

6.2 Computational details

6.2.1 Static density

The structure model and crystallographic data of Crambin were taken from the PDB (PDB ID:3NIR (Schmidt et al., 2011)). Initially, the solvent correction has been done by the method of flat bulk-solvent model (Phillips, 1980; Jiang and Brünger, 1994). Then by following the same strategy according to Schmidt et al. (2011) the IAM refinement was carried out using the computer program MoPro (Jelsch et al., 2005). Here we refined alternately the scale, the coordinates and ADPs of ordered, non-H atoms with a temperature factor B <8 Å^2 against all reflections until convergence. During the refinement H atoms were kept fixed to the bond distance obtained by neutron values (Allen and Bruno, 2010) and their ADPs were constrained to 1.2 or 1.5 × U_{eq} of their parent atoms. After convergence, an IAM refinement against high-order reflections (IAM-HO) in the resolution range of 0.50 to 1.0 Å has been performed in order to improve the deconvolution of static electron density from the ADPs (Guillot et al., 2008). In the subsequent steps, only the scale factor was refined and a complete set of structure factors and the final IAM-HO model were obtained. Refinement statistics are given in Table 6.1. Using the final IAM-HO model, the corresponding static density ($\rho_{\mathrm{stat}}^{\mathrm{IAM-HO}}(\mathbf{x})$) has been generated by superposition of atomic densities by the program VMoPro (Jelsch et al., 2005).

To obtain the MP model, we have transferred the multipoles from the latest database ELMAM2 (Domagała et al., 2012) (for convenience, it is called now on as ELMAM2 model) to the final IAM-HO model. And then in subsequent steps, scale, XYZ and ADPs of ordered non-H atoms with a temperature factor of $B < 8$ Å^2 were refined alternately against all reflections in the resolution range of 0.48 - 20 Å. During the refinement, multipole parameters were kept fixed. The refinement statistics are given in Table 6.1. The corresponding static ELMAM2 density ($\rho_{\mathrm{stat}}^{\mathrm{ELMAM2}}(\mathbf{x})$) has been calculated by superposition of aspherical atomic densities by the program VMoPro (Jelsch et al., 2005).

6.2.2 Dynamic density

The dynamic density of the protein Crambin has been obtained by the computer program PRIOR (van Smaalen et al., 2003) using the procedure as mentioned in Chapter 4. Dynamic densities of both IAM-HO ($\rho_{\mathrm{dyn}}^{\mathrm{IAM-HO}}(\mathbf{x})$) and ELMAM2 ($\rho_{dyn}^{\mathrm{ELMAM2}}(\mathbf{x})$) models are obtained on a grid of $576 \times 512 \times 1024$ pixels, which corre-

Table 6.1: Crystallographic data of Crambin (PDB ID: 3NIR) (Schmidt et al., 2011) and refinement statistics (0.48-20Å) of the present work.

Crystal System	Monoclinic
space group	$P2_1$
Z	2
a (Å)	22.329
b (Å)	18.471
c (Å)	40.769
$\beta(^\circ)$	90.55
V (Å^3)	16813.95
Temperature (K)	100
$[sin\theta/\lambda]_{max}$ (Å^{-1})	1.04
Resolution in d (Å)	0.48
completeness (%)	97
Number of unique reflections	156860
Redundancy	3.7
Refinement statistics:	
IAM	
R_F (%)	13.77
wR_F (%)	15.84
IAM-HO	
R_F (%)	14.46
wR_F (%)	16.59
ELMAM2	
R_F (%)	13.83
wR_{F^2} (%)	15.79

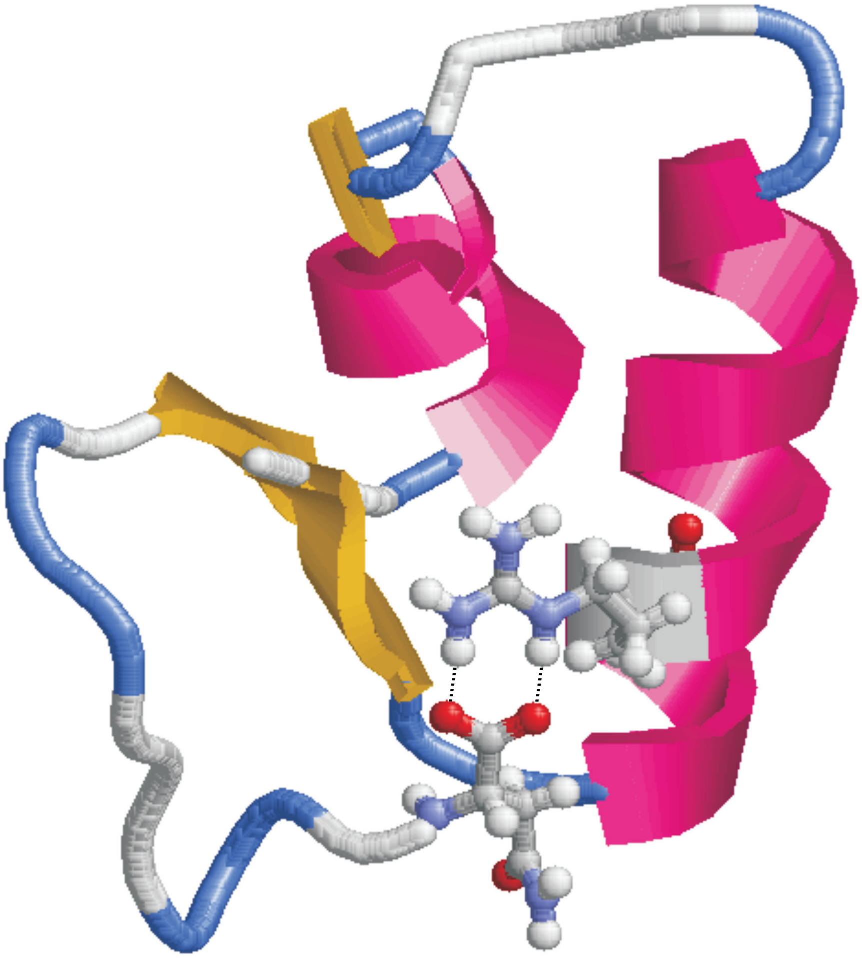

Figure 6.1: A cartoon representation of Crambin molecule with highlight of salt-bridge (dotted lines) formed between ARG10 and ASN46 residues.

sponds to a mesh of ≈ 0.04 Å. This grid size ensures the absence of series termination effect in the calculated maps (Chapter 4).

The topological analysis of static and dynamic densities were carried out using computer program VMoPro of the MoPro package (Jelsch et al., 2005) and by EDMA (Palatinus et al., 2012), respectively. This provides local maxima of the electron density, atomic charges, bond critical points (BCPs), electron density at BCPs ($\rho(\mathbf{BCP})$), eigenvalues ($\lambda_1, \lambda_2, \lambda_3$) of the Hessian matrix and the Laplacian value at BCPs ($\nabla^2\rho(\mathbf{BCP})$).

6.3 Results and Discussion

6.3.1 Electron Densities

The electron density maps obtained from $\rho_{\mathrm{stat}}^{\mathrm{IAM-HO}}(\mathbf{x})$ and $\rho_{\mathrm{stat}}^{\mathrm{ELMAM2}}(\mathbf{x})$ exhibit considerable differences between them [Fig. 6.2 (a,b) and 6.3(a,b)]. The density contours of nitrogen atoms in the displayed plane of $\rho_{\mathrm{stat}}^{\mathrm{ELMAM2}}(\mathbf{x})$ show deviations from the spherical shape, in contrast to the $\rho_{\mathrm{stat}}^{\mathrm{IAM-HO}}(\mathbf{x})$. These differences indicate effects of chemical bonding in $\rho_{\mathrm{stat}}^{\mathrm{ELMAM2}}(\mathbf{x})$. Furthermore, the inspection of static deformation density [Fig. 6.4(a)] in the peptide-bond plane shows the accumulation of deformation electron density on the covalent bonds and exhibits the lone pair of the oxygen atom. Thus, the effect of chemical bonding on electron density is taken into account by the aspherical model of $\rho_{\mathrm{stat}}^{\mathrm{ELMAM2}}(\mathbf{x})$. This shows the importance of considering aspherical model density for a proper description of chemical bonds.

As opposed to the static densities, the dynamic electron densities $\rho_{\mathrm{dyn}}^{\mathrm{IAM-HO}}(\mathbf{x})$ and $\rho_{\mathrm{dyn}}^{\mathrm{ELMAM2}}(\mathbf{x})$ exhibit almost similar features [Fig. 6.2 (c,d) and 6.3(c,d)]. Dynamic electron density maps for either model show an elliptical distortion of apparent atomic shapes, indicating considerably large anisotropic ADPs. As a result, the dynamic deformation density map calculated according to Eq. 5.4 [$\rho_{\mathrm{PRIOR}}^{\mathrm{MEM}}(\mathbf{x})$ in Eq. 5.4 is here replaced by $\rho_{\mathrm{dyn}}^{\mathrm{ELMAM2}}(\mathbf{x})$], does not show any bonding features, but only the lone pair of the oxygen atom [Fig. 6.4(b)]. Here the effects of chemical bonding on electron density are overlapped by ADPs (Netzel and van Smaalen, 2013). On this account, B-factors of Crambin at 100 K have been inspected and compared with corresponding values of D,L-serine at 100 K and 298 K [Fig. 6.5]. The B-factors of the ARG10 residue at 100 K have similar magnitudes as in D,L-serine at 298 K. Atoms of the ANS46 residue, which is located at the C-terminal loop of Crambin, shows even larger B-factors for Crambin at 100 K than the same in

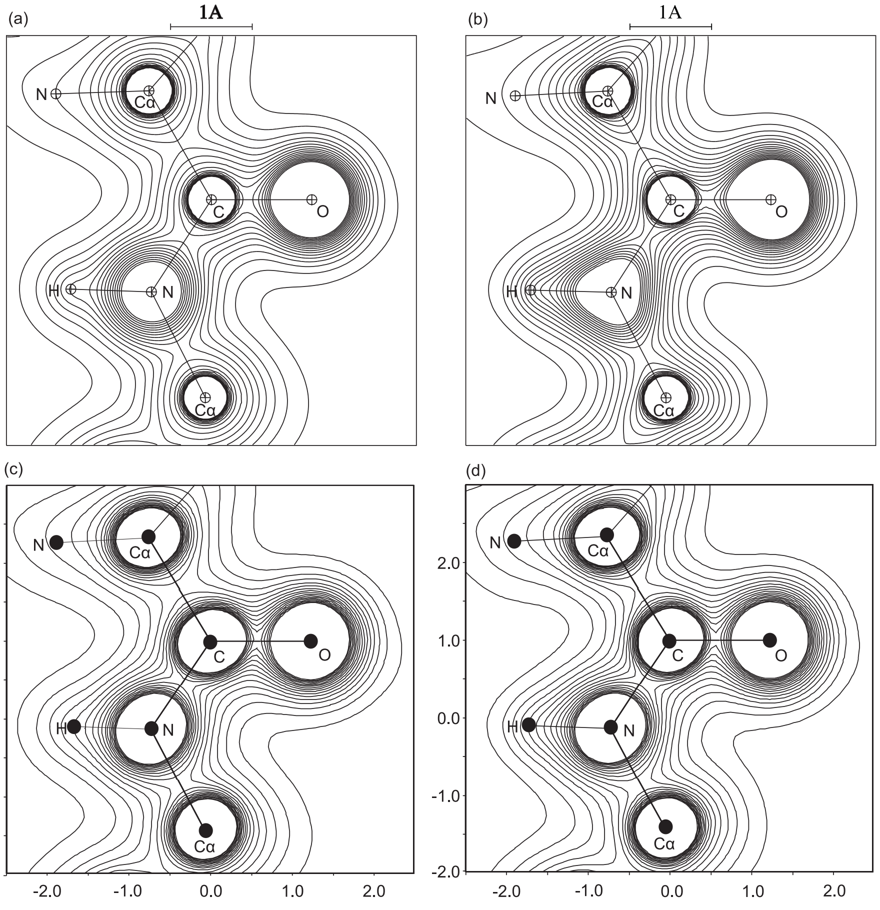

Figure 6.2: Electron density maps through the peptide bond plane (C_9-O_9-N_10) formed by ALA9 and ARG10 residue. (a)$\rho_{\mathrm{stat}}^{\mathrm{IAM-HO}}(\mathbf{x})$, (b)$\rho_{\mathrm{stat}}^{\mathrm{ELMAM2}}(\mathbf{x})$, (c)$\rho_{\mathrm{dyn}}^{\mathrm{IAM-HO}}(\mathbf{x})$ and (d)$\rho_{\mathrm{dyn}}^{\mathrm{ELMAM2}}(\mathbf{x})$. Contour lines of electron density maps are drawn at 0.2 e/Å^3 up to 3.5 e/Å^3.

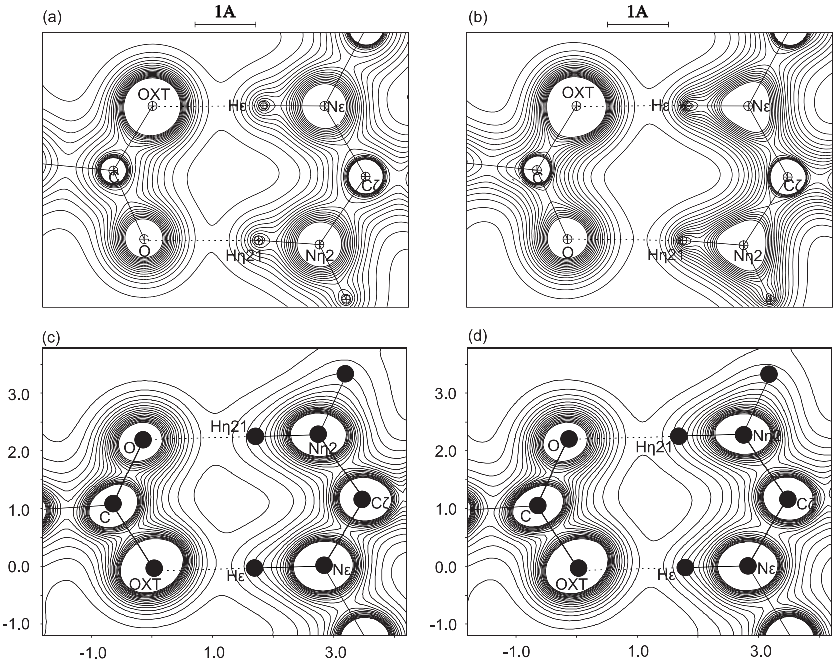

Figure 6.3: Electron density maps through the salt-bridge (OXT_46-N_{ϵ}_10-$N_{\eta 2}$_10) formed by ARG10 and ASN46 residue. (a)$\rho_{\mathrm{stat}}^{\mathrm{IAM-HO}}(\mathbf{x})$, (b)$\rho_{\mathrm{stat}}^{\mathrm{ELMAM2}}(\mathbf{x})$, (c)$\rho_{\mathrm{dyn}}^{\mathrm{IAM-HO}}(\mathbf{x})$ and (d)$\rho_{\mathrm{dyn}}^{\mathrm{ELMAM2}}(\mathbf{x})$. Contour lines of electron density maps are drawn at 0.2 e/Å^3 up to 3.5 e/Å^3.

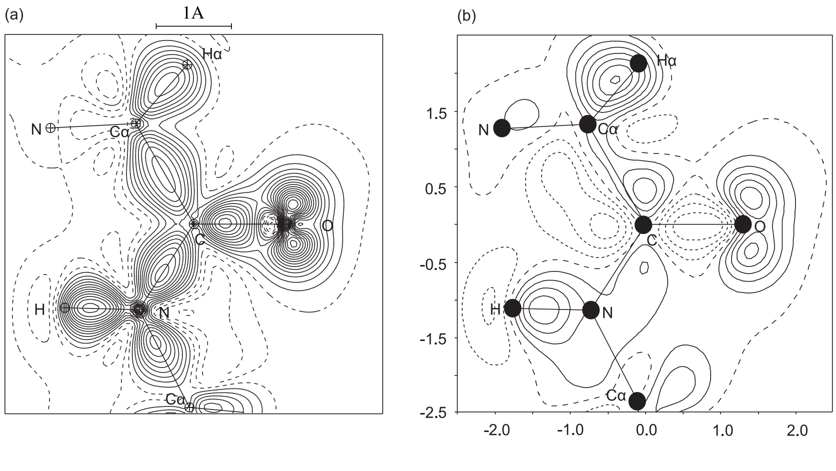

Figure 6.4: Deformation density map through the peptide bond plane (C_9-O_9-N_10) formed by ALA9 and ARG10 residue. (a)Static deformation density and (b) Dynamic deformation density [Eq. 5.4]. Contours are at 0.05 e/Å^3; Solid lines denote positive values, dotted lines denote negative values and dashed lines are the zero contour.

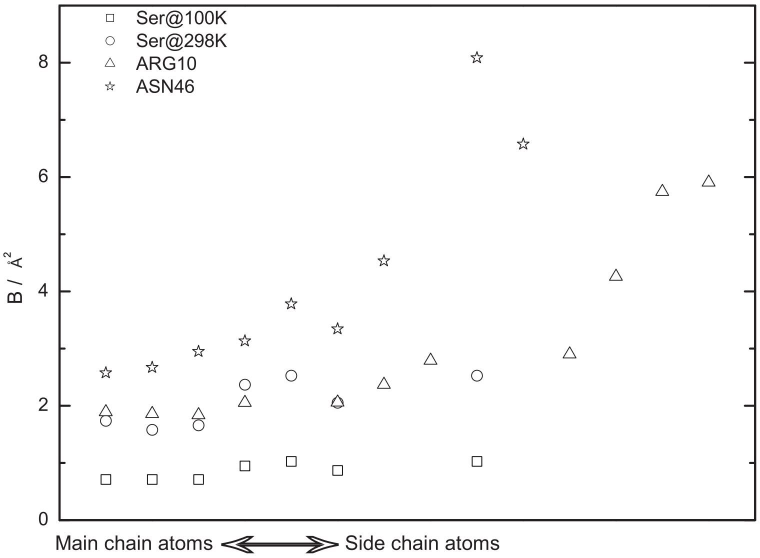

Figure 6.5: B-factors of ARG10 (up triangles), ASN46 (asterisks) from Crambin at 100 K and corresponding B-factors from D, L-serine at 100 K (squares) and at 298 K (circles).

D, L-serine at 298 K. However, the large B-factors of proteins at 100 K may be regarded less as thermal motion but mainly as frozen disorder, which reflects the intrinsic flexibility of proteins (Netzel and van Smaalen, 2013). Irrespective of their origin, the large B-factors of Crambin are too large for a free refinement of multipole parameters or a typical electron density study (Gatti and Macchi, 2012). It might lead to improper deconvolution of the thermal motion and electron density and prevents a meaningful description of the chemical bonds. Thus, the only possibility remains is the employment of fixed multipole parameters from a database without refinement. This approach has been shown to lead to an improved deconvolution of electron density and thermal motion for small molecules at room temperature (Dittrich et al., 2005).

6.3.2 Topological properties

Full topological analysis of static and dynamic electron densities have been performed for the ARG10 and ASN46 residues for both the IAM-HO and the ELMAM2 models [Tables 6.2, 6.3, 6.4, 6.5]. Except for the covalent bonds involving H atoms in dynamic densities, BCPs for all covalent and hydrogen bonds have been found in all four density maps. Due to thermal smearing in dynamic densities, separate maxima for H atoms were not observed. However, the charges of H atoms are included in the atomic basins of the parent atoms to which they are covalently bonded to, which is a common feature in dynamic electron densities (Hofmann et al., 2007a).

The comparison of two static densities reveals that, values of $\rho_{\rm stat}^{\rm ELMAM2}$(BCP) of covalent bonds are systematically larger than the $\rho_{\rm stat}^{\rm IAM-HO}$(BCP), with an average increase in values found to be 0.6 e/Å^3, indicating the effect of chemical bonding on electron density in ELMAM2 model. Bonding effects are clearly visible in static deformation density [Fig. 6.4(a)].

Due to thermal smearing in dynamic electron densities, the values of $\rho_{\rm dyn}^{\rm ELMAM2}$ (BCP) of covalent bonds are found to be smaller than the $\rho_{\rm stat}^{\rm ELMAM2}$(BCP), with an average difference of 0.4 e/Å^3. And in case of IAM-HO densities, $\rho_{\rm stat}^{\rm IAM-HO}$(BCP) is found to be possessing similar (average difference $\sim$ 0.15 e/Å^3) or smaller values than $\rho_{\rm dyn}^{\rm IAM-HO}$(BCP).

However, the comparison of two dynamic densities of Crambin does not show any systematic difference between the values of $\rho_{\rm dyn}^{\rm ELMAM2}$(BCP) and $\rho_{\rm dyn}^{\rm IAM-HO}$(BCP) in covalent bonds, except for polar C-O bonds. Here the values of $\rho_{\rm dyn}^{\rm IAM-HO}$(BCP) of polar C-O bonds are found to be larger than the $\rho_{\rm dyn}^{\rm ELMAM2}$(BCP). This can be attributed to the peculiar behavior of polar C-O bonds, as it has been reported in case of small molecules (Mondal et al., 2012; Prathapa et al., 2013; Roversi et al., 1996; Benabicha et al., 2000; Birkedal et al., 2004; Netzel and van Smaalen, 2009) and proteins (Netzel and van Smaalen, 2013). Overall, the average difference between $\rho_{\rm dyn}^{\rm IAM-HO}$(BCP) and $\rho_{\rm dyn}^{\rm ELMAM2}$(BCP) is very small $\sim$ 0.08 e/Å^3, as it is also evident by the attenuated features in dynamic deformation density map [Fig. 6.4(a,b)]. Nevertheless, values of $\rho_{\rm dyn}^{\rm ELMAM2}$(BCP) in Crambin are found to be reasonable to characterize the covalent bonds according to QTAIM.

As opposed to ρ(BCP), the values of $\nabla^2\rho$(BCP) of covalent bonds show considerable differences between static and dynamic electron densities. The $\nabla^2\rho$(BCP) values of covalent bonds in $\rho_{\rm stat}^{\rm ELMAM2}(\mathbf{x})$ are strongly negative, indicating the covalent character, whereas in case of $\rho_{\rm dyn}^{\rm ELMAM2}(\mathbf{x})$ and in $\rho_{\rm dyn}^{\rm IAM-HO}(\mathbf{x})$, the values are postive for all covalent bonds [Tables 6.2, 6.3]. Moreover, these positive $\nabla^2\rho$(BCP) values in dynamic electron densities of Crambin are found to be similar with the values of dynamic electron density of D,L-serine at 298 K, for which large ADPs are correlated with positive values of Laplacians (Mondal et al., 2012). Hence, as we have found from the electron density analysis [Section. 6.3.1], topological properties also indicate large effects of ADPs on electron densities in Crambin.

The topological properties of hydrogen bonds involved in forming the salt-bridge

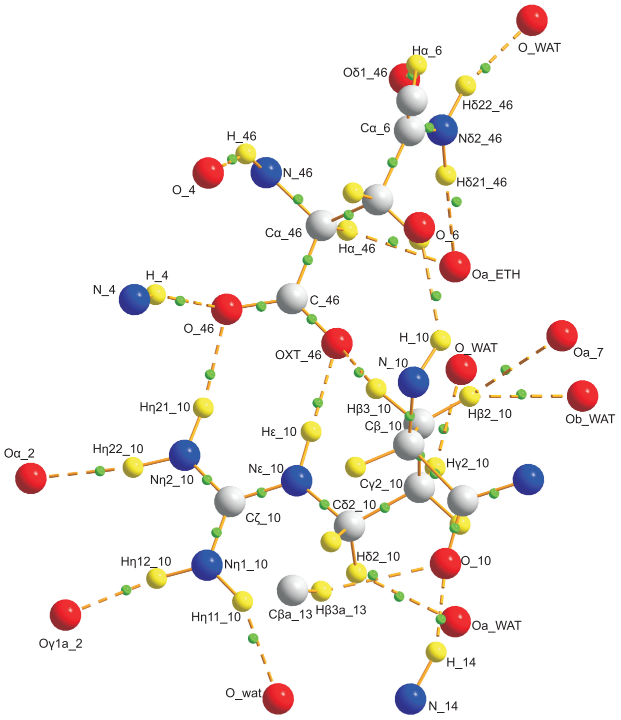

Figure 6.6: Schematic representation of hydrogen bonds formed by ARG10 and ASN46 residues which are involved in salt bridge. Dashed line indicates the hydrogen bonds and their BCPs are indicated by small green coloured spheres.

between ARG10 and ASN46 residues of Crambin and other hydrogen bonds are given in Tables 6.4, 6.5. The schematic representation of these hydrogen bonds is displayed in Figure. 6.6. In case of hydrogen bonds, ρ(BCP) are found to be differing systematically in all four density maps. The general trend observed is $\rho_{\text{dyn}}^{\text{IAM-HO}}(BCP) > \rho_{\text{dyn}}^{\text{ELMAM2}}(BCP) > \rho_{\text{stat}}^{\text{IAM-HO}}(BCP) > \rho_{\text{stat}}^{\text{ELMAM2}}(BCP)$. The slightly larger values of ρ(BCP) of hydrogen bonds in dynamic densities might be caused due to smearing of density at high-density regions, which in turn leads to increased values in low-density regions. The corresponding $\nabla^2\rho$(BCP) values in all four density maps, exhibits positive values, which is typical for hydrogen bonds and it represents closed-shell interaction. And the values of $\nabla^2\rho$(BCP) do not show much variation in all four density maps, indicating the nature of hydrogen bonds which are less prone to the type of density (static or dynamic).

Table 6.2: Topological properties of covalent bonds in ARGININE (ARG-10) residue: ρ(BCP) (e/Å^3: first line) and $\nabla^2\rho$(BCP) (e/Å^5; second line) for four different density maps.

	IAM-HO		**ELMAM2**	
Bond	**static**	**dynamic**	**static**	**dynamic**
C-O	2.121	2.407	2.684	2.115
	5.71	35.60	-25.45	39.94
C_γ-C_δ	1.194	1.226	1.635	1.275
	1.33	5.56	-9.64	6.15
C_α-C	1.185	1.164	1.615	1.276
	1.34	0.64	-9.16	-1.29
C_α-C_β	1.183	1.187	1.598	1.108
	1.44	1.55	-8.97	3.28
C_β-C_γ	1.183	1.178	1.561	1.193
	1.44	2.01	-8.47	1.87
C-N_11	1.802	1.872	2.301	1.920
	-3.89	15.41	-23.75	11.37
C_ζ-$N_{\eta1}$	1.863	2.253	2.454	1.965
	-5.11	29.01	-27.49	22.64
C_ζ-$N_{\eta2}$	1.754	1.752	2.398	1.743
	-2.77	18.50	-24.51	15.41
C_ζ-N_ϵ	1.775	1.838	2.439	1.679
	-3.21	19.25	-26.52	21.37
C_9-N	1.766	1.931	2.241	1.930
	-3.18	18.76	-21.59	14.51
C_α-N	1.464	1.482	1.733	1.490
	2.18	7.24	-9.48	6.38
C_δ-N_ϵ	1.461	1.488	1.715	1.446
	2.23	10.56	-9.66	13.06
C_α-H_α	1.204	-	1.870	-
	-3.82	-	-18.65	-
C_β-$H_{\beta2}$	1.221	-	1.802	-
	-4.10	-	-16.95	-
C_β-$H_{\beta3}$	1.221	-	1.803	-
	-4.10	-	-16.95	-
C_γ-$H_{\gamma2}$	1.221	-	1.803	-

Continued on next page...

Table 6.2: Continued

Bond	**static**	**dynamic**	**static**	**dynamic**
	-4.10	-	-16.94	-
C_γ-$H_{\gamma3}$	1.221	-	1.803	-
	-4.10	-	-16.94	-
C_δ-$H_{\delta2}$	1.219	-	1.866	-
	-4.10	-	-18.64	-
C_δ-$H_{\delta3}$	1.219	-	1.867	-
	-4.09	-	-18.63	-
N-H	1.567	-	2.297	-
	-8.68	-	-39.10	-
N_ϵ-H_ϵ	1.567	-	2.326	-
	-8.64	-	-40.55	-
$N_{\eta1}$-$H_{\eta11}$	1.567	-	2.227	-
	-8.70	-	-36.47	-
$N_{\eta1}$-$H_{\eta12}$	1.568	-	2.289	-
	-8.67	-	-39.66	-
$N_{\eta2}$-$H_{\eta21}$	1.566	-	2.289	-
	-8.69	-	-39.69	-
$N_{\eta2}$-$H_{\eta22}$	1.566	-	2.290	-
	-8.68	-	-39.71	-

6.4 Conclusions

We have successfully reconstructed the static and dynamic electron densities of the protein Crambin at 100 K from both the IAM-HO and the ELMAM2 models. It has been found that B-factors of Crambin at 100 K possess larger values than the small molecule D, L-serine at 298 K. Large B-factors present in Crambin hamper a proper deconvolution of thermal motion and electron density, which in turn prevent a meaningful description of the chemical bonds by a free refinement of multipole parameters (Gatti and Macchi, 2012). Therefore the employment of fixed multipole parameters from a database is the recommended procedure to model the electron density in Crambin (Pichon-Pesme et al., 1995; 2004; Volkov et al., 2004; Dittrich et al., 2006; Zarychta et al., 2007; Dominiak et al., 2007; Jarzembska and Dominiak, 2012; Domagała et al., 2012). However, the large B-factors of Crambin at 100 K should be

Table 6.3: Topological properties of covalent bonds in ASPARAGINE (ASN-46) residue: ρ(BCP) (e/Å^3: first line) and $\nabla^2\rho$(BCP) (e/Å^5; second line) for four different density maps.

	IAM-HO		**ELMAM2**	
Bond	**static**	**dynamic**	**static**	**dynamic**
C_γ-$O_{\delta 1}$	2.166	2.949	2.799	2.713
	9.08	20.91	-18.33	30.80
C-O	2.073	3.260	2.714	3.018
	2.68	34.35	-32.53	38.19
C-OXT	2.044	2.221	2.723	1.962
	8.91	30.43	-32.07	36.74
C_β-C_γ	1.230	1.409	1.637	1.398
	9.40	14.78	-9.70	15.56
C_α-C_β	1.185	1.162	1.469	1.167
	1.43	3.25	-7.60	1.28
C_α-C	1.159	1.379	1.675	1.319
	1.54	14.73	-10.97	15.58
C_γ-$N_{\delta 2}$	1.819	1.884	2.309	2.010
	-4.19	22.04	-23.61	22.27
C_45-N	1.795	1.685	2.285	1.720
	-3.79	11.51	-23.14	9.84
C_α-N	1.467	1.520	1.939	1.592
	2.12	11.30	-11.17	8.37
C_α-H_α	1.205	-	1.873	-
	-3.82	-	-18.63	-
C_β-$H_{\beta 2}$	1.221	-	1.801	-
	-4.10	-	-16.96	-
C_β-$H_{\beta 3}$	1.221	-	1.801	-
	-4.10	-	-16.96	-
$N_{\delta 2}$-$H_{\delta 21}$	1.567	-	2.284	-
	-8.68	-	-39.49	-
$N_{\delta 2}$-$H_{\delta 22}$	1.565	-	2.284	-
	-8.71	-	-39.47	-
N-H	1.567	-	2.317	-
	-8.68	-	-40.12	-

Table 6.4: Topological properties of hydrogen bonds formed by ARGININE (ARG-10) residue: ρ(BCP) (e/Å^3: first line) and $\nabla^2\rho$(BCP) (e/Å^5; second line) for four different density maps.

	IAM-HO		**ELMAM2**	
Bond	**static**	**dynamic**	**static**	**dynamic**
OXT_46....H$_{\epsilon}$_10-N$_{\epsilon}$_10	0.282	0.356	0.258	0.295
	2.81	2.17	1.79	2.10
O_46....H$_{\eta 21}$_10-N$_{\eta 2}$_10	0.230	0.294	0.182	0.243
	2.40	1.57	1.65	1.82
O$_{\gamma 1a}$_2...H$_{\eta 12}$_10-N$_{\eta 1}$_10	0.263	0.309	0.204	0.260
	2.61	1.43	2.00	1.72
O$_{\alpha}$_2....H$_{\eta 22}$_10-N$_{\eta 2}$_10	0.226	0.265	0.176	0.211
	2.33	1.51	1.57	1.63
O_10....H_14-N_14	0.216	0.244	0.175	0.192
	2.30	2.25	1.62	1.95
O_WAT....H$_{\eta 11}$_10-N$_{\eta 1}$_10	0.181	0.230	0.120	0.168
	2.02	1.65	1.59	1.82
O_6....H_10-N_10	0.100	0.123	0.078	0.094
	1.20	1.36	0.92	1.09
OXT_46....H$_{\beta 3}$_10-C$_{\beta}$_10	0.077	0.093	0.055	0.066
	0.93	1.04	0.85	0.98
O_10....H$_{\beta 3a}$_13-C$_{\beta a}$_13	0.071	0.086	0.052	0.073
	0.86	0.98	0.81	1.01
Oa_7...H$_{\beta 2}$_10-C$_{\beta}$_10	0.068	0.086	0.051	0.065
	0.83	0.96	0.75	0.91
O_WAT...H$_{\gamma 2}$_10-C$_{\gamma}$_10	0.050	0.060	0.038	0.046
	0.63	0.71	0.49	0.57
O$_{a}$_WAT....H$_{\delta 2}$_10-C$_{\delta 2}$_10	0.037	0.053	0.023	0.036
	0.46	0.62	0.35	0.54
O$_{b}$_WAT....H$_{\beta 2}$_10-C$_{\beta}$_10	0.031	0.043	0.021	0.031
	0.40	0.50	0.31	0.43

Table 6.5: Topological properties of hydrogen bonds formed by ASPARAGINE (ASN-46) residue: ρ(BCP) (e/Å^3: first line) and $\nabla^2\rho$(BCP) (e/Å^5; second line) for four different density maps.

	IAM-HO		**ELMAM2**	
Bond	**static**	**dynamic**	**static**	**dynamic**
O$_a$_ETH....HD$_{\delta21}$_46-N$_{\delta2}$_46	0.245	0.320	0.172	0.251
	2.47	1.19	1.56	1.62
O_WAT....H$_{\delta22}$_46-N$_{\delta2}$_46	0.216	0.414	0.156	0.343
	2.30	-0.02	1.49	0.79
O_46...H_4-N_4	0.210	0.256	0.175	0.207
	2.24	2.24	1.54	1.96
O_4...H_46-N_46	0.174	0.206	0.140	0.160
	1.93	1.91	1.39	1.67
O$_{\delta1}$_46...H$_\alpha$_6-C$_\alpha$_6	0.083	0.101	0.061	0.078
	1.01	1.12	0.96	1.15
O$_a$_ETH...H$_\alpha$_46-C$_\alpha$_46	-	-	0.037	0.057
	-	-	0.49	0.73

considered as frozen disorder rather than thermal vibrations, which demonstrate an intrinsic flexibility which may be required for the function of Crambin (Netzel and van Smaalen, 2013). In dynamic electron densities, the frozen disorder is visible as distortions of the electron density [Fig. 6.2 (a,b) and 6.3(a,b)]. The distortion of the dynamic electron density in contrast to static electron densities indicate the heavy thermal smearing in dynamic electron densities.

The consideration of $\rho_{\text{stat}}^{\text{ELMAM2}}(\mathbf{x})$ revealed the effects of chemical bonding on the electron density, as is visualised in the static deformation density. It has been quantified by comparing the topological properties of covalent bonds obtained from both static IAM and ELMAM2 densities. But in case of dynamic densities, it is demonstrated that effects on electron densities by chemical bonding are masked by the frozen disorder present in Crambin at 100 K. Nevertheless, the comparison of topological properties of covalent bonds between static and dynamic densities revealed the effect of thermal smearing at BCPs. Due to this large effect of thermal smearing, topological properties of covalent bonds in dynamic densities of Crambin at 100 K are found to be on par with the topological properties of dynamic densities of D, L-serine at 298 K (Chapter 4). On the other hand, the topological properties of hydrogen bonds are found to be least affected by the type of electron densities.

Chapter 7

Summary

Knowledge of electron density distributions in molecular materials can provide insights into the nature of chemical interactions. The advent of Bader's quantum theory of atoms in molecules (QTAIM) allows the analysis of static density obtained from multipole (MP) models and has become a de facto standard. However, static densities do not contain information on thermal vibrations. In reality, atoms are always vibrating about their mean positions even at very low temperatures. Chemical interactions depend on temperature, as it is evident from the temperature-dependent phase transitions. In fact, the Bragg reflections measured by X-ray diffraction directly reflect the dynamic electron density (time-averaged electron density). The present thesis deals with the notion of dynamic electron density and describes the effect of temperature on the electron density distribution by analysing both static and dynamic densities.

Static and dynamic electron densities corresponding to independent atom models (IAM) and MP models have been constructed for several molecular crystals. In addition to these two types of model, structure models based on high-order refinement of the IAM (IAM-HO) and invariom (INV) models have also been considered. IAM-HO model leads to an improved deconvolution of static electron density and gives a better estimate of the anisotropic displacement parameters (ADPs) compared to the IAM. The INV model is considered as an alternative to the MP model, when free refinement of MP parameters is not possible (specially in case of proteins). It is obtained by using fixed values of MP parameters from a database. Based on all four structure models (IAM, IAM-HO INV and MP), the static and dynamic electron densities have been calculated and compared using the low-temperature ($T \simeq 20$ K) high resolution data sets of integrated intensities of Bragg reflections of α-glycine, D, L-serine, L-alanine and L-alanyl-L-tyrosyl-L-alanine (Ala-Tyr-Ala) taken from the literature (Chapters 4 and 5). A multi-temperature data set of D, L-serine at 20 K, 100 K and 298 K from the literature has been employed in order to find out the effect of temperature on electron densities (Chapter 4). The feasibility of obtaining static and dynamic electron densities of a protein has been tested for low-temperature (T= 100 K) data of Crambin taken from the Protein Data Bank (PDB) (Chapter 6).

The dynamic electron density corresponding to a structure model can be obtained by convoluting the static atomic electron densities with the atomic thermal parameters. It has been successfully computed by inverse Fourier transform of accurately computed structure factors from the structure model by employing the method of fast Fourier transform (FFT). The modified computer program PRIOR has been employed to compute the dynamic electron densities. A series of calculations for grids of varying mesh show that the structure factors need to be incorporated up to very high resolution of $[\sin(\theta)/\lambda]_{max} \approx 6.25$ Å^{-1} which corresponds to a mesh of 0.04 Å in direct space, in order to obtain a dynamic electron density free of series termination effects. This has been established by smooth contours in dynamic electron density maps and the absence of non-atomic maxima (Chapters 4 and 5).

For the topological analysis of dynamic electron densities the program EDMA (Electron Density Map Analysis) have been employed. Recent developments and functionality of the program EDMA are provided in Chapter 3. A series of test calculations is presented for electron densities obtained from a structure model consisting of two Gaussian peaks. It has thus been established that the relative accuracy of the positions of the critical points, the electron densities and Laplacian at the critical points obtained by EDMA is of the order of 10^{-4} or better.

Topological properties of electron densities of small molecules show a considerable difference between the static and dynamic electron densities due to presence of zero-point vibrations in the dynamic electron densities analyzed at T $\backsimeq$ 20 K (Chapters 4 and 5). The values of electron densities at atomic maxima in dynamic densities are found to be much smaller than in the static densities, in accordance with the literature. This can be attributed to the thermal smearing in dynamic densities. These values become even lower at higher temperatures, as is found in dynamic densities of D, L-serine at T=20 K, 100 K and 298 K. The electron densities at bond critical points (BCPs) of covalent bonds obtained from dynamic electron densities possess slightly smaller values in comparison to the static densities. But rather larger differences have been observed for Laplacians and it increases with increasing polarity of the bond and with increasing temperature. In contrast to covalent bonds, electron densities at BCPs of hydrogen bonds possess slightly larger values in dynamic electron densities compared to static densities. This can be understood from the fact that the smearing of a density from high-density regions leads to increased values in low-density regions.

In case of the protein Crambin, it has been found that the ADPs of Crambin at 100 K are larger or equal to ADPs of D,L-serine at 298 K. Large ADPs of Crambin at 100 K mainly reflect frozen disorder and is visible as distortion of the electron density. However, these large ADPs prevent a free refinement of multipole parameters. Hence, the aspherical model has been constructed by transferring fixed values of MP parameters from the ELMAM2 database. In corresponding dynamic densities, bonding features have been found to be attenuated due to the masking effects of large ADPs. As a result, the topological properties obtained from dynamic densities of Crambin at 100 K appear to be similar with the topological properties of small molecules at room temperature.

The maximum entropy method (MEM) has been employed to obtain model-independent dynamic electron densities. MEM calculations have been performed for all small molecules studied in this thesis by employing the dynamic model densities of IAM, IAM-HO, INV and MP models as procrystal prior. It is shown that MEM density maps and dynamic deformation density maps exhibit almost similar features in all four MEM densities and show a tendency to converge to a density map that is independent of choice of prior. Electron densities at BCPs of covalent bonds, except for polar C-O bonds exhibit an excellent agreement between IAM-HO, INV and MP priors. A larger influence of the prior is observed for Laplacians at BCPs, with increasing differences for covalent bonds of increasing polarity. But in case of hydrogen bonds, similar values of electron densities and Laplacians at BCPs are obtained with all four kinds of MEM densities. The results shows that the MEM densities obtained by the IAM-HO, INV and MP prior densities produces reasonable values of the electron density and Laplacian at BCPs. But IAM prior leads to MEM densities that is clearly different from the other MEM densities. In those cases where free refinement of an MP model is not possible, especially for proteins, it is recommended to use the IAM-HO and / or INV dynamic model densities as procrystal prior.

From the studies presented in this thesis it is concluded that one can successfully reconstruct the dynamic electron density directly from the structure models of small molecules and macromolecules. Comparative analysis of static and dynamic densities has reveled the influence of temperature on electron-density distribution. At low-temperatures (T $\lesssim$ 20 K) dynamic model densities show similar topological properties like static densities near BCPs. It is demonstrated that a good characterization of chemical bonds, at least in organic molecules, can be obtained by the MEM using IAM-HO and INV dynamic model densities as procrystal prior.

Chapter 8

Zusammenfassung

Kenntnisse der Elektronendichteverteilung in molekularen Materialien liefern Einsichten in die Natur der chemischen Wechselwirkungen. Mit dem Aufkommen von Baders Quantentheorie der Atome in Molekülen (QTAIM) hat sich die Analyse der statischen Elektronendichte von Multipol-Modellen (MP-Modellen) zu einer Standard methode entwickelt. Allerdings beinhalten statische Dichten keine Information über thermische Schwingungen. In Wirklichkeit vibrieren Atome aber selbst bei sehr niedrigen Temperaturen um ihre mittlere Atomlagen. Zudem sind chemische Wechselwirkungen abhängig von der Temperatur, wie sich am Auftreten von temperaturabhängigen Phasenübergängen zeigt. Tatsächlich spiegeln die durch Röntgenbeugung gemessenen Bragg-Reflexe direkt die dynamische Elektronendichte (als die zeitlich gemittelte Elektronendichte) wider. Die vorliegende Arbeit beschäftigt sich mit dem Konzept der dynamischen Elektronendichte und beschreibt die Wirkung der Temperatur auf die Elektronendichteverteilung anhand der Analyse statischer sowie auch dynamischer Elektronendichten.

Statische und dynamische Elektronendichten entsprechend unabhängigen Atom-Modellen (IAM), und MP-Modelle wurden für mehrere Molekülkristalle entwickelt. Zusätzlich zu diesen beiden Arten von Modellen wurden Strukturmodelle aus Verfeinerungen des IAM gegen Daten beschränkt auf dem hochauflösenden Bereich (IAM-HO) sowie Invariom-Modelle (INV-Modelle) verwendet. Das IAM-HO-Modell führt zu einer besseren Entfaltung der statischen Elektronendichte und einer besseren Abschätzung der anisotropen Verschiebungsparameter (ADP) gegenüber dem IAM-Modell. Das INV-Modell stellt eine Alternative zum MP-Modell dar, wenn keine freie Verfeinerung der MP Parameter erfolgen kann (insbesondere im Falle von Proteinen). Es wird erstellt durch die Verwendung fester Werte von Multipolparametern, die einer Datenbank für die Modellierung asphärischer Elektronendichten entstammen. Basierend auf den vier Strukturmodellen (IAM, IAM-HO, INV und MP-Modell) wurden die statischen und dynamischen Elektronendichten unter Verwendung von hochauflösenden Datensätzen für α-Glycin, D,L-Serin, L-Alanin und L-Alanyl-L-tyrosyl-L-Alanin (Ala-Tyr-Ala) berechnet und verglichen (Kapitel 4 und 5). Die hierzu verwendeten Datensätze entstammen Tieftemperaturmessungen bei T $\backsimeq$ 20 K und wurden der Literatur entnommen. Temperaturabhänige Messungen an D,L-Serin bei 20 K, 100 K und 298 K wurden verwendet, um den Einfluss der Temperatur auf die Elektronendichten zu untersuchen (Kapitel 4). Die Möglichkeiten der statischen und dynamischen Elektronendichtebestimmungen an Proteinen wurde mittels Tieftemperatur-Daten (für T= 100 K), welche der Protein-Datenbank (PDB) für das Protein Crambin entnommen wurden, getestet (Kapitel 6).

Die einem Strukturmodell entsprechende dynamische Elektronendichte kann durch Faltung der statischen atomaren Elektronendichte mit den atomaren thermischen Parametern erhalten werden. Sie wurde erfolgreich durch inverse Fourier-Transformation von genau berechneten Strukturfaktoren aus dem Strukturmodell mit Hilfe des Verfahrens der schnellen Fourier-Transformation (FFT) bestimmt. Das modifizierte Computerprogramm PRIOR wurde angewandt, um die dynamischen Elektronendichten zu berechnen. Eine Reihe von Berechnungen für Netze unterschiedlicher Maschenweiten zeigt, dass die Strukturfaktoren bis zu einer sehr hohen Auflösung von $[\sin(\theta)/\lambda]_{max} \approx 6{,}25$ Å^{-1}, Was einer Maschenweite von 0,04 Å im direkten Raum entspricht, berücksichtigt werden müssen, um eine dynamische Elektronendichte zu erhalten, welche frei von Abbrucheffekten ist. Dies wurde durch glatte Konturen in dynamischen Elektronendichtekarten und die Abwesenheit von nicht-atomaren Maxima nachgewiesen (Kapitel 4 und 5).

Für die topologische Analyse von dynamischen Elektronendichten wurde das Programm EDMA (Electron Density Map Analysis) eingesetzt. Jüngste Entwicklungen und Funktionen des Programms EDMA werden in Kapitel 3 beschrieben. Eine Reihe von Testrechnungen werden für Elektronendichten aus Strukturmodellen bestehend aus zwei Gauß-Peaks dargestellt. Diese zeigen, dass die relative Genauigkeit der durch EDMA bestimmten Lagen der kritischen Punkte, der Elektronendichten sowie der Laplace-Werte an den kritischen Punkten in der Größenordnung von 10^{-4} liegt.

Die topologische Eigenschaften der Elektronendichten kleiner Moleküle weisen durch das Auftreten von Nullpunktschwingungen in der dynamischen Elektronendichten deutliche Unterschiede in den für T $\backsimeq$ 20 K ermittelten statischen und dynamischen Elektronendichten auf (Kapitel 4 und 5). Für die Elektronendichte werden an den atomaren Maxima in Übereinstimmung mit der Literatur viel kleinere Werte für die dynamische Elektronendichte als für die entsprechenden statischen Elektronendichten gefunden. Dies kann auf ein thermisches Verschmieren der dynamischen Dichten zurückgeführt werden. Bei höheren Temperaturen nehmen die Werte sogar noch weiter ab, wie anhand der dynamischen Dichten von $D,L-Serin$ für T = 20 K, 100 K und 298 K gezeigt werden konnte. Für die Elektronendichten an bindungskritischen Punkten (BCP) kovalenter Bindungen ergeben sich mit den dynamischen Elektronendichte-Verteilungen geringfügig kleinere Werte als mit den statische Dichten. Größere Unterschiede hingegen können für die Laplace-Werte beobachtet werden, welche mit zunehmender Polarität der Bindungen und mit steigender Temperatur zunehmen. Im Gegensatz zu kovalenten Bindungen besitzen Elektronendichten an den BCP von Wasserstoffbrückenbindungen etwas größere Werte in den dynamischen Elektronendichtenkarten verglichen mit den Werten in den statische Dichten. Dies kann dahingehend verstanden werden, dass das Verschmieren von Elektronendichten in einer Regionen hoher Dichte zu einer Erhöhung der Elektronendichte-Werten in Regionen niedriger Elektronendichten führt.

Im Falle des Proteins Crambin wurde gezeigt, dass die ADPs in Crambin bei 100 K größer oder gleich der ADPs in $D,L-Serin$ bei T=298 K sind. Die bei 100 K vorliegenden großen ADP-Werte in Crambin spiegeln in erster Linie das Auftreten von eingefrorener Fehlordnung, die sich in Verzerrungen der Elektronendichte äußert. Die großen ADP behindern eine freie Verfeinerung der Multipolparameter. Deshalb wurde das asphärische Modell unter Verwendung fester MP-Parameterwerte, die der Datenbank ELMAM2 entnommen wurden, erstellt. In den sich entsprechenden Bereichen der dynamischen Dichten wurden Bindungseigenschaften über den Verdeckungseffekt der großen ADPs abgeschwächt. Hierdurch sind die topologischen Eigenschaften der dynamischen Dichten von Crambin bei 100 K den topologischen Eigenschaften kleiner Moleküle bei Raumtemperatur ähnlich.

Die maximale Entropie-Methode (MEM) wurde eingesetzt, um modellunabhängige dynamische Elektronendichten zu erhalten. Die MEM Berechnungen wurden für alle in dieser Arbeit untersuchten kleinen Moleküle durch den Einsatz der dynamischen Modelldichten IAM, IAM-HO, INV sowie des MP-Modells als Startmodell für die Berechnungen (sogenannte procrystal prior) durchgeführt. Es wurde gezeigt, dass die erhaltenen MEM-Elektronendichtekarten und die Deformationsdichtekarten der dynamischen Elektronendichte ähnliche Merkmale für alle vier MEM-Dichten zeigen und tendenziell unabhängig von der Wahl des Startmodells prior zu der selben Elektronendichtekarte konvergieren. Die Elektronendichten am BCP von kovalenten Bindungen weisen mit Ausnahme der polaren CO-Bindungen eine ausgezeichnete Übereinstimmung zwischen den über die Startmodelle IAM-HO, INV und MP prior erhaltenen Elektronendichten auf. Eine größere Abhängigkeit von der Wahl der Startmodelle wurde für die Laplace-Werte an den BCP beobachtet, für welche mit steigender Polarität der kovalenten Bindungen eine zunehmende Abweichung der Werte festgestellt wurde. Im Fall von Wasserstoffbrückenbindungen wurden jedoch für die über die vier Startmodelle bestimmten MEM-Dichten jeweils ähnliche Elektronendichte-Werte und Laplace-Werte an den BCP erhalten. Die Ergebnisse zeigen, dass die über die Modelle IAM-HO, INV und MP erhaltenen MEM-Elektronendichten zu vernünftige Werten für die Elektronendichte und die Laplace-Werte an den BCP führen. über das Modell IAM werden hingegen MEM-Elektronendichten bestimmt, die sich deutlich von den anderen MEM-Elektronendichten unterscheiden. Für die Fälle, in denen die freie Verfeinerung vom MP-Modell nicht erfolgen konnte, insbesondere für Proteine, empfiehlt es sich, das Modell IAM-HO und / oder INV als dynamisches Elektronendichtemodell als Startmodell zu verwenden.

Aus den Untersuchungen dieser Arbeit wird geschlossen, dass man erfolgreich die dynamische Elektronendichte aus dem Strukturmodelle von kleinen Molekülen und Makromolekülen rekonstruieren kann. Über eine vergleichende Analyse der statischen und dynamischen Elektronendichten wurde der Einfluss der Temperatur auf die Elektronendichte-Verteilung ermittelt. Bei niedrigen Temperaturen ($T \lesssim 20$ K) zeigen die über die dynamischen Modell-Dichten bestimmten Elektronendichten ähnliche topologische Eigenschaften wie sie durch Verwenden von statischen Modelldichten in der Nähe von BCP entstehen. Es wurde gezeigt, dass über die MEM zumindest für organische Moleküle eine gute Charakterisierung von chemischen Bindungen durch Verwenden der dynamischen Modell-Dichten IAM-HO und INV erfolgen kann.

Appendices

Appendix A

Supplementary materials of experimental dynamic electron densities of multipole models at different temperatures

A.1 Establishment of the strategy for MP refinement

In order to have consistency, we decided to use a single multipole formalism to obtain aspherical models for all compounds. For this, we have chosen to use the multipolar formalism of Hansen and Coppens (Hansen and Coppens, 1978; Coppens, 1997) as implemented in the program XD2006 (Volkov et al., 2006). During the process to determine the best possible strategy for multipole refinement using XD2006, we have faced difficulties to exactly reproduce the model of Destro and coworkers (Destro et al., 2000); who have employed the software VALRAY (Stewart and Spackman, 1983). Eight different multipole refinements of α-Glycine have been carried out on the basis of different criteria as follows,

1. Local symmetry restrictions: Whether any restrictions for the refinement of the multipole parameters (on the basis of approximate 3-fold local symmetry of the ammonium nitrogen atom and mirror local symmetry for all other non-hydrogen atoms) have been made.

2. Chemical constraints: Whether the multipole parameters of hydrogen atoms from each groups (CH_2 and NH_3) were constrained to be the same (within the group).

3. Bond directed multipoles: For hydrogen atoms, whether only bond directed multipoles or all multipoles up to the level $l = 2$ (quadrupoles) were refined.

4. Hydrogen atom positions: The strategy used to refine/fix hydrogen atom positions.

5. Atomic displacement parameters (ADPs) for hydrogen atoms: The strategy for treating the thermal parameters of hydrogen atoms.

6. Observed criteria for reflections: Whether criteria for observed reflections were chosen as $F_{obs} > 0$ or $F_{obs} > 3\sigma(F_{obs})$. The second criteria is the default option of XD2006.

7. κ and κ': The strategy for refining κ and κ'.

8. Extinction parameters: How the extinction parameters were refined.

Detailed comparisons of different strategies are given in Table A.1, and the comparison of charge densities (ρ_{BCP}) and the Laplacians ($\nabla^2\rho_{BCP}$) at bond critical points (BCPs) are given in Table A.2. None of these different methods were able to exactly reproduce the model of Destro et al. (2000). Small differences in topological properties from that of Destro *et al.* (2000) persisted for all models. This is not very surprising, because we have used a different multipole formalism according to Hansen and Coppens (Hansen and Coppens, 1978) and a different computer program (Volkov et al., 2006), where as Destro *et al.* (2000) have used the multipolar formalism according to stewart (Stewart, 1976; Flensburg et al., 1995) as implemented in the computer program VALRAY (Stewart and Spackman, 1983). Besides, we have used the data bank of Su and Coppens (Su and Coppens, 1998) for the atomic scattering factors, which is more recent than what (Clementi and Roetti, 1974) Destro *et al.* have used. From Table A.2, one can notice that the method 8, which is closest to the approach as Destro et al. (2000), also cannot reproduce exactly the same results. These small differences can be attributed to the use of different multipolar formalism, different software and different scattering factors. We do not concentrate much on these small differences in topological properties, as our primary goal is to compute static and dynamic densities directly from a sufficiently good multipole model. For this purpose, we choose the method 1, which is currently the state of art for performing multipole refinement using XD2006 with lowest number of refined parameters and minimum residual densities. Topological properties obtained from method 1 are similar to other amino acids and fall within the standard deviation limits for amino acids as reported by Mebs and coworkers (Mebs et al., 2006).

Table A.1: Comparison between different methods performed using different strategies for multipole refinements.

Methods	Destro *et al.* (2000)	Method1	Method2	Method3	Method4	Method5	Method6	Method7	Method8
Local symmetry restriction	No	Yes	Yes	Yes	Yes	Yes	Yes	No	No
Chemical constraint	No	Yes	Yes	No	No	Yes	Yes	Yes	No
Bond directed MP for H atoms	No (all up to quadrupole were refined)	Yes (up to quadrupole)	Yes (up to quadrupole)	yes (up to quadrupole)	yes (up to quadrupole)	yes (up to quadrupole)	yes (up to quadrupole)	No (all up to quadrupole were refined)	No (all up to quadrupole were refined)
H atom positions	Refined	Initially set to neutron distances, refined with $(sin\theta/\lambda) \leq$ 0.5 Å^{-1} and then again fixed to neutron distances	Initially set to neutron distances, refined with $(sin\theta/\lambda) \leq$ 0.5 Å^{-1} and then again fixed to neutron distances	Initially set to neutron distances, refined with $(sin\theta/\lambda) \leq$ 0.5 Å^{-1} and then kept fixed to these new distances	Initially set to neutron distances, refined with $(sin\theta/\lambda) \leq$ 0.5 Å^{-1} and then kept fixed to these new distances	Initially set to neutron distances, refined with $(sin\theta/\lambda) \leq$ 0.5 Å^{-1} and then again fixed to neutron distances	Initially set to neutron distances, refined with $(sin\theta/\lambda) \leq$ 0.5 Å^{-1} and then again fixed to neutron distances	Refined	Refined
ADPs of H atoms	Anisotropic (fixed)	Isotropic, (1.2 times of the parent)	Isotropic, (1.2 times of the parent)	Isotropic, (refined)	Isotropic, (refined)	Anisotropic (fixed, same as Destro)	Anisotropic (fixed, same as Destro)	Anisotropic (fixed, same as Destro)	Anisotropic (fixed, same as Destro)
κ and κ'	NA	Refined for non-H atoms	Refined for non-H atoms	Refined for non-H atoms	Refined for non-H atoms	Refined for non-H atoms	Refined for non-H atoms	Initially refined for non-H, and then kept fixed	Initially refined for non-H, and then kept fixed
Extinction	Anisotropic (fixed)	Anisotropic (refined)	Anisotropic (refined)	Anisotropic (refined)	Anisotropic (refined)	Anisotropic (refined)	Anisotropic (refined)	Anisotropic (fixed,same as Destro)	Anisotropic (fixed,same as Destro)

Continued on next page...

Table A.1: Continued

Methods	Destro *et al.* (2000)	Method1	Method2	Method3	Method4	Method5	Method6	Method7	Method8
Observed criteria,	$F^2(obs) > 0$	$F(obs) > 3\sigma$	$F(obs) > 0$	$F(obs) > 3\sigma$	$F(obs) > 0$	$F(obs) > 3\sigma$	$F(obs) > 0$	$F(obs) > 0$	$F(obs) > 0$
observed reflections	3789	3603	3789	3603	3789	3603	3789	3789	3789
Number of parameters	216	131	131	145	145	131	131	189	216
$\Delta\rho_{min}$ (e/Å^3)	–	−0.132	−0.144	−0.137	−0.153	−0.152	−0.162	−0.158	−0.167
$\Delta\rho_{max}$ (e/Å^3)	–	0.154	0.164	0.151	0.167	0.167	0.170	0.186	0.191
$R_F(obs)$	0.0129	0.0124	0.0137	0.0123	0.0136	0.0128	0.0140	0.0138	0.0134
R_{F^2}	0.0172	0.0184	0.0184	0.0184	0.0185	0.0189	0.0190	0.0198	0.0194
wR_{F^2}	-	0.0293	0.0295	0.0287	0.0289	0.0303	0.0305	0.0292	0.0283
GoF	1.041	1.041	1.1588	1.1551	1.1376	1.2124	1.1930	1.1524	1.1234

Table A.2: Electron densities and Laplacians at the BCPs of covalent bonds of α-Glycine. Values are given for ρ_{bcp} (e/Å^3: first line) and $\nabla^2{}_{\rho_{bcp}}$ (e/Å^5; second line).

Bond	Destro *et al.* (2000)	Method1	Method2	Method3	Method4	Method5	Method6	Method7	Method8
C1-O1	2.77(2)	2.770	2.770	2.763	2.763	2.773	2.773	2.751	2.758
	-32.8(9)	-36.57	-36.71	-35.94	-36.03	-36.40	-36.44	-32.81	-33.85
C1-O2	2.67(2)	2.733	2.727	2.733	2.728	2.715	2.710	2.660	2.693
	-30.5(9)	-35.07	-34.97	-35.06	-34.98	-34.43	-34.37	-30.84	-32.73
C1-C2	1.78(1)	1.735	1.736	1.758	1.759	1.740	1.741	1.780	1.774
	-15.6(4)	-12.80	-12.84	-13.50	-13.53	-13.08	-13.12	-14.76	-14.33
C2-N	1.69(1)	1.691	1.689	1.693	1.691	1.698	1.696	1.673	1.674
	-11.9(5)	-10.42	-10.45	-10.75	-10.76	-10.91	-10.93	-10.18	-10.12
C2-H4	1.99(1)	1.940	1.942	1.892	1.894	1.969	1.970	1.980	2.054
	-22.7(6)	-22.24	-22.32	-21.50	-21.59	-23.98	-24.05	-24.69	-25.55
C2-H5	1.91(2)	1.907	1.907	1.891	1.891	1.863	1.863	1.855	1.799
	-21.2(7)	-21.74	-21.79	-21.55	-21.59	-21.07	-21.11	-21.07	-20.05
N-H1	2.20(2)	2.084	2.083	2.043	2.040	2.071	2.070	2.142	2.185
	-35.4(13)	-35.78	-35.79	-35.47	-35.43	-35.65	-35.65	-4.07	-40.05
N-H2	2.21(2)	2.086	2.085	1.989	1.984	2.072	2.071	2.074	2.028
	-36.2(13)	-35.86	-35.86	-35.54	-35.50	-35.71	-35.71	-37.11	-40.39
N-H3	2.24(2)	2.084	2.083	1.962	1.961	2.069	2.069	2.144	2.189
	-33.0(11)	-35.76	-35.77	-34.10	-34.13	-35.60	-35.60	-40.93	-38.15

A.2 Effects of shifts in bond critical points on topological properties

Comparative analysis of static and dynamic multipole densities has revealed that BCPs in static densities (BCPs^{static}) slightly differ in position from the corresponding BCPs in dynamic densities (BCPs^{dynamic}). Magnitudes of these differences increase with temperature, as is found for D,L-Serine (Dittrich et al., 2005) at three different temperatures (Tables A.3, A.4 and A.5). A maximum shift of 0.0795 Å between BCPs^{static} and BCPs^{dynamic} has been observed for C1–O1 bond at 298K (Table A.5). To find the effects of these shifts, topological properties of static densities in D,L-Serine at the positions of BCPs^{static} and of BCPs^{dynamic} have been calculated and compared. These topological properties of static densities have been further compared with the corresponding properties of dynamic densities at BCPs^{dynamic}. We have found that, below 100K, static properties at positions of BCPs^{static} as well as at BCPs^{dynamic} are almost equal (Tables A.6 & A.7), with a maximum difference of 0.003 e/Å^3 for the ρ_{BCP} and 3.15 e/Å^5 for the Laplacian of the C1–O1 bond at 100K. Larger differences have been observed at 298 K (Table A.8), however properties of static densities are still reasonable within the scope of the quantum

Table A.3: Coordinates of BCPs for D, L-Serine from static and dynamic densities at 20 K.

Bonds	Coordinates of BCPs^{static}	Coordinates of BCPs^{dynamic}	Distance (Å)
C1-O1	0.71242 0.40949 0.57309	0.711978 0.409521 0.572458	0.0049
C1-O2	0.77919 0.45022 0.70047	0.779159 0.450022 0.700500	0.0019
C3-O3	0.90562 0.19860 0.86703	0.905430 0.198843 0.869956	0.0149
C1-C2	0.75123 0.34592 0.77428	0.751245 0.346113 0.774225	0.0018
C2-C3	0.82110 0.24942 0.92130	0.821600 0.249377 0.922031	0.0055
C2-N1	0.71039 0.23563 0.82015	0.711017 0.236348 0.821271	0.0098
O1...H4-O3	0.61988 0.51909 0.36079	0.619486 0.519025 0.361269	0.0054
O3...H11-N1	0.52040 0.26122 0.71670	0.519808 0.261055 0.714965	0.0090
O2...H12-N1	0.66031 0.07084 1.02780	0.660410 0.069911 1.027448	0.0088
O2...H13-N1	0.66631 0.08088 0.45373	0.666745 0.080841 0.453148	0.0061
O1...H2-C2	0.70033 0.35666 1.20523	0.701021 0.356350 0.207473	0.0115

theory of atoms in molecules (QTAIM) (Bader, 1990). Corresponding properties (especially Laplacians) of dynamic densities at same positions are clearly different.

These results indicate that up to 100K, the differences in topological properties of static and dynamic densities are not due to the differences in the positions of BCPs, but due to the fact that, dynamic densities indeed posses different characteristics than the static densities. This is also evidenced by the fact that the topological properties of dynamic densities at BCPs are not just uniformly smaller than the corresponding properties of static densities with increasing temperature, but basically different.

At 298 K, Laplacians of static densities at BCPs of C–O bonds are already different for the BCPs^{dynamic} position than for the real position, but the difference with the Laplacians of dynamic densities at the same position is even larger. This indicates that, differences in the positions of BCPs might play a part behind the difference between properties of static and dynamic densities at room temperature. However, different positions of BCPs are not sufficient to fully explain the differences between the static and the dynamic densities.

Table A.4: Coordinates of BCPs D, L-Serine from static and dynamic densities at 100 K.

Bonds	Coordinates of BCPs^{static}	Coordinates of BCPs^{dynamic}	Distance (Å)
C1-O1	0.71330 0.40837 0.57365	0.711612 0.408511 0.570543	0.0199
C1-O2	0.77988 0.44903 0.70061	0.780750 0.449716 0.701396	0.0110
C3-O3	0.90574 0.19703 0.86823	0.905862 0.196956 0.870873	0.0124
C1-C2	0.75143 0.34497 0.77460	0.751487 0.345354 0.774502	0.0036
C2-C3	0.82108 0.24817 0.92105	0.821968 0.248093 0.922336	0.0098
C2-N1	0.71035 0.23463 0.81999	0.711214 0.235654 0.821724	0.0141
O1...H4-O3	0.62100 0.51790 0.35979	0.620374 0.517923 0.360353	0.0079
O3...H11-N1	0.52082 0.26222 0.71670	0.520033 0.262037 0.713981	0.0134
O2...H12-N1	0.66036 0.07017 1.02917	0.660646 0.069085 1.028519	0.0111
O2...H13-N1	0.66565 0.07989 0.45386	0.666192 0.079970 0.453431	0.0068
O1...H2-C2	0.70088 0.35533 1.20560	0.702068 0.354944 0.208145	0.0153

Table A.5: Coordinates of BCPs D, L-Serine from static and dynamic densities at 298 K.

Bonds	Coordinates of BCPs^{static}	Coordinates of BCPs^{dynamic}	Distance (Å)
C1-O1	0.71670 0.40466 0.57587	0.710262 0.405263 0.562817	0.0795
C1-O2	0.78214 0.44494 0.70141	0.787042 0.449350 0.705637	0.0648
C3-O3	0.90631 0.19188 0.87140	0.909128 0.189420 0.866709	0.0482
C1-C2	0.75294 0.34132 0.77458	0.753060 0.342489 0.774094	0.0111
C2-C3	0.82110 0.24369 0.92052	0.823344 0.243527 0.924057	0.0253
C2-N1	0.71038 0.23147 0.81935	0.709279 0.231005 0.820112	0.0140
O1...H4-O3	0.62170 0.51350 0.36113	0.619588 0.514534 0.362896	0.0280
O3...H11-N1	0.52133 0.26324 0.72013	0.519976 0.262383 0.714268	0.0290
O2...H12-N1	0.65827 0.06677 1.02774	0.659001 0.065158 1.025061	0.0224
O2...H13-N1	0.66399 0.07617 0.45410	0.664909 0.076327 0.455122	0.0098
O1...H2-C2	0.70300 0.35183 1.20569	0.706058 0.351153 0.208417	0.0323

Table A.6: Topological properties of static and dynamic densities at different points for D, L-Serine at 20 K. ρ (e/Å^3) is given in the first line and $\nabla^2\rho$ (e/Å^5) in the second line

Bond	From static densities at the position of BCPs^{static}	From static densities at the position of BCPs^{dynamic}	From dynamic densities at the position of BCPs^{dynamic}
C1-O1	2.810	2.810	2.723
	-32.18	-31.50	-23.40
C1-O2	2.791	2.791	2.693
	-35.32	-35.59	-24.15
C3-O3	1.869	1.871	1.807
	-16.64	-18.39	-9.02
C1-C2	1.710	1.710	1.670
	-11.77	-11.78	-11.23
C2-C3	1.726	1.726	1.684
	-12.29	-12.32	-13.60
C2-N1	1.684	1.685	1.664
	-10.06	-10.70	-12.20
O1...H4-O3	0.258	0.258	0.279
	4.29	4.29	3.91
O3...H11-N1	0.219	0.219	0.237
	3.89	3.91	4.10
O2...H12-N1	0.200	0.200	0.218
	3.47	3.49	3.71
O2...H13-N1	0.185	0.185	0.202
	3.42	3.43	3.84
O1...H2-C2	0.075	0.075	0.086
	1.53	1.53	1.97

Table A.7: Topological properties of static and dynamic densities at different points for D, L-Serine at 100 K. ρ (e/Å^3) is given in the first line and $\nabla^2\rho$ (e/Å^5) in the second line

Bond	From static densities at the position of BCPs^{static}	From static densities at the position of BCPs^{dynamic}	From dynamic densities at the position of BCPs^{dynamic}
C1-O1	2.814	2.817	2.716
	-32.30	-29.15	-12.04
C1-O2	2.795	2.796	2.661
	-35.50	-33.49	-13.22
C3-O3	1.874	1.874	1.791
	-16.80	-18.09	-2.16
C1-C2	1.713	1.713	1.649
	-11.84	-11.85	-11.25
C2-C3	1.730	1.730	1.662
	-12.36	-12.42	-13.41
C2-N1	1.686	1.688	1.661
	-10.09	-11.03	-11.19
O1...H4-O3	0.259	0.259	0.288
	4.31	4.31	3.79
O3...H11-N1	0.217	0.217	0.238
	3.83	3.86	4.02
O2...H12-N1	0.200	0.200	0.224
	3.51	3.52	3.74
O2...H13-N1	0.183	0.183	0.207
	3.40	3.41	3.81
O1...H2-C2	0.075	0.075	0.090
	1.53	1.54	2.03

Table A.8: Topological properties of static and dynamic densities at different points for D, L-Serine at 298 K. ρ (e/Å^3) is given in the first line and $\nabla^2\rho$ (e/Å^5) in the second line

Bond	From static densities at the position of BCPs^{static}	From static densities at the position of BCPs^{dynamic}	From dynamic densities at the position of BCPs^{dynamic}
C1-O1	2.831	2.896	2.793
	-32.82	-18.75	8.03
C1-O2	2.814	2.855	2.648
	-36.28	-23.79	8.90
C3-O3	1.888	1.900	1.874
	-17.30	-12.34	18.63
C1-C2	1.716	1.716	1.568
	-11.87	-11.95	-10.09
C2-C3	1.735	1.737	1.584
	-12.46	-12.70	-11.10
C2-N1	1.690	1.690	1.669
	-10.17	-9.58	-2.62
O1...H4-O3	0.252	0.252	0.305
	4.20	4.15	3.00
O3...H11-N1	0.209	0.208	0.248
	3.71	3.75	3.71
O2...H12-N1	0.187	0.187	0.233
	3.29	3.30	3.40
O2...H13-N1	0.175	0.174	0.221
	3.27	3.27	3.58
O1...H2-C2	0.074	0.074	0.104
	1.52	1.52	2.19

Appendix B

Supplementary materials of electron densities by the maximum entropy method for various types of prior densities: a case study on three amino acids and a tripeptide

As discussed in Section 5.3.7 of the Chapter 5, local maxima in different density maps of a single compound are found at nearly equal positions. Tables B.1–B.4 compare the exact coordinates of corresponding local maxima within the eight density maps for each compound, α-Glycine, D,L-Serine, L-Alanine and Ala-Tyr-Ala$_{Etoh}$, respectively. A good agreement is also found between positions of bond critical points (BCPs) of the covalent and hydrogen bonds in different density maps of a single compound (Tables B.5–B.8).

The values of the electron density, ρ_{BCP}, and the Laplacian, $\nabla^2\rho_{BCP}$, at the BCPs in the static and dynamic model density maps of the INV and MP models are compared in Tables B.9–B.12 for α-Glycine, D,L-Serine, L-Alanine and Ala-Tyr-Ala$_{Etoh}$, respectively. A comparison of these quantities between all four dynamic model densities and all four MEM densities of each compound is incorporated in the Chapter 5.

The number of electrons in and volumes of the atomic basins are given for the four MEM density maps of each compound in Tables B.13–B.16. Atomic charges derived from these values are given in Tables B.17–B.20.

Finally, the values of the electron density and the Laplacian at the the local maxima in the four dynamic model density maps of each compound are compiled in Tables B.21–B.24.

Figures are provided of selected sections of the residual density (difference Fourier map), dynamic deformation density (Eq. 5.4 in the Chapter 5) and MEM density for each of the four MEM densities for D,L-Serine, L-Alanine and Ala-Tyr-Ala$_{Etoh}$ (Figs. B.1–B.6). Difference density maps (Eq. 5.3 in the Chapter 5) for the MEM densities with INV and MP priors are provided for each compound in Fig. B.7. The Chapter 5 includes similar figures for α-Glycine.

Table B.1: Coordinates of atomic maxima in eight different density maps of α-Glycine: Dynamic model densities and MEM density maps for IAM (first line), IAM-HO(second line), INV (third line) and MP (fourth line).

	Dynamic model density			MEM density		
Atom	x	y	z	x	y	z
C1	0.069390	0.125125	0.065821	0.069390	0.125130	0.065823
	0.069372	0.125146	0.065893	0.069377	0.125146	0.065878
	0.069391	0.125151	0.065832	0.069393	0.125152	0.065826
	0.069332	0.125159	0.065784	0.069334	0.125160	0.065782
C2	0.942035	0.854144	0.214085	0.942046	0.854147	0.214091
	0.942084	0.854141	0.214142	0.942085	0.854143	0.214138
	0.942104	0.854123	0.214122	0.942098	0.854127	0.214122
	0.942053	0.854140	0.214081	0.942049	0.854140	0.214080
O1	0.302380	0.093779	0.236580	0.302382	0.093776	0.236580
	0.302145	0.093783	0.236464	0.302179	0.093782	0.236476
	0.302167	0.093765	0.236447	0.302172	0.093769	0.236449
	0.302167	0.093777	0.236481	0.302169	0.093778	0.236482
O2	0.844485	0.142350	0.106570	0.844475	0.142362	0.106564
	0.844629	0.142380	0.106527	0.844605	0.142384	0.106524
	0.844639	0.142382	0.106533	0.844631	0.142385	0.106529
	0.844662	0.142400	0.106559	0.844657	0.142401	0.106559

Continued on next page...

Table B.1: Continued

Atom	x	y	z	x	y	z
N	0.795040	0.411631	0.240529	0.795048	0.411633	0.240526
	0.794975	0.411620	0.240512	0.795000	0.411624	0.240513
	0.795096	0.411617	0.240492	0.795096	0.411620	0.240496
	0.794968	0.411614	0.240447	0.794970	0.411617	0.240451
H4	0.933848	0.767334	0.243315		-	
	0.934178	0.767362	0.242926		-	
	0.929145	0.779652	0.236394		-	
		-			-	
H5	0.362661	0.384024	0.143026	0.375856	0.382268	0.153181
	0.361074	0.384233	0.141443	0.371727	0.382925	0.149768
	0.386129	0.382193	0.162571	0.385648	0.380739	0.162145
		-		0.386866	0.380316	0.162572

Table B.2: Coordinates of atomic maxima in eight different density maps of D,L-Serine: Dynamic model densities and MEM density maps for IAM (first line), IAM-HO(second line), INV (third line) and MP (fourth line).

	Dynamic model density			MEM density		
Atom	x	y	z	x	y	z
C1	0.253576	0.589520	0.333834	0.253577	0.589526	0.333839
	0.253548	0.589542	0.333933	0.253555	0.589547	0.333936
	0.253550	0.589540	0.333844	0.253554	0.589542	0.333848
	0.253558	0.589541	0.333882	0.253560	0.589542	0.333884
C2	0.245520	0.716450	0.121080	0.245528	0.716450	0.121086
	0.245561	0.716493	0.121096	0.245560	0.716481	0.121095
	0.245533	0.716443	0.121097	0.245540	0.716444	0.121098
	0.245565	0.716475	0.121194	0.245566	0.716474	0.121194
C3	0.610519	0.716383	0.030168	0.610513	0.716372	0.030175
	0.610500	0.716301	0.030268	0.610498	0.716308	0.030263

Continued on next page...

Table B.2: Continued

Atom	x	y	z	x	y	z
	0.610495	0.716355	0.030117	0.610494	0.716352	0.030122
	0.610497	0.716364	0.030201	0.610496	0.716362	0.030199
O1	0.158577	0.092971	0.427202	0.158578	0.092969	0.427197
	0.158703	0.092979	0.427398	0.158682	0.092978	0.427375
	0.158631	0.092962	0.427373	0.158631	0.092962	0.427375
	0.158652	0.092965	0.427469	0.158651	0.092964	0.427468
O2	0.671165	0.011055	0.248263	0.671163	0.011058	0.248260
	0.671245	0.010977	0.248463	0.671229	0.010990	0.248432
	0.671221	0.010993	0.248349	0.671219	0.010994	0.248343
	0.671227	0.010981	0.248313	0.671225	0.010983	0.248308
O3	0.571156	0.675502	0.278788	0.571151	0.675500	0.278782
	0.571181	0.675350	0.278308	0.571173	0.675379	0.278371
	0.571219	0.675377	0.278529	0.571219	0.675378	0.278537
	0.571198	0.675417	0.278510	0.571199	0.675421	0.278519
N	0.846779	0.673434	0.256313	0.846779	0.673433	0.256310
	0.846814	0.673435	0.256397	0.846806	0.673434	0.256377
	0.846786	0.673423	0.256272	0.846785	0.673425	0.256276
	0.846780	0.673451	0.256247	0.846779	0.673451	0.256250
H2	0.234045	0.173591	0.062048	0.236067	0.181518	0.039990
	0.234364	0.173112	0.063144	0.235762	0.180555	0.043167
	0.234592	0.178119	0.051320	0.235563	0.180487	0.047280
	0.233839	0.178646	0.048953	0.235232	0.180545	0.046420
H31	0.890659	0.130541	0.105515	0.891397	0.141085	0.087573
	0.890440	0.130197	0.106778	0.891437	0.141308	0.087666
	0.891875	0.135934	0.095748	0.891651	0.138198	0.092383
	0.892385	0.135398	0.096592	0.891861	0.136761	0.094732
H32	0.454322	0.205393	0.082627	0.448972	0.212465	0.075857
	0.454745	0.205613	0.082854	0.447660	0.213459	0.073316

Continued on next page...

Table B.2: Continued

Atom	x	y	z	x	y	z
	0.450510	0.212512	0.078741	0.449080	0.212821	0.076061
	0.451025	0.211501	0.078006	0.448986	0.212913	0.074810

Table B.3: Coordinates of atomic maxima in eight different density maps of *L*-Alanine: Dynamic model densities and MEM density maps for IAM (first line), IAM-HO(second line), INV (third line) and MP (fourth line).

	Dynamic model density			MEM density		
Atom	x	y	z	x	y	z
C1	0.945850	0.859160	0.099790	0.945846	0.859162	0.099796
	0.945860	0.859256	0.099934	0.945858	0.859250	0.099928
	0.946011	0.859187	0.099903	0.946000	0.859187	0.099899
	0.945876	0.859192	0.099843	0.945874	0.859192	0.099845
C2	0.533760	0.661039	0.145358	0.533756	0.661040	0.145376
	0.533777	0.661036	0.145645	0.533771	0.661038	0.145639
	0.533709	0.661103	0.145488	0.533705	0.661101	0.145500
	0.533610	0.661040	0.145627	0.533613	0.661040	0.145631
C3	0.740148	0.590708	0.196736	0.740153	0.590707	0.196733
	0.740279	0.590721	0.196686	0.740272	0.590719	0.196685
	0.740068	0.590612	0.196675	0.740080	0.590616	0.196675
	0.740116	0.590654	0.196639	0.740123	0.590658	0.196642
O1	0.772976	0.916264	0.124390	0.772979	0.916268	0.124390
	0.773204	0.916249	0.124376	0.773190	0.916252	0.124374
	0.773169	0.916228	0.124389	0.773169	0.916230	0.124391
	0.773084	0.916259	0.124432	0.773087	0.916261	0.124435
O2	0.940810	0.315831	0.238711	0.940807	0.315836	0.238707
	0.940725	0.315943	0.238781	0.940731	0.315938	0.238774
	0.940992	0.315968	0.238711	0.940983	0.315965	0.238715
	0.940802	0.315931	0.238720	0.940802	0.315930	0.238719

Continued on next page...

Table B.3: Continued

Atom	x	y	z	x	y	z
N	0.647303	0.137507	0.182925	0.647287	0.137509	0.182931
	0.647093	0.137554	0.182978	0.647098	0.137550	0.182980
	0.647197	0.137513	0.182939	0.647195	0.137516	0.182940
	0.647045	0.137559	0.183065	0.647052	0.137560	0.183067
H1		-			-	
		-			-	
	0.699641	0.066084	0.195466	0.697789	0.067485	0.195108
		-			-	
H2		-			-	
		-			-	
	0.771971	0.182726	0.202565	0.767466	0.181950	0.201976
		-			-	
H3		-			-	
		-			-	
	0.596012	0.146460	0.031858	0.595304	0.146737	0.032253
		-			-	
H4	0.577405	0.744212	0.155646	0.575900	0.742427	0.157484
	0.577988	0.744321	0.154381	0.575935	0.742185	0.156484
	0.576860	0.743427	0.160754	0.576489	0.743306	0.161313
	0.576758	0.742557	0.160070	0.576409	0.742554	0.160313
H5	0.200461	0.108222	0.147062	0.202089	0.107187	0.150748
	0.200428	0.108261	0.146743	0.202295	0.107346	0.150505
	0.199299	0.109386	0.150184	0.199719	0.109445	0.149785
	0.201157	0.108694	0.150891	0.201060	0.108777	0.150395
H6	0.857305	0.606328	0.078529	0.858167	0.605675	0.079191
	0.857147	0.606231	0.079780	0.857970	0.605589	0.080230
	0.859371	0.603354	0.081606	0.860837	0.603441	0.080464
	0.856299	0.605074	0.081669	0.858150	0.604562	0.080908

Continued on next page...

Table B.3: Continued

Atom	x	y	z	x	y	z
H7	0.703098	0.517972	0.192167		-	
	0.701820	0.515855	0.191471		-	
	0.697739	0.513028	0.193434	0.698291	0.513361	0.193263
	0.699264	0.513757	0.192623	0.700434	0.514726	0.192399

Table B.4: Coordinates of atomic maxima in eight different density maps of Ala-Tyr-Ala$_{Etoh}$: Dynamic model densities and MEM density maps for IAM (first line), IAM-HO(second line), INV (third line) and MP (fourth line).

	Dynamic model density			MEM density		
Atom	x	y	z	x	y	z
C1	0.497196	0.199084	0.392133	0.497197	0.199084	0.392127
	0.497255	0.199099	0.392074	0.497246	0.199101	0.392075
	0.497167	0.200705	0.392081	0.497163	0.200704	0.392080
	0.497103	0.199141	0.392049	0.497104	0.199141	0.392050
C2	0.456573	0.284119	0.492763	0.456570	0.284114	0.492767
	0.456519	0.284173	0.492798	0.456519	0.284168	0.492797
	0.456616	0.285760	0.492787	0.456615	0.285756	0.492788
	0.456624	0.284094	0.492787	0.456622	0.284094	0.492786
C3	0.563182	0.774969	0.310572	0.563182	0.774963	0.310573
	0.563164	0.774933	0.310595	0.563162	0.774933	0.310592
	0.563136	0.776555	0.310571	0.563134	0.776552	0.310569
	0.563165	0.774917	0.310604	0.563161	0.774915	0.310598
C4	0.504642	0.668297	0.220255	0.504645	0.668298	0.220250
	0.504687	0.668269	0.220235	0.504688	0.668275	0.220234
	0.504606	0.669884	0.220210	0.504609	0.669887	0.220210
	0.504652	0.668337	0.220218	0.504653	0.668338	0.220218
C5	0.431252	0.639958	0.025754	0.431256	0.639961	0.025751
	0.431323	0.639992	0.025764	0.431322	0.639994	0.025762
	0.431265	0.641611	0.025734	0.431268	0.641611	0.025738

Continued on next page...

Table B.4: Continued

Atom	x	y	z	x	y	z
	0.431310	0.640035	0.025737	0.431310	0.640035	0.025739
C6	0.440601	0.140179	0.052094	0.440599	0.140181	0.052099
	0.440587	0.140236	0.052143	0.440588	0.140236	0.052142
	0.440652	0.141879	0.052111	0.440648	0.141878	0.052113
	0.440622	0.140222	0.052099	0.440620	0.140224	0.052102
C7	0.665752	0.217945	0.374128	0.665752	0.217942	0.374127
	0.665766	0.217833	0.374107	0.665764	0.217843	0.374108
	0.665699	0.219470	0.374110	0.665698	0.219471	0.374109
	0.665713	0.217885	0.374097	0.665711	0.217884	0.374098
C8	0.716645	0.195377	0.034786	0.716653	0.195372	0.034791
	0.716640	0.195509	0.034861	0.716649	0.195489	0.034855
	0.716671	0.196985	0.034731	0.716675	0.196984	0.034736
	0.716723	0.195314	0.034741	0.716722	0.195316	0.034746
C20	0.735276	0.808490	0.302077	0.735277	0.808489	0.302076
	0.735299	0.808529	0.302060	0.735297	0.808529	0.302060
	0.735165	0.809852	0.302093	0.735171	0.809863	0.302088
	0.735232	0.808503	0.302064	0.735232	0.808503	0.302062
C21	0.833970	0.671628	0.306256	0.833971	0.671630	0.306262
	0.834023	0.671631	0.306307	0.834018	0.671635	0.306305
	0.833967	0.673243	0.306294	0.833964	0.673243	0.306296
	0.833959	0.671674	0.306280	0.833957	0.671674	0.306282
C22	0.860036	0.595837	0.210194	0.860038	0.595840	0.210193
	0.860032	0.595933	0.210231	0.860031	0.595932	0.210227
	0.860089	0.597475	0.210249	0.860088	0.597475	0.210241
	0.860056	0.595946	0.210200	0.860057	0.595945	0.210195
C23	0.944744	0.465170	0.213030	0.944751	0.465169	0.213026
	0.944887	0.465223	0.213017	0.944882	0.465222	0.213016
	0.944820	0.466762	0.213034	0.944822	0.466762	0.213032

Continued on next page...

Table B.4: Continued

Atom	x	y	z	x	y	z
	0.944812	0.465193	0.213036	0.944813	0.465193	0.213035
C24	0.004006	0.407942	0.313306	0.004015	0.407933	0.313309
	0.004054	0.407884	0.313362	0.004056	0.407886	0.313360
	0.004019	0.409436	0.313321	0.004022	0.409438	0.313322
	0.004004	0.407856	0.313352	0.004011	0.407858	0.313351
C25	0.983706	0.484692	0.409660	0.983710	0.484690	0.409666
	0.983765	0.484701	0.409706	0.983763	0.484698	0.409707
	0.983727	0.486180	0.409664	0.983728	0.486179	0.409666
	0.983733	0.484609	0.409686	0.983734	0.484609	0.409688
C26	0.898679	0.615365	0.405659	0.898678	0.615371	0.405667
	0.898629	0.615522	0.405714	0.898630	0.615519	0.405715
	0.898572	0.617003	0.405646	0.898573	0.617006	0.405655
	0.898567	0.615508	0.405704	0.898569	0.615508	0.405709
C31	0.080712	0.980068	0.132979	0.080700	0.980085	0.132971
	0.080697	0.980397	0.132941	0.080690	0.980381	0.132940
	0.080574	0.981795	0.132935	0.080575	0.981806	0.132931
	0.080596	0.980384	0.132875	0.080597	0.980390	0.132876
C32	0.133342	0.917075	0.244005	0.133342	0.917072	0.243991
	0.133427	0.917093	0.243897	0.133418	0.917099	0.243911
	0.133309	0.918671	0.243954	0.133306	0.918666	0.243932
	0.133261	0.917053	0.243913	0.133266	0.917055	0.243902
O1	0.420374	0.416475	0.485673	0.420369	0.416477	0.485673
	0.420399	0.416393	0.485692	0.420391	0.416402	0.485691
	0.420433	0.417859	0.485679	0.420422	0.417864	0.485677
	0.420283	0.416461	0.485686	0.420280	0.416463	0.485684
O2	0.496395	0.533827	0.239354	0.496404	0.533825	0.239356
	0.496478	0.533942	0.239387	0.496478	0.533936	0.239387
	0.496290	0.535608	0.239389	0.496305	0.535604	0.239390

Continued on next page...

Table B.4: Continued

Atom	x	y	z	x	y	z
	0.496480	0.533879	0.239366	0.496486	0.533879	0.239367
O3	0.328407	0.224410	0.032948	0.328410	0.224416	0.032949
	0.328459	0.224390	0.032950	0.328456	0.224402	0.032952
	0.328539	0.225978	0.033000	0.328535	0.225986	0.032999
	0.328463	0.224524	0.032917	0.328462	0.224530	0.032917
O4	0.461388	0.055827	0.134932	0.461379	0.055829	0.134933
	0.461288	0.055927	0.134888	0.461292	0.055924	0.134893
	0.461358	0.057495	0.134897	0.461353	0.057493	0.134895
	0.461261	0.055910	0.134908	0.461259	0.055908	0.134906
O5	0.081570	0.275741	0.320058	0.081569	0.275741	0.320056
	0.081516	0.275932	0.319941	0.084063	0.139045	0.132918
	0.081512	0.277602	0.320075	0.081510	0.277594	0.320072
	0.081561	0.275868	0.319956	0.081561	0.275866	0.319956
O6	0.083880	0.138995	0.132871	0.083890	0.139008	0.132870
	0.084080	0.139028	0.132930	0.081519	0.275915	0.319955
	0.084178	0.140499	0.132836	0.084171	0.140506	0.132831
	0.084021	0.139095	0.132898	0.084018	0.139095	0.132894
N1	0.401506	0.257518	0.296121	0.401509	0.257513	0.296121
	0.401566	0.257524	0.296203	0.401562	0.257521	0.296194
	0.401531	0.259076	0.296152	0.401530	0.259074	0.296151
	0.401581	0.257438	0.296194	0.401578	0.257439	0.296193
N2	0.533848	0.706918	0.414000	0.533856	0.706919	0.414002
	0.533983	0.706947	0.414027	0.533977	0.706949	0.414026
	0.533909	0.708447	0.414010	0.533909	0.708447	0.414009
	0.533949	0.707026	0.413980	0.533948	0.707024	0.413979
N3	0.470975	0.729202	0.122503	0.470968	0.729196	0.122504
	0.470926	0.729211	0.122500	0.470924	0.729209	0.122501
	0.470950	0.730795	0.122500	0.470946	0.730791	0.122500

Continued on next page...

Table B.4: Continued

Atom	x	y	z	x	y	z
	0.470921	0.729111	0.122498	0.470918	0.729109	0.122498
H1	0.466973	0.088421	0.399666	0.469238	0.092698	0.398650
	0.466527	0.087528	0.399488	0.468929	0.091796	0.398627
		-			-	
	0.474136	0.101019	0.398634		-	
H3	0.503368	0.876081	0.302821	0.504744	0.872930	0.302718
	0.502923	0.877111	0.302438	0.504160	0.874013	0.302388
		-			-	
	0.503507	0.868868	0.301588	0.504560	0.868389	0.301552
H5	0.422554	0.531827	0.052165	0.421944	0.535456	0.050956
	0.421354	0.532044	0.052257	0.421147	0.536357	0.050708
		-			-	
		-			-	
H7a	0.727208	0.179502	0.434827		-	
	0.728581	0.179227	0.435938	0.724130	0.179756	0.433438
		-			-	
		-			-	
H7c	0.691372	0.161528	0.311783	0.692694	0.164847	0.313386
	0.691878	0.160261	0.310405	0.692734	0.163460	0.311823
		-			-	
		-			-	
H8c	0.199347	0.686821	0.009733	0.204354	0.689247	0.008357
	0.197304	0.686170	0.010015	0.202775	0.688659	0.008633
		-			-	
		-			-	
H20a	0.745775	0.866299	0.232937	0.743992	0.859828	0.236953
	0.747823	0.867143	0.232513	0.745241	0.860755	0.236284
	0.737620	0.858250	0.231937	0.738741	0.858375	0.234747

Continued on next page...

Table B.4: Continued

Atom	x	y	z	x	y	z
		-			-	
H20b	0.768171	0.878509	0.358995	0.766595	0.873800	0.357570
	0.768652	0.878068	0.357588	0.766558	0.873204	0.356658
	0.766258	0.876263	0.364512	0.766779	0.876606	0.362988
	0.764961	0.874705	0.356844	0.765863	0.874583	0.357066
H23	0.959281	0.407779	0.143650	0.961762	0.412373	0.146347
	0.958603	0.407470	0.143978	0.961079	0.412093	0.147045
		-			-	
		-			-	
H25	0.028095	0.437260	0.481237	0.026427	0.441059	0.477764
	0.027868	0.437597	0.481441	0.025828	0.441853	0.477141
		-			-	
		-			-	
H26	0.883548	0.669923	0.473015		-	
	0.884681	0.670642	0.473775		-	
		-			-	
		-			-	
H32a	0.072694	0.954239	0.297032		-	
	0.073174	0.955142	0.298346	0.078246	0.952233	0.292653
		-			-	
		-			-	

Table B.5: Coordinates of BCPs in eight different density maps of α-Glycine: Dynamic model densities and MEM density maps for IAM (first line), IAM-HO(second line), INV (third line) and MP (fourth line).

	Dynamic model density			MEM density		
Bond	x	y	z	x	y	z
C1-O1	0.657408	0.386761	0.630687	0.648703	0.386088	0.626674
	0.657033	0.386717	0.630434	0.651657	0.386523	0.629810
	0.659444	0.386958	0.630902	0.653695	0.386856	0.629442
	0.657760	0.386791	0.630732	0.653586	0.386850	0.629295
C1-O2	0.484688	0.368389	0.581224	0.490142	0.369824	0.576308
	0.484927	0.368385	0.581207	0.488714	0.369727	0.576990
	0.480953	0.367791	0.577757	0.486222	0.368888	0.577433
	0.484096	0.368255	0.580609	0.486748	0.368909	0.577618
C1-C2	0.936507	0.864409	0.074176	0.938724	0.864633	0.078175
	0.936522	0.864384	0.074149	0.938892	0.864724	0.075687
	0.933796	0.865582	0.073966	0.936274	0.864043	0.081525
	0.936113	0.864794	0.077312	0.936259	0.864132	0.080471
C2-N1	0.335786	0.619986	0.734730	0.345158	0.624579	0.729474
	0.335843	0.619981	0.734758	0.344735	0.624528	0.729197
	0.341426	0.620439	0.735514	0.348500	0.624846	0.727875
	0.341260	0.621531	0.734130	0.349217	0.624758	0.728171
O1...H1-N	0.287851	0.096922	0.431046	0.282769	0.098066	0.430689
	0.288923	0.096729	0.431216	0.280350	0.097364	0.429801
	0.288530	0.096904	0.440504	0.290774	0.095772	0.441037
	0.284803	0.098200	0.438897	0.291673	0.095888	0.441407
O2...H2-N	0.626369	0.126627	0.957301	0.622006	0.124782	0.943587
	0.626236	0.126860	0.957554	0.626193	0.121417	0.944594
	0.617238	0.125914	0.947182	0.610202	0.132617	0.944052
	0.616335	0.127703	0.949144	0.610045	0.133175	0.943302

Continued on next page...

Table B.5: Continued

Bond	x	y	z	x	y	z
O2. . . H3-N	0.729323	0.554116	0.326691	0.709478	0.544571	0.330367
	0.728788	0.554142	0.326576	0.708793	0.545040	0.329762
	0.732188	0.549069	0.320558	0.705215	0.543244	0.314054
	0.741749	0.552335	0.319642	0.711619	0.543801	0.317147
O1. . . H3-N	0.480057	0.969027	0.770940	0.433766	0.969596	0.709516
	0.479968	0.968992	0.770807	0.437843	0.969455	0.711125
	0.476806	0.975798	0.765836	0.465346	0.963081	0.776867
	0.478775	0.976299	0.764862	0.463283	0.961372	0.773295
O1. . . H4-C2	0.558636	0.806807	0.758849	0.503885	0.811812	0.700627
	0.558768	0.806922	0.758657	0.503537	0.812762	0.699015
	0.553111	0.803733	0.755632	0.530902	0.803714	0.725127
	0.546795	0.802582	0.755536	0.520915	0.803992	0.723085
O2. . . H4-C2	0.310559	0.787342	0.811623	0.364051	0.793558	0.835732
	0.310683	0.787469	0.811493	0.364255	0.794240	0.837189
	0.307033	0.784185	0.807335	0.344850	0.790686	0.824033
	0.311258	0.783065	0.805644	0.340828	0.790776	0.817615

Table B.6: Coordinates of BCPs in eight different density maps of D, L-Serine: Dynamic model densities and MEM density maps for IAM (first line), IAM-HO(second line), INV (third line) and MP (fourth line).

	Dynamic model density			MEM density		
Bond	x	y	z	x	y	z
C1-O1	0.712326	0.409322	0.574065	0.713941	0.409760	0.579469
	0.712763	0.409322	0.574989	0.712943	0.409077	0.573776
	0.711973	0.408760	0.573699	0.712906	0.409284	0.575100
	0.711978	0.409521	0.572458	0.712254	0.409490	0.572233
C1-O2	0.778355	0.449341	0.699340	0.775175	0.446907	0.697864
	0.778063	0.449003	0.698882	0.777025	0.450098	0.699742

Continued on next page...

Table B.6: Continued

Bond	x	y	z	x	y	z
	0.779451	0.448853	0.702909	0.776808	0.448760	0.700473
	0.779159	0.450022	0.700500	0.778031	0.450178	0.700969
C3-O3	0.906238	0.198651	0.866576	0.902097	0.200004	0.868565
	0.906204	0.198580	0.866871	0.901057	0.200321	0.873061
	0.906847	0.198334	0.869129	0.902439	0.199695	0.870208
	0.905430	0.198843	0.869956	0.903155	0.199473	0.868697
C1-C2	0.750535	0.347225	0.772676	0.751335	0.344934	0.775004
	0.750543	0.347208	0.772643	0.751115	0.345024	0.773883
	0.750308	0.346840	0.770767	0.751452	0.345113	0.774632
	0.751245	0.346113	0.774225	0.751239	0.345181	0.773551
C2-C3	0.822185	0.250119	0.925017	0.822263	0.247387	0.923965
	0.822187	0.250080	0.925009	0.822489	0.247404	0.924510
	0.821683	0.249764	0.923100	0.821986	0.247535	0.923465
	0.821600	0.249377	0.922031	0.821671	0.247971	0.923863
C2-N1	0.709015	0.234279	0.818951	0.711650	0.235429	0.822288
	0.708934	0.234203	0.818866	0.711545	0.235647	0.821977
	0.710767	0.235426	0.818709	0.711984	0.235107	0.823200
	0.711017	0.236348	0.821271	0.712217	0.235728	0.823671
O1. . . H4-O3	0.620782	0.514700	0.357884	0.616842	0.519317	0.361644
	0.620812	0.514492	0.356961	0.616524	0.518317	0.362790
	0.620130	0.519163	0.362311	0.614753	0.519600	0.357172
	0.619486	0.519025	0.361269	0.616364	0.519327	0.359358
O3. . . H11-N1	0.513889	0.261887	0.706253	0.515352	0.259349	0.704093
	0.513754	0.261747	0.707038	0.514702	0.260361	0.703735
	0.517740	0.260268	0.706162	0.514675	0.256749	0.701384
	0.519808	0.261055	0.714965	0.516858	0.258752	0.703372
O2. . . H12-N1	0.660840	0.064049	1.032432	0.669064	0.067041	1.031131
	0.660820	0.063934	1.032508	0.670227	0.069100	1.033184

Continued on next page...

Table B.6: Continued

Bond	x	y	z	x	y	z
	0.659473	0.066835	1.023642	0.670204	0.068057	1.030896
	0.660410	0.069911	1.027448	0.668500	0.068091	1.030240
O2. . . H13-N1	0.667638	0.079853	0.441572	0.668098	0.078269	0.458068
	0.667544	0.080061	0.440898	0.670561	0.076058	0.464196
	0.668383	0.081621	0.453809	0.668385	0.079425	0.456363
	0.666745	0.080841	0.453148	0.665911	0.078051	0.456870
O1. . . H2-C2	0.703359	0.360992	0.222035	0.698564	0.354457	0.213788
	0.703710	0.361144	0.222477	0.695661	0.349612	0.208309
	0.703997	0.358691	0.217757	0.694611	0.353610	0.205922
	0.701021	0.356350	0.207473	0.698502	0.351689	0.207334

Table B.7: Coordinates of BCPs in eight different density maps of *L*-Alanine: Dynamic model densities and MEM density maps for IAM (first line), IAM-HO(second line), INV (third line) and MP (fourth line).

	Dynamic model density			MEM density		
Bond	x	y	z	x	y	z
C1-O1	0.379900	0.619095	0.890871	0.382181	0.621809	0.891579
	0.380574	0.619125	0.890689	0.381066	0.622117	0.891934
	0.379707	0.618887	0.891658	0.381079	0.619418	0.891373
	0.379628	0.618893	0.892229	0.379707	0.619366	0.891208
C1-O2	0.489291	0.657296	0.838495	0.486292	0.656137	0.844221
	0.488939	0.657183	0.838767	0.486873	0.656172	0.843155
	0.492007	0.658168	0.839466	0.490007	0.656304	0.841755
	0.489286	0.657245	0.839861	0.489677	0.656652	0.840657
C1-C2	0.489805	0.650952	0.022630	0.488646	0.649456	0.023133
	0.489843	0.650911	0.022666	0.489314	0.649663	0.023254
	0.488264	0.650664	0.023077	0.488145	0.649244	0.020995
	0.489379	0.651015	0.027438	0.489337	0.649488	0.025197

Continued on next page...

Table B.7: Continued

Bond	x	y	z	x	y	z
C2-C3	0.362644	0.125916	0.328983	0.365881	0.125859	0.329864
	0.362570	0.125917	0.328873	0.364943	0.125457	0.329400
	0.360695	0.125782	0.328419	0.362414	0.126274	0.327629
	0.361243	0.125894	0.328064	0.363904	0.126391	0.329216
C2-N1	0.452242	0.650452	0.222782	0.454839	0.650252	0.216369
	0.452402	0.650494	0.222844	0.454474	0.650102	0.218705
	0.454246	0.650092	0.220215	0.454230	0.650440	0.216409
	0.462722	0.651241	0.212319	0.459727	0.650495	0.210943
O2...H3-N	0.531104	0.161516	0.921143	0.513733	0.154647	0.928108
	0.531737	0.161567	0.920832	0.515545	0.155493	0.928672
	0.538053	0.160542	0.928523	0.526902	0.158641	0.931362
	0.537108	0.161713	0.929909	0.526213	0.158309	0.931043
O2...H2-N	0.156026	0.736867	0.274552	0.169842	0.737578	0.264715
	0.156001	0.736847	0.273523	0.169585	0.737325	0.263201
	0.163245	0.734411	0.281284	0.166682	0.733281	0.270840
	0.167788	0.736241	0.278019	0.169505	0.733725	0.265316
O1...H1-N	0.230221	0.496251	0.834100	0.223945	0.493289	0.833780
	0.231499	0.496035	0.832843	0.222061	0.494150	0.832297
	0.229447	0.492072	0.833069	0.221262	0.490439	0.847632
	0.226989	0.492208	0.837202	0.227572	0.489683	0.843353

Table B.8: Coordinates of BCPs in eight different density maps of Ala-Tyr-Ala$_{Etoh}$: Dynamic model densities and MEM density maps for IAM (first line), IAM-HO(second line), INV (third line) and MP (fourth line).

	Dynamic model density			MEM density		
Bond	x	y	z	x	y	z
C2-O1	0.442350	0.335203	0.490091	0.443275	0.331966	0.489942
	0.442488	0.334874	0.490101	0.443095	0.332300	0.489972

Continued on next page...

Table B.8: Continued

Bond	x	y	z	x	y	z
	0.441433	0.337161	0.493357	0.442406	0.335182	0.491190
	0.440878	0.335236	0.489386	0.441286	0.334399	0.488705
C4-O2	0.498716	0.116704	0.772497	0.500082	0.120948	0.772847
	0.498599	0.117039	0.772575	0.500128	0.120642	0.772826
	0.501197	0.117037	0.775671	0.500513	0.120147	0.774309
	0.499342	0.116097	0.772100	0.499630	0.116797	0.772107
C6-O3	0.395649	0.173137	0.044615	0.397880	0.171104	0.043910
	0.395925	0.173063	0.044690	0.397276	0.171463	0.044152
	0.395894	0.175194	0.044279	0.397156	0.174779	0.043873
	0.395520	0.174175	0.043808	0.395997	0.174107	0.043466
C6-O4	0.448543	0.107590	0.083999	0.447131	0.109834	0.081143
	0.448496	0.107779	0.083904	0.447229	0.109498	0.081210
	0.450824	0.107995	0.083964	0.449210	0.109820	0.082467
	0.450112	0.106878	0.084081	0.448979	0.107767	0.083077
C24-O5	0.035509	0.354012	0.315751	0.032121	0.355423	0.313787
	0.035549	0.354146	0.315758	0.031860	0.354917	0.313835
	0.035575	0.355390	0.315844	0.035788	0.356697	0.315232
	0.035799	0.356409	0.315095	0.035027	0.356349	0.314585
C31-O6	0.918304	0.546113	0.867404	0.918087	0.542393	0.867135
	0.918250	0.546273	0.867427	0.918979	0.541940	0.867766
	0.918499	0.546792	0.868560	0.918413	0.543921	0.869773
	0.915991	0.540559	0.866697	0.916795	0.540066	0.868715
C1-N1	0.454279	0.225229	0.348926	0.456219	0.225923	0.352893
	0.454328	0.225219	0.348928	0.455967	0.226623	0.352098
	0.455780	0.226972	0.350372	0.455632	0.227299	0.351066
	0.458081	0.224373	0.350908	0.456643	0.225769	0.351270
C2-N2	0.460583	0.251815	0.531821	0.460369	0.256263	0.526389
	0.460481	0.251883	0.531839	0.460839	0.255764	0.527397

Continued on next page...

Table B.8: Continued

Bond	x	y	z	x	y	z
	0.460278	0.254834	0.531565	0.459606	0.257089	0.528964
	0.460328	0.252871	0.531950	0.459566	0.255080	0.529758
C3-N2	0.449976	0.244720	0.643260	0.446935	0.249091	0.646764
	0.449933	0.244746	0.643236	0.447340	0.248685	0.646642
	0.449943	0.246664	0.644068	0.447971	0.249325	0.645438
	0.450468	0.246392	0.644168	0.447518	0.248202	0.645766
C4-N3	0.509315	0.193660	0.820585	0.508499	0.192221	0.815161
	0.509312	0.193642	0.820580	0.508814	0.193294	0.817353
	0.509523	0.193765	0.820187	0.508825	0.192947	0.817586
	0.509739	0.193091	0.820992	0.509218	0.193137	0.819592
C5-N3	0.551194	0.179590	0.931073	0.551398	0.179308	0.932937
	0.551179	0.179626	0.931074	0.551432	0.179005	0.932749
	0.551257	0.181643	0.932363	0.553053	0.180206	0.933777
	0.552727	0.177434	0.931608	0.553676	0.176674	0.933465
C1-C2	0.476963	0.241510	0.442545	0.477155	0.240847	0.440940
	0.477003	0.241566	0.442543	0.477343	0.240920	0.441154
	0.478061	0.241129	0.439301	0.477868	0.242262	0.440220
	0.478784	0.241493	0.441228	0.478600	0.240350	0.440532
C1-C7	0.581985	0.208272	0.383124	0.587827	0.207451	0.384667
	0.582007	0.208247	0.383099	0.586279	0.207107	0.384981
	0.583464	0.209256	0.382942	0.587768	0.208796	0.383503
	0.588169	0.207232	0.384617	0.589954	0.207504	0.384752
C3-C4	0.466119	0.221618	0.734657	0.466095	0.221450	0.733620
	0.466079	0.221559	0.734651	0.466068	0.221198	0.733390
	0.463433	0.225113	0.731624	0.464887	0.223141	0.732680
	0.466023	0.222532	0.734660	0.466075	0.221810	0.733954
C3-C20	0.350702	0.291961	0.693687	0.349885	0.294747	0.691981
	0.350716	0.291974	0.693710	0.350810	0.294259	0.691703

Continued on next page...

Table B.8: Continued

Bond	x	y	z	x	y	z
	0.352156	0.294231	0.692502	0.351625	0.294676	0.693539
	0.348921	0.290312	0.693429	0.350169	0.291685	0.694047
C5-C6	0.495345	0.639906	0.986780	0.493834	0.641960	0.987042
	0.495360	0.639948	0.986748	0.493847	0.642138	0.986616
	0.496878	0.642464	0.987800	0.496238	0.643080	0.987596
	0.494706	0.641369	0.988256	0.495126	0.640652	0.987861
C5-C8	0.643664	0.167475	0.004623	0.646820	0.168627	0.002207
	0.643630	0.167558	0.004659	0.646766	0.167964	0.001726
	0.645562	0.168979	0.004788	0.646729	0.169434	0.003061
	0.647257	0.169105	0.005174	0.647643	0.169550	0.003254
C20-C21	0.215145	0.240093	0.695897	0.216785	0.238784	0.695598
	0.215038	0.240145	0.695870	0.216601	0.238402	0.695714
	0.213789	0.241217	0.695897	0.213945	0.239059	0.696478
	0.216665	0.239068	0.697112	0.215897	0.236991	0.697327
C21-C22	0.847247	0.633605	0.258153	0.848381	0.633895	0.257011
	0.847268	0.633660	0.258182	0.848979	0.634932	0.257938
	0.847527	0.634786	0.256709	0.847496	0.637261	0.258368
	0.846956	0.634113	0.258246	0.847288	0.636842	0.259701
C22-C23	0.902487	0.530412	0.211814	0.899852	0.532005	0.212943
	0.902553	0.530501	0.211818	0.900120	0.531582	0.213369
	0.903307	0.530842	0.211679	0.901911	0.531899	0.212048
	0.903009	0.529929	0.212217	0.901519	0.530766	0.212140
C23-C24	0.025741	0.936716	0.736881	0.026448	0.937941	0.739426
	0.025675	0.936740	0.736845	0.025820	0.936717	0.738339
	0.025265	0.937086	0.738151	0.024416	0.937567	0.738320
	0.025283	0.935493	0.738176	0.024452	0.936304	0.738118
C24-C25	0.006175	0.446497	0.361543	0.004358	0.948583	0.635930
	0.006142	0.946525	0.638450	0.003846	0.947739	0.636663

Continued on next page...

Table B.8: Continued

Bond	x	y	z	x	y	z
	0.005688	0.948117	0.636458	0.005869	0.947890	0.636396
	0.005569	0.945868	0.637358	0.006668	0.946228	0.636755
C25-C26	0.941273	0.549915	0.407527	0.944665	0.547518	0.406904
	0.941221	0.549986	0.407560	0.942450	0.550172	0.407025
	0.941224	0.551392	0.407285	0.943085	0.549665	0.406691
	0.941196	0.549664	0.406938	0.942531	0.547680	0.406633
C21-C26	0.133374	0.143324	0.643937	0.132101	0.144767	0.648174
	0.133387	0.143376	0.643901	0.130978	0.142998	0.645952
	0.132922	0.144818	0.642277	0.131460	0.144363	0.642858
	0.133243	0.143157	0.643762	0.132267	0.141914	0.643942
C31-C32	0.892794	0.446602	0.811691	0.892030	0.446116	0.807725
	0.892847	0.446654	0.811763	0.891922	0.446136	0.808197
	0.892154	0.449579	0.810211	0.891387	0.448142	0.806993
	0.890883	0.445786	0.808715	0.890713	0.445311	0.806622
O6...H15-O5	0.923020	0.695865	0.791484	0.919681	0.697438	0.789344
	0.923174	0.696077	0.791751	0.921008	0.698509	0.789557
	0.926055	0.699033	0.788316	0.920827	0.699058	0.788099
	0.921278	0.697886	0.788607	0.922026	0.696112	0.788750
O3...H16-O6	0.228251	0.191813	0.074025	0.219262	0.197918	0.069950
	0.227799	0.191902	0.073519	0.219213	0.198338	0.070244
	0.226132	0.189608	0.075662	0.221864	0.192608	0.072045
	0.223542	0.189660	0.075317	0.220098	0.191072	0.071052
O4...H11A-N1	0.572706	0.636794	0.804376	0.563723	0.636007	0.798198
	0.573089	0.637080	0.804620	0.566339	0.635142	0.798619
	0.571853	0.642828	0.802137	0.565053	0.640933	0.799304
	0.570375	0.640100	0.800716	0.564137	0.641697	0.800891
O2...H11C-N1	0.538706	0.924267	0.737640	0.528375	0.918559	0.741725
	0.538030	0.924161	0.737760	0.527373	0.918240	0.740719

Continued on next page...

Table B.8: Continued

Bond	x	y	z	x	y	z
	0.543933	0.923938	0.738905	0.542012	0.921933	0.743490
	0.543063	0.921167	0.737786	0.539060	0.918609	0.742551
O5...H11B-N1	0.790481	0.770586	0.688206	0.785246	0.783856	0.690806
	0.790752	0.771036	0.688500	0.785924	0.784119	0.691336
	0.784948	0.770561	0.688001	0.784140	0.779780	0.690413
	0.783717	0.772121	0.688849	0.782769	0.774291	0.689324
O4...H13-N3	0.528896	0.426287	0.874845	0.522166	0.423565	0.869348
	0.528565	0.426368	0.874538	0.515899	0.424298	0.868964
	0.526379	0.421480	0.878474	0.532087	0.420959	0.880359
	0.533732	0.413578	0.872910	0.534780	0.414932	0.879162
O1...H1-C1	0.484217	0.515423	0.549344	0.477121	0.509178	0.557819
	0.484320	0.515404	0.549453	0.476513	0.509454	0.559228
	0.480972	0.517937	0.550882	0.473004	0.514264	0.559118
	0.471371	0.528451	0.548196	0.474756	0.522184	0.558145
O1...H12-N2	0.473777	0.524778	0.445766	0.478535	0.520195	0.435444
	0.473915	0.524700	0.446013	0.480407	0.517217	0.433326
	0.472861	0.533974	0.443349	0.480550	0.531861	0.443750
	0.468080	0.537786	0.448390	0.472431	0.531265	0.440547

Table B.9: Topological properties of covalent and hydrogen bonds of α-Glycine: ρ_{BCP} (e/Å^3; first line) and $\nabla^2\rho_{BCP}$ (e/Å^5; second line) for the static and dynamic model densities of the INV and MP models. See tables in the Chapter 5 for values in other dynamic model densities as well as in MEM densities.

	Dynamic		Static	
Bond	INV	MP	INV	MP
C1-O1	2.636	2.701	2.699	2.770
	-17.18	-19.44	-31.82	-36.57
C1-O2	2.598	2.648	2.680	2.733
	-21.83	-23.61	-31.23	-35.07
C1-C2	1.696	1.698	1.735	1.735
	-14.28	-13.28	-13.89	-12.80
C2-N	1.749	1.657	1.788	1.691
	-11.65	-10.21	-11.54	-10.42
O1...H1-N	0.256	0.289	0.239	0.283
	3.46	2.51	3.81	2.68
O2...H2-N	0.209	0.249	0.194	0.240
	3.61	2.77	3.19	2.29
O2...H3-N	0.127	0.158	0.116	0.151
	2.01	1.61	1.93	1.51
O1...H3-N	0.069	0.072	0.062	0.065
	1.24	1.29	1.18	1.24
O1...H4-C2	0.082	0.070	0.075	0.063
	1.11	1.04	1.03	0.95
O2...H4-C2	0.086	0.077	0.080	0.070
	1.16	1.13	1.14	1.09

Table B.10: Topological properties of covalent and hydrogen bonds of D, L-Serine: ρ_{BCP} (e/Å^3; first line) and $\nabla^2\rho_{BCP}$ (e/Å^5; second line) for the static and dynamic model densities of the INV and MP models. See tables in the Chapter 5 for values in other dynamic model densities as well as in MEM densities.

	Dynamic		Static	
Bond	INV	MP	INV	MP
C1-O1	2.632	2.723	2.709	2.810
	-19.44	-23.40	-32.04	-32.18
C1-O2	2.585	2.693	2.666	2.791
	-16.79	-24.15	-30.75	-35.32
C3-O3	1.752	1.807	1.804	1.869
	-6.83	-9.02	-12.26	-16.64
C1-C2	1.674	1.669	1.719	1.710
	-12.67	-11.23	-13.28	-11.77
C2-C3	1.707	1.684	1.752	1.726
	-14.28	-13.60	-13.01	-12.29
C2-N	1.746	1.664	1.769	1.684
	-12.33	-12.20	-9.83	-10.06
O1...H4-O3	0.287	0.279	0.266	0.258
	3.94	3.91	4.24	4.29
O3...H11-N	0.235	0.237	0.218	0.219
	3.93	4.10	3.65	3.89
O2...H12-N	0.220	0.218	0.203	0.200
	3.61	3.71	3.29	3.47
O2...H13-N	0.210	0.202	0.194	0.185
	3.65	3.84	3.13	3.42
O1...H2-C2	0.119	0.086	0.110	0.075
	1.88	1.97	1.41	1.53

Table B.11: Topological properties of covalent and hydrogen bonds of *L*-Alanine: ρ_{BCP} (e/Å^3; first line) and $\nabla^2\rho_{BCP}$ (e/Å^5; second line) for the static and dynamic model densities of the INV and MP models. See tables in the Chapter 5 for values in other dynamic model densities as well as in MEM densities.

	Dynamic		Static	
Bond	INV	MP	INV	MP
C1-O1	2.656	2.807	2.727	2.902
	-17.82	-27.51	-32.18	-43.72
C1-O2	2.577	2.649	2.657	2.743
	-20.13	-24.01	-30.46	-38.20
C1-C2	1.673	1.696	1.714	1.736
	-12.90	-12.51	-13.24	-12.78
C2-C3	1.642	1.611	1.680	1.649
	-11.16	-10.67	-11.17	-10.67
C2-N	1.736	1.614	1.769	1.650
	-10.06	-11.52	-9.93	-13.45
O2...H3-N	0.231	0.258	0.222	0.249
	3.61	3.52	3.56	3.54
O2...H2-N	0.195	0.215	0.186	0.206
	3.19	3.22	3.10	3.19
O1...H1-N	0.188	0.206	0.179	0.197
	3.05	3.00	2.96	2.97

Table B.12: Topological properties of covalent and hydrogen bonds of Ala-Tyr-Ala$_{Etoh}$: ρ_{BCP} (e/Å^3; first line) and $\nabla^2\rho_{BCP}$ (e/Å^5; second line) for the static and dynamic model densities of the INV and MP models. See tables in the Chapter 5 for values in other dynamic model densities as well as in MEM densities.

	Dynamic		Static	
Bond	INV	MP	INV	MP
C2-O1	2.495	2.711	2.595	2.829
	-8.97	-14.97	-30.11	-35.54
C4-O2	2.462	2.807	2.587	2.984
	-12.46	-24.86	-30.09	-42.60
C6-O3	2.609	2.728	2.683	2.812
	-7.73	-11.58	-31.74	-30.01
C6-O4	2.473	2.594	2.599	2.741
	-16.32	-20.73	-28.34	-34.27
C24-O5	1.904	1.954	1.992	2.052
	-10.25	-11.12	-14.10	-19.35
C31-O6	1.656	1.607	1.759	1.730
	-5.30	-3.16	-10.81	-20.40
C1-N1	1.700	1.665	1.742	1.703
	-8.81	-8.40	-9.51	-9.15
C2-N2	2.203	2.319	2.304	2.428
	-19.98	-21.60	-22.94	-24.24
C3-N2	1.732	1.779	1.788	1.842
	-10.38	-12.35	-10.30	-12.60
C4-N3	2.222	2.416	2.319	2.530
	-20.09	-24.30	-23.64	-26.85
C5-N3	1.720	1.797	1.783	1.874
	-9.30	-12.99	-10.08	-14.39
C1-C2	1.744	1.692	1.803	1.753
	-12.23	-13.48	-12.05	-13.63
C1-C7	1.613	1.733	1.655	1.788
	-11.39	-13.90	-10.85	-13.73
C3-C4	1.742	1.708	1.793	1.760
	-11.46	-12.48	-11.80	-13.01
C3-C20	1.628	1.603	1.648	1.625
	-11.08	-11.57	-10.03	-10.90

Continued on next page...

Table B.12: Continued

Bond	INV	MP	INV	MP
C5-C6	1.634	1.715	1.681	1.770
	-13.51	-14.84	-12.70	-14.25
C5-C8	1.580	1.614	1.642	1.681
	-9.78	-9.99	-10.61	-10.95
C20-C21	1.700	1.636	1.752	1.679
	-11.31	-9.61	-11.15	-9.23
C21-C22	1.955	1.999	2.046	2.094
	-16.61	-17.94	-16.93	-18.49
C22-C23	1.984	2.011	2.074	2.103
	-16.57	-16.92	-17.02	-17.32
C23-C24	2.019	2.029	2.100	2.110
	-16.01	-16.00	-16.42	-16.42
C24-C25	1.997	2.021	2.095	2.122
	-17.07	-18.06	-17.38	-18.45
C25-C26	1.999	1.984	2.091	2.069
	-16.04	-15.02	-16.37	-15.01
C21-C26	1.957	1.995	2.038	2.073
	-15.97	-15.40	-16.80	-16.01
C31-C32	1.670	1.680	1.704	1.704
	-11.02	-10.37	-11.52	-10.99
O6...H15-O5	0.308	0.310	0.269	0.270
	3.54	4.48	4.36	5.22
O3...H16-O6	0.284	0.285	0.253	0.262
	3.66	3.63	4.09	4.04
O4...H11A-N1	0.246	0.251	0.220	0.236
	3.33	3.28	3.52	3.44
O2...H11C-N1	0.250	0.268	0.230	0.252
	3.61	3.59	3.80	3.94
O5...H11B-N1	0.198	0.210	0.175	0.189
	2.98	3.43	2.82	3.41
O4...H13-N3	0.150	0.104	0.136	0.091
	2.19	2.50	2.01	2.38
O1...H1-C1	0.118	0.105	0.107	0.095
	1.70	1.63	1.53	1.48

Continued on next page...

Table B.12: Continued

Bond	INV	MP	INV	MP
O1…H12-N2	0.119	0.107	0.109	0.095
	1.84	2.09	1.76	2.02

Table B.13: Number of electrons in atomic basins and volumes of the atomic basins in MEM-electron-density maps of α-Glycine obtained with different prior densities as indicated. Hydrogen atoms in the brackets indicate that they are included in the atomic basin of the corresponding parent atom.

	IAM		IAM-HO		INV		MP	
Atom	Electrons	Volume	Electrons	Volume	Electrons	Volume	Electrons	Volume
C1	4.40	5.11	4.48	5.33	4.47	4.66	4.46	4.69
C2(+H4)	6.76	13.79	6.77	13.79	6.72	13.71	6.76	13.82
O1	9.11	14.94	9.07	14.77	9.20	15.72	9.19	15.69
O2	9.11	15.13	9.10	15.05	9.24	15.78	9.26	15.95
N1(+H11+H12+H13)	9.74	20.85	9.73	21.00	9.65	20.20	9.64	20.30
H5	0.88	5.79	0.85	5.71	0.72	5.72	0.69	5.34
Total	40.00	75.61	40.00	75.65	40.00	75.79	40.00	75.79

Table B.14: Number of electrons in atomic basins and volumes of the atomic basins in MEM-electron-density maps of D, L-Serine obtained with different prior densities as indicated. Hydrogen atoms in the brackets indicate that they are included in the atomic basin of the corresponding parent atom.

	IAM		IAM-HO		INV		MP	
Atom	Electrons	Volume	Electrons	Volume	Electrons	Volume	Electrons	Volume
C1	4.25	4.91	4.43	5.18	4.33	4.77	4.41	4.97
C2	5.73	7.97	5.73	7.76	5.63	7.42	5.63	7.22
C3	6.15	9.42	6.11	9.17	6.15	9.07	6.16	9.10
O1	9.28	16.16	9.28	16.13	9.35	17.14	9.27	16.18
O2	9.16	16.94	9.08	16.71	9.23	17.92	9.12	16.89
O3(+H4)	9.16	16.57	9.24	16.88	9.17	16.62	9.23	17.07
N1(+H11+H12+H13)	9.23	20.98	9.23	21.04	9.15	19.57	9.29	21.47
H2	0.78	4.85	0.82	5.20	0.87	5.58	0.86	5.67
H31	0.97	6.36	0.93	6.38	0.93	6.25	0.94	6.50
H32	1.23	8.86	1.15	8.83	1.17	8.92	1.09	8.21
Spurious maxima-1	0.05	0.27	-	-	-	-	-	-
Total	55.99	113.29	56.00	113.28	55.98	113.26	56.00	113.28

Table B.15: Number of electrons in atomic basins and volumes of the atomic basins in MEM-electron-density maps of *L*-Alanine obtained with different prior densities as indicated. Hydrogen atoms in the brackets indicate that they are included in the atomic basin of the corresponding parent atom.

	IAM		IAM-HO		INV		MP	
Atom	Electrons	Volume	Electrons	Volume	Electrons	Volume	Electrons	Volume
C1	4.58	5.98	4.62	5.87	4.57	5.51	4.56	5.16
C2	5.84	8.42	5.84	8.06	5.85	7.48	5.82	8.00
C3(+H7)	7.32	17.88	7.29	17.93	7.23	17.17	7.38	18.20
O1	8.91	15.20	8.90	15.18	9.11	18.00	9.04	16.63
O2	8.96	14.01	8.95	13.95	9.14	16.13	9.15	15.78
N1(+H1+H2+H3)	9.89	25.49	9.86	25.62	9.58	21.39	9.76	23.22
H4	0.83	5.46	0.84	5.64	0.83	5.82	0.75	5.42
H5	0.87	6.75	0.88	6.86	0.91	8.05	0.83	7.31
H6	0.81	6.06	0.82	6.16	0.78	5.73	0.71	5.55
Total	48.01	105.25	48.00	105.27	48.00	105.28	48.00	105.27
H1	-	-	-	-	0.35	2.00	-	-
H2	-	-	-	-	0.33	1.80	-	-
H3	-	-	-	-	0.40	1.92	-	
H7	-	-	-	-	0.76	5.67	0.68	5.41

Table B.16: Number of electrons in atomic basins and volumes of the atomic basins in MEM-electron-density maps of Ala-Tyr-Ala$_{Etoh}$ obtained with different prior densities as indicated. Hydrogen atoms in the brackets indicate that they are included in the atomic basin of the corresponding parent atom.

	IAM		IAM-HO		INV		MP	
Atom	Electrons	Volume	Electrons	Volume	Electrons	Volume	Electrons	Volume
C1(+H1)	6.59	13.15	6.58	13.31	6.65	13.21	6.61	12.45
C2	4.76	6.14	4.82	6.37	4.82	6.44	4.85	6.28
C3(+H3)	6.66	12.82	6.68	13.06	6.71	12.82	6.65	13.04
C4	4.73	6.07	4.81	6.25	4.86	6.14	4.84	6.04
C5(+H5)	6.81	18.24	6.82	17.63	6.68	16.14	6.60	14.38
C6	4.55	6.05	4.59	5.97	4.61	6.63	4.66	6.70
C7(+H7a+H7b+H7c)	8.25	29.74	8.75	36.73	8.70	34.08	8.72	34.29
C8(+H8a+H8b+H8c)	8.98	36.33	8.96	36.15	8.94	35.81	9.03	36.51
C20(+H20a)	7.38	17.87	7.40	17.76	7.41	17.68	7.36	18.02
C21	6.01	9.44	6.05	9.10	6.02	9.93	5.96	9.69
C22(+H22)	6.77	18.27	6.79	18.19	7.01	20.48	7.01	20.50
C23(+H23)	7.05	21.44	7.03	21.31	7.05	22.22	7.00	22.28
C24	5.80	12.76	5.78	12.89	5.68	10.34	5.68	10.73
C25(+H25)	6.89	21.61	6.91	21.74	6.95	21.62	6.93	22.70
C26(+H26)	7.17	22.79	7.09	22.93	7.04	21.15	7.03	21.83
C31(+H31a+H31b)	7.49	26.93	7.44	26.86	7.61	25.48	7.42	24.37
C32(+H32a+H32b+H32c)	8.84	38.96	8.78	39.56	9.06	39.82	8.75	37.68
O1	9.13	16.84	9.13	16.85	9.04	18.74	9.04	18.76
O2	9.28	17.07	9.30	17.20	9.10	19.09	9.22	20.11
O3	8.85	16.96	8.85	17.62	8.83	17.91	8.91	19.97

Continued on next page...

Table B.16: Continued

Atom	Electrons	Volume	Electrons	Volume	Electrons	Volume	Electrons	Volume
O4	9.07	13.51	9.09	13.97	9.13	16.02	9.17	16.01
O5(+H15)	9.56	18.03	9.46	18.16	9.57	20.75	9.72	20.45
O6(+H16)	9.44	18.30	9.58	18.15	9.35	18.48	9.54	18.99
N1(+H11a+H11b+H11c)	9.71	23.48	9.72	23.59	9.40	21.08	9.64	22.58
N2(+H12)	8.47	17.69	8.46	17.53	8.45	17.21	8.47	16.60
N3(+H13)	8.43	16.08	8.37	15.35	8.47	15.89	8.41	15.68
H20b	0.74	6.57	0.72	6.42	0.84	6.34	0.74	6.04
Spurious maxima-1	0.01	0.51	0.01	0.59	0.00	0.31	0.01	0.54
Spurious maxima-2	0.00	1.36	0.00	1.49	0.02	1.81	0.00	0.22
Spurious maxima-3	0.02	0.45	-	-	-	-	-	-
Spurious maxima-4	0.00	0.19	-	-	-	-	-	-
Spurious maxima-5	0.01	0.18	-	-	-	-	-	-
Total	197.45	485.83	197.97	492.73	198.00	493.62	197.97	493.44
H1	0.75	5.86	0.76	6.13	-	-	-	-
H3	0.88	5.98	0.90	6.32	-	-	0.72	5.12
H5	0.79	9.85	0.75	8.99	-	-	-	-
H7a	-	-	0.61	7.44	-	-	-	-
H7c	0.75	8.16	0.77	8.33	-	-	-	-
H8c	0.65	7.79	0.68	7.59	-	-	-	-
H20a	0.76	7.48	0.77	7.42	0.75	6.68	-	-
H23	0.72	6.50	0.70	6.49	-	-	-	-
H25	0.67	7.01	0.63	6.93	-	-	-	-
H32a	-	-	0.59	7.82	-	-	-	-

Table B.17: Atomic charges (Q) obtained from the integrated number of electrons in atomic basins for MEM-electron-density maps of α-Glycine as obtained with different prior densities as indicated.

Atom	IAM	IAM-HO	INV	MP
C1	+1.60	+1.52	+1.53	+1.54
C2(+H4)	+0.24	+0.23	+0.28	+0.24
O1	-1.11	-1.07	-1.20	-1.19
O2	-1.11	-1.10	-1.24	-1.26
N1(+H1+H2+H3)	+0.26	+0.27	+0.35	+0.36
H5	+0.12	+0.15	+0.28	+0.31
Total	0.00	0.00	0.00	0.00

Table B.18: Atomic charges (Q) obtained from the integrated number of electrons in atomic basins for MEM-electron-density maps of D,L-Serine as obtained with different prior densities as indicated.

Atom	IAM	IAM-HO	INV	MP
C1	+1.75	+1.57	+1.67	+1.59
C2	+0.27	+0.27	+0.37	+0.37
C3	-0.15	-0.11	-0.15	-0.16
O1	-1.28	-1.28	-1.35	-1.27
O2	-1.16	-1.08	-1.23	-1.12
O3(+H4)	-0.16	-0.24	-0.17	-0.23
N1(+H11+H12+H13)	+0.73	+0.77	+0.85	+0.71
H2	+0.22	+0.18	+0.13	+0.14
H31	+0.03	+0.07	+0.07	+0.06
H32	-0.23	-0.15	-0.17	-0.09
Total	+0.02	0.00	+0.02	0.00

Table B.19: Atomic charges (Q) obtained from the integrated number of electrons in atomic basins for MEM-electron-density maps of *L*-Alanine as obtained with different prior densities as indicated.

Atom	IAM	IAM-HO	INV	MP
C1	+1.42	+1.38	+1.43	+1.44
C2	+0.16	+0.16	+0.15	+0.18
C3(+H7)	-0.32	-0.29	-0.23	-0.38
O1	-0.91	-0.90	-1.11	-1.04
O2	-0.96	-0.95	-1.14	-1.15
N1(+H1+H2+H3)	+0.11	+0.14	+0.42	+0.24
H4	+0.17	+0.16	+0.17	+0.25
H5	+0.13	+0.12	+0.09	+0.17
H6	+0.19	+0.18	+0.22	+0.29
Total	-0.01	0.00	0.00	0.00

Table B.20: Atomic charges (Q) obtained from the integrated number of electrons in atomic basins for MEM-electron-density maps of Ala-Tyr-Ala$_{Etoh}$ as obtained with different prior densities as indicated.

Atom	IAM	IAM-HO	INV	MP
C1(+H1)	+0.41	+0.42	+0.35	+0.39
C2	+1.24	+1.18	+1.18	+1.15
C3(+H3)	+0.34	+0.32	+0.29	+0.35
C4	+1.27	+1.19	+1.14	+1.16
C5(+H5)	+0.19	+0.18	+0.32	+0.40
C6	+1.45	+1.41	+1.39	+1.34
C7(+H7a+H7b+H7c)	+0.75	+0.25	+0.30	+0.28
C8(+H8a+H8b+H8c)	+0.02	+0.04	+0.06	-0.03
C20(+H20a)	-0.38	-0.40	-0.41	-0.36
C21	-0.01	-0.05	-0.02	+0.04
C22(+H22)	+0.23	+0.21	-0.01	-0.01
C23(+H23)	-0.05	-0.03	-0.05	0.00
C24	+0.20	+0.22	+0.32	+0.32
C25(+H25)	+0.11	+0.09	+0.05	+0.07
C26(+H26)	-0.17	-0.09	-0.04	-0.03
C31(+H31a+H31b)	+0.51	+0.56	+0.39	+0.58
C32(+H32a+H32b+H32c)	+0.16	+0.22	-0.06	+0.25
O1	-1.13	-1.13	-1.04	-1.04
O2	-1.28	-1.30	-1.10	-1.22
O3	-0.85	-0.85	-0.83	-0.91
O4	-1.07	-1.09	-1.13	-1.17
O5(+H15)	-0.56	-0.46	-0.57	-0.72
O6(+H16)	-0.44	-0.58	-0.35	-0.54
N1(+H11a+H11b+H11c)	+0.29	+0.28	+0.60	+0.36
N2(+H12)	-0.47	-0.46	-0.45	-0.47
N3(+H13)	-0.43	-0.37	-0.47	-0.41
H20b	+0.26	+0.28	+0.16	+0.26
Spurious maxima-1	0.01	0.01	0.00	0.01
Spurious maxima-2	0.00	0.00	0.02	0.00
Spurious maxima-3	0.02	-	-	-
Spurious maxima-4	0.00	-	-	-
Spurious maxima-5	0.01	-	-	-
Total	+0.59	+0.04	+0.02	+0.04

Table B.21: Topological properties at atomic maxima of α-Glycine: ρ_{max} (e/Å^3; first line) and $\nabla^2\rho_{max}$ (e/Å^5; second line) for four different dynamic model density maps.

	Dynamic Model density			
Atom	IAM	IAM-HO	INV	MP
C1	136.2	140.0	136.2	135.5
	-52150.4	-54944.0	-52163.2	-51750.0
C2	116.3	119.4	116.2	115.9
	-39152.9	-41073.7	-39014.8	-38877.7
O1	153.1	158.4	154.6	153.9
	-54940.5	-58613.4	-55843.0	-55455.3
O2	146.6	151.9	148.4	147.4
	-51329.6	-54837.0	-52332.5	-51672.7
N	138.7	143.0	138.7	138.0
	-48984.0	-51862.2	-48920.5	-48494.5

Table B.22: Topological properties at atomic maxima of D,L-Serine: ρ_{max} (e/Å^3; first line) and $\nabla^2\rho_{max}$ (e/Å^5; second line) for four different dynamic model density maps.

	Dynamic Model density			
Atom	IAM	IAM-HO	INV	MP
C1	98.1	107.9	101.4	104.9
	-28694.3	-34177.2	-30419.6	-32453.4
C2	97.3	107.1	101.1	104.8
	-28200.6	-33731.5	-30279.2	-32405.8
C3	83.2	90.0	85.4	88.3
	-20998.5	-24215.2	-21961.7	-23311.1
O1	109.3	120.9	113.4	117.0
	-29024.6	-35166.2	-31306.1	-32939.7
O2	107.4	118.1	111.3	114.2
	-28472.9	-34024.2	-30342.7	-31738.9
O3	105.5	114.0	107.8	110.8
	-28525.7	-32710.3	-29358.3	-30701.1
N	109.5	119.9	113.1	116.5
	-31706.1	-37420.4	-33562.0	-35401.7

Table B.23: Topological properties at atomic maxima of *L*-Alanine: ρ_{max} (e/Å^3; first line) and $\nabla^2\rho_{max}$ (e/Å^5; second line) for four different dynamic model density maps.

	Dynamic Model density			
Atom	IAM	IAM-HO	INV	MP
C1	121.5	123.8	128.9	127.2
	-42105.9	-43623.4	-47042.8	-45974.2
C2	116.5	120.0	123.4	121.9
	-39081.9	-41347.7	-43539.0	-42630.1
C3	83.7	85.3	86.4	86.2
	-21372.4	-22122.9	-22607.3	-22500.2
O1	128.1	132.7	136.5	136.0
	-39491.8	-42377.1	-44409.7	-44276.0
O2	134.3	138.6	144.2	140.8
	-43572.9	-46270.5	-49810.1	-47475.4
N	130.1	131.9	135.0	134.8
	-43358.6	-44383.9	-46255.1	-45968.4

Table B.24: Topological properties at atomic maxima of Ala-Tyr-Ala$_{Etoh}$: ρ_{max} (e/Å^3; first line) and $\nabla^2\rho_{max}$ (e/Å^5; second line) for four different dynamic model density maps.

	Dynamic Model density			
Atom	IAM	IAM-HO	INV	MP
C1	82.7	85.7	86.3	87.4
	-20911.4	-22299.9	-22631.2	-23092.6
C2	88.3	91.6	92.7	93.8
	-23537.1	-25227.0	-25957.9	-26469.3
C3	89.0	91.5	93.1	94.6
	-23922.5	-25085.6	-25936.7	-26645.1
C4	90.4	93.2	94.5	96.1
	-24576.6	-26093.0	-26853.0	-27770.8
C5	79.9	81.6	83.0	84.2
	-19665.0	-20396.6	-21052.0	-21527.1
C6	84.8	87.4	88.1	89.6
	-21806.4	-23027.1	-23388.9	-24108.8
C7	53.5	54.9	55.2	55.9
	-9460.5	-9909.3	-9960.9	-10194.6
C8	47.5	48.3	48.7	49.3
	-7988.3	-8254.9	-8329.9	-8523.2
C20	75.2	77.2	78.9	79.1
	-17378.9	-18279.1	-19024.5	-19029.0
C21	76.1	77.6	79.3	80.2
	-17733.9	-18423.9	-19132.2	-19542.7
C22	67.8	68.8	70.5	71.1
	-14561.4	-15000.6	-15653.4	-15886.4
C23	64.1	65.7	66.7	67.5
	-13172.0	-13815.3	-14194.1	-14508.1
C24	70.0	71.7	72.5	73.3
	-15282.2	-15938.3	-16278.6	-16596.3
C25	62.4	64.8	65.2	66.0
	-12600.4	-13502.8	-13669.3	-13996.8
C26	66.1	68.0	69.1	69.8
	-13953.9	-14685.3	-15146.0	-15434.2

Continued on next page...

Table B.24: Continued

Atom	IAM	IAM-HO	INV	MP
C31	41.3	41.9	42.3	42.6
	-6135.6	-6302.7	-6351.5	-6435.0
C32	34.9	35.4	35.7	36.1
	-4534.6	-4687.6	-4686.6	-4807.8
O1	95.1	99.4	99.3	100.4
	-23467.2	-25627.8	-25595.7	-25914.1
O2	87.7	90.8	92.2	92.6
	-20830.2	-22418.5	-23169.1	-23022.0
O3	79.9	82.0	83.4	84.5
	-16522.9	-17363.5	-17916.6	-18324.9
O4	100.5	104.0	105.0	106.0
	-25709.4	-27242.7	-27730.3	-28094.3
O5	79.8	82.7	82.5	84.0
	-16528.6	-17640.7	-17568.9	-18037.6
O6	70.8	73.3	73.2	74.9
	-13108.4	-13991.6	-13864.9	-14495.3
N1	93.2	96.4	96.6	98.5
	-23708.7	-25194.9	-25314.5	-26095.4
N2	102.7	105.2	106.9	108.6
	-29014.5	-30283.6	-31080.9	-32022.4
N3	101.4	104.1	106.0	107.7
	-28295.5	-29728.2	-30634.4	-31557.2

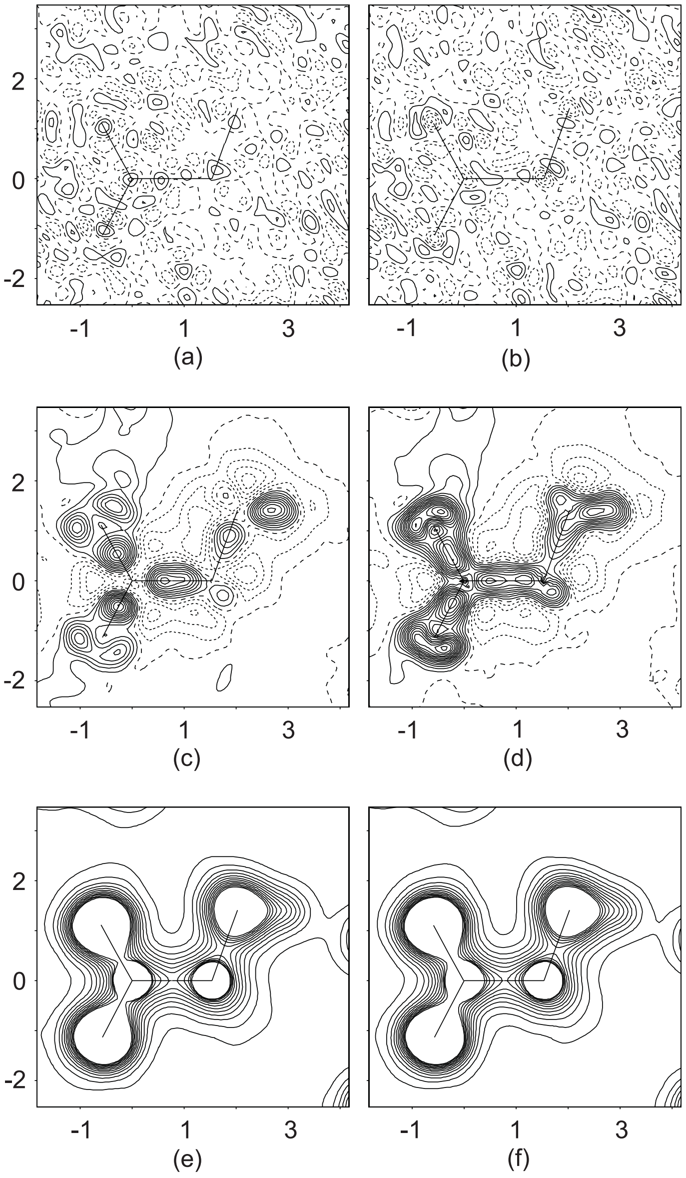

Figure B.1: C1-C2-N plane of density maps of D, L-serine. (a, b) residual density (difference Fourier map) with contours at 0.05 e/Å^3; (c, d) dynamic deformation density [Eq. 4] with contours at 0.05 e/Å^3; and (e, f) MEM density with contours at 0.2 e/Å^3 up to 2.5 e/Å^3. For (a, c, e) the IAM prior, and for (b, d, f) the IAM-HO prior has been used. Numbers on axes indicate the distance in Å with respect to an arbitrarily selected origin. Solid lines denote positive values, dotted lines denote negative values and dashed lines are the zero contour.

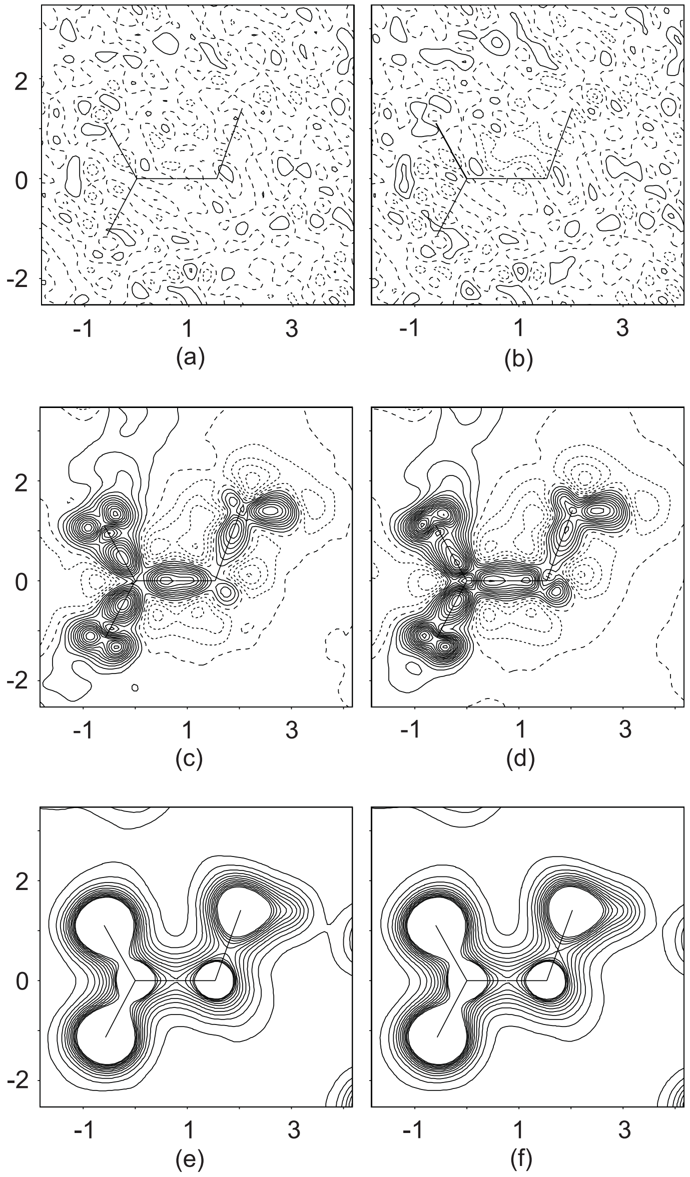

Figure B.2: C1-C2-N plane of density maps of D, L-serine. (a, b) residual density (difference Fourier map) with contours at 0.05 e/Å^3; (c, d) dynamic deformation density [Eq. 4] with contours at 0.05 e/Å^3; and (e, f) MEM density with contours at 0.2 e/Å^3 up to 2.5 e/Å^3. For (a, c, e) the INV prior, and for (b, d, f) the MP prior has been used. Numbers on axes indicate the distance in Å with respect to an arbitrarily selected origin. Solid lines denote positive values, dotted lines denote negative values and dashed lines are the zero contour.

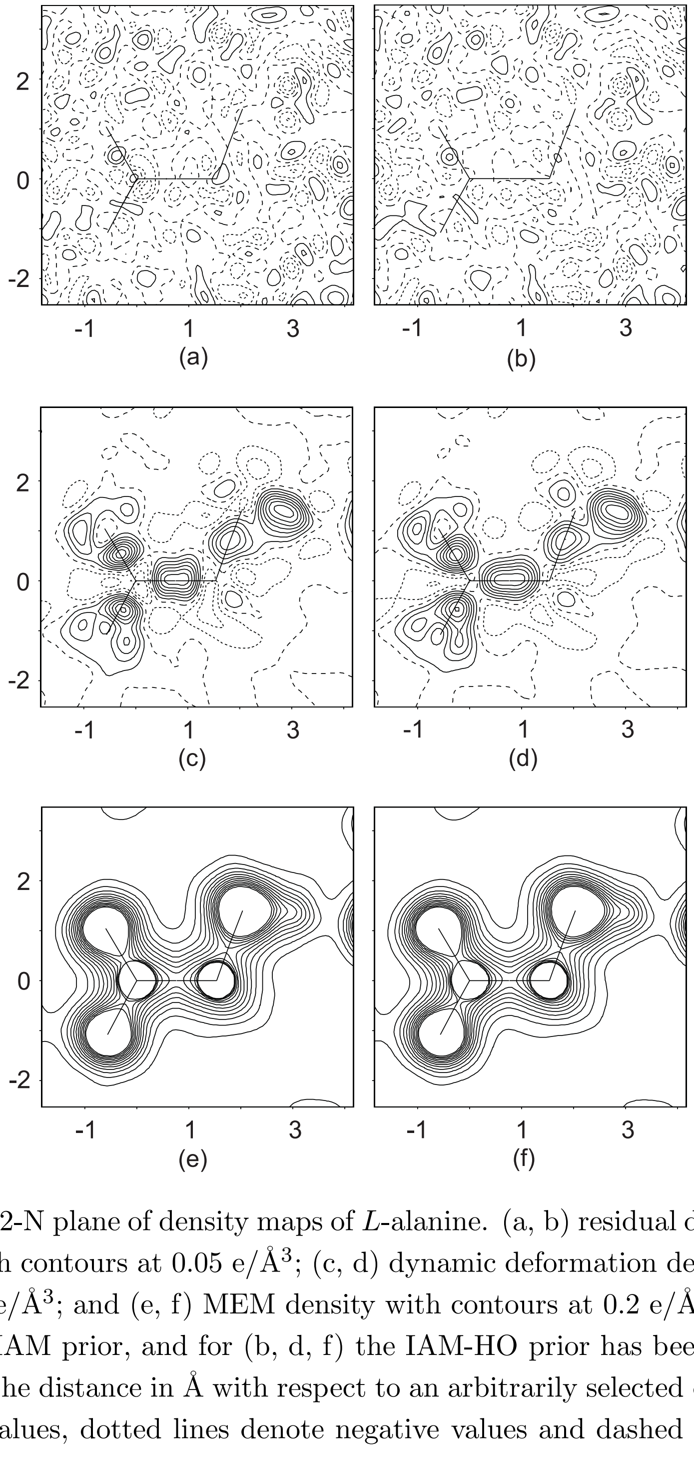

Figure B.3: C1-C2-N plane of density maps of *L*-alanine. (a, b) residual density (difference Fourier map) with contours at 0.05 e/Å^3; (c, d) dynamic deformation density [Eq. 4] with contours at 0.05 e/Å^3; and (e, f) MEM density with contours at 0.2 e/Å^3 up to 2.5 e/Å^3. For (a, c, e) the IAM prior, and for (b, d, f) the IAM-HO prior has been used. Numbers on axes indicate the distance in Å with respect to an arbitrarily selected origin. Solid lines denote positive values, dotted lines denote negative values and dashed lines are the zero contour.

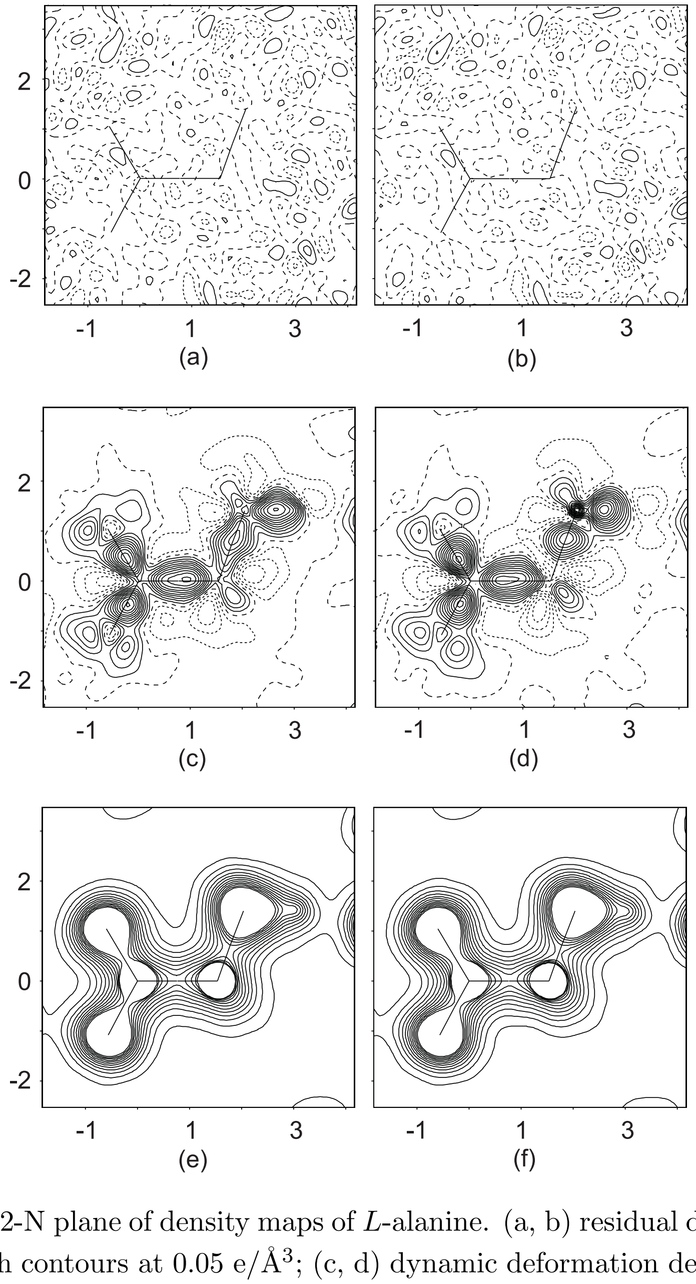

Figure B.4: C1-C2-N plane of density maps of *L*-alanine. (a, b) residual density (difference Fourier map) with contours at 0.05 e/Å^3; (c, d) dynamic deformation density [Eq. 4] with contours at 0.05 e/Å^3; and (e, f) MEM density with contours at 0.2 e/Å^3 up to 2.5 e/Å^3. For (a, c, e) the INV prior, and for (b, d, f) the MP prior has been used. Numbers on axes indicate the distance in Å with respect to an arbitrarily selected origin. Solid lines denote positive values, dotted lines denote negative values and dashed lines are the zero contour.

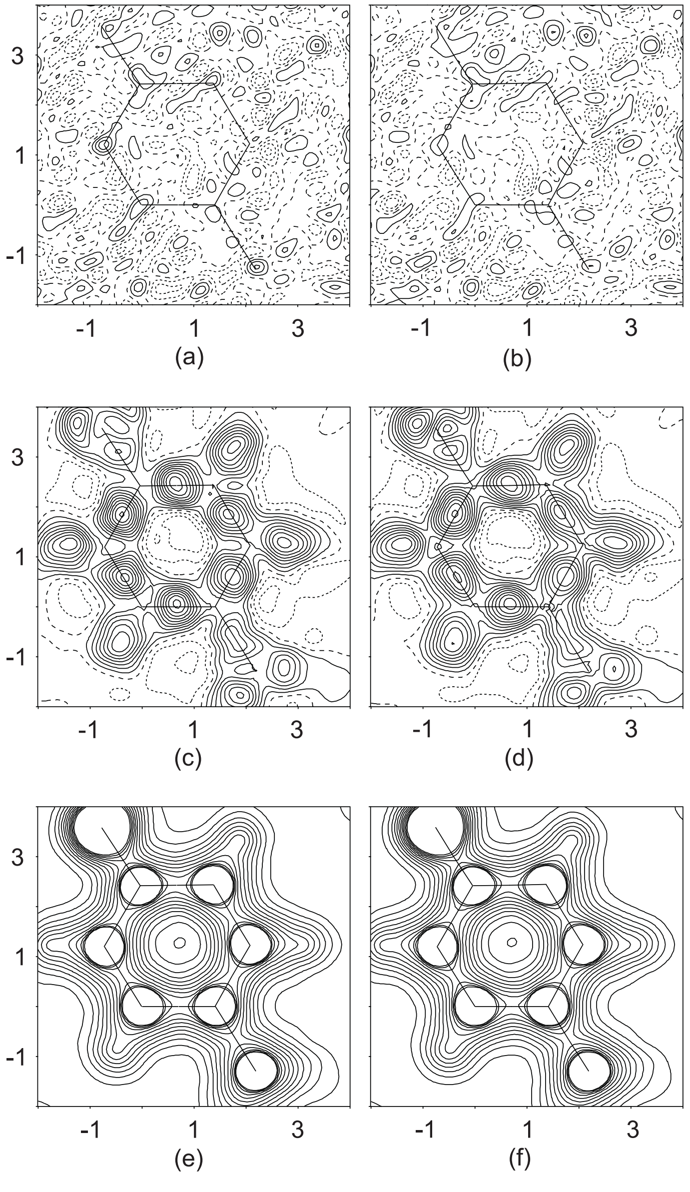

Figure B.5: Phenyl ring plane of density maps of Ala-Tyr-Ala$_{Etoh}$. (a, b) residual density (difference Fourier map) with contours at 0.05 e/Å^3; (c, d) dynamic deformation density [Eq. 4] with contours at 0.05 e/Å^3; and (e, f) MEM density with contours at 0.2 e/Å^3 up to 2.5 e/Å^3. For (a, c, e) the IAM prior, and for (b, d, f) the IAM-HO prior has been used. Numbers on axes indicate the distance in Å with respect to an arbitrarily selected origin. Solid lines denote positive values, dotted lines denote negative values and dashed lines are the zero contour.

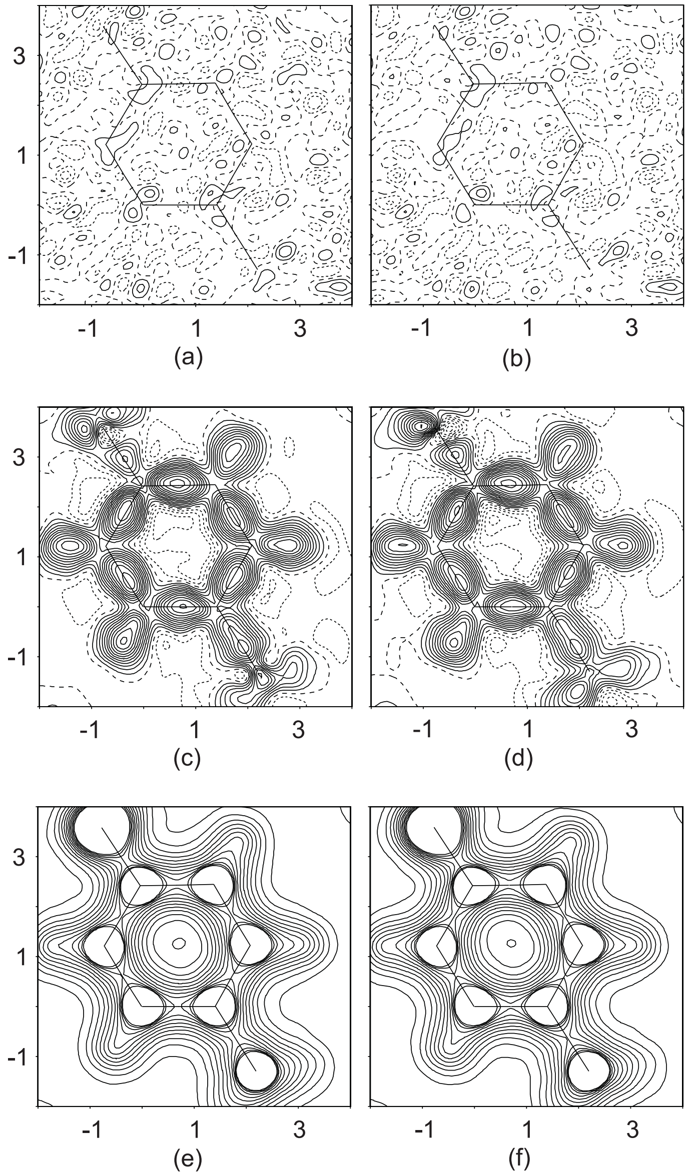

Figure B.6: Phenyl ring plane of density maps of Ala-Tyr-Ala$_{Etoh}$. (a, b) residual density (difference Fourier map) with contours at 0.05 e/Å^3; (c, d) dynamic deformation density [Eq. 4] with contours at 0.05 e/Å^3; and (e, f) MEM density with contours at 0.2 e/Å^3 up to 2.5 e/Å^3. For (a, c, e) the INV prior, and for (b, d, f) the MP prior has been used. Numbers on axes indicate the distance in Å with respect to an arbitrarily selected origin. Solid lines denote positive values, dotted lines denote negative values and dashed lines are the zero contour.

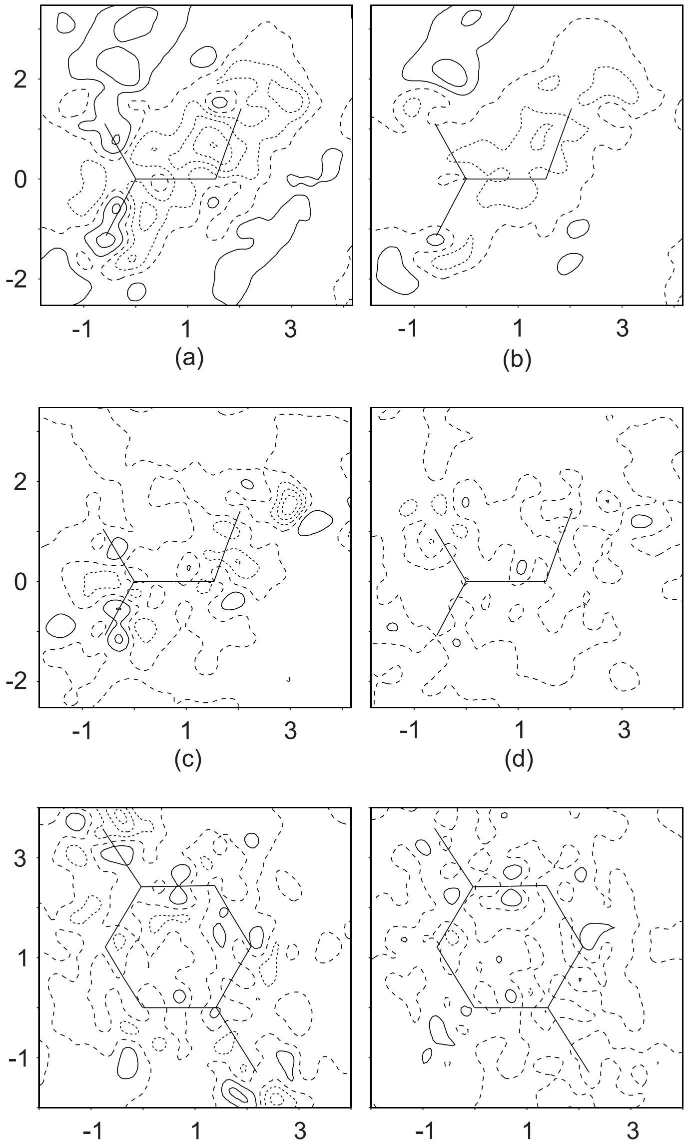

Figure B.7: C1-C2-N plane of difference density maps (Eq. 3) with contours at 0.05 e/Å^3. (a) INV prior and (b) MP prior of D, L-serine; (c) INV prior and (d) MP prior of L-alanine; (e) INV prior and (f) MP prior of Ala-Tyr-Ala$_{Etoh}$. Numbers on axes indicate the distance in Å with respect to an arbitrarily selected origin. Solid lines denote positive values, dotted lines denote negative values and dashed lines are the zero contour.

Bibliography

Allen, F. H. and Bruno, I. J. (2010). Bond lengths in organic and metal-organic compounds revisited: X–H, bond lengths from neutron diffraction data, *Acta. Cryst.* **B66**: 380–386.

Bader, R. F. W. (1990). *Atoms in Molecules: A Quantum Theory*, Clarendon Press, Oxford Science Publications, Oxford.

Bader, R. F. W. (1998). A bond path: A universal indicator of bonded interactions, *J. Phys. Chem. A.* **102**: 7314–7323.

Bader, R. F. W. (2002). A comment on some fundamental problems with zero-flux partitioning of electron densities, *Theor. Chem. Acc.* **107**: 381–382.

Bader, R. F. W. (2012). *AIMPAC*, http://www.chemistry.mcmaster.ca/aimpac/, McMaster University, Canada.

Bagautdinov, B., Luedecke, J., Schneider, M. and van Smaalen, S. (1998). Disorder in the crystal structure of Cs2HgCl4 studied by the maximum entropy method, *Acta. Cryst.* **B54**: 626–634.

Bak, J. M., Dominiak, P. M., Wilson, C. C. and Wozniak, K. (2009). Experimental charge-density study of paracetamol - multipole refinement in the presence of a disordered methyl group, *Acta Cryst.* **A65**: 490–500.

Bang, D., Tereshko, V., Kossiakoff, A. A. and Kent, S. B. H. (2009). Role of a salt bridge in the model protein crambin explored by chemical protein synthesis: X-ray structure of a unique protein analogue, [V15A]crambin-a-carboxamide., *Mol. BioSyst.* **5**: 750–756.

Benabicha, F., Pichon-Pesme, V., Jelsch, C., Lecomte, C. and Khmou, A. (2000). Experimental charge density and electrostatic potential of glycyl-L-threonine dihydrate, *Acta Cryst.* **B56**: 155–165.

Betteridge, P. W., Carruthers, J. R., Cooper, R. I., Prout, K. and Watkin, D. J. (2003). *CRYSTALS* version 12: software for guided crystal structure analysis, *J. Appl. Cryst.* **36**: 1487.

Bianchi, R. and Forni, A. (2005). Valtopo: a program for the determination of atomic and molecular properties from experimental electron densities, *J. Appl. Cryst.* **38**: 232–236.

Biegler-König, F. and Schönbohm, J. (2002). An update of the AIM2000-program for atoms in molecules, *J. Comput. Chem.* **23**: 1489–1494.

Biegler-König, F., Schönbohm, J. and D., B. (2001). AIM2000 - a program to analyze and visualize atoms in molecules, *J. Comput. Chem.* **22**: 545–559.

Bindzus, N. and Iversen, B. B. (2012). Maximum-entropy-method charge densities based on structure-factor extraction with the commonly used rietveld refinement programs *gsas*, *fullprof* and *jana2006*, *Acta Cryst.* **A68**: 750–762.

Birkedal, H., Madsen, D., Mathiesen, R. H., Knudsen, K., Weber, H.-P., Pattison, P. and Schwarzenbach, D. (2004). The charge density of urea from synchrotron diffraction data, *Acta Cryst.* **A60**: 371–381.

Bönisch, H., Schmidt, C. L., Bianco, P. and Ladenstein, R. (2005). Ultrahigh-resolution study on *pyrococcus abyssi* rubredoxin. i. 0.69 Å x-ray structure of mutant w4l/r5s, *Acta Cryst.* **D61**: 990–1004.

Branden, C. and Tooze, J. (1999). *Introduction to Protein Structure*, Garland, Newyork.

Bricongne, G. (1988). A bayesian statistical theory of the phase problem. i. a multichannel maximum-entropy formalism for constructing generalized joint probability distributions of structure factors, *Acta. Cryst.* **A44**: 517–545.

Brünger, A. (1992). *X-PLOR - A system for X-ray Crystallography and NMR*, The Howard Hughes Medical Institute and Department of Molecular Biophysics and Biochemistry, Yale University, New Haven.

Car, R. and Parrinello, M. (1985). Unified approach for molecular dynamics and density-functional theory, *Phys. Rev. Lett.* **55**: 2471–2474.

Cassam-Chenaï, P. and Jayatilaka, D. (2001). Some fundamental problems with zero flux partitioning of electron densities, *Theor. Chem. Acc.* **105**: 213–218.

Cassam-Chenaï, P. and Jayatilaka, D. (2002). A complement to some fundamental problems with zero flux partitioning of electron densities, *Theor. Chem. Acc.* **107**: 383–384.

Cavazzoni, C., Colle, R., Farchioni, R. and Grosso, G. (2002). Car-parrinello molecular dynamics study of electronic and structural properties of neutral polyanilines, *Phys. Rev. B* **66**: 165110.

Checinska, L., Mebs, S., Hübschle, C. B., Frster, D., Morgenroth, W. and Luger, P. (2006). Reproducibilitz and transferabilitz of topological data: experimental, charge density study of two modifications of l-alanyl-l-tyrosyl-l-alanine, *Org. Biomol. Chem.* **4**: 3242–3251.

Clementi, E. and Roetti, C. (1974). Roothaan-Hartree-Fock atomic wavefunctions: Basis functions and their coefficients for ground and certain excited states of neutral and ionized atoms, Z$\leq$54, *Atomic Data and Nuclear Data Tables* **14**: 177–478.

Collins, D. M. (1982). Electron density images from imperfect data by iterative entropy maximization, *Nature* **298**: 49–51.

Coppens, P. (1997). *X-Ray Charge Densities and Chemical Bonding*, Oxford University Press, New York.

Coppens, P. (1998). Charge-density analysis at the turn of the century, *Acta. Cryst.* **A54**: 779–788.

Coppens, P. (2005). Charge densities come of age, *Angew. Chem. Int. Ed.* **44**: 6810–6811.

Coppens, P., Guru Row, T. N., Leung, P., Stevens, E. D., Becker, P. J. and Yang, Y. W. (1979). Net atomic charges and molecular dipole moments from spherical-atom x-ray refinements, and the relation between atomic charge and shape, *Acta. Cryst.* **A35**: 63–72.

Coppens, P. and Volkov, A. (2004). The interplay between experiment and theory in charge-density analysis, *Acta Cryst.* **A60**: 357–364.

Cyranski, M. K., Jezierska, A., Klimentowska, P., Panek, J. J., Zukowska, G. Z. and Sporzynski, A. (2008). Structural and spectroscopic properties of an aliphatic boronic acid studied by combination of experimental and theoretical methods, *J. Chem. Phys.* **128**: 124512.

Dauter, Z., Lamzin, V. S. and Wilson, K. S. (1997). The benefits of atomic resolution, *Curr. Opin. Struct. Biol.* **7**: 681–688.

de Vries, R., Briels, W., Fell, D., Velde, G. t. and Baerends, E. (1996). Charge density study with the Maximum Entropy Method on model data of silicon. A search for non-nuclear attractors, *Can. J. Chem.* **74**: 1054–1058.

de Vries, R. Y., Briels, W. J. and Feil, D. (1994). Novel treatment of the experimental data in the application of the maximum-entropy method to the determination of the electron-density distribution from X-ray experiments, *Acta Cryst.* **A50**: 383–391.

de Vries, R. Y., Briels, W. J. and Feil, D. (1996). Critical analysis of non-nuclear electron-density maxima and the maximum entropy method, *Phys. Rev. Lett.* **77**: 1719–1722.

Delle Site, L. (2002). Baders interatomic surfaces are unique, *Theor. Chem. Acc.* **107**: 378–380.

Destro, R., Marsh, R. E. and Bianchi, R. (1988). A low-temperature (23 K) study of L-alanine, *J. Phys. Chem.* **92**: 966–973.

Destro, R., Roversi, P., Barzaghi, M. and Marsh, R. E. (2000). Experimental charge density of *alpha*-glycine at 23 K, *J. Phys. Chem. A* **104**: 1047–1054.

Dinnebier, R. E., Schneider, M., van Smaalen, S., Olbrich, F. and Behrens, U. (1999). Disorder detrmined by high-resoultion powder diffraction: structure of pentamethylcyclopentadienyllithium, *Acta. Cryst.* **B55**: 35–44.

Dittrich, B., Hübschle, C. B., Luger, P. and Spackman, M. A. (2006). Introduction and validation of an invariom database for amino-acid, peptide and protein molecules, *Acta Cryst.* **D62**: 1325–1335.

Dittrich, B., Hübschle, C. B., Messerschmidt, M., Kalinowski, R., Girnt, D. and Luger, P. (2005). The invariom model and its application: refinement of *D*,*L*-serine at different temperatures and resolution, *Acta Cryst.* **A61**: 314–320.

Dittrich, B., Hübschle, C. B., Pröpper, K., Dietrich, F., Stolper, T. and Holstein, J. (2013). The generalized invariom database (GID), *Acta Cryst.* **B69**: sn5118.

Dittrich, B., Hübschle, C., Holstein, J. and Fabbiani, F. P. (2009). Towards extracting the charge density from normal-resolution data, *J. Appl. Cryst.* **42**: 1110–1121.

Dittrich, B., Koritsanszky, T. and Luger, P. (2004). A simple approach to nonspherical electron densities by using invarioms, *Angew. Chem. Int. Ed.* **43**: 2718–2721.

Dittrich, B., McKinnon, J. J. and Warren, J. E. (2008). Improvement of anisotropic displacement parameters from invariom-model refinements for three L-hydroxylysine structures, *Acta Cryst.* **B64**: 750–759.

Dittrich, B., Munshi, P. and Spackman, M. A. (2007). Redetermination, invariom model and multipole refinement of L-ornithine hydrochloride, *Acta Cryst.* **B63**: 505–509.

Dittrich, B., Strumpel, M., Schäfer, M., Spackman, M. A. and Koritsánszky, T. (2006a). Invarioms for improved absolute structure determination of light-atom crystal structures, *Acta Cryst.* **A62**: 217–223.

Dittrich, B., Weber, M., Kalinowski, R., Grabowsky, S., Hübschle, C. B. and Luger, P. (2009a). How to easily replace the independent atom model - the example of bergenin, a potential anti-HIV agent of traditional Asian medicine, *Acta Cryst.* **B65**: 749–756.

Domagała, S., Fournier, B., Liebschner, D., Guillot, B. and Jelsch, C. (2012). An improved experimental databank of transferable multipolar atom models elmam2. construction details and applications, *Acta. Cryst.* **A68**: 337–351.

Dominiak, P. M., Volkov, A., Li, X., Messerschmidt, M. and Coppens, P. (2007). A theoretical databank of transferable aspherical atoms and its application to electrostatic interaction energy calculations of macromolecules, *J. Chem. Theory and Comput.* **3**: 232–247.

Downs, R. T., Gibbs, G. V., Jr., M. B. B. and Rosso, K. M. (2002). A comparison of procrystal and ab initio model representations of the electron-density distributions of minerals, *Phys. Chem. Miner.* **29**: 369–385.

Espinosa, E., Souhassou, M., Lachekar, H. and Lecomte, C. (1999). Topolgical analysis of the electron density in hydrogen bonds, *Acta Cryst.* **B55**: 563–572.

Farrugia, L. J. (1999). *WinGX* suite for small-molecule single-crystal crystallography, *J. Appl. Cryst.* **32**: 837–838.

Farrugia, L. J. (2012). Personal communication.

Flensburg, C., Larsen, S. and Stewart, R. F. (1995). Experimental charge density study of methylammonium hydrogen succinate monohydrate. a salt with a very short o–h–o hydrogen bond, *J. Phys. Chem.* **99**: 10130–10141.

Gaigeot, M.-P. (2008). Alanine polypeptide structural fingerprints at room temperature: What can be gained from non-harmonic carparrinello molecular dynamics simulations, *J. Phys. Chem. A* **112**: 13507–13517.

Gatti, C. and Macchi, P. (2012). *Modern Charge-Density Analysis*, Springer.

Ghermani, N., Bouhmaida, N. and Lecomte, C. (1992). *ELECTROS: Computer program to calculate electrostatic properties from high-resolution x-ray diffraction*, University of Nancy 1, Nancy, France.

Gilmore, C. J. (1996). Maximum Entropy and Bayesian Statistics in Crystallography: a Review of Practical Applications, *Acta Cryst.* **A52**: 561–589.

Guillot, B., Jelsch, C., Podjarny, A. and Lecomte, C. (2008). Charge density analysis of a protein structure at subatomic resolution the human aldose reductase case, *Acta. Cryst.* **D64**: 567–588.

Gull, S. F. (1989). *Maximum Entropy and Bayesian Methods*, Dordrecht:Kluwer.

Gull, S. F. and Daniell, G. J. (1978). Image reconstruction ffrom incomplete and noisy data, *Nature* **272**: 686–690.

Hakanpää, J., Linder, M., Popov, A., Schmidt, A. and Rouvinen, J. (2006). Hydrophobin hfbii in detail: ultrahigh-resolution structure at 0.75 Å, *Acta Cryst.* **D62**: 356–367.

Hall, S. R. and McMahon, B. (eds) (2006). *International Tables for Crystallography Vol. G*, Online edition, http://it.iucr.org/G/.

Hansen, N. K. and Coppens, P. (1978). Testing aspherical atom refinements on small-molecule data sets, *Acta Cryst.* **A34**: 909–921.

Henkelman, G., Arnaldsson, A. and Jónsson, H. (2006). A fast and robust algorithm for bader decomposition of charge density, *Comput. Mater. Sci.* **36**: 354–360.

Hirshfeld, F. L. (1976). Can X-ray data distinguish bonding effects from vibrational smearing?, *Acta Cryst.* **A32**: 239–244.

Hirshfeld, F. L. (1991). Electron density distributions in molecules, *Crystallography Reviews* **2**: 169–200.

Hofmann, A., Kalinowski, R., Luger, P. and van Smaalen, S. (2007b). Accurate charge density of the tripeptide ala-pro-ala with the maximum entropy method (mem): influence of data resolution, *Acta Cryst.* **B63**: 633–643.

Hofmann, A., Netzel, J. and van Smaalen, S. (2007a). Accurate charge density of trialanine: a comparison of the multipole formalism and the maximum entropy method (MEM), *Acta Cryst.* **B63**: 285–295.

Housset, D., Benabicha, F., Pichon-Pesme, V., Jelsch, C., Maierhofer, A., David, S., Fontecilla-Camps, J. C. and Lecomte, C. (2000). Towards the charge-density study of proteins: a room-temperature scorpion-toxin structure at 0.96 Å resolution as a first test case, *Acta. Cryst.* **D56**: 151–160.

Hübschle, C. B. and Dittrich, B. (2011). MoleCoolQt - a molecule viewer for charge-density research, *J. Appl. Cryst.* **44**: 238–240.

Hübschle, C. B., Luger, P. and Dittrich, B. (2007). Automation of invariom and of experimental charge density modelling of organic molecules with the preprocessor program invariomtool, *J. Appl. Cryst.* **40**: 623–627.

Iversen, B. B., Krebs Larsen, F., souhassou, M. and Takata, M. (1995). Experimental evidence for the existence of non-nuclear maxima in the electron-density distribution of metallic beryllium. a comparative study of the maximum entropy method and the multipole refinement method, *Acta Cryst.* **B51**: 580–591.

Jarzembska, K. N. and Dominiak, P. M. (2012). New version of the theoretical databank of transferable aspherical pseudoatoms, ubdb2011 – towards nucleic acid modelling, *Acta Cryst.* **A68**: 139–147.

Jauch, W. (1994). The maximum-entropy method in charge-density studies. II. General aspects of reliability, *Acta. Cryst.* **A50**: 650–652.

Jauch, W. and Palmer, A. (1993). The maximum-entropy method in charge-density studies: aspects of reliability, *Acta. Cryst.* **A49**: 590–591.

Jaynes, E. T. (1957). Information theory and statistical mechanics, *Phys. Rev.* **106**: 620–630.

Jaynes, E. T. (1979). *The Maximum Entropy Formalism*, Cambridge: MIT Press, Cambridge.

Jaynes, E. T. (1986). *Maximum Entropy and Bayesian Methods in Applied Statistics*, Cambridge University Press, Cambridge.

Jelsch, C., Guillot, B., Lagoutte, A. and Lecomte, C. (2005). Advances in protein and small-molecule charge-density refinement methods using *mopro*, *J. Appl. Cryst.* **38**: 38–54.

Jelsch, C., Pichon-Pesme, V., Lecomte, C. and Aubry, A. (1998). Transferability of multipole charge-density parameters: Application to very high resolution oligopeptide and protein structures, *Acta Cryst.* **D54**: 1306–1318.

Jelsch, C., Teeter, M. M., Lamzin, V., Pichon-Pesme, V., Blessing, R. H. and Lecomte, C. (2000). Accurate protein crystalklography at ultra high resoltuion: Valence electron distribution in crambin, *Proc. Natl. Acad. Sci. U. S. A.* **97**: 3171–3176.

Jiang, J. S. and Brünger, A. T. (1994). Protein hydration observed by x-ray diffraction solvation properties of penicillopepsin and neuraminidase crystal structures, *J. Mol. Biol.* **243**: 100–115.

Kang, B. S., Devedjiev, Y., Derewenda, U. and Derewenda, Z. S. (2004). The pdz2 domain of syntenin at ultra-high resolution: Bridging the gap between macromolecular and small molecule crystallography, *J. Mol. Biol.* **338**: 483–493.

Katan, C., Rabiller, P., Lecomte, C., Guezo, M., Oison, V. and Souhassou, M. (2003). Numerical computation of critical properties and atomic basins from three-dimensional grid electron densities, *J. Appl. Cryst.* **36**: 65–73.

Kato, K., Ohishi, Y., Takata, M., Nishibori, E., Sakata, M. and Moritomo, Y. (2005). Evidence of a pressure-induced orbital transition in a layered manganite, *Phys. Rev. B* **71**: 012404.

Keith, T. A. (2011). *AIMAll*, TK Gristmill Software, aim.tkgristmill.com, Overland Park KS, USA.

Ko, T.-P., Robinson, H., Gao, Y.-G., Cheng, C.-H. C., DeVries, A. L. and Wang, A. H.-J. (2003). The refined crystal structure of an eel pout type iii antifreeze protein rd1 at 0.62 Å resolution reveals structural microheterogeneity of protein and solvation, *Biophysical Journal* **84**: 1228–1237.

Koritsanszky, T. S. and Coppens, P. (2001). Chemical applications of x-ray charge-density analysis, *Chemical Reviews* **101**: 1583–1628.

Kryachko, E. S. (2002). Comments on some fundamental problem with zero flux partitioning of electron densities, *Theor. Chem. Acc.* **107**: 375–377.

Kumazawa, S., Takata, M. and Sakata, M. (1995). An accurate detrmination of teh thermal vibration of rutile from the nuclear densuty distribution of the maximum-entropy analysis, *Acta. Cryst.* **A51**: 651–658.

Li, J. (2005). General explicit difference formulas for numerical differentiation, *J. Comput. Appl. Math.* **183**: 29–52.

Li, L., Wolfel, A., Schonleber, A., Mondal, S., Schreurs, A. M. M., Kroon-Batenburg, L. M. J. and van Smaalen, S. (2011). Modulated anharmonic adps are intrinsic to aperiodic crystals: a case study on incommensurate Rb_2ZnCl_4, *Acta Cryst.* **B67**: 205–217.

Macchi, P. (2012). Personal communication.

Martin, A. and Pinkerton, A. A. (1998). Charge density studies using ccd detectors: Oxalic acid at 100 K revisited, *Acta. Cryst.* **B54**: 471–477.

Matta, C. F. and Boyd, R. J. (eds) (2007). *The Quantum Theory of Atoms in Molecules: From Solid State to DNA and Drug Design*, Wiley-VCH, Weinheim.

Mebs, S., Messerschmidt, M. and Luger, P. (2006). Experimental charge density of an l-phenylalanine formic acid complex with a short hydrogen bond determined at 25 K, *Z. Kristallogr.* **221**: 656–664.

Meindl, K. and Henn, J. (2008). Foundations of residual-density analysis, *Acta Cryst.* **A64**: 404–418.

Mohallem, J. R. (2002). Molecular structure and baders theory, *Theor. Chem. Acc.* **107**: 372–374.

Mondal, S., Prathapa, S. J. and van Smaalen, S. (2012). Experimental dynamic electron densities of multipole models at different temperatures, *Acta. Cryst.* **A68**: 568–581.

Netzel, J., Hofmann, A. and van Smaalen, S. (2008). Accurate charge density of α-glycine by the maximum entropy method, *Cryst. Eng. Comm.* **10**: 335–343.

Netzel, J. and van Smaalen, S. (2009). Topological properties of hydrogen bonds and covalent bonds from charge densities obtained by the maximum entropy method (MEM), *Acta. Cryst.* **B65**: 624–638.

Netzel, J. and van Smaalen, S. (2013). Static and dynamic densiies of lysozyme, *unpublished* .

Nijveldt, D. and Vos, A. (1988). Single-crystal x-ray geometries and electron density distributions of cyclopropane, bicyclopropyl and vinylcyclopropane. II. multipole refinements and dynamic electron density distributions, *Acta Cryst.* **B44**: 289–296.

Nishibori, E., Sunaoshi, E., Yoshida, A., Aoyagi, S., Kato, K., Takata, M. and Sakata, M. (2007). Accurate structure factors and experimental charge densities from synchrotron x-ray powder, *Acta Cryst.* **A63**: 43–52.

Noury, S., Krokidis, X., F., F. and Silvi, B. (1999). Computational tools for the electron localization function topological analysis, *Computers and Chemistry* **23**: 597–604.

Ohno, A., Sasaki, S., Nishibori, E., Aoyagi, S., Sakata, M. and Iversen, B. B. (2007). X-ray charge density study of chemical bonding in skutterudite cosb3, *Phys. Rev. B* **76**: 064119.

Palatinus, L. (2003). *Maximum Entropy Method in Superspace Crystallography*, University Bayreuth, Bayreuth, Germany. Doctoral Thesis.

Palatinus, L. (2004). *Ab intitio* determination of incommensurately modulated structures by charge flipping in superspace, *Acta Cryst.* **A60**: 604–610.

Palatinus, L. and Chapuis, G. (2007). *SUPERFLIP* – a computer program for the solution of crystal structures by charge flipping in arbitrary dimensions, *J. Appl. Cryst.* **40**: 786–790.

Palatinus, L., Prathapa, S. J. and van Smaalen S. (2012). Edma - a computer program for the topological analysis of discrete electron densities, *J. Appl. Cryst.* **45**: 575–580.

Palatinus, L. and van Smaalen, S. (2002). The generalized F constraint in the maximum-entropy method – a study on simulated data, *Acta Cryst.* **A58**: 559–567.

Palatinus, L. and van Smaalen, S. (2004). Incommensurate modulations made visible by the maximum entropy method in superspace, *Z. Kristallogr.* **219**: 719–729.

Palatinus, L. and van Smaalen, S. (2005). The prior-derived F constraints in the maximum-entropy method, *Acta Cryst.* **A61**: 363–372.

Papoular, R. J., Collin, G., Colson, D. and Viallet, V. (2002). Direct imaging of fractional oxygen o[sub delta] in hg-based high-t[sub c] superconductors, *AIP Conference Proceedings* **617**: 204–226.

Parthasarathy, S. and Murthy, M. (2000). Protein thermal stability: insights from atomic displacement parameters (b values)., *Protein. Eng.* **13**: 9–13.

Petříček, V., Dušek, M. and Palatinus, L. (2006). *The crystallographic computing system JANA2006*, Institute of Physics, Praha, Czech Republic.

Phillips, S. E. V. (1980). Structure and refinement of oxymyoglobin at l.6 Å resolution, *J. Mol. Biol.* **142**: 531–554.

Pichon-Pesme, V., Jelsch, C., Guillot, B. and Lecomte, C. (2004). A comparison between experimental and theoretical aspherical-atom scattering factors for charge-density refinement of large molecules, *Acta. Cryst.* **A60**: 204–208.

Pichon-Pesme, V., Lecomte, C. and Lachekar, H. (1995). On building a data bank of transferable experimental electron density parameters: Application to polypeptides, *J. Phys. Chem.* **99**: 6242–6250.

Podjarny, A., Howard, E., Mitschler, A., Chevrier, B., Lecomte, C., Guillot, B., Pichon-Pesme, V. and Jelsch, C. (2002). X-ray crystallography at subatomic resolution, *Europhysics News* **33**: 113–117.

Popelier, P. L. A. (1996). Morphy, a program for an automatic atoms in molecules analysis, *Comp. Phys. Comm.* **93**: 212–240.

Prathapa, S. J., Mondal, S. and van Smaalen, S. (2013). Electron densities by the maximum entropy method for various types of prior densities: a case study on three amino acids and a tripeptide, *Acta Cryst.* **B69**: 203–213.

Press, W. H., Teukolsky, S. A., Vetterling, W. T. and Flannery, B. P. (1996). *Numerical Recipes in Fortran 77, Second Edition*, Cambridge University Press.

Rabiller, P., Souhassou, M., Katan, C., Gatti, C. and Lecomte, C. (2004). Accuracy of topological analysis of gridded electron densities, *J. Phys. Chem. Sol.* **65**: 1951–1955.

Röttger, K., Endriss, A., Ihringer, J., Doyleb, S. and Kuhs, W. F. (2012). Lattice constants and thermal expansion of H_2O and D_2O ice I*h* between 10 and 265 K. Addendum, *Acta Cryst.* **B68**: 91.

Roversi, P., Irwin, J. J. and Bricogne, G. (1998). Accurate Charge-Density Studies as an Extension of Bayesian Crystal Structure Determination, *Acta Cryst.* **A54**: 971–996.

Roversi, P., Merati, F., Destro, R. and Barzaghi, M. (1996). Charge density in crystalline citrinin from x-ray diffraction at 19 K, *Can. J. Chem.* **74**: 1145–1161.

Ruysink, A. F. J. and Vos, A. (1974). Theoretical calculation of the time-averaged electron density distribution for vibrating ethyne molecules in a model crystal structure, *Acta Cryst.* **A30**: 497–502.

Sakata, M. and Sato, M. (1990). Accurate structure analysis by the maximum-entropy method, *Acta Cryst.* **A46**: 263–270.

Samy, A., Dinnebier, R. E., van Smaalen, S. and Jansen, M. (2010). Maximum entropy method and charge flipping, a powerful combination to visualize the true nature of structural disorder from in situ x-ray powder diffraction data, *Acta. Cryst.* **B66**: 184–195.

Sanville, E., Kenny, S. D., Smith, R. and Henkelman, G. (2007). An improved grid-based algorithm for bader charge allocation, *J. Comp. Chem.* **28**: 899–908.

Schmidt, A. and Lamzin, V. S. (2002). Veni, vidi, vici atomic resolution unravelling the mysteries of protein function, *Curr. Opin. Struct. Biol.* **12**: 698–703.

Schmidt, A., Teeter, M., Weckert, E. and Lamzin, V. S. (2011). Crystal structure of small protein crambin at 0.48 Å resolution, *Acta. Cryst.* **F67**: 424–428.

Shaik, S., Danovich, D., Silvi, B., Lauvergnat, D. L. and Hibert, P. C. (2005). Charge-shift bonding—a class of electron-pair bonds that emerges from valence bond theory and is supported by the electron localization function approach, *Chem. Eur. J.* **11**: 6358–6371.

Shannon, C. E. (1948). A mathematical theory of communication, *Bell Sys. Tech.* **27**: 379–423.

Sheldrick, G. M. (2008a). A short history of *SHELX*, *Acta. Cryst.* **A64**: 112–122.

Sheldrick, G. M. (2008b). A short history of *shelx*, *Acta Cryst.* **A64**: 112–122.

Skilling, J. (1989). *Maximum Entropy and Bayesian Methods*, Dordrecht:Kluwer.

Skilling, J. and Bryan, R. K. (1984). Maximum entropy image reconstruction: general algorithm, *Mon. Not. R. astr. Soc.* **211**: 111–124.

Souhassou, M. and Blessing, H. (1999). Topological analysis of experimental electron densities, *J. Appl. Cryst.* **32**: 210–217.

Spackman, M. A. (1992). Molecular electric moments from x-ray diffraction data, *Chemical Reviews* **92**: 1769–1797.

Spackman, M. A. (1999). Hydrogen bond energetics from topological analysis of eperimental electron densities: Recognising the importance of the promolecule, *Chem. Phys. Lett.* **301**: 425–429.

Stash, A. I. and Tsirelson, V. G. (2002a). Winxpro: a program for calculating crystal and molecular properties using multipole parameters of the electron density, *J. Appl. Cryst.* **35**: 371–373.

Stash, A. I. and Tsirelson, V. G. (2005). Modern possibilities for calculating some properties of molecules and crystals from the experimental electron density, *Crystallogr. Rep.* **50**: 202–209.

Stash, A. and Tsirelson, V. (2002b). Winxpro: a program for calculating crystal and molecular properties using multipole parameters of the electron density, *J. Appl. Cryst.* **35**: 371–373.

Stevens, E. D., Rys, J. and Coppens, P. (1977). Calculation of dynamic electron density distributions from static molecular wave functions, *Acta Cryst.* **A33**: 333–338.

Stewart, R. F. (1968a). The influence of thermal parameters on electron density maps, *Acta Cryst.* **A24**: 497–505.

Stewart, R. F. (1968b). Valence Structure from Coherent X-Ray Scattering: Fourier Difference Synthesis, *J. Chem. Phys* **48**: 4882–4889.

Stewart, R. F. (1969). Generalized X-Ray Scattering Factors, *J. Chem. Phys* **51**: 4569–4577.

Stewart, R. F. (1973). Electron population analysis with generalized x-ray scattering factors: Higher multipoles, *J. Chem. Phys.* **58**: 1668–1676.

Stewart, R. F. (1976). Electron population analysis with rigid pseudoatoms, *Acta Cryst.* **A32**: 565–574.

Stewart, R. F. and Spackman, M. A. (1983). VALRAY Users Manual, Department of Chemistry, Carnegie-Mellon University: Pittsburgh.

Stewart, R. F., Spackman, M. A. and Flensburg, C. (1998). *VALRAY98, Users Manual*, Carnegie Mellon University, Pittsburgh, USA, and University of Copenhagen, Denmark.

Su, Z. and Coppens, P. (1998). Nonlinear Least-Squares Fitting of Numerical Relativistic Atomic Wave Functions by a Linear Combination of Slater-Type Functions for Atoms with $Z = 1$–36, *Acta Cryst.* **A54**(5): 646–652.

Takata, M. (2008). The MEM / Rietveld method with nano-applications - accurate charge-density studies of nano-structured materials by synchrotron-radiation powder diffraction, *Acta. Cryst.* **A64**: 232–245.

Takata, M., Umeda, B., Nishibori, E., Sakata, M., Saitot, Y., Ohno, M. and Shinohara, H. (1995). Confirmation by x-ray diffraction of the endohedral nature of the metallofullerene y@c82, *Nature* **377**: 46–49.

Tanaka, H., Takata, M., Nishibori, E., Kato, K., Iishi, T. and Sakata, M. (2002). Enigma: maximum-entropy method program package for huge systems, *J. Appl. Cryst.* **35**: 282–286.

Tang, W., Sanville, E. and Henkelman, G. (2009). A grid-based bader analysis algorithm without lattice bias, *J. Phys.: Condens. Matter* **21**: 084204.

Teeter, M. M. and Hendrickson, W. A. (1979). Highly ordered crystals of the plant seed protein crambin, *J. Mol. Biol.* **127**: 219–223.

van Smaalen, S. (2007). *Incommensurate crystallography*, Oxford University Press, Oxford.

van Smaalen, S. and Li, L. (2009). Modulation functions of aperiodic crystals by the maximum entropy method in superspace, *Phys. Scr.* **79**: 048305.

van Smaalen, S. and Netzel, J. (2009). The maximum-entropy method in accurate charge density studies, *Phys. Scr.* **79**: 048304.

van Smaalen, S., Palatinus, L. and Schneider, M. (2003). Maximum entropy method in superspace, *Acta Cryst.* **A59**: 459–469.

VanEtten, C. H., Nielsen, H. C. and Peters, J. E. (1965). A crystalline polypeptide from the seed of crambe abyssinica, *Phytochemistry.* **4**: 467–473.

Volkov, A., Abramov, Y., Coppens, P. and Gatti, C. (2000). On the origin of topological differences between experimental and theoretical crystal charge densities, *Acta Cryst.* **A56**: 332–339.

Volkov, A., Gatti, C., Abramov, Y. and Coppens, P. (2000). Evaluation of net atomic charges and atomic and molecular electrostatic moments through topological analysis of the experimental charge density, *Acta Cryst.* **A56**: 252–258.

Volkov, A., Li, X., Koritsanszky, T. and Coppens, P. (2004). Ab initio quality electrostatic atomic and molecular properties including intermolecular energies from a transferable theoretical pseudoatom databank, *J. Phys. Chem. A.* **108**: 4283–4300.

Volkov, A., Macchi, P., Farrugia, L. J., Gatti, C., Mallinson, P. R., Richter, T. and Koritsanszky, T. (2006). *XD2006, A Computer Program Package for Multipole Refinement, Topological Analysis of Charge Densities and Evaluation of Intermolecular Energies from Experimental or Theoretical Structure Factors.*

Volkov, A., Messerschmidt, M. and Coppens, P. (2007). Improving the scattering-factor formalism in protein refinement: application of the University at Buffalo Aspherical-Atom Databank to polypeptide structures, *Acta Cryst.* **D63**: 160–170.

Wang, C. R., Kai, T., Tomiyama, T., Yoshida, T., Kobayashi, Y., Nishibori, E., Takata, M., Sakata, M. and Shinohara, H. (2001). A scandium carbide endohedral metallofullerene: (sc2c2)@c84, *Angew. Chem. Int. Ed.* **40**: 397–399.

Wang, J., Dauter, M., Alkire, R., Joachimiak, A. and Dauter, Z. (2007). Triclinic lysozyme at 0.65 Å resolution, *Acta Cryst.* **D63**: 1254–1268.

Weber, T., Dshemuchadse, J., Kobas, M., Conrad, M., Harbrecht, B. and Steurer, W. (2009). Large, larger, largest – a family of cluster-based tantalum copper aluminides with giant unit cells. i. structure solution and refinement, *Acta Cryst.* **B65**: 308–317.

Yamano, A. and Teeter, M. M. (1994). Correlated disorder of the pure pro^{22}/leu^{25} form of crambin at 150 K refined to 1.05-Å resolution., *J. Biol. Chem.* **269**: 13956–13965.

Yuan, Z., Zhao, J. and Wang, Z.-X. (2003). Flexibility analysis of enzyme active sites by crystallographic temperature factors., *Protein. Eng.* **16**: 109–114.

Zarychta, B., Pichon-Pesme, V., Guillot, B., Lecomte, C. and Jelsch, C. (2007). On the application of an experimental multipolar pseudo-atom library for accurate refinement of small-molecule and protein crystal structures, *Acta. Cryst.* **A63**: 108–125.

Zhang, L., Ying, F., Wu, W., Hiberty, P. C. and Shaik, S. (2009). Topology of electron charge density for chemical bonds from valence bond theory: a probe of bonding types, *Chemistry* **15**: 2979–2989.

Publications

Parts of this thesis published in the international scientific literature or have been submitted for publication:

Chapter 3:
L. Palatinus, S. J. Prathapa, S. Van Smaalen
EDMA: a computer program for topological analysis of discrete electron densities.
Journal of Applied Crystallography, **45**, 575-580, (2012)

Chapter 4:
S. Mondal, S. J. Prathapa, S. Van Smaalen
Experimental dynamic electron densities of multipole models at different temperatures.
Acta Crystallographica A, **68**, 568-581, (2012).

Chapter 5:
S. J. Prathapa, S. Mondal, S. Van Smaalen
Electron densities by the maximum entropy method (MEM) for various types of prior densities: a case study on three amino acids and a tripeptide.
Acta Crystallographica B, **69**, 203-213, (2013).

Chapter 6:
S. J. Prathapa, J. Netzel, S. Van Smaalen
Topological Properties of Chemical bonds from Static and Dynamic Electron Densities.
Z. Anorg. Allg. Chem., in press (2013).

Acknowledgements

First of all, I would like to express my deepest gratitude towards my research supervisor and mentor, Prof. dr. Sander van Smaalen for giving me an opportunity to pursue my PhD in the Laboratory of Crystallography, University of Bayreuth. His constant encouragement, support, and invaluable suggestions made this thesis possible.

I am thankful to Dr. Lukáš Palatinus for the computer program EDMA and all the collaborative work.

I would like to thank Dr. Swastik Mondal for his valuable suggestions and discussions throughout my PhD life and also for proof reading of my thesis.

I sincerely thank Dr. Joachim Angelkort who helped me at different stages of my PhD life. Especially, I would like to mention his help to translate my English summary into the Zusammenfassung of my PhD thesis. A special thank goes to PD Dr. Andreas Schönleber and Alexander Wölfel who also helped me in different issues throughout my PhD life as well as for correcting my poor German writing.

I would like to thank Denise Kelk-Huth, for all her help both professionally and personally during my stay in Bayreuth. I am grateful to Franz Fischer and Alfred Suttner who has helped me whenever I had a problem with computers or other technical issues.

I am very much thankful to my present lab members, SK Imran Ali, Zhang Jian, Leila Nohinejaad, Somnath dey, Maxim Bykov, Dr. Jeanette Netzel and Dr. Julian Henn. And my past lab members Dr. Li Liang and Dr. Magdalena Małecka who all made my stay in Bayreuth quite enjoyable.

My special thank goes to my dear friends Dr. Yamini Avadhut and Kedar who have helped me immensely during the various stages of my PhD life in Bayreuth. I am indebted to them for providing me the accommodation during the final stages of my PhD life. Their love and caring nature made me feel at home. My special thanks goes to Bayreuth Indians group for nice get-togethers and interactions.

My sincere thank goes to Prof. dr. T. N. Guru Row, IISc, Bengaluru who has introduced me to the the field of crystallography. Last but not the least, I would like to thank my parents, all members of my family and my dear friends for their never ending support, encouragements, affection and care which kept me focused and motivated.

Declaration

Ich versichere hiermit eidesstattlich, dass ich diese Dissertation selbstständig und nur unter Verwendung angebener Quellen und zulässiger Hilfsmittel erstellt habe. Ich habe bisher keine Promotionsversuche unternommen. Ich habe bisher weder die Hilfe von gewerblichen Promotionsberatern bzw. -vermittlern in Anspruch genommen, noch werde ich sie künftig in Anspruch nehmen.

Prathapa Siriyara Jagannatha

Bayreuth, 2013